Rangin, C., Silver, E., von Breymann, M. T., et al., 1990
Proceedings of the Ocean Drilling Program, Initial Reports, Vol. 124

10. SITE 767[1]

Shipboard Scientific Party[2]

HOLE 767A

Date occupied: 10 November 1988

Date departed: 10 November 1988

Time on hole: 21 hr

Position: 4°47.47′N, 123°30.21′E

Bottom felt (rig floor; m, drill-pipe measurement): 4916.3

Distance between rig floor and sea level (m): 10.70

Water depth (drill-pipe measurement from sea level, m): 4905.6

Total depth (rig floor; m): 4920.50

Penetration (m): 4.20

Number of cores (including cores with no recovery): 1

Total length of cored section (m): 4.20

Total core recovered (m): 4.14

Core recovery (%): 98

Oldest sediment cored:
Depth (mbsf): 4.20
Nature: clayey silt and vitric ash
Age: Pleistocene
Measured velocity (km/s): not available (see text)

HOLE 767B

Date occupied: 10 November 1988

Date departed: 20 November 1988

Time on hole: 10 days, 5 hr, 15 min

Position: 4°47.49′N, 123°30.20′E

Bottom felt (rig floor; m, drill-pipe measurement): 4916.0

Distance between rig floor and sea level (m): 10.70

Water depth (drill-pipe measurement from sea level, m): 4905.3

Total depth (rig floor; m): 5655.00

Penetration (m): 739.00

Number of cores (including cores with no recovery): 78

Total length of cored section (m): 739.00

Total core recovered (m): 585.05

Core recovery (%): 79

Oldest sediment cored:
Depth (mbsf): 739.00
Nature: claystone
Age: late Oligocene
Measured velocity (km/s): not available (see text)

[1] Rangin, C., Silver, E., von Breymann, M. T., et al., 1990. *Proc. ODP, Init. Repts.*, 124: College Station, TX (Ocean Drilling Program).

[2] Shipboard Scientific Party is as given in the list of participants preceding the contents.

HOLE 767C

Date occupied: 20 November 1988

Date departed: 26 November 1988

Time on hole: 5 days, 3 hr

Position: 4°47.50′N, 123°30.21′E

Bottom felt (rig floor; m, drill-pipe measurement): 4916.0

Distance between rig floor and sea level (m): 10.70

Water depth (drill-pipe measurement from sea level, m): 4905.3

Total depth (rig floor; m): 5710.10

Penetration (m): 794.10

Number of cores (including cores with no recovery): 13

Total length of cored section (m): 114.1

Total core recovered (m): 44.67

Core recovery (%): 39

Oldest sediment cored:
Depth (mbsf): 786.6
Nature: claystone
Age: late middle Eocene
Measured velocity (km/s): 1.93

Basement:
Depth (mbsf): 786.9
Nature: basalt
Measured velocity (km/s): 4.91

Principal results: Three holes were drilled at Site 767 (4°47.5′N, 123° 30.2′E, water depth 4905 mbsl) (Table 1). This site records several major events in the history of the Celebes Sea. The basement is basalt and is overlain by middle Eocene red clays. The age is consistent with the magnetic anomaly interpretation by Weissel (1980), but not with the hypothesis of Lee and McCabe (1986). The basal red clays indicate an open-ocean environment. This part of the section corresponds well with that observed at Deep Sea Drilling Project (DSDP) Site 291 (Ingle, Karig, et al., 1975) in the southern Philippine Sea just to the east of the Philippine Islands.

The boundary between Units II and III (Table 2) at 406 mbsf is present in a number of indicators. Methane, ethane, and total organic carbon (TOC) are very low above this level and increase sharply below. The continentality index of clays (defined here as the log of the sum of the abundances of chlorite, smectite, and illite, divided by the abundance of smectite) increases dramatically at 406 mbsf, and then decreases to red clay levels in the lower part of Subunit IIIC. Biotite disappears below 406 mbsf, and volume magnetic susceptibility drops dramatically. The high susceptibility and biotite content above 406 mbsf indicates the abundance of volcanic ash, whereas the high quartz and plant debris, plus the high TOC, methane, and ethane below that level is a clear indication of continentality.

The maximum in continental indicators and abundances of continent-derived turbidites in Subunit IIIB indicates the greatest continental influence in the middle Miocene. A significant lithologic change occurs between Subunits IIB and IIC (base of the Pliocene) at 300 mbsf, above which the background sediment is silt and below, clay. Bulk and GRAPE density show a decrease just below 300 mbsf, with a corresponding increase in porosity and void ratio. This change suggests greater proximity to the volcanic source region in the Pliocene. Calcareous turbidites are most abundant in Subunit IIB in early Pliocene to Pleistocene time.

Table 1. Coring summary, Site 767.

Core no.	Date (Nov. 1988)	Time (UTC)	Depth (mbsf)	Cored (m)	Recovered (m)	Recovery (%)
1H	10	0130	0-4.2	4.2	4.14	98.6
Coring totals				4.2	4.14	98.6
1H	10	0800	0-9.0	9.0	8.99	99.9
2H	10	0850	9.0-18.5	9.5	9.93	104.0
3H	10	1010	18.5-28.0	9.5	9.92	104.0
4H	10	1115	28.0-37.5	9.5	9.27	97.6
5H	10	1215	37.5-47.0	9.5	10.00	105.2
6H	10	1400	47.0-56.5	9.5	10.00	105.2
7H	10	1700	56.5-66.0	9.5	9.87	104.0
8H	10	1900	66.0-71.5	5.5	5.63	102.0
9H	10	2045	71.5-81.0	9.5	10.04	105.7
10H	10	2150	81.0-90.5	9.5	10.06	105.9
11X	10	2315	90.5-100.0	9.5	0.68	7.2
12X	11	0200	100.0-109.6	9.6	0	0
13X	11	0300	109.6-119.3	9.7	2.77	28.5
14X	11	0350	119.3-128.9	9.6	0.30	3.1
15X	11	0440	128.9-138.6	9.7	3.91	40.3
16X	11	0530	138.6-148.3	9.7	0	0
17X	11	0620	148.3-158.0	9.7	5.58	57.5
18X	11	0710	158.0-167.6	9.6	9.58	99.8
19X	11	0800	167.6-177.3	9.7	9.66	99.6
20X	11	0900	177.3-183.8	6.5	3.96	60.9
21X	11	1001	183.8-193.5	9.7	9.78	101.0
22X	11	1100	193.5-203.3	9.8	8.47	86.4
23X	11	1230	203.3-213.1	9.8	4.04	41.2
24X	11	1345	213.1-222.9	9.8	5.55	56.6
25X	11	1425	222.9-232.6	9.7	9.75	100.0
26X	11	1545	232.6-242.2	9.6	9.20	95.8
27X	11	1645	242.2-251.9	9.7	9.92	102.0
28X	11	1745	251.9-261.4	9.5	9.91	104.0
29X	11	1850	261.4-271.0	9.6	8.70	90.6
30X	11	1950	271.0-280.7	9.7	8.67	89.4
31X	11	2050	280.7-290.4	9.7	3.78	38.9
32X	11	2200	290.4-300.1	9.7	9.25	95.3
33X	11	2345	300.1-309.8	9.7	9.68	99.8
34X	12	0105	309.8-319.4	9.6	9.34	97.3
35X	12	0210	319.4-329.1	9.7	7.46	76.9
36X	12	0320	329.1-338.8	9.7	7.42	76.5
37X	12	0430	338.8-348.5	9.7	7.63	78.6
38X	12	0555	348.5-358.1	9.6	4.48	46.6
39X	12	0711	358.1-367.8	9.7	9.28	95.7
40X	12	0840	367.8-377.5	9.7	7.45	76.8
41X	12	1020	377.5-387.1	9.6	9.69	101.0
42X	12	1150	387.1-396.8	9.7	9.35	96.4
43X	12	1320	396.8-406.5	9.7	4.87	50.2
44X	12	1500	406.5-416.2	9.7	7.74	79.8
45X	12	1810	416.2-425.8	9.6	9.79	102.0
46X	13	1010	425.8-435.4	9.6	9.76	101.0
47X	13	1130	435.4-445.1	9.7	5.28	54.4
48X	13	1315	445.1-454.8	9.7	9.39	96.8
49X	13	1500	454.8-464.1	9.3	3.05	32.8
50X	13	1715	464.1-474.8	10.7	9.78	91.4
51X	13	1915	474.8-484.4	9.6	5.83	60.7
52X	13	2145	484.4-493.0	8.6	9.79	114.0
53X	13	2345	493.0-502.5	9.5	9.60	101.0
54X	14	0145	502.5-512.2	9.7	6.47	66.7
55X	14	0350	512.2-521.1	8.9	8.46	95.0
56X	14	0605	521.1-530.8	9.7	7.05	72.7
57X	14	0800	530.8-540.5	9.7	5.61	57.8
58X	14	1020	540.5-550.2	9.7	9.81	101.0
59X	14	1330	550.2-559.8	9.6	7.84	81.6
60X	14	1730	559.8-569.4	9.6	9.79	102.0
61X	14	1930	569.4-579.1	9.7	4.71	48.5
62X	14	2205	579.1-588.8	9.7	9.77	101.0
63X	15	0045	588.8-598.5	9.7	4.67	48.1
64X	15	0355	598.5-608.2	9.7	9.35	96.4
65X	15	0540	608.2-617.8	9.6	3.90	40.6
66X	15	0740	617.8-627.4	9.6	4.51	47.0
67X	15	1015	627.4-637.1	9.7	9.84	101.0
68X	15	1220	637.1-646.3	9.2	9.79	106.0
69X	15	1450	646.3-656.0	9.7	9.68	99.8
70X	15	1700	656.0-665.6	9.6	7.25	75.5
71X	15	1855	665.6-675.3	9.7	9.78	101.0
72X	15	2100	675.3-684.9	9.6	9.80	102.0
73X	15	2245	684.9-694.6	9.7	9.72	100.0
74X	16	0100	694.6-704.2	9.6	9.74	101.0
75X	16	0300	704.2-713.5	9.3	9.87	106.0

Table 1 (continued).

Core no.	Date (Nov. 1988)	Time (UTC)	Depth (mbsf)	Cored (m)	Recovered (m)	Recovery (%)
76X	16	0450	713.5-723.2	9.7	9.74	100.0
77X	16	0710	723.2-732.9	9.7	2.75	28.3
78X	16	0940	732.9-739.0	6.1	1.32	21.6
Coring totals				739.0	585.05	79.2
1R	21	1745	680.0-689.5	9.5	4.68	49.2
2R	21	1925	689.5-698.5	9.0	3.01	33.4
3R	21	2110	698.5-707.5	9.0	2.27	25.2
4R	21	2350	707.5-716.5	9.0	3.62	40.2
5R	22	0100	716.5-726.2	9.7	4.54	46.8
6R	22	0555	726.2-735.8	9.6	8.17	85.1
7R	22	1445	735.8-743.3	7.5	2.53	33.7
8R	23	0130	743.3-753.0	9.7	4.86	50.1
9R	23	0410	753.0-762.7	9.7	3.55	36.6
10R	23	0725	762.7-772.4	9.7	0	0
11R	23	1330	772.4-782.1	9.7	2.62	27.0
12R	23	1720	782.1-791.7	9.6	4.82	50.2
13R	23	2210	791.7-794.1	2.4	0	0
Coring totals				114.1	44.67	40.0

Paleomagnetic studies of the oriented advanced hydraulic piston corer (APC) samples showed a very clear magnetic stratigraphy in the upper 100 m of the site. Changes in declination document the Brunhes/Matuyama boundary, both boundaries of the Jaramillo Event within the Matuyama, and an unidentified, short event below the Jaramillo, which may indicate a regional excursion or local sedimentary slumps.

The Celebes Sea originated in the middle Eocene in a setting like that of the southern Philippine Sea. From the early Miocene onward, the sea has been the site of high rates of volcanogenic turbidite deposition; but, from the early to late middle Miocene, continental sources played a major role in providing sediments to the basin. By late Miocene time the continental sources were cut off, perhaps because of the initiation of the Cotabato and North Sulawesi trenches, which now act to trap sediment along the margins of the basin. In the late Pleistocene, abundant volcanic ash dominated the sedimentation of the Celebes Sea.

BACKGROUND AND OBJECTIVES

Background

The Celebes Sea is an enclosed marginal basin, surrounded by Mindanao and the Sangihe Arc on the east, the north arm of Sulawesi on the south, Borneo on the west, and the Sulu Archipelago on the north (Fig. 1). The eastern and southern margins of the basin are major thrust belts, although the two thrusts (called the Cotabato Trench on the north and the North Sulawesi Trench on the south) do not connect. A major zone of subduction occurs on the east side of the Sangihe Arc, moving Molucca Sea crust beneath the Celebes Sea (Hatherton and Dickinson, 1968; Silver and Moore, 1978; Hamilton, 1979). Major seismicity is associated with the Cotabato Trench, including a magnitude 8 earthquake in August 1976. Although the Celebes Sea is an enclosed basin, it is open to the Indian Ocean through the Makassar Strait at depths slightly shallower than 1000 m, and to the Pacific Ocean through passages in the Sangihe Arc at depths of about 1500 m (Fig. 2).

Several attempts have been made to date the origin of the Celebes Sea (Fig. 3). Weissel (1980) interpreted the presence of northeast-trending Magnetic Anomalies 18–20 in the western part of the basin, implying an Eocene age for that crust. Lee and McCabe (1986) on the other hand, inferred an age of Late Cretaceous for the whole basin, on the basis of the same magnetic data. Heat flow measurements by Murauchi et al. (1973) lie in the range of 60 mW/m^2 (1.5 HFU), consistent with either estimated age. Corrected depth to basement on Site 767 is

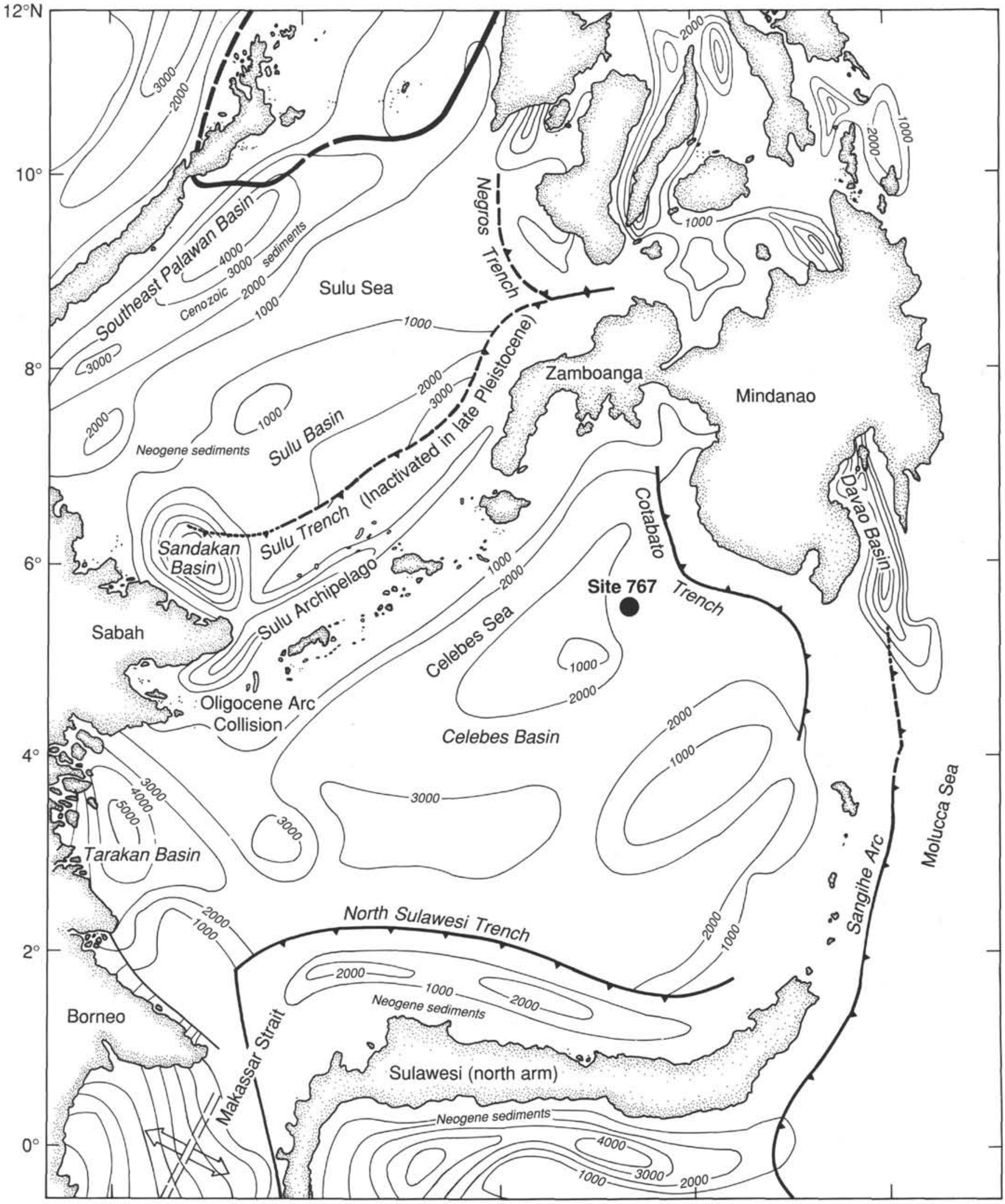

Figure 1. Location map of the Celebes Sea and surrounding region, showing locations of geographic features discussed in text (from Hamilton, 1979). Isopachs for Celebes Basin are for Cenozoic sediments.

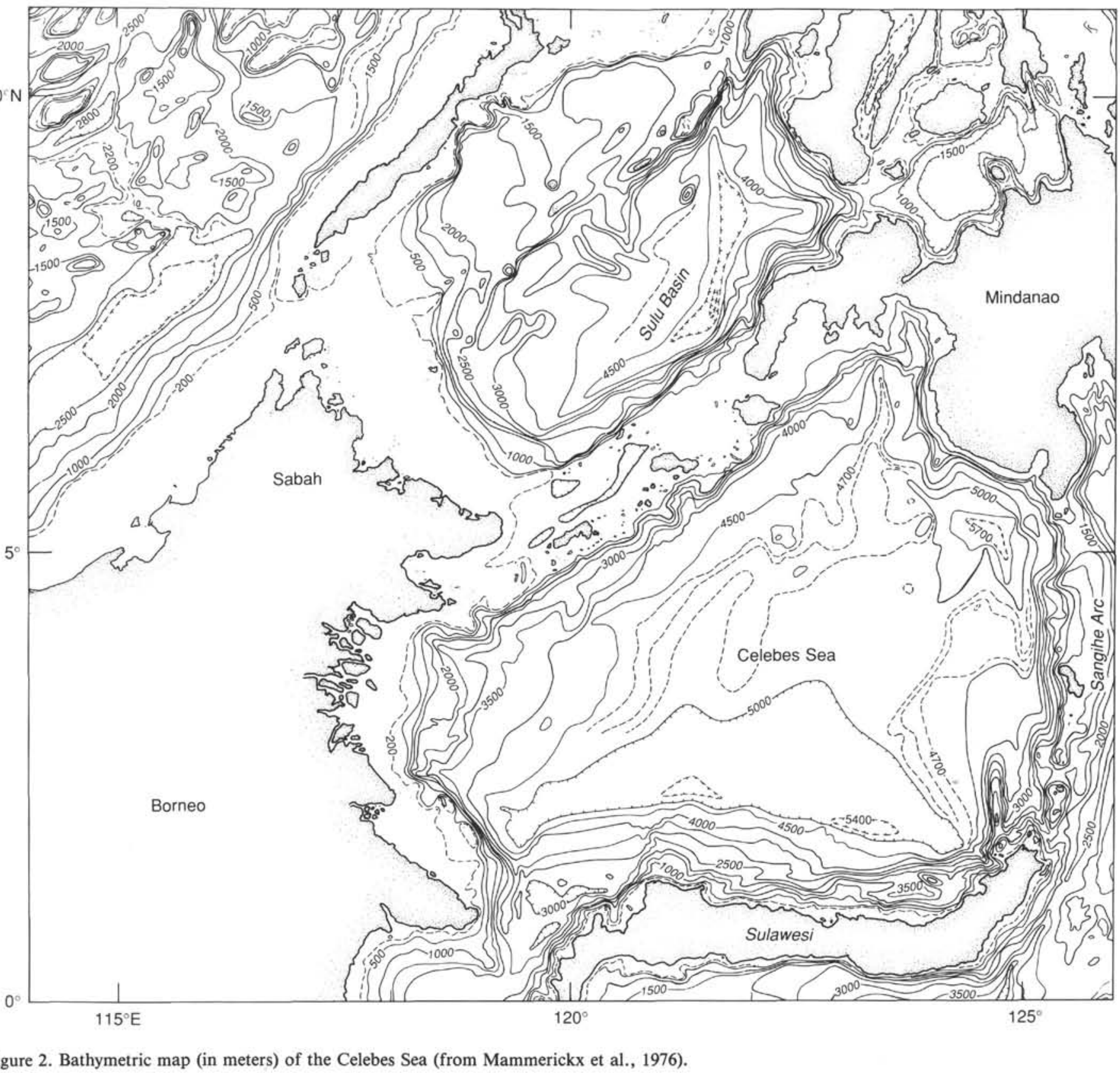

Figure 2. Bathymetric map (in meters) of the Celebes Sea (from Mammerickx et al., 1976).

5200 m, implying an age of approximately 65 Ma (Sclater et al., 1981, determined an age range of 52–65 m.y. based on the age-depth relationship to corrected depth). The actual depth of water at Site 767 is 4905.6 mbsl, with an additional sediment load at the site of approximately 1000 m.

Little seismic study has been made of the Celebes Sea. Hamilton (1979) has published a few Lamont Doherty Geological Observatory single channel seismic profiles, revealing that the sediments thin from more than 2 km thick in the southern part of the basin to less than 1 km in the northern part. No outcrops of Celebes seafloor basement have been observed in the basin. Hinz (BGR unpubl. rept., 103.463, 1988) acquired three multichannel seismic profiles of the northern part of the Cotabato Trench. The structure of the downgoing plate is characterized by tilted fault blocks, but the structural fabric of the oceanic plate is not sufficiently constrained with the available data.

These normal faults are weakly reactivated, possibly due to the flexure of the plate. Evidence for large-scale flexure of the crust may be inferred from the gravity map of the region (Watts, 1975), which shows a broad gravity high of approximately 25 mGal in amplitude and trends roughly parallel to the Cotabato Trench (Fig. 4). Site 767 is located near the crest of the gravity high. Hamilton (1979) reported the presence of a submarine volcano that erupted in 1955, about 130 km south-southeast of the drilling site. The volcano is also located on the crest of the gravity high in the eastern part of the Celebes Sea.

To the east and south, the Celebes Basin is fringed by various subduction zones. Hamilton (1979) and Silver et al. (1983) presented a series of seismic lines across the North Sulawesi Trench and included some coverage of the southern margin of the Celebes Sea. They showed that the accretionary wedge of the northern arm of the Sulawesi increases in width to the west and dies out at the eastern tip. Moore and Silver (1983) published a set of seismic profiles of the southern part of the Cotabato Trench showing that the trench dies out to the south, in the central region of the western Sangihe Arc. In addition, only a few small

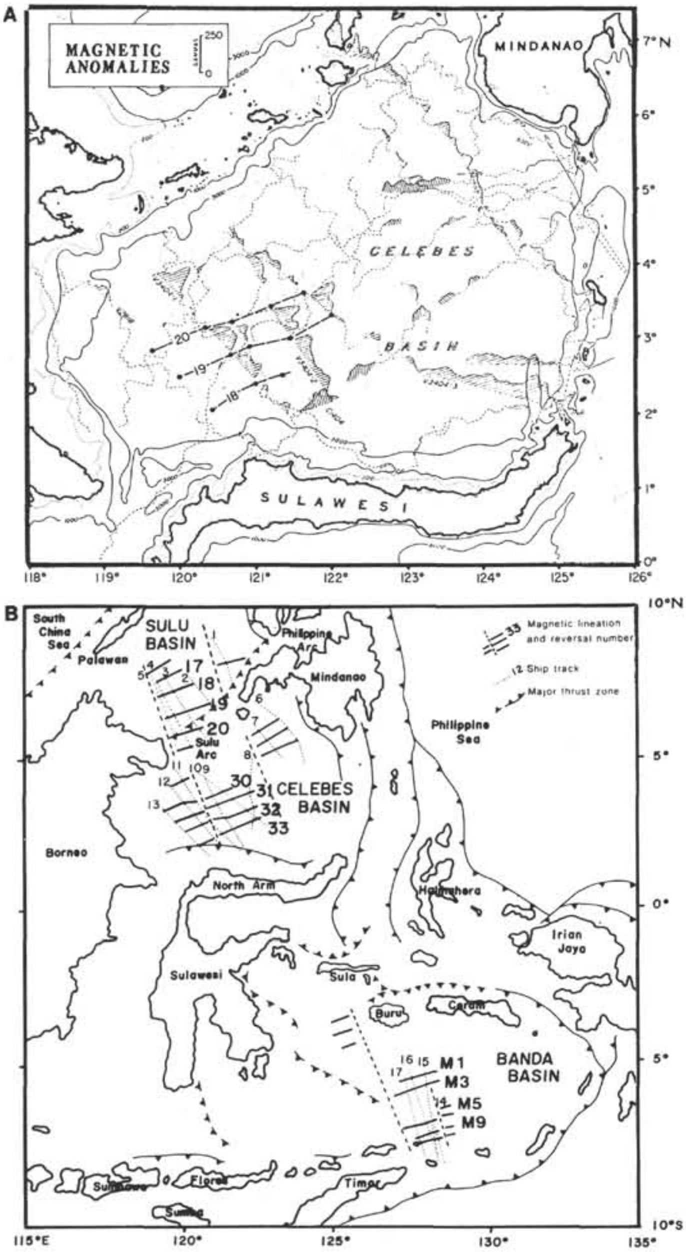

Figure 3. Magnetic anomaly pattern in the Celebes Sea. **A.** Interpretation of Weissel (1980). **B.** Interpretation of Lee and McCabe (1986).

volcanoes are known in the region of the Cotabato Trench, probably related to the trench. They are located onshore between the cities of Cotabato and General Santos. The small volcanoes and the southward dying out of the volcanoes suggests that the trench is a young feature, although we do not have a date on its origin.

The presence of the Cotabato Trench traps sediment brought into the Celebes Sea from Mindanao, just as the North Sulawesi Trench traps debris from north Sulawesi. At the time the Cotabato Trench developed, one would have expected that the sediment supply from Mindanao to the area of Site 767 would have been significantly cut off. Similarly, when the North Sulawesi Trench developed, the sediment supply from the north arm would have greatly diminished. Drilling at Site 767 was intended to provide information on the timing of the development of these trenches.

The structure of the southern margin of the Sulu Ridge was documented by single-channel seismic profiles (Hamilton, 1979). The slope of the southern margin is blanketed by a thick sedimentary apron that covers southeastward-tilted blocks, suggesting a passive margin origin. In contrast, refraction data (Murauchi et al., 1973) reveal an apparent flexure of the Celebes crust approaching the Sulu Archipelago. This flexure was interpreted by Hamilton (1979), Mitchell et al. (1986), and Rangin (1989) as indicating a former north-dipping subduction zone.

Objectives

Drilling in the Celebes Sea was designed to answer several questions, one of which was the age of the basin. Basement age data should help resolve the existing discrepancies in the interpretation of magnetic anomalies in the basin, and also provide a major constraint on the mode of origin of the basin.

In addition, we had several objectives in studying the stratigraphic record of the basin. The first was to determine the history of events leading to the present Celebes marginal basin. Was Celebes once closer to China and later moved away when such younger basins as the Sulu Sea and the South China Basin opened? Alternatively, was the Celebes marginal basin once part of one of the larger ocean basins, such as the Indian Ocean or the Pacific Basin, and later became trapped and isolated in its present position? Each of these two alternatives will reveal a different stratigraphic history. The first would show an early development enriched in Asian provenance, becoming less enriched upsection. The second would show Indian, Pacific, or Philippine provenance lower in the section and become more affected by the adjacent arcs and continental masses upsection. If the stratigraphy became more oceanic with depth in the core, we planned to compare it with that of other DSDP sites in the western Pacific region.

We also wanted to study the cores' paleomagnetism to determine the latitudes of basin formation and any cross-latitude motion with time. We planned to determine the changes in declination of the sediments through time in order to estimate local rotations of the basin.

A second objective in studying the stratigraphy was to determine the paleoceanography of the region through time, including changes in ocean circulation, and paleoenvironmental analysis. In addition, we hoped that a study of the distribution of volcanic ashes within the cores could provide a record of volcanic events surrounding the Celebes Sea, as well as provide potentially recognizable marker horizons for comparisons with other marginal basins, such as the Sulu Sea or the already drilled Philippine Sea.

Our third major objective was to measure directions and magnitudes of stress in the Celebes Sea. We planned to make stress orientations with the borehole televiewer (BHTV) to measure breakouts in the borehole.

Our objectives in basement sampling were to date the basement rocks, to determine their petrology and chemistry, and to derive radioisotope ratios. In this way, we would be able to characterize the crust as either open ocean (MORB), back-arc basin, or thinned-arc crust. This determination was important for understanding the paleoenvironments of the basin and for better interpreting the paleoceanographic record of the cores. If successful this would provide us with constraints for tectonic reconstruction of the Celebes Sea region.

Inorganic geochemistry data provide evidence of fluid flow in the section. Site 767 is located approximately 100 km from the Cotabato Trench. Studies in other regions, such as Barbados (Moore et al., 1988), have shown the effects of fluid transport to significant distances seaward of the trench axis. In addition to the tectonic implications, geochemistry provides an understanding of diagenetic changes within the section.

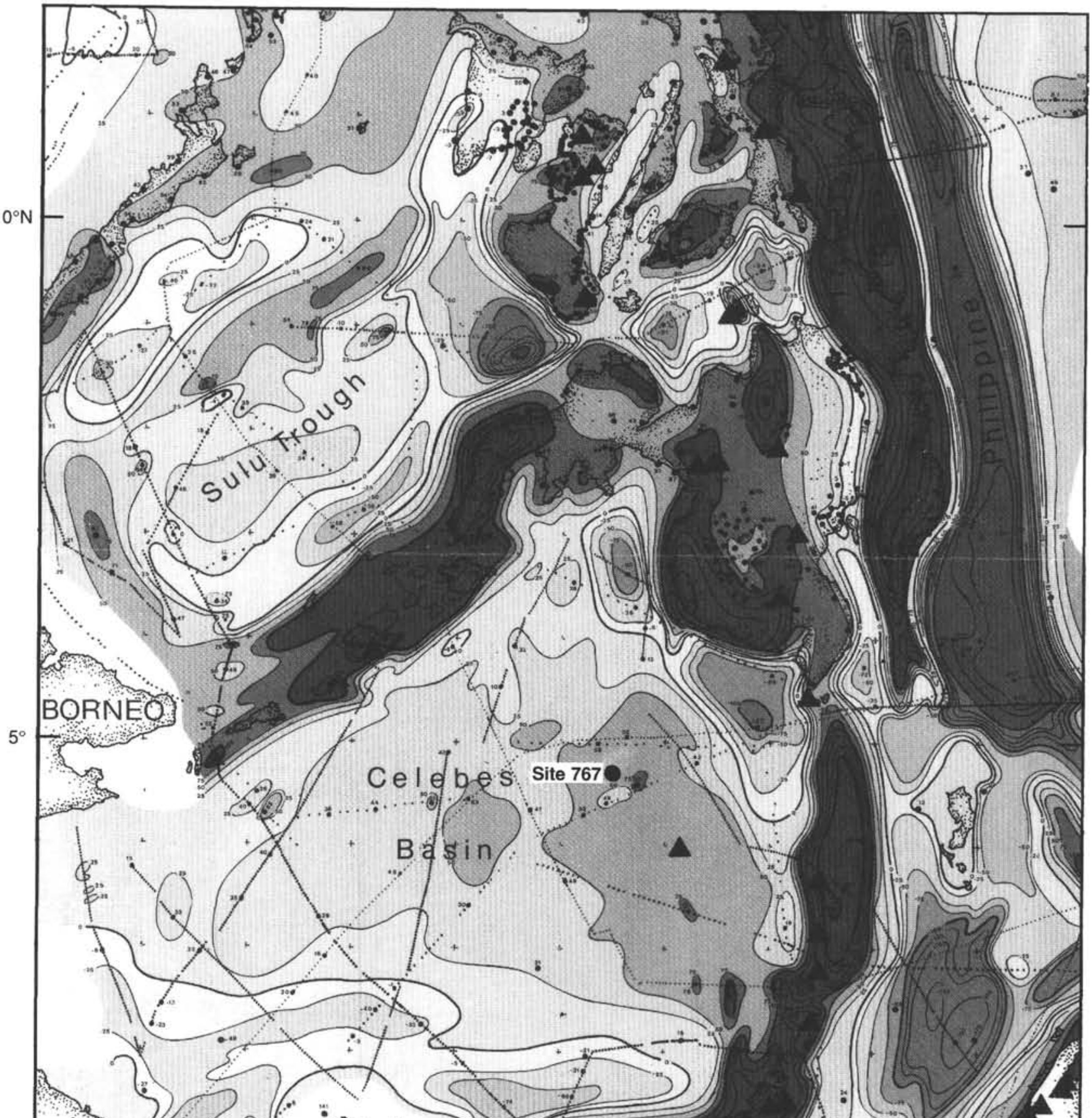

Figure 4. Gravity map of the Celebes Sea (from Watts, 1975).

Site Selection

Proposed Site CS-1 is located in the northeast part of the Celebes Sea. It was chosen because the sedimentary section is thin enough to drill to basement, yet the section appears complete enough on the seismic record to obtain a good stratigraphic history of the basin. Elsewhere in the basin, turbidite sedimentation is very thick. Final Site 767 is located on a local basement high, with a total sediment thickness of 800 m. The entire stratigraphic section appears to be present above the basement. The final site location has a thinner sedimentary section than originally planned, but this difference was very fortunate, since we encountered very sticky material at about 700 m that became critical at 800 m of penetration.

OPERATIONS

Singapore to Site 767

The voyage commenced on 1 November 1988 at Singapore. Since the island of Borneo lay between Singapore and the first drill site, the transit route was across the southern end of the South China Sea, along the northwest coast of Borneo, through the Balabac Strait, across the Sulu Sea, and finally into the Celebes Sea. Proposed Site CS-1 (later renamed Site 767) was located in the Celebes Sea about 150 nmi southeast of the Philippine port of Zamboanga. With about 25 nmi to go, the vessel was slowed and the seismic gear was streamed.

We made a direct approach to the site from the west-northwest and launched a positioning beacon at 0954 hr (UTC), 9 November 1988. *JOIDES Resolution* made a wide turn and returned to cross the beacon on reference profile S049-02 (see "Seismic Stratigraphy" section, this chapter), continuing past the site about 2 mi. The gear was retrieved and the rig returned to take station for drilling operations. The records obtained during the survey are presented in the "Seismic Stratigraphy" section (this chapter).

Site 767

Hole 767A

Hole 767A was spudded at 0045 hr (UTC), 10 November 1988, at a depth of 4905 mbsl (water depths reported are drill-pipe measurements corrected to sea level). The seafloor APC recovered 4.1 m of sediment. Because Site 767 was a potential reentry site, a jet-in soil test was required to determine the conductor casing setting depth. Following the mud-line core, a dummy extended core barrel (XCB) was pumped into place at the bit, and the bit was jetted ahead without rotation. The sediments proved quite soft and suitable for casing emplacement, and the test was ended at 104 m below seafloor (mbsf), a depth in excess of any anticipated casing requirement.

The water-sampler/temperature/pressure (WSTP) probe was then deployed for a "heat-flow" temperature measurement. With zero heave conditions and no hole fill, the mechanics of the operation were flawless; the temperature data were unusable, however, which indicated an instrument problem. The drill string was then pulled clear of the seafloor in preparation for deeper APC/XCB penetration of Hole 767B.

Hole 767B

Because the seafloor sediments were of particular scientific interest, Hole 767B was again started with a "mud-line" APC core. The APC operations continued to 91 mbsf, where a 60,000 lb overpull was required to withdraw the core barrel from the sediment. The switch was then made to XCB coring to protect the equipment and the hole. Sediment recovery was over 103% of the APC-cored interval.

As the sediments became firmer, XCB core recovery was excellent and averaged about 79% for the hole. The fine recovery figures were somewhat offset by a high degree of "biscuiting" disturbance in the cores over the entire XCB-cored interval.

Hole conditions were good to about 410 mbsf, where rotary torque and circulating pressure began to rise. A "wiper trip" encountered drag over the lower 90 m of the hole interval, but it was successful in alleviating the problem until it returned at about 500 mbsf. At 560 mbsf conditions forced a "mini-trip" back to 450 mbsf. Again conditions stabilized, and coring continued with pressure and torque for about a day. As the bit passed 700 mbsf, the hole again began to squeeze the bottom hole assembly (BHA). At 739 mbsf it was no longer possible to turn the drill string or to circulate cuttings up the annulus. Because the drilling plan required a switch to the rotary core barrel (RCB) coring system for the penetration of basement rocks, coring operations in Hole 767B were ended.

Logging operations at Hole 767B began at 1000 hr (UTC) on 16 November 1988. Hole conditioning included a wiper trip with extensive reaming and circulating in the unstable lower third of the hole, followed by filling the hole with KCl-inhibited bentonite mud.

The seismic stratigraphic combination was rigged up at 0000 hr (UTC) on 17 November 1988. This tool consisted of Schlumberger long-spaced sonic, phaser resistivity, natural gamma, and caliper tools, plus the L-DGO temperature tool. Downgoing logs were obtained from the base of pipe (110 mbsf) to a firm bridge at 300 mbsf, and upcoming logs were obtained from 298 to 81 mbsf as open-hole logs and from 81 to 0 mbsf as through-pipe logs. To get the tool string past bridges, the sidewall-entry sub (SES) was rigged up and used in all subsequent logging at the site.

The second run of the seismic stratigraphic combination confirmed that the 300-mbsf obstruction was a bridge and not a ledge, through an unsuccessful attempt to get past the obstruction with the tool centralized by pipe at 290 mbsf. Both the pipe and tool string were then run down toward the bottom of the hole, for simultaneous open-hole logging and pulling pipe. However, a cable short required us to pull the tool out of the hole and remove about 5 m of kinked and twisted cable.

The third run of the seismic stratigraphy combination successfully obtained open-hole logs for 648–110 mbsf while pulling pipe, and obtained through-pipe logs for 110–0 mbsf. The interval below 648 mbsf was not logged because it was so badly bridged that the logging tool could not get entirely out of the pipe.

The geochemical combination was run next. At this site the geochemical combination consisted of Schlumberger natural gamma, gamma spectroscopy, and aluminum clay tools. The L-DGO temperature tool was also on this string, but it generated no data because of premature starting of its data-acquisition clock. Again, both pipe and tool string were lowered to near the bottom of the hole, but both had to be raised about 60 m to find a sufficiently unbridged interval to get the tool string into open hole. Open-hole logs were obtained for the interval from 662 to 110 mbsf while pulling pipe, and through-pipe logs were obtained from 110 to 0 mbsf.

Because of a failure of the gamma spectroscopy tool at 115 mbsf, the interval from 129 to 29 mbsf was relogged. In all, 14 hr were used for initial hole conditioning and 49.5 hr were used for logging.

Low velocity readings from the sonic log indicated less sediment overlying basement than had been anticipated, and the stabilized hole conditions made deepening Hole 767B with the RCB system a desirable option. After all logging operations were completed, a free-fall reentry funnel (FFF) was bolted together around the drill pipe and dropped to the seafloor. The drill string was then recovered, the BHA was converted for RCB coring, and the bit was run back to reentry depth. The hole crater was located with the TV/sonar scanning, but the FFF had disappeared. After two unsuccessful reentry attempts, the bit was pulled clear of the seafloor and the rig was offset 35 m north to clear the disturbed area.

Hole 767C

Hole 767C was spudded at 1430 hr (UTC) on 20 November 1988. The hole was drilled quickly to 500 mbsf, where the "wash" core barrel was retrieved and a multishot survey was taken at total depth. The drift of the hole was a surprising 9.5° from vertical. A wiper trip was then made, and the tight hole was reamed from 370 to 500 mbsf. A center bit was used to drill to the coring point at 680 mbsf. A second wiper trip was made to

344 mbsf, and it was necessary to ream from 646 mbsf to total depth.

Continuous RCB coring then began, overlapping the inconsistently recovered lower section of Hole 767B. Because of the greater hole angle, Hole 767C was stratigraphically about 9 m shallower than the equivalent depth in Hole 767B.

The anticipated hole problems began at about 714 mbsf. For nearly 2 days, high rotary torque and circulating pressure were battled, with only about half the time spent on coring operations. The symptoms indicated that an interval of indeterminate thickness below 714 mbsf was closing in on the 8¼-in. drill collars and acting as a seal.

Basaltic basement rock was finally recovered in the core catcher of Core 124-767C-12R, but the pipe became firmly stuck after 2.4 m had been cut on Core 124-767C-13R. The pipe could not be worked free, and the inner core barrel could not be recovered (apparently because of drill cuttings above the latch). Logging was not attempted because of this obstruction.

The drill string was finally severed and worked free of the hole after four attempts with the explosive severing system. Hole trouble and stuck pipe accounted for 2.8 days of lost time at Hole 767C.

LITHOSTRATIGRAPHY

Sedimentary Units

The recovered sedimentary section overlying basaltic basement at Site 767 is 787 m thick. The section can be divided into four lithologic units (Table 2 and Fig. 5) on the basis of visual description and smear-slide analysis of the recovered cores. Figure 6 shows variations in relative abundance vs. depth for several key sediment components that are indicators of varying provenance within the sequence.

Unit I

Depth: 0–56.8 mbsf
Interval: Core 124-767A-1H and Core 124-767B-1H through Section 124-767B-7H-1 at 34 cm
Thickness: 56.8 m
Age: Pleistocene to Holocene

Unit I consists of volcanogenic clayey silt interpreted as hemipelagic in origin, with sparse interbeds of volcanic ash. The clayey silt is slightly to highly bioturbated, resulting in color mottling and a lack of preservation of primary sedimentary structures; only in the upper 75–85 cm are diffuse thick laminae preserved. This uppermost interval is yellowish brown, with dark greenish gray to olive gray colors characterizing the bulk of the unit.

The silt component of the clayey silt is primarily volcanic ash, including glass, pumiceous glass, rock fragments, feldspar, and hornblende. Biogenic grains form only a minor component of the clayey silt, with siliceous material (spicules, radiolarians, diatoms, and silicoflagellates) more abundant than the scarce calcareous grains (foraminifers and nannofossils). The carbonate content of the sediment is generally very low (<4%; see "Sediment Inorganic Geochemistry" section, this chapter). A few calcareous clayey silt layers (up to 24.2% $CaCO_3$) are present in Cores 124-767B-1H and -5H; these layers contain common foraminifers and calcareous nannofossils dispersed within the clayey silt.

We interpret the volcanogenic clayey siltstone in Unit I as hemipelagic in origin. The low biogenic carbonate content of the sediment is consistent with deposition below the carbonate compensation depth (CCD). The present depth of the CCD in the Celebes Basin is not known; comparison with the Sulu Sea and South China Sea suggests that it probably occurs between 4000 and 4500 mbsl, significantly shallower than the present water depth at Site 767. The rare calcareous layers in Unit I contain assemblages of foraminifers that have been redeposited from shallower depths (see "Biostratigraphy" section, this chapter). These layers most likely represent calcareous turbidites that have been completely disrupted by bioturbation, mixing the redeposited sediment with the surrounding hemipelagic sediment.

The ash layers in Unit I are thin to very thin, with sharp basal contacts and normal grading. The coarsest grains in most beds are silt size, but a few beds have sand-size material at the base. The ash layers in the upper 35 m of the unit are olive brown to gray vitric ash with minor rock fragments, feldspar, hornblende, and biotite. In the lower part of Unit I, the ash composition is more varied, including vitric, lithic-vitric, lithic, and vitric-crystal ashes. The crystal components of these lower ashes are similar to the overlying vitric ashes, with the addition of minor biotite. The mode of deposition of the ash layers is uncertain. Their sharp basal contacts and normal grading are consistent with either air-fall deposition or redeposition by turbidity currents, but the lack of contamination with nonvolcanic material that characterizes most of the beds points to air-fall deposition.

Table 2. Lithologic units, Site 767.

Unit	Subunit	Depth (mbsf)	Thickness (m)	Age
I		0–56.8	56.8	Pleistocene to Holocene
II		56.8–406.5	349.7	late Miocene to Pleistocene
	IIA	56.8–109.6	52.8	Pleistocene
	IIB	109.6–300.1	190.5	early Pliocene to Pleistocene
	IIC	300.1–406.5	106.4	late Miocene to early Pliocene
III		406.5–698.9	292.4	early to late Miocene
	IIIA	406.5–484.4	77.9	middle to late Miocene
	IIIB	484.4–573.7	89.3	middle Miocene
	IIIC	573.7–698.9	125.2	early to middle Miocene
IV		698.9–786.6	87.7	middle Eocene to early Miocene

Unit II

Depth: 56.8–406.5 mbsf
Interval: Section 124-767B-7H-1 at 34 cm through Core 124-767B-43X
Thickness: 349.7 m
Age: late Miocene to Pleistocene

Unit II consists primarily of volcanogenic clayey silt/siltstone grading downward into volcanogenic silty claystone, both interpreted as hemipelagic in origin. Interbeds of carbonate silt/siltstone and carbonate sand/sandstone interpreted as turbidites are also present, along with minor volcanic ash/tuff beds. The unit can be divided into three subunits based on the changing relative proportions of these lithotypes.

Subunit IIA

Depth: 56.8–109.6 mbsf
Interval: Section 124-767B-7H-1 at 34 cm through Core 124-767B-12X
Thickness: 52.8 m
Age: Pleistocene

Volcanogenic clayey silt is the dominant lithology in Subunit IIA, accompanied by rare interbeds of volcanic ash, and rare layers of carbonate silt that we interpret as turbidite deposits. As in Unit I, the volcanogenic clayey silt consists of silt-size volcanic ash particles and clay minerals; recognizable ash components are feldspar, rock fragments, and glass, with minor hornblende, biotite, and pyroxene. The carbonate content of this

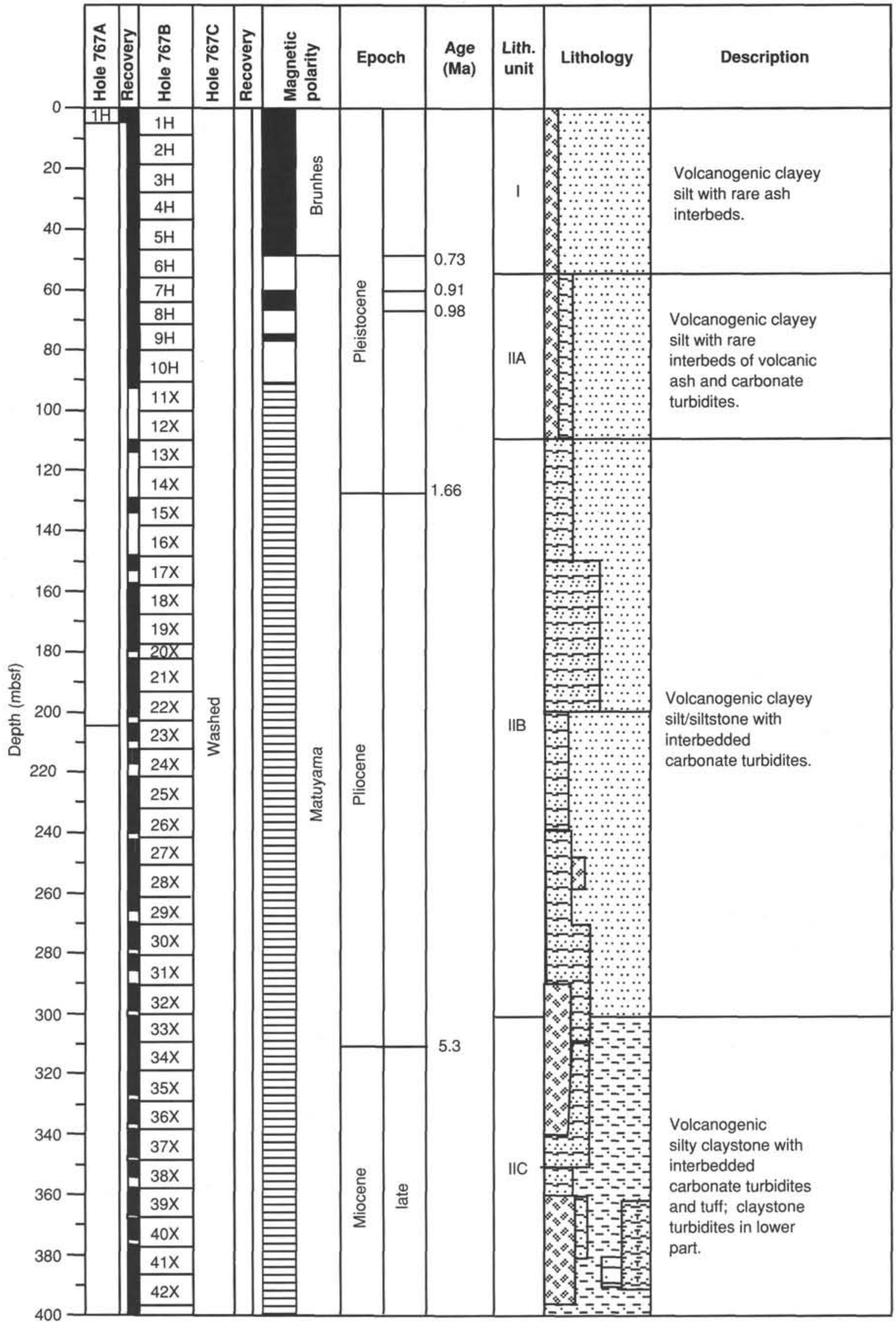

Figure 5. Graphic log of lithologic variations and units at Site 767.

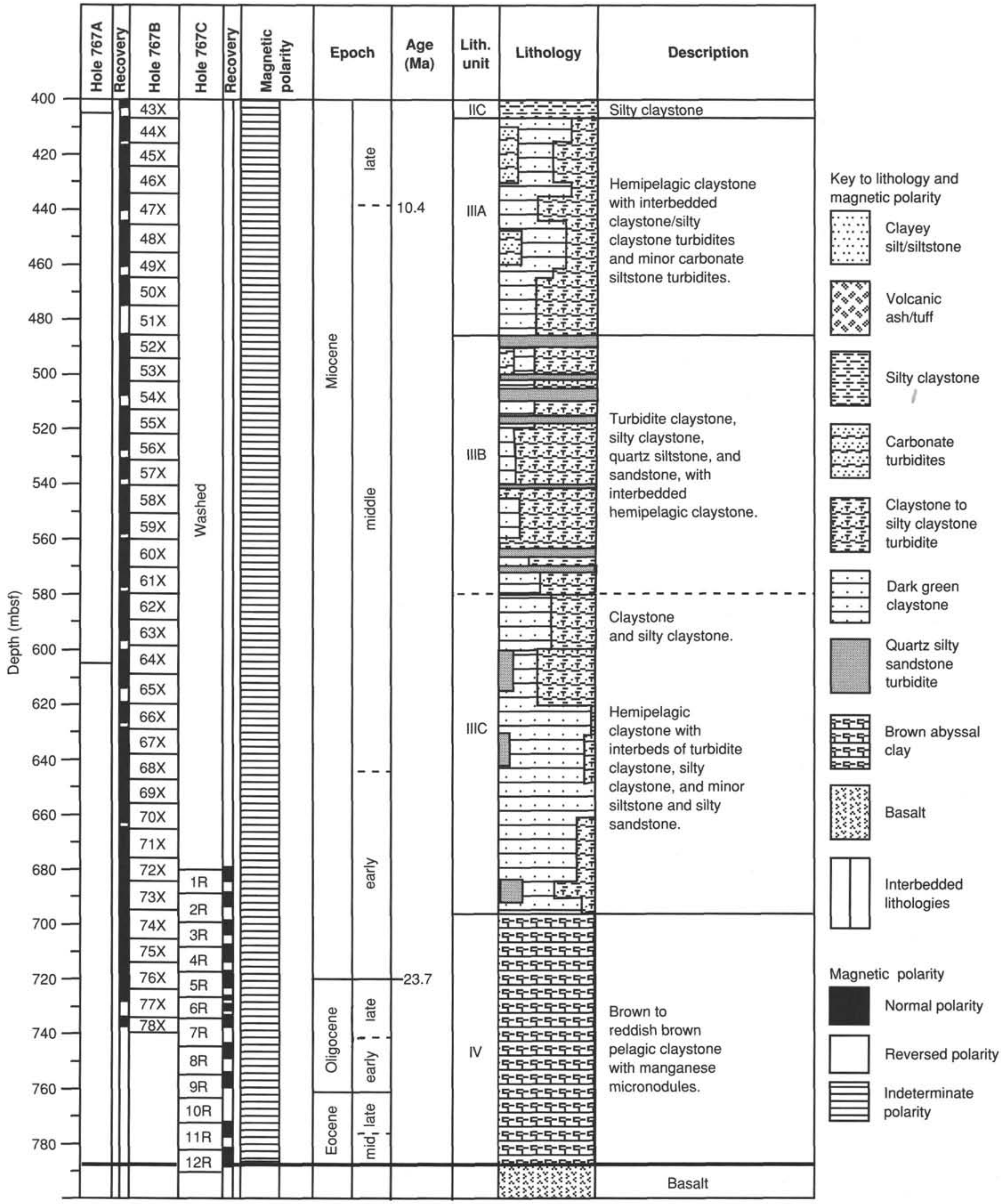

Figure 5 (continued).

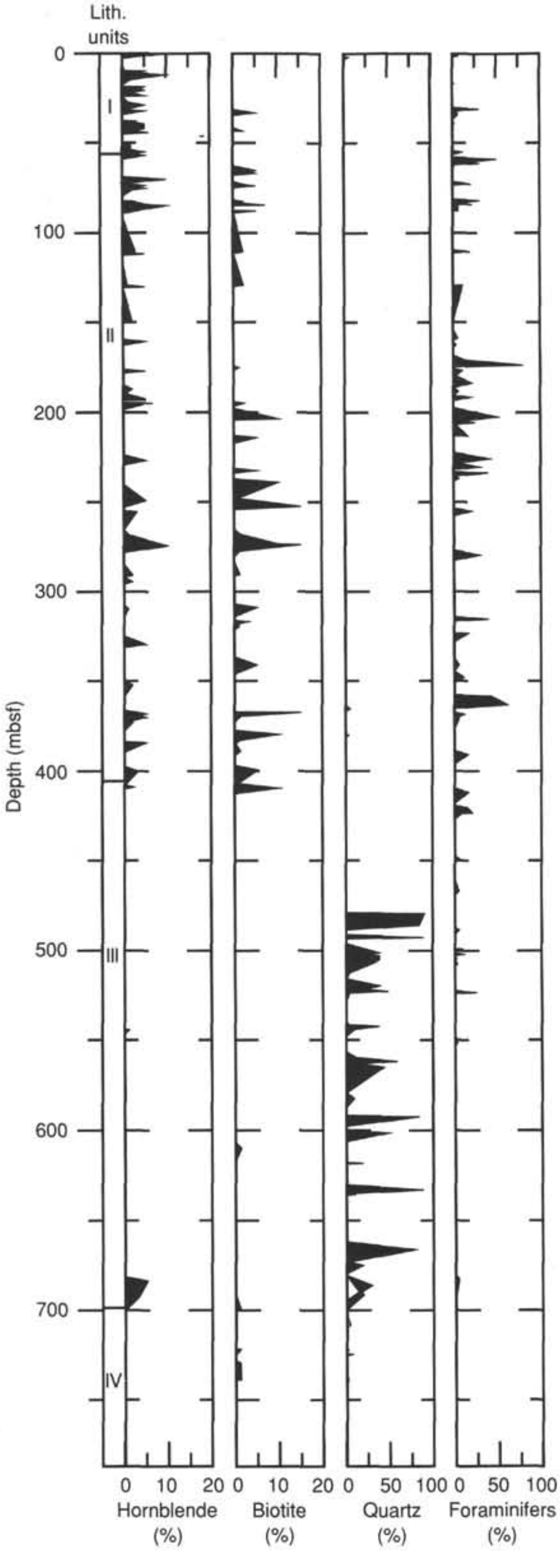

Figure 6. Abundance plot of variation with depth for several sediment components that are important indicators of provenance at Site 767. Hornblende and biotite are found in discrete ash layers and as dispersed grains in hemipelagic sediment. Quartz and foraminifers are found almost exclusively in beds interpreted as turbidites. Significant changes in the abundance of these grains coincide with the boundaries of the major lithologic units (shown in the right-hand column). Data are derived from shipboard smear slide analyses of all lithologies (major and minor) present in the section.

sediment is uniformly less than 1%, and biogenic components are restricted to siliceous spicules and radiolarians, with only trace amounts of foraminifers and calcareous nannofossils. The clayey silt occurs in thick to very thick beds that are structureless except for mottling caused by slight to moderate bioturbation. Separating these thick beds are thin, less intensely bioturbated zones in which thick clayey silt laminae are preserved. The sediment color is olive gray, dark greenish gray, and dark gray. We interpret this lithology as hemipelagic in origin.

The rare ash layers in Subunit IIA are very thin, with sharp basal contacts and normal grading (Fig. 7), and consist of predominantly silt-size grains. The ash composition is variable, from very pure vitric ash to various mixtures of glass, lithic fragments, and crystals. Feldspar with lesser hornblende, pyroxene, and biotite are the mineral phases present in the ash layers. A few medium beds of clayey volcanic ash with foraminifers occur in Core 124-767B-9H. These thicker beds exhibit planar lamination in addition to sharp basal contacts and normal grading; we interpret them as reworked ash deposited by turbidity currents.

The rare carbonate layers in Subunit IIA are 3–25 cm thick, becoming thicker and more abundant downward. They have sharp basal contacts and planar lamination, and grade from al-

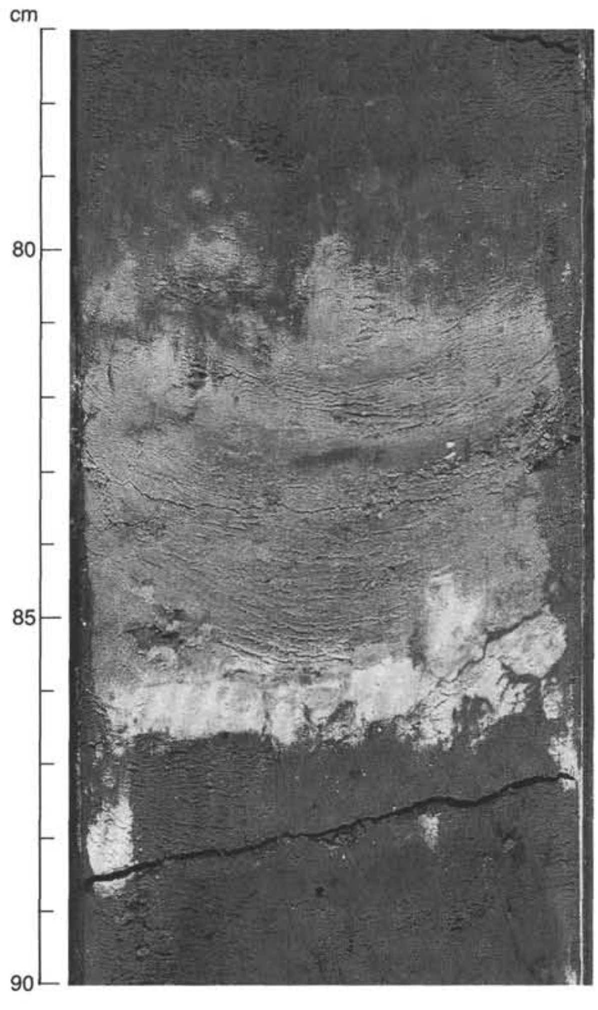

Figure 7. An example of discrete ash layers in Units I and II (Section 124-767B-10H-6, 77–90 cm). At 86 cm a very thin bed of pale gray vitric ash is composed entirely of silt-size volcanic glass fragments. Above there is a second, thicker bed of reworked volcanic ash.

most pure carbonate silt at the base to micritic clay at the top. The carbonate material is a variable mixture of pellets, bioclasts, foraminifers, and micrite, with minor siliceous spicules, radiolarians, and ash. The structure and composition of these layers lead us to interpret them as turbidite deposits.

Subunit IIB

Depth: 109.6–300.1 mbsf
Interval: Cores 124-767B-13X through -32X
Thickness: 190.5 m
Age: early Pliocene to Pleistocene

As in Subunit IIA, the dominant lithology in Subunit IIB is hemipelagic volcanogenic clayey silt/siltstone with dispersed silt-size ash particles, including glass, rock fragments, feldspar, pyroxene, and biotite. The clayey silt/siltstone is thick-bedded and bioturbated; trace fossils are common and include *Chondrites, Planolites,* and *Zoophycos.* The carbonate content of the clayey silt/siltstone is typically less than 3%. This subunit differs from Subunit IIA in that carbonate turbidites are more abundant and coarser, as indicated by the sawtooth calcium carbonate profile (see "Sediment Inorganic Geochemistry" section, this chapter), and discrete ash layers are almost completely absent.

Graded carbonate sand/sandstone and silt/siltstone layers make up 10%–50% of the section in Subunit IIB. The maximum abundance of these layers occurs in Cores 124-767B-17X through -23X (148–213 mbsf). Their thickness varies from 3 cm to 2.75 m, but most are 5–30 cm thick. The beds have sharp bases overlain in some cases by planar lamination and grade from sand or silt at the base to micritic clayey silt at the tops. The gradational tops of these beds are marked by a color change from olive gray (carbonate layers) to dark greenish gray (volcanogenic clayey silt/siltstone), and are commonly bioturbated (Fig. 8). The carbonate material consists of a variable mixture of foraminifers and other bioclasts, pellets, nannofossils, and micrite, accompanied by minor radiolarians, siliceous spicules, and volcanic rock fragments.

A few very thin beds of lithic and vitric-crystal tuff occur in the middle and lower part of the Subunit IIB; some of these layers are graded and laminated and may be turbidite deposits (Fig. 9).

Subunit IIC

Depth: 300.1–406.5 mbsf
Interval: Cores 124-767B-33X through -43X
Thickness: 106.4 m
Age: late Miocene to early Pliocene

The top of Subunit IIC is defined by the appearance of silty claystone as the dominant lithology, in contrast to the clayey siltstone typical of the overlying subunits. Subunit IIC contains less abundant carbonate turbidites and an increase in the occurrence of tuff beds compared with Subunit IIB; the lower part of the subunit also includes some thick-graded beds of silty claystone to claystone, which we interpreted as turbidite deposits.

The silty claystone in Subunit IIC occurs in thick, moderately to highly bioturbated beds (Fig. 10) with rare thin intervals preserving planar lamination. It is dark olive gray, dark greenish gray, or dark gray in color. *Chondrites, Planolites,* and *Zoophycos* occur intermittently through the section (Fig. 11). As in the overlying subunits, the silt component of the silty claystone is volcanic in origin, in this case primarily rock fragments and feldspar. The carbonate content of the silty claystone is typically below 1%, and biogenic particles are absent from most samples. As in the overlying subunits, we interpret this lithology as a hemipelagic deposit.

Thin- to medium-bedded redeposited carbonate beds (Fig. 12) decrease in abundance downward through Subunit IIC; they make up 10% of the section at the top of the unit, but become absent 20 m above the base. The coarsest material at the base of the beds varies from silt to silty micrite and grades with increasing terrigenous clay content to silty claystone. The major constituents of these beds are foraminifers, pellets, calcareous nannofossils, micrite, and clay minerals.

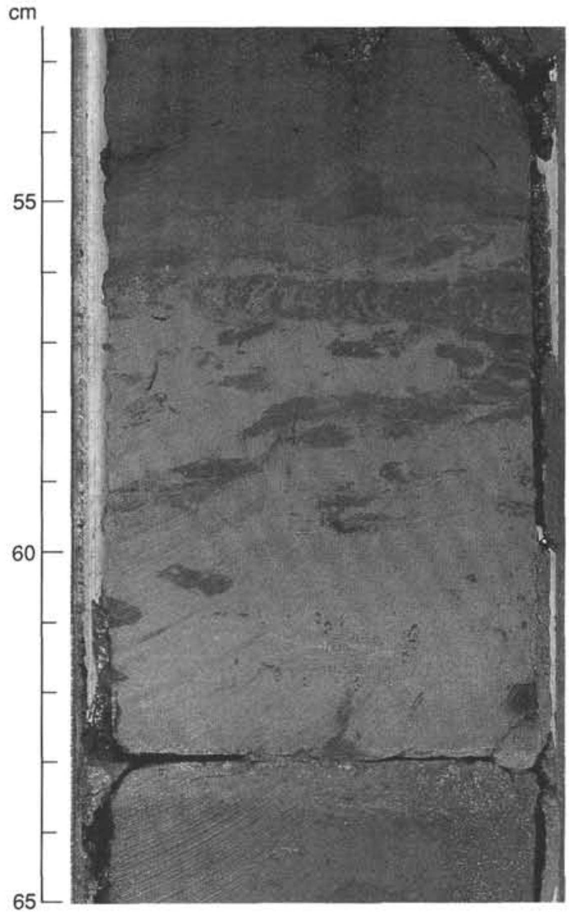

Figure 8. A fine carbonate turbidite bed in Subunit IIB with a sharp base and a diffuse, bioturbated top (Sample 124-767B-26X-4, 52.5–65 cm). Trace fossils include *Zoophycos* and smeared burrows.

Rare, very thin beds of dark brown to black lithic and crystal-lithic tuff also occur sporadically throughout Subunit IIC.

Within the lower 40 m of Subunit IIC are thick beds that grade from silty claystone to claystone. The beds may have planar lamination just above the typical sharp basal contact, but the bulk of each bed is structureless and homogeneous. Bioturbation is only evident near the top of the beds, which grade into overlying highly bioturbated silty claystone. Given the structures present in these beds, we interpreted them as very fine-grained turbidite deposits interbedded with the bioturbated hemipelagic silty claystone.

Unit III

Depth: 406.5–698.9 mbsf
Interval: Core 124-767B-44X through Section 124-767B-74X-3 at 76 cm; Core 124-767C-1R through Section 124-767C-3R-1 at 38 cm
Thickness: 292.4 m
Age: early to late Miocene

Unit III is characterized by the presence of quartz-rich sandstone, siltstone, and associated claystone, all interpreted as tur-

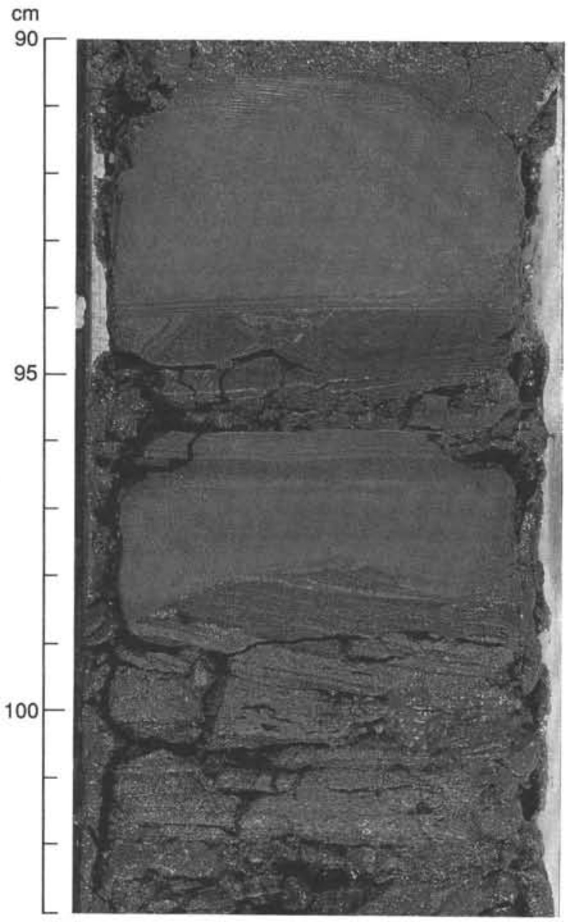

Figure 9. Siltstones and claystones of volcanic material in Unit IIB (Section 124-767B-25X-4, 90–103 cm) that display planar, cross, and convolute laminations. At 94 cm convolute laminae are truncated by planar laminae that grade up into claystone with bioturbation by *Chondrites*. These features suggest deposition by a pulsating turbidity current.

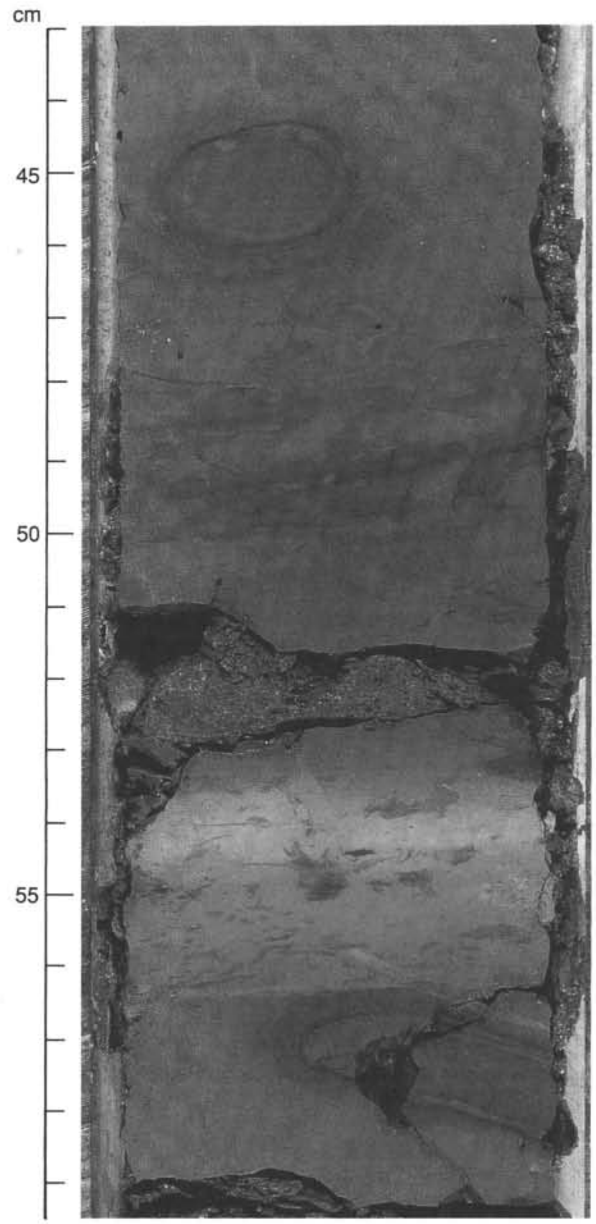

Figure 10. Silty claystones in Subunit IIC (Section 124-767B-40X-4, 43–59.5 cm). The pale bed between 56.5 and 53.5 cm is a bioturbated carbonate turbidite deposit. Above and below are darker deposits with bioturbation and diagenetic reaction rings around burrows at 45 and 57 cm.

bidite deposits of continental provenance, interbedded with subordinate bioturbated hemipelagic claystone. In contrast to the overlying units, ash beds and dispersed volcanic silt particles are virtually absent, as illustrated by the plots of hornblende and biotite abundance in Figure 6. We recognized three subunits on the basis of the relative proportions of coarse and fine turbidites and hemipelagic claystone.

Subunit IIIA

Depth: 406.5–484.4 mbsf
Interval: Cores 124-767B-44X through -51X
Thickness: 77.9 m
Age: middle to late Miocene

The dominant lithologies in Subunit IIIA are medium- to thick-bedded claystone and silty claystone, with sparse interbeds of carbonate siltstone. Beds of bioturbated claystone alternate with beds that grade up from laminated silty claystone to massive claystone that becomes more bioturbated toward the top. The bases of these graded units are normally sharp. Massive, homogeneous thick beds of claystone also occur. There is a sparse fauna of foraminifers and calcareous nannofossils that contribute to the moderate carbonate content of some of the graded silty claystones and claystones. Pyrite is common, occurring as discrete nodules and as disseminated crystals in this subunit. Plant debris is rather rare. These beds are dark gray to dark olive gray in color.

We interpreted the graded silty claystone/claystone beds as thick, fine-grained terrigenous turbidite deposits, whereas the highly bioturbated claystones are hemipelagic in origin. The relative proportion of these lithologies changes downward through Subunit IIIA. In the upper part of the subunit hemipelagic claystone makes up a somewhat greater proportion of the section, whereas graded silty claystone/claystone units dominate the section in the lower part.

Carbonate siltstone makes up $<10\%$ of this subunit and occurs as thin beds with normal grading and planar lamination. They are pale green in color, are frequently bioturbated, and consistd of pellets, foraminifers, radiolarians, micrite, and clay. These beds are interpreted as distal carbonate turbidite deposits.

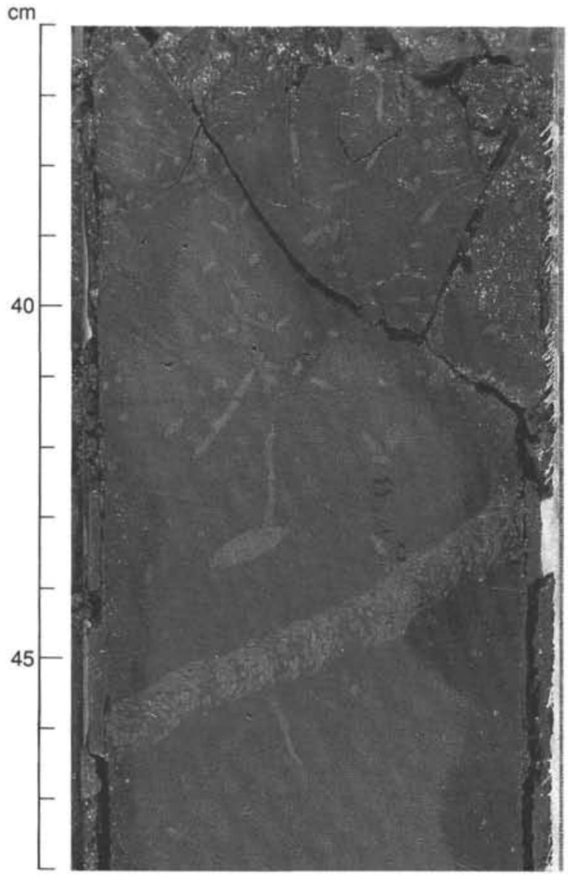

Figure 11. *Chondrites* and *Zoophycos* in dark silty claystones of Subunit IIC (Section 124-767-36X-3, 36–48 cm).

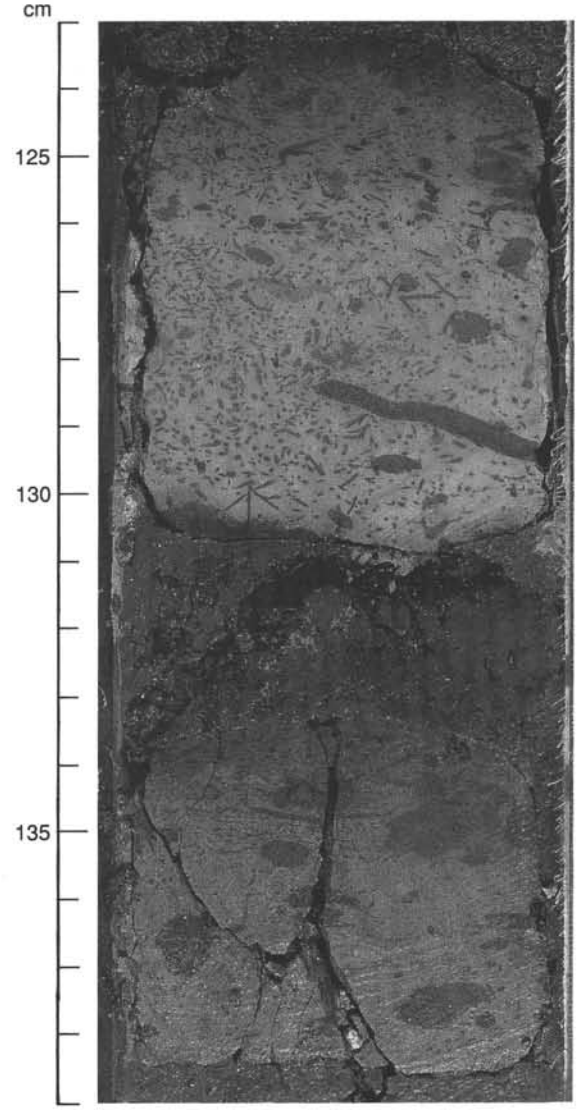

Figure 12. Carbonate turbidite deposits from Subunit IIC (Section 124-767B-34X-5, 123–139 cm). The pale olive gray fine carbonate is bioturbated by *Chondrites* between 130 and 124 cm with darker volcanogenic claystones filling the burrows.

Subunit IIIB

Depth: 484.4–573.7 mbsf
Interval: Core 124-767B-52X through Section 124-767B-61X-3 at 130 cm
Thickness: 89.3 m
Age: middle Miocene

Subunit IIIB is similar in lithology to the lower part of Subunit IIIA, with the addition of interbeds of greenish gray quartz sandstone and siltstone containing plant material. The sandstone and siltstone occur in medium to thick beds that are thickly planar laminated; the laminae are accentuated by variations in the concentrations of plant fragments (Fig. 13). Quartz grains are rounded, and other mineral species are rare in these arenites. The sandstones are the basal parts of very thick upward-fining beds that may have a mud-clast lag at the base. Within these beds, the sandstone grades upward into laminated siltstone, which in turn grades up into thick, homogeneous claystone with common plant debris.

Similar claystone occurs as very thick massive or laminated beds with sharp bases alternating with much thinner beds of claystone that display bioturbation. A single thick (55-cm) conglomerate bed occurs at 505 mbsf, in the middle of the subunit. It is made up of rounded claystone clasts and coalified plant material up to 2 cm across suspended in a matrix of silty sand (Fig. 14). The claystone clasts are similar in color and texture to the interbedded hemipelagic claystone, and therefore may be rip-up clasts.

We interpreted the upward-fining sequences of quartz sandstone to claystone as turbidite deposits, and the thick massive claystone beds as the deposits of muddy turbidity currents that lacked the coarser component. Claystones of a different character occur in thin beds that make up less than 25% of this unit. These beds are more green in color, intensely bioturbated throughout, and do not show grading. They are considered to be hemipelagic deposits derived from a volcanic source area.

Rare carbonate turbidites occur in the upper part of Unit IIIB. They are thin to thick, normally graded beds of carbonate siltstone and clayey micrite consisting of bioclasts, pellets, and foraminifers, with micrite and clay. Authigenic pyrite is common, such as in the claystone of Subunit IIB, in the form of disseminated crystal clusters and small nodules. A hard dolomite concretion 5 cm thick occurs in claystone near the base of the subunit (563 mbsf).

Subunit IIIC

Depth: 573.7–698.9 mbsf
Interval: Section 124-767B-61X-3 at 130 cm through Section 124-767B-74X-3 at 76 cm; Core 124-767C-1R through Section 124-767C-3R-1 at 38 cm

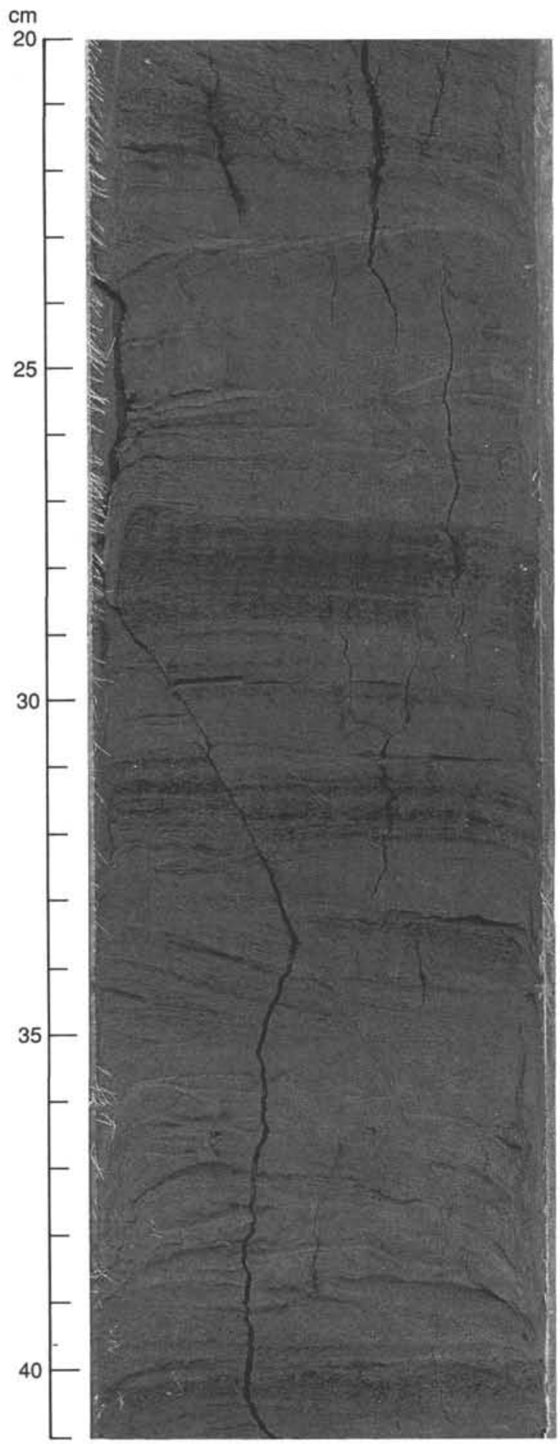

Figure 13. Poorly consolidated quartz silty sandstones typical of Subunit IIIB (Section 124-767B-52X-3, 20–41 cm). The laminations are alternations of quartz sandstone and layers rich in plant debris.

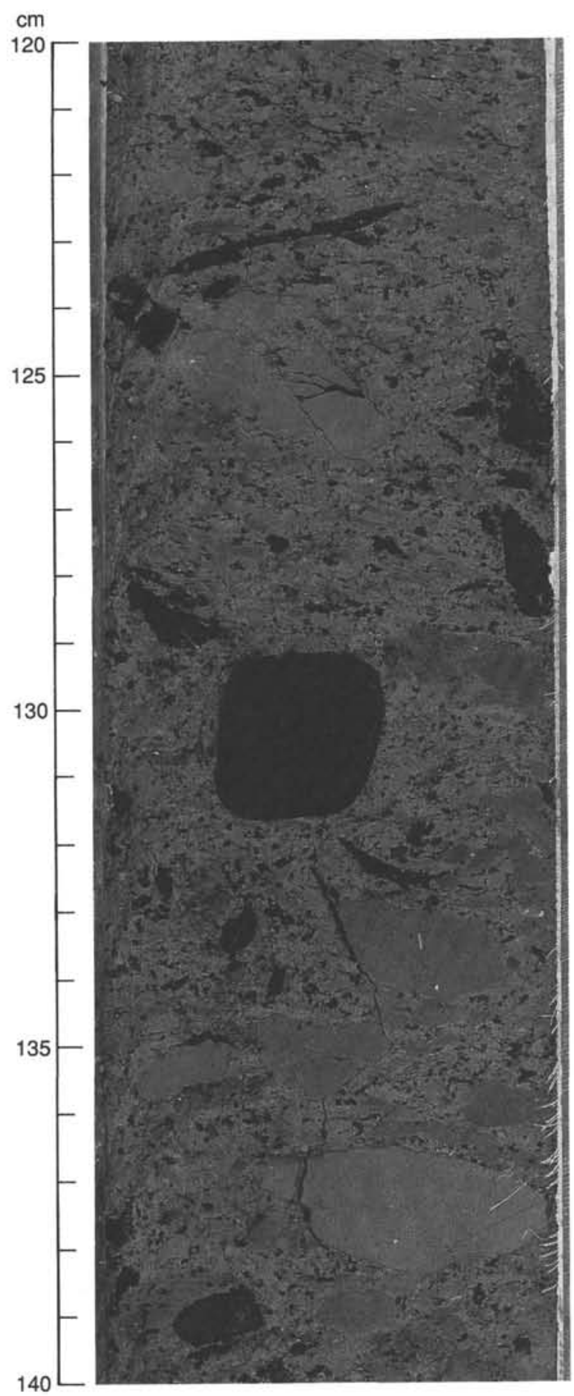

Figure 14. Part of a conglomerate bed in Subunit IIIB (Section 124-767B-54X-3, 120–140 cm). The conglomerate is composed of rounded, black coalified plant material and mud clasts in a matrix of quartz sand and silt.

Thickness: 125.2 m
Age: early to middle Miocene

Subunit IIIC differs from Subunit IIIB in its decreased abundance of sandstone and siltstone, and in the lower ratio of turbidite to hemipelagic claystone. Claystone and silty claystone of two types compose the bulk of Subunit IIIC (Fig. 15). Intensely bioturbated dark gray to dark greenish gray claystone occurs in medium to thick beds. Trace fossils include *Zoophycos, Chondrites,* and *Planolites.* The bioturbated claystone beds are interpreted as hemipelagic deposits and are interbedded with silty claystone and claystone that occur in thick to very thick graded beds. The graded beds start with a sharp-based laminated or cross-laminated siltstone (Fig. 16) that is overlain by massive claystone showing little or no bioturbation.

In some cases, there is planar and cross-laminated sandstone and silty sandstone at the bottom of the bed. The coarser material is largely quartz with some feldspar, plant material, and py-

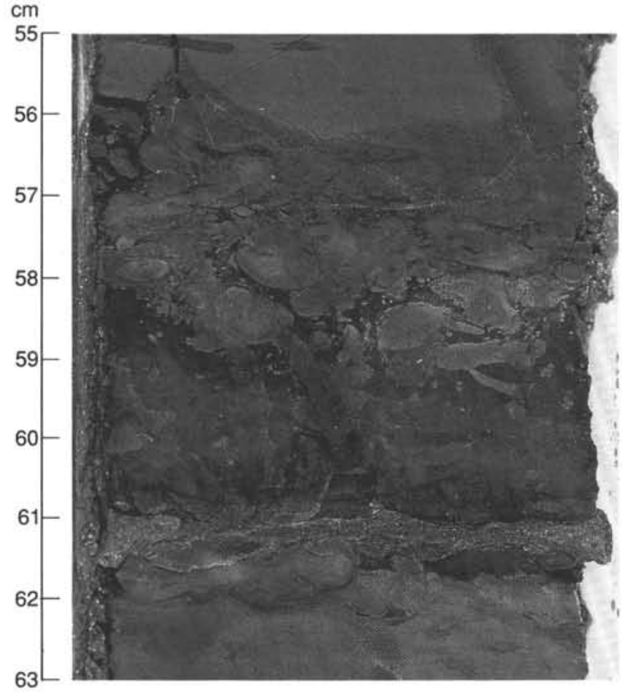

Figure 15. A thin, dark hemipelagic claystone bed in Subunit IIIC (Section 124-767B-70X-4, 55–63 cm) displays more intense bioturbation than the homogenous claystones above and below, which are considered to be muddy turbidite deposits.

rite. We interpret these upward-fining beds to be fine-grained turbidite deposits. The proportion of terrigenous turbidites decreases toward the base of Subunit IIIC, becoming subordinate to hemipelagic claystone in the lower part. Subunit IIIC, therefore, represents a period of gradually increasing terrigenous turbidite influx that culminated with the sandy turbidites of Subunit IIIB. Thin turbidites of volcanogenic material also occur near the base of the Subunit IIIC.

Authigenic pyrite is common throughout the claystone in Subunit IIIC. Between 600 and 625 mbsf, several thin sandstone beds are quite hard because of the extensive cementation by calcite.

Unit IV

Depth: 698.9–786.6 mbsf
Interval: Section 124-767B-74X-3 at 76 cm through Core 124-767B-78X; Section 124-767C-3R-1 at 38 cm through Section 124-767C-12R-3
Thickness: 87.7 m
Age: middle Eocene to early Miocene

Unit IV is composed mainly of dark grayish brown to reddish brown claystone. The claystone is generally homogeneous and structureless in the upper part, becoming somewhat bioturbated downward. Bioturbation is indicated by very slight color mottling and could be more common than is evident in the cores. The claystone becomes more laminated near the base of the unit (Fig. 17). The laminations are color variations possibly caused by variations in the concentration of manganese oxides, which also occur as small (1–5 mm diameter) nodules in this unit.

Nodules of native copper occur sporadically throughout the unit. Clay minerals are the principal component, with rare silt-grade quartz, feldspar, and opaque minerals (sulfides, oxides, and copper); zeolites occur as discrete white grains in the lower half of the unit. The carbonate content is very low (0.2%) throughout the unit. Agglutinated foraminifers are moderately common, and radiolarians and fish teeth and bones are minor components.

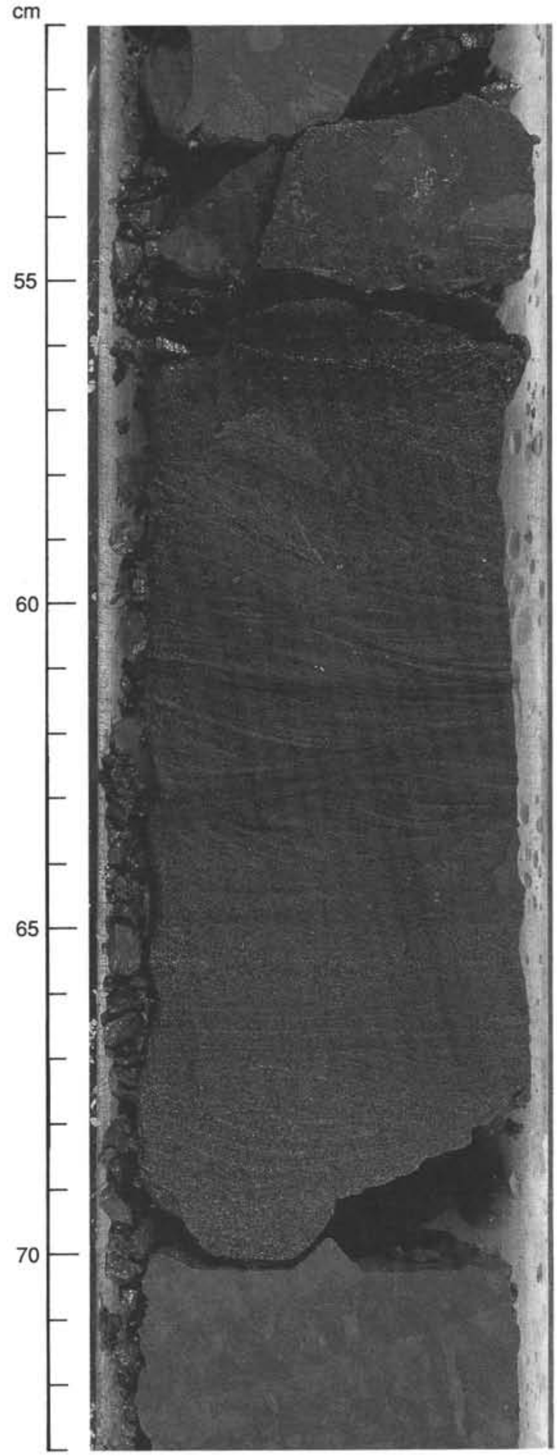

Figure 16. Climbing ripple cross-lamination in the lower part of a turbidite in Subunit IIIC (Section 124-767C-1R-2, 51–73 cm). The silty sandstone is made up of volcanic material (plagioclase and rock fragments).

The fine grain size and color of the claystone, along with the presence of manganese nodules and fish remains, leads us to interpret Unit IV as a pelagic clay, which accumulated very slowly below the CCD.

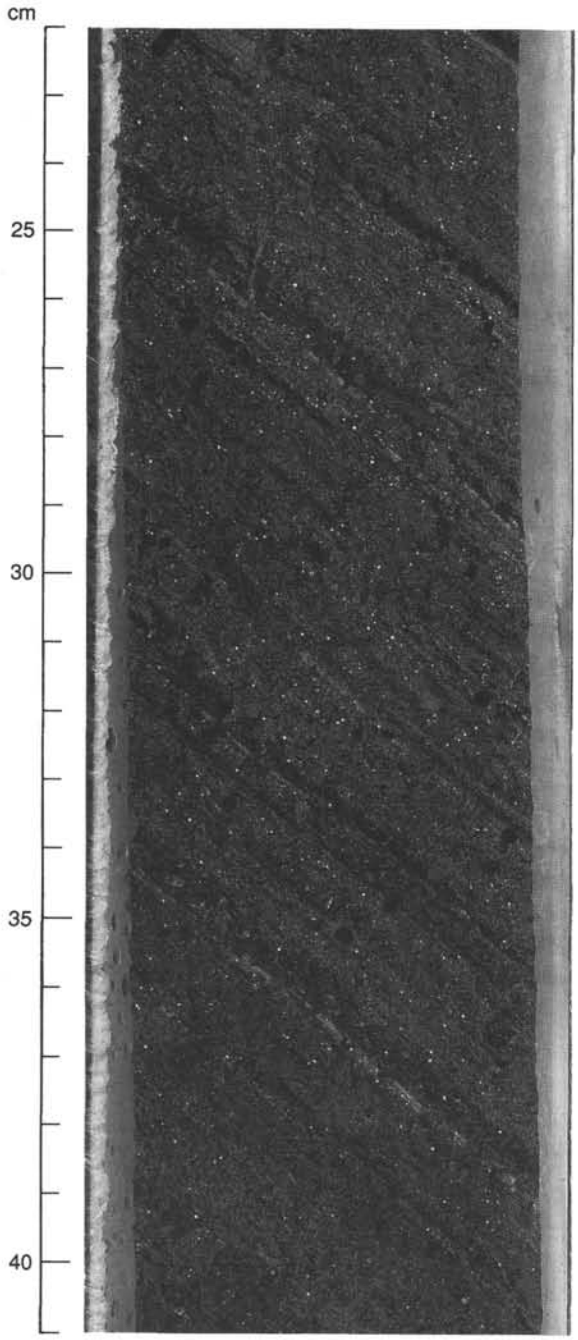

Figure 17. Reddish brown claystone in Unit IV is laminated and slightly bioturbated. Black manganese oxide nodules and pale agglutinated foraminifers and zeolites speckle the sediment. In this example (Section 124-767C-12R-2, 22–41 cm), the laminae are inclined at 40° because of tectonic disturbance in the lowest part of Unit IV.

Greenish gray, laminated volcaniclastic siltstone (plagioclase, biotite, and volcanic lithic fragments) occurs rarely in the upper part of Unit IV. The beds are normally graded with sharp bases; we interpret them as distal volcanogenic turbidites. They occur at the bases of decimeter-thick rhythmic sequences in Core 124-767B-76X, overlain by mottled reddish brown claystone, structureless claystone, and finally darker brown claystone with scattered manganese nodules. These rhythms probably represent an initial increase in sedimentation rate with the volcanic siltstones, followed by a gradual return to very slow pelagic sedimentation.

Unit IV overlies altered basalt, although the contact is not preserved in the cores.

Clay Mineralogy

Introduction

The <2-μm size fraction was separated from samples taken from 69 cores collected from Site 767 (for methods, see "Explanatory Notes" chapter, this volume). The X-ray diffraction (XRD) data are reported as the weight percentages of smectite, illite, kaolinite, and chlorite relative to the sum of these four minerals (Fig. 18 and Table 3). The abundances of other minor phases sometimes noted in the XRD scans and of nondiffracting (amorphous) material are not included. The techniques used for these analyses are, at best, "semiquantitative" and the significance of the data reported here lies in the patterns revealed rather than in the absolute abundances.

Smectite

The smectite abundance is high in the upper portions (0–430 mbsf), averaging about 70% of the total clay fraction (Fig. 18). Between 430 and 560 mbsf, smectite levels are variable and lower; approximately one half of the abundance in the upper part of the hole. Below 560 mbsf smectite levels are somewhat higher, averaging about 55% down to the bottom of the hole. This lowest interval corresponds to the "red clay" in the lowest part of the hole (Unit IV).

Illite

Illite is abundant in the first 90 mbsf, averaging around 20% of the clay fraction (Fig. 18). It falls off in abundance below 90 mbsf and is only detected in a few samples in the interval from 90 to 430 mbsf. Illite becomes very common in the interval from 430 to 560 mbsf, averaging around 40%. The illite abun-

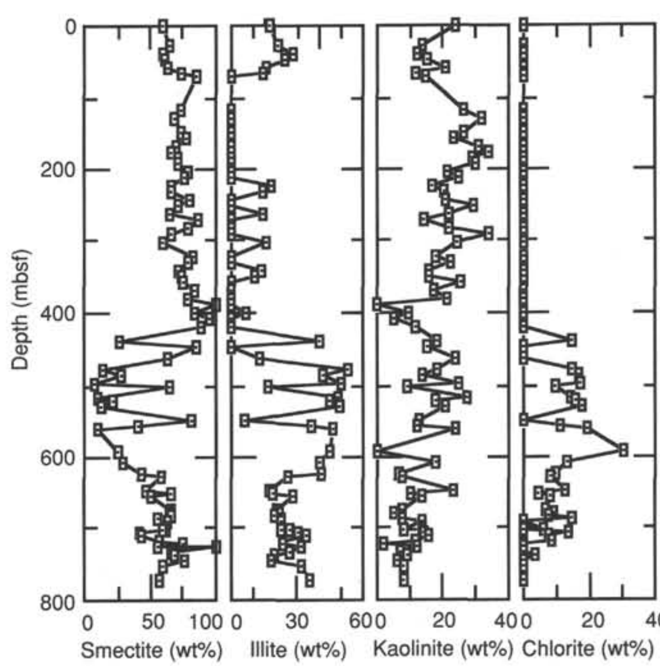

Figure 18. Abundance of smectite, illite, kaolinite, and chlorite in the <2-μm size fraction, Site 767.

Table 3. Clay mineral data, Site 767.

Core, section, interval (cm)	Depth (mbsf)	Smectite (wt %)	Illite (wt %)	Kaolinite (wt %)	Chlorite (wt %)	Continentality index
124-767B-						
1H-1, 46-52	0.46	58.89	17.13	23.98	0.00	0.11
4H-1, 53-59	28.53	64.75	21.46	13.79	0.00	0.12
5H-1, 55-61	38.05	59.79	27.97	12.24	0.00	0.17
6H-1, 50-56	47.50	60.18	24.51	15.32	0.00	0.15
7H-1, 47-53	56.97	63.50	15.80	20.70	0.00	0.10
8H-1, 107-110	67.07	73.58	14.60	11.82	0.00	0.08
9H-1, 48-54	71.98	85.19	0.00	14.81	0.00	0.00
14X-1, 3-8	119.13	73.61	0.00	26.39	0.00	0.00
15X-1, 54-60	129.44	68.09	0.00	31.91	0.00	0.00
17X-1, 70-76	149.00	73.68	0.00	26.32	0.00	0.00
18X-1, 34-40	158.34	76.92	0.00	23.08	0.00	0.00
19X-1, 36-42	167.96	69.05	0.00	30.95	0.00	0.00
20X-1, 54-60	177.84	66.31	0.00	33.69	0.00	0.00
21X-1, 54-60	184.34	71.05	0.00	28.95	0.00	0.00
22X-1, 40-46	193.90	70.37	0.00	29.63	0.00	0.00
23X-1, 24-30	203.54	78.68	0.00	21.32	0.00	0.00
24X-1, 35-41	213.45	75.36	0.00	24.64	0.00	0.00
25X-1, 49-55	223.39	65.47	17.94	16.59	0.00	0.11
26X-1, 49-55	233.09	65.53	14.15	20.31	0.00	0.08
27X-1, 47-53	242.67	79.31	0.00	20.69	0.00	0.00
28X-1, 43-49	252.33	70.73	0.00	29.27	0.00	0.00
29X-1, 49-55	261.89	64.08	14.08	21.83	0.00	0.09
30X-1, 44-50	271.44	85.71	0.00	14.29	0.00	0.00
31X-1, 40-46	282.60	77.98	0.00	22.02	0.00	0.00
32X-1, 44-50	290.84	66.04	0.00	33.96	0.00	0.00
33X-1, 50-56	300.60	59.46	16.22	24.32	0.00	0.10
35X-1, 57-63	319.97	82.14	0.00	17.86	0.00	0.00
36X-1, 45-51	329.55	77.95	0.00	22.05	0.00	0.00
37X-1, 46-52	339.26	70.50	13.88	15.62	0.00	0.08
38X-1, 88-92	349.38	73.80	10.48	15.72	0.00	0.06
39X-1, 32-38	358.42	74.87	0.00	25.13	0.00	0.00
40X-1, 12-18	369.42	82.98	0.00	17.02	0.00	0.00
41X-1, 134-140	380.34	78.69	0.00	21.31	0.00	0.00
42X-1, 126-130	388.36	100.00	0.00	0.00	0.00	0.00
43X-1, 12-15	401.42	83.25	7.18	9.57	0.00	0.04
44X-1, 142-147	407.92	94.82	0.00	5.18	0.00	0.00
45X-1, 48-53	419.68	88.51	0.00	11.49	0.00	0.00
47X-3, 130-136	439.70	26.80	40.32	18.41	14.47	0.48
48X-1, 44-50	445.54	84.91	0.00	15.09	0.00	0.00
50X-1, 31-36	464.41	63.68	12.63	23.68	0.00	0.08
51X-3, 92-98	478.72	14.01	52.84	18.24	14.92	0.77
52X-3, 80-86	488.20	27.87	41.97	13.57	16.59	0.49
53X-4, 108-114	498.58	7.48	50.42	24.84	17.26	1.00
54X-1, 46-52	502.96	64.81	16.42	9.20	9.57	0.15
55X-5, 106-112	519.26	9.86	48.71	27.35	14.09	0.87
56X-1, 44-46	521.50	21.95	44.78	17.64	15.64	0.57
57X-1, 8-15	530.88	12.11	49.34	20.81	17.73	0.82
58X-6, 44-51	548.44	80.73	6.42	12.85	0.00	0.03
59X-4, 140-146	556.10	40.66	36.25	12.01	11.08	0.34
60X-1, 10-16	559.90	10.20	46.56	23.78	19.46	0.87
63X-1, 100-106	592.80	25.28	44.57	0.00	30.15	0.60
64X-6, 42-47	606.42	29.09	40.00	17.62	13.29	0.45
66X-4, 6-12	621.93	42.70	41.29	6.56	9.45	0.34
67X-1, 130-136	628.70	58.23	25.91	7.61	8.25	0.20
68X-CC, 21-27	646.68	46.91	17.35	23.23	12.51	0.21
69X-4, 10-16	650.90	66.28	18.97	10.03	4.72	0.13
70X-1, 55-61	656.55	50.36	28.08	13.58	7.98	0.23
71X-6, 29-34	673.39	65.90	20.31	7.44	6.34	0.15
72X-2, 70-76	677.50	63.97	22.25	4.82	8.95	0.17
73X-2, 89-95	687.29	55.26	22.51	7.78	14.44	0.22
74X-7, 31-38	703.91	59.41	26.85	13.73	0.00	0.16
75X-1, 4-10	704.24	41.58	30.24	14.37	13.81	0.31
76X-CC, 5-11	722.95	74.51	23.53	1.96	0.00	0.12
77X-1, 57-63	723.77	56.01	31.63	12.36	0.00	0.19
78X-CC, 0-6	733.87	65.89	26.80	7.31	0.00	0.15
124-767C-						
1R-1, 40-45	680.40	65.43	19.45	7.56	7.56	0.15
2R-1, 29-35	689.79	63.45	22.76	13.79	0.00	0.13
3R-2, 22-26	700.22	62.55	23.11	8.32	6.02	0.17
4R-1, 37-44	707.87	42.74	34.19	15.46	7.61	0.30
5R-1, 80-86	717.30	56.42	23.68	11.54	8.36	0.20
6R-1, 72-79	726.92	100.00	0	0	0	0
7R-1, 44-49	736.24	68.07	19.69	8.94	3.30	0.13
8R-2, 74-80	745.54	75.68	18.38	5.94	0.00	0.09
9R-1, 83-87	753.82	59.81	32.15	8.04	0.00	0.19
11R-1, 60-66	773.00	56.61	35.52	7.87	0.00	0.21

dance falls to around 25% in the interval from 560 mbsf to the bottom of the hole.

Kaolinite

Kaolinite shows little variation in the hole except for a generally decreasing trend with depth, falling from 15%-20% of the clay fraction in the upper parts of the hole to 5%-10% near the bottom (Fig. 18).

Chlorite

The detection limit for chlorite is probably around 5% by the methods used in this study. Chlorite appears to be absent in the upper parts of the hole, but it is probably present at levels below the detection limit (Fig. 18). Below 430 mbsf, however, chlorite averages 10%-15% of the clay fraction and mimics the abundance of illite.

Discussion

In an attempt to illuminate the evolution of sediment sources, we have constructed a "continentality index" (Fig. 19), which is the logarithm of the sum of the abundances of smectite, illite, and chlorite, divided by the abundance of smectite (log [smectite + illite + chlorite/smectite]). The association of illite with the weathering of continental igneous and high-grade metamorphic rocks and of chlorite with the erosion of low-grade metamorphic rocks is compared in the continentality index to the volcanic association of smectite. The continentality index provides a crude numerical estimate of the changing influence of continental sediment sources on the deposition of clay in the basin, with higher values signaling a more pronounced contribution of continental sediment. This index shows a clear pattern.

In the upper parts of Hole 767B (0-400 mbsf, Units I and II), the index has a value well below 0.2, suggesting that the source of this material is not dominated by the weathering and erosion of continental crust. In the same interval, the high smectite abundance appears to be the result of the alteration of the products of arc volcanism. The association of these high smectite levels with the abundant ash beds is a clear indication of a fairly close source of arc-volcanic material, not surprising in the current tectonic setting of the Celebes Sea.

From 400 to 640 mbsf (Subunits IIIA, IIIB, and the upper part of IIIC), the continentality index is variable and generally

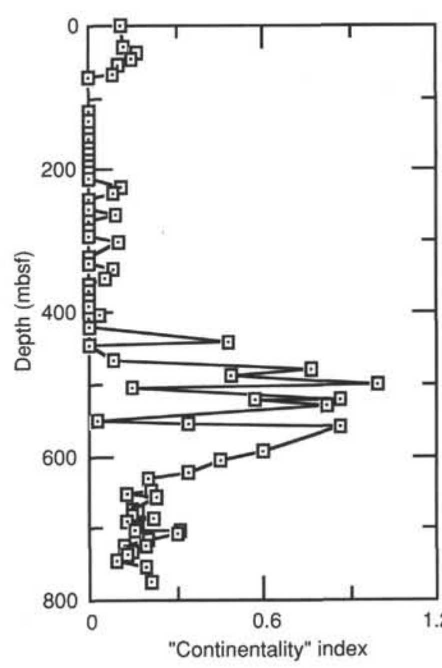

Figure 19. "Continentality" index, Site 767. See text for discussion ("Clay Mineralogy" subsection, "Lithostratigraphy," this chapter).

very high. Continent-derived material dominates over smectite by a substantial amount, suggesting a very different source region for detritus within this interval. It must, however, be noted that these data do not represent mass accumulation rates. Thus, changes in the continentality index may only reflect the decrease or increase of one of the parts of the fraction, and the change in the interval from 400 to 640 mbsf could represent only a diminution of (for example) the smectite source without any increase in the influx of continent-derived illite and chlorite. However, this interval consists of thick muddy turbidite beds with lower divisions of quartzose siltstone and sandstone, interbedded with subordinate hemipelagic claystone. The high continentality index in the interval, therefore, clearly reflects a significant increase in the proportion of sediment with a continental source, in the form of terrigenous turbidites.

The continentality index falls to low levels below 640 mbsf (lower part of Subunit IIIC and Unit IV), but these levels remain higher than in the section above 400 mbsf. In the major portion of this interval, the sediment is characterized as pelagic "red" clay. An inspection of the clay mineral abundance maps of Griffin et al. (1968) suggests that recent pelagic clays in the western Pacific at the latitude of Site 767 are composed of approximately 55% smectite, 25% illite, 10% kaolinite, and 15% chlorite, a composition very similar to that measured in the interval below 560 mbsf. Since the continentality index is fairly low but smectite is not dominant, these sediments may be open-ocean pelagic clay with no indication of a nearby source of either continent-derived or arc-volcanic material.

There is an interesting high in the illite abundance in cores from the interval between 0 and 90 mbsf (Unit I and Subunit IIA; Pleistocene-Holocene). In other parts of the section, illite concentrations above 15% are usually accompanied by modest chlorite levels. In the top 90 mbsf, illite appears without detectable chlorite. The occurrence of this pattern in the sediments representing the last million years suggests that there may be a relationship with the very high periglacial dust production in eastern Asia at this time, which led to the production of the Chinese loess deposits. Post-cruise palynological analyses may shed more light on the origin of this elevated illite concentration.

Grain Size Measurements (Cores 124-767B-1H through -10H)

The upper 90 mbsf of sediment at Site 767 (Units I and IIA) appears to contain a continuous and potentially high-resolution record of mid-Pleistocene to Holocene sedimentation in the Celebes Sea. The present water depth at the site is 4905 m, well below the present CCD in the Celebes Sea. Consequently, no undisturbed calcareous pelagic sediments are preserved in this portion of the record. The dominant lithology is a carbonate-free clayey silt with a significant fraction of unweathered volcanic material. To examine the grain-size variability within this important interval, we measured the particle size distribution of the clayey silt in Cores 124-767B-1H through -10H.

A Lasentec, Lab-Tec 100 particle size analyzer was used to provide data on the sand/silt/clay ratio as well as mean grain size. A description and discussion of methods involved in the particle size analysis are contained in the "Explanatory Notes" chapter (this volume). Particles are classified into one of eight channels ranging from sand to clay. The resulting size/frequency data presented here (Table 4) are not expressed as weight percent (wt%) but are based on the optical cross-sectional area of the grains. Duplicate analyses of selected samples indicates that the data are internally consistent.

Figure 20A displays the mean grain size variability in the upper 90 m of the record for the dominant hemipelagic clayey silt. Interbedded ash layers and carbonate turbidites are not included in the data presented. The downcore variations in relative abundance of the clay and silt fractions show no obvious trends and are not displayed graphically. The computed mean grain size data display a consistent coarsening-downward trend to approximately the depth of the Brunhes/Matuyama paleomagnetic boundary (50–55 mbsf) (see "Paleomagnetics" section, this chapter). Be-

Table 4. Mean grain-size data for hemipelagic clayey siltstone, Site 767.

Core, section	Depth (mbsf)	Mean grain size (μm)	Sand (%)	Silt (%)	Clay (%)	Lithology
124-767A-						
1H-1	0.30	6.7	0	73	37	D
1H-1	0.77	6.3	0	63	37	D
1H-2	2.40	5.5	0	58	42	D
124-767B-						
1H-3	3.84	8.3	1	70	29	D
1H-4	5.11	5.7	0	61	39	M
1H-5	7.87	5.8	0	59	41	M
1H-6	9.60	8.1	1	69	30	D
2H-1	10.97	6.4	1	61	38	D
2H-1	11.18	6.7	0	65	36	D
2H-1	11.29	7.6	1	67	32	D
2H-2	12.79	7.7	1	67	32	M
2H-3	12.85	7.5	1	69	30	D
2H-7	18.38	6.5	0	65	35	M
3H-1	18.80	8.0	1	67	32	D
3H-1	19.31	7.3	0	71	29	D
3H-1	19.40	6.8	1	66	33	M
3H-2	20.50	8.9	2	69	29	D
3H-4	23.30	8.1	1	65	33	D
3H-4	23.79	6.3	1	60	39	M
3H-6	26.60	9.2	3	68	29	D
4H-2	30.73	8.7	1	71	28	M
4H-3	31.82	10.7	3	63	24	M
4H-3	31.90	8.5	1	68	31	D
4H-5	34.41	10.3	3	71	26	D
4H-5	34.57	8.7	1	70	29	D
4H-5	34.75	9.0	2	73	25	M
5H-2	39.40	9.0	2	67	31	D
5H-5	43.78	10.0	3	64	29	D
5H-5	44.65	8.7	2	67	31	M
5H-7	46.80	8.2	1	71	28	M
6H-2	49.08	12.5	5	68	27	D
6H-3	51.10	10.9	3	69	28	D
6H-5	53.76	11.1	3	70	27	D
6H-7	56.00	10.3	3	71	26	M
7H-1	56.87	11.9	4	69	27	D
7H-1	57.21	9.5	3	68	29	D
7H-2	58.54	10.2	3	70	27	D
7H-3	60.10	12.8	6	68	25	M
7H-4	61.09	10.6	3	67	29	D
7H-4	61.55	9.3	3	68	29	D
7H-4	62.11	8.4	1	82	17	D
7H-5	63.29	7.9	1	62	36	D
7H-7	65.79	11.8	4	74	22	M
8H-1	66.31	11.9	1	78	20	M
8H-2	68.16	16.2	7	75	18	M
8H-2	68.69	6.9	0	65	35	D
8H-3	70.35	8.0	1	62	36	M
8H-4	71.17	8.5	1	71	28	M
9H-1	72.42	9.9	3	76	28	D
9H-3	75.10	8.7	1	70	29	M
9H-3	75.70	10.9	2	74	26	D
9H-4	76.64	9.7	3	70	27	M
9H-7	80.54	7.6	2	54	43	D
10H-1	81.20	7.9	1	70	28	D
10H-1	82.00	7.3	1	76	23	D
10H-3	84.70	7.2	1	66	33	D
10H-3	85.11	13.6	6	70	24	M
10H-5	88.28	11.4	2	74	24	M
10H-6	89.44	13.3	5	72	23	M

Note: D = dominant and M = minor.

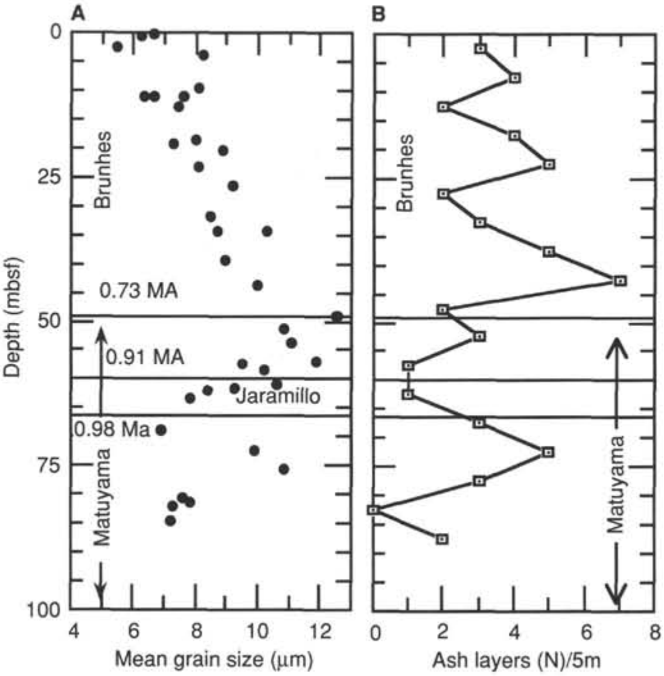

Figure 20. Mean grain-size data and ash bed frequency, Site 767, Celebes Sea (Cores 124-767B-1H through -10H). **A.** Mean particle size of hemipelagic clayey siltstone. Note location and age of paleomagnetic datums. **B.** Number of volcanic ash layers per 5 m of core.

low this maximum, higher frequency variability occurs. Variability in sedimentation rate is most likely not a contributing factor to this trend in mean grain size.

The position of the Brunhes/Matuyama (0.73 Ma) paleomagnetic reversal boundary, and the upper and lower boundaries of the Jaramillo event (0.91 and 0.98 Ma, respectively) are depicted in Figure 20A. On the basis of these paleomagnetic datums, the average sedimentation rate for the last 0.73 m.y. was 67 m/m.y. (6.7 cm/1000 yr). A nearly identical accumulation rate of 72 m/m.y. occurs between the bottom of the Jaramillo event and the Brunhes/Matuyama boundary (0.73 Ma). Sediment accumulation rates appear to have remained fairly constant at Site 767 when averaged over the last 1 Ma (see "Sediment Accumulation Rates" section, this chapter), even though on shorter glacial/interglacial time scales, regional climatic and sea-level oscillations apparently produced notable changes in the sedimentation rate in the South China Sea (Broecker et al., 1988), and probably in the entire Indonesian archipelago.

The number of observed ash layers per every 5 m of core is shown in Figure 20B. Considering the significant volcanic component in sediments of Units I and IIA, an increased abundance of ash layers might be expected to directly correspond to larger mean grain size, but this is clearly not the case. In addition, ash-layer frequency is notably low in the interval containing the coarsest mean grain size. This interval also coincides with the Brunhes/Matuyama boundary and the upper part of the Jaramillo event. At present, we can offer no explanation for this correlation. Future work with more closely spaced samples may clarify the significance of the preliminary relationships observed in this data.

Distribution of Volcaniclastic Material

Volcaniclastic material is present at Site 767 as discrete ash layers (air-fall deposits), as a component of hemipelagic deposits, and in some turbidites. The volcanic component of the sediment occurs as rock fragments, glass, and crystals (plagioclase, hornblende, pyroxene, and biotite), and as clay minerals derived from the breakdown of these materials.

In Figure 21, the total thickness of ash in each core is plotted vs. depth (mbsf). This shows that contemporaneous volcanic activity was at a peak between 30 and 40 mbsf (Unit I: Pleistocene), with other peaks at 290–310 mbsf (Subunits IIB and IIC: lower Pliocene) and 400 mbsf (Subunit IIC: upper Miocene). However, an examination of smear slides of hemipelagic deposits shows that dispersed fine-grained ash occurs sporadically as a minor or major component from the base of Unit II to the top of the sequence. Evidently, nearby volcanism influenced sedimentation in the Celebes Basin to varying, but significant, degrees throughout late Miocene to Holocene time.

Petrographic data from volcaniclastic beds with over 90% volcanic components from Site 767 are summarized in Figure 22. The data include material derived from the erosion of volcanic terranes around the basin, as well as from primary pyroclastic deposits. The percentages of the three major volcanic components (glass, crystals, and rock fragments) are plotted vs. depth (mbsf); the plot for "Others" includes clay resulting from the breakdown of volcanic rocks and up to 10% of nonvolcanic material.

By means of these data and other petrographic observations, the sequence at Site 767 can be divided into four intervals:

1. From the bottom of the sequence up to 700 mbsf (Unit IV: middle Eocene to lower Miocene), the dominant pelagic claystone contains no obvious dispersed ash component; there is no evidence in the sediment of nearby contemporaneous volcanism. Interbedded with the claystone are volcaniclastic sandy siltstone and siltstone turbidites that consist of rock fragments, plagioclase, and rare glass. These beds are considered to be the products of erosion of a volcanic terrane.
2. Between 700 and 406 mbsf (Unit III: lower to upper Miocene), the proportion of volcanogenic sediment in the sequence as a whole is minor and consists mainly of fine-grained plagioclase in claystone/silty claystone turbidites, and greenish hemipelagic claystone interpreted to be partly volcanogenic in origin. No discrete ash layers are recognizable in this part of the se-

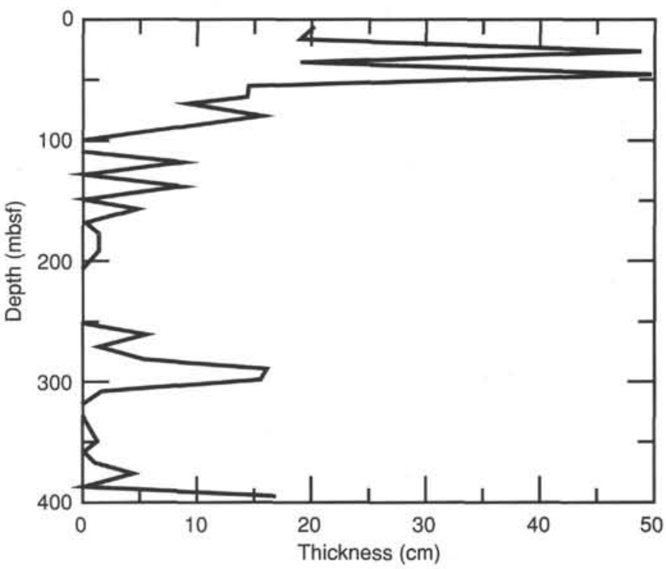

Figure 21. Total thickness plot of discrete ash layers in each core vs. depth, Hole 767B.

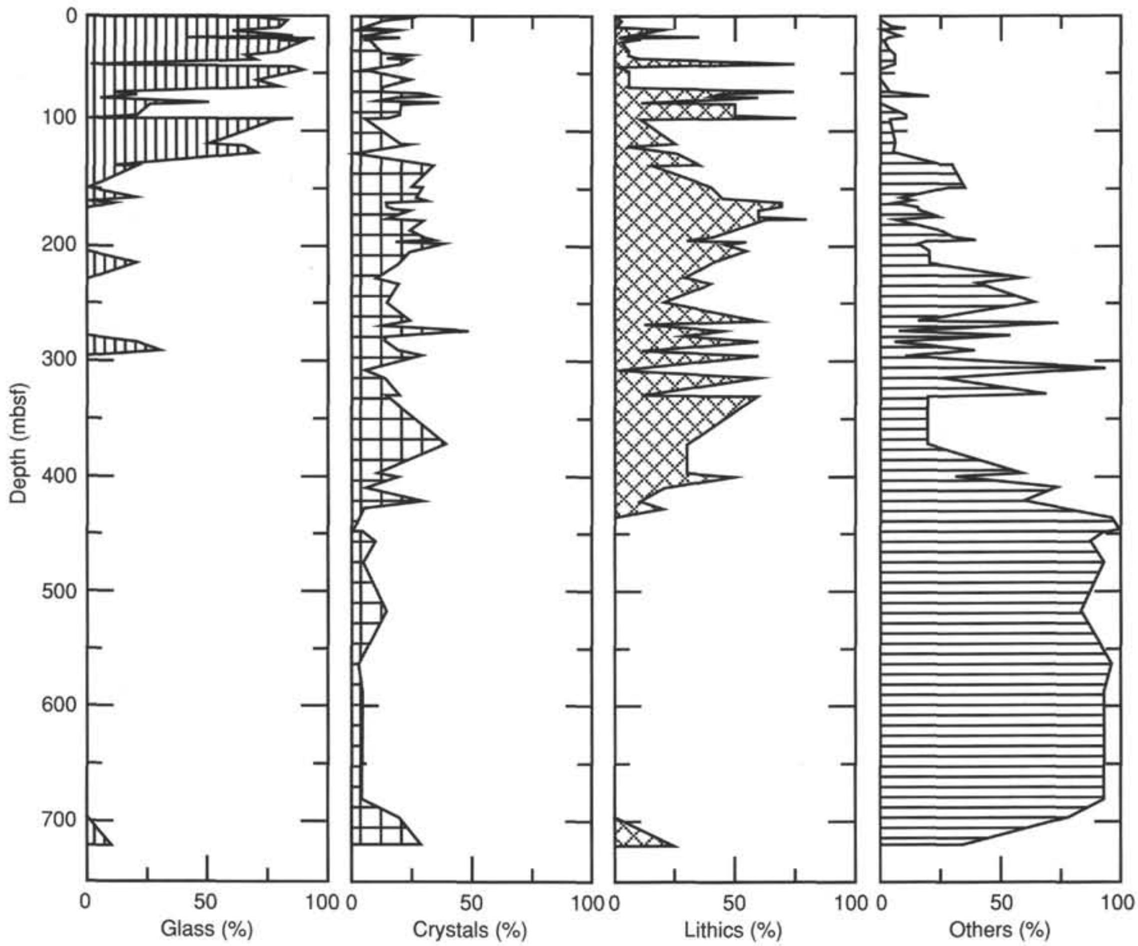

Figure 22. Abundance plot vs. depth for the major components of discrete volcaniclastic sediment layers (>90% identifiable volcanic components) at Site 767. These layers are chiefly ash beds and volcaniclastic turbidites; hemipelagic sediments are not plotted. The plot for "Others" includes clay that results from the diagenetic breakdown of volcanic grains and up to 10% nonvolcanic material. Data are derived from shipboard analysis of smear slides.

quence. The volcanic component probably does not represent contemporaneous explosive volcanic activity, but is more likely to be the product of erosion of preexisting volcanic rocks of basaltic to andesitic composition.

3. Scattered lithic ash beds occur between 406 and 250 mbsf (Subunit IIC and lower Subunit IIB: upper Miocene to lower Pliocene), representing a period of intermittent ash deposition. The deposits contain only minor amounts of glass and are mainly composed of rock fragments, plagioclase, hornblende, and pyroxenes. The rock fragments and assemblage of mineral phases indicate a probable andesitic composition for the ash, suggesting contemporaneous volcanic-arc activity during late Miocene time.

4. Vitric ashes become important above 200 mbsf (upper Pliocene to Holocene). Pyroclastic deposits in this part of the sequence contain between 40% and 95% glass, which gives the layers a white or light gray color (Fig. 22). However, there is also a significant crystalline component of biotite, feldspar, and hornblende. The petrology of these young ash beds is discussed in the following section.

In summary, ash beds and dispersed ash in hemipelagic deposits indicate that explosive arc volcanism began significantly influencing sedimentation in the Celebes Basin in late Miocene time. A continuing volcanic influence is evident from late Miocene through Holocene time, with major peaks in ash production in the late Miocene, early Pliocene, and Pleistocene. Rare volcaniclastic turbidites in Unit IV and a minor volcanic component in turbidites and hemipelagic claystone of Unit III indicate that erosion of exposed volcanic terranes supplied a minor but increasingly significant amount of sediment to the basin in middle Eocene through middle Miocene time.

Petrology of Ashes

Preliminary investigations of the petrographical, mineralogical, and chemical features of fresh volcaniclastic sediments occurring in the interval from 0 to 200 mbsf of Hole 767B have been made with the purpose of a petrologic characterization of the related volcanism. We have studied petrographically 60 samples of ashes containing more than 90% volcanic components, and five have been selected for chemical analyses as representative of the magmatic compositions of the volcanic sources.

On the basis of the relative proportions of crystals, glass, and volcanic rock fragments, and of the mineral assemblage occurring in the crystal component, the following groups have been distinguished:

1. VV = dominantly vitric ashes, consisting of more than 95% glass shards and containing very few crystals and rock fragments. The crystals are mostly plagioclase, and in addition clinopyroxene, hornblende, and accessories (magnetite and apatite) occur in some samples. The glass shards are both vesicular

and massive and are colorless, with a refractive index (RI) = 1.51 to 1.52.

2. VX1 = vitric ashes (95%–45% glass) containing plagioclase and clinopyroxene with or without orthopyroxene as a crystal component. The glass is colorless (RI = ~1.52) and, rarely, pale brown (RI = ~1.53). The lithic component consists of fragments with hyalopilitic to intersertal texture composed of plagioclase, clinopyroxene, and magnetite microliths.

3. VX2 = vitric ashes (95%–40% glass) containing a crystal assemblage of plagioclase, clinopyroxene, hornblende, biotite, and red-yellow alkaline amphibole. The lithic component is fairly scarce and consists of fragments with vitrophyric texture, containing assemblages of either plagioclase-clinopyroxene or plagioclase-hornblende-biotite among the microliths.

4. LV1 = lithic vitric ashes, consisting of colorless and pale brown glass, vitrophyric plagioclase-magnetite with or without clinopyroxene rock fragments, and a crystal component formed of plagioclase (calcic andesine), orthopyroxene, clinopyroxene, and accessories. A small proportion of glass shards show either exsolutions of fine-grained magnetite (colorless glass) or crystallites of plagioclase (brown glass), suggesting a difference in the composition of the related liquid phase.

5. LL1 = lithic ashes similar in crystal and lithic components to group LV1, but containing less than 20% glass.

Chemical data from three representative ash samples are presented in Table 5. Some major and trace elements are plotted in binary variation diagrams (Fig. 23). The analyzed vitric ashes can be considered to represent magmatic compositions, given the low content of crystals, as can be expected in oversaturated magmas erupted at early stages of crystallization (absence of modal quartz). However, their high loss on ignition (LOI), indicating a high volatile content on the basis of chemical analyses,

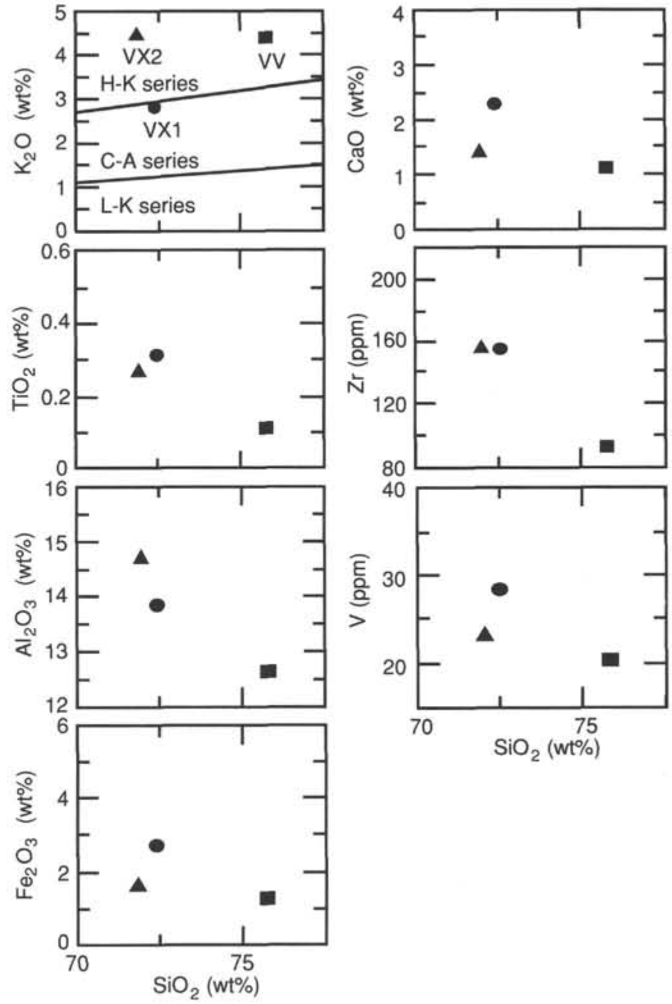

Figure 23. Variation diagrams of major and trace elements for selected ash samples, Hole 767B. In the K_2O vs. SiO_2 diagram, the boundaries of the low-K calc-alkaline (L-K), calc-alkaline (C-A), and high-K calc-alkaline (H-K) series are after Ewart (1979). The meanings of VX2 (triangles), VX1 (circles), and VV (squares) are discussed in text.

which can be related mainly to the secondary hydration of glass, suggests possible changes of the contents of mobile elements. With these uncertainties, some significant indications can be inferred from the chemical data, as follows:

1. The vitric ashes can be referred to distinct rhyolitic magmas and to different stages of fractionation;

2. The vitric ashes distinguished by crystal assemblages (groups VX1 and VX2) are also distinct in chemistry, notably in K_2O contents. In the K_2O vs. SiO_2 diagram (Fig. 23). the ash from group VX1 (Sample 124-767B-2H-2, 58 cm) plots in the field of calc-alkaline series, whereas the ash from group VX2, marked by the occurrence of biotite (Sample 124-767B-5H-5, 10 cm), plots in the field of high-K calc-alkaline series;

3. The vitric ash from the VV group (Sample 124-767B-10H-6, 86 cm) is a silica-rich rhyolite and shows an affinity to the high-K series.

In a preliminary way, we concluded that the analyzed ash layers record mainly the most fractionated products of at least two volcanic series. One is a calc-alkaline, andesite-dacite-rhyolite series rich in K_2O, which includes group VX1. The other one, represented only by potassium-rich rhyolites (VV and VX2),

Table 5. Chemical analyses of representative ash samples, Hole 767B.

Group sample	VX2 5H-5, 10 cm	VX1 2H-2, 58 cm	VV 10H-6, 86 cm
Major elements:			
SiO_2	71.98	72.50	75.87
TiO_2	0.27	0.31	0.11
Al_2O_3	14.70	13.79	12.59
$Fe_2O_3^{tot}$	1.59	2.67	1.25
MnO	0.09	0.07	0.05
MgO	0.59	0.83	0.31
CaO	1.42	2.27	1.10
Na_2O	3.60	3.01	2.83
K_2O	4.47	2.79	4.34
P_2O_5	0.06	0.05	0.02
Total	[a]98.76	98.29	98.46
LOI	5.02	5.09	4.69
Minor elements:			
Nb	3	6	4
Zr	157	155	93
Y	23	28	20
Sr	132	124	33
Rb	62	57	67
Zn	44	39	21
Cu	10	45	13
Cr	0	0	2
V	16	46	6
Ce	27	47	19
Ba	406	273	368

Note: Major elements are given in wt% and minor elements in ppm.
[a] Totals systematically below 100% have been obtained for on-board analyses and are interpreted as the result of hydration of the sample between ignition and weight.

could belong to a potassium-rich andesite-dacite-rhyolite series. Both series are typical of island-arc volcanism at mature stages of evolution.

Depositional Environment and Processes

The unifying theme in the sedimentary history recorded at Site 767 is deposition within a deep basin below the CCD, as evidenced by the low carbonate content and paucity of calcareous biogenic particles in the pelagic/hemipelagic background sediment. Within that depositional framework are major changes in depositional processes and provenance of sediment. The major changes we have recognized are (1) an upward transition from pelagic brown clay deposition in Unit IV to deposition of greenish gray hemipelagic mud in Units III to I; (2) a major influx of quartz-bearing muddy to sandy turbidites with continental provenance in Unit III; (3) an upward coarsening of hemipelagic muds from claystone in Unit III to clayey silt in Unit I, largely because of an increase in abundance of volcanogenic silt in Units II and I; (4) a variable influx of fine-grained carbonate turbidites in Units III and II; and (5) significant changes in the frequency and composition of volcanic ash (described in the preceding section).

Overlying the apparent oceanic basement at Site 767 is a sequence of nearly 100 m of reddish brown claystones (Unit IV) that accumulated from middle Eocene to early Miocene time. These deposits have the characteristics of deep-ocean pelagic clay: the fauna is sparse, consisting mainly of fish teeth, poorly preserved radiolarians, and agglutinated foraminifers; manganese oxide occurs as discrete micronodules; and rates of sedimentation were low, averaging 4 m/m.y. (see "Sediment Accumulation Rates" section, this chapter). Thin turbidites of volcanogenic silt in the upper part of Unit IV provide the first indication of volcanogenic sediment influx into the basin.

Unit III (lower to upper Miocene) records a significant increase in the rate of sedimentation in the basin as the result of a major episode of terrigenous turbidite deposition, accompanied by a change from pelagic brown clay to hemipelagic greenish gray clay as the background sediment. The well-rounded quartz, abundant plant fragments, and coal clasts in the turbidites clearly demonstrate a continental provenance. The turbidite package appears to represent a single symmetrical depositional megacycle, with turbidite progradation followed by a waning of terrigenous turbidite deposition. The turbidites coarsen upward from silty claystone and claystone in Subunit IIIC to fine sand in Subunit IIIB, then fine upward again through Subunit IIIA. The variation in grain size is accompanied by a change in relative proportion of turbidite to hemipelagic sediment: turbidites make up over 75% of the section in Subunit IIIB and decrease upward and downward in Subunits IIIA and IIIC, respectively. The large volume of thick yet fine-grained turbidite beds and the abundance of plant debris suggest that the most likely source for this sediment was a major delta complex within a low-lying coastal plain.

During deposition of the early to late Miocene terrigenous turbidite cycle, the background hemipelagic sediment was predominantly clay. Within the overlying Unit II, the hemipelagic sediment gradually coarsens upward to clayey silt, with the silt-size component consisting largely of volcanic ash. This increase in grain size records a major increase in influx of airborne ash to the basin in late Miocene time, which is also reflected in the appearance of common ash layers in Unit II. This important volcanic influence on sedimentation has continued up to the present, as illustrated by the plot of aggregate ash thickness per core (Fig. 21) and the plots of hornblende and biotite abundance in Figure 6. Hornblende and biotite appear to be almost entirely of volcanic origin at Site 767 and are virtually restricted to Units II and I.

The waning of terrigenous turbidite deposition in the upper part of Unit III (middle to upper Miocene) was accompanied by the appearance of carbonate turbidite layers, which persist throughout the overlying Unit II (upper Miocene to Pleistocene). The abundance plot of foraminifers vs. depth in Figure 6 is a good indicator of the vertical extent of carbonate turbidites within the section. The composition and structures of these turbidites and the absence of carbonate in the enclosing hemipelagic sediment clearly indicate redeposition of shallower-water sediment into a deep basin below the CCD. Both shelf and deeper-water sources are indicated by the nature of the biogenic constituents in the turbidites, with a decrease in shelf-derived carbonate from early Pliocene to Pleistocene time (see "Biostratigraphy" section, this chapter). Redeposited carbonate beds are rare in Unit I.

BIOSTRATIGRAPHY

Biostratigraphic Summary

Three holes were drilled at Site 767 in the Celebes Sea. Only one core, of Pleistocene age, was taken in Hole 767A. Hole 767B was drilled to a total depth of 739.0 mbsf. Hole 767C was washed down to 680.0 mbsf and then cored to 794.1 mbsf. The sedimentary sequence ranges in age from Holocene to late middle Eocene and overlies basaltic basement, which was encountered in Section 124-767C-12R-CC.

Calcareous micro- and nannofossils are only present within the carbonate turbidites from the Pleistocene (NN20/NN21) to upper middle Miocene (NN8) (0–598.5 mbsf), which are interbedded in barren volcaniclastic and clastic sediments and are deposited below the CCD. In these turbidites, material from a shallower environment was displaced into the basin, as shown by the presence of shallow-water benthic foraminifers, benthic diatoms, and tunicate spines.

The sediments also contain sponge spicules, volcanic ashes, rare plant fragments, and reworked planktonic foraminifers and nannofossils. Because of the rapid sedimentation of the turbidites, the calcareous fossils are still preserved, although they are dissolved in pelagic-dominated sediments. Generally, the calcareous fossils, where present, are well preserved, showing traces of dissolution only in certain levels.

Age determinations for the upper part of the sequence were mainly determined on the basis of calcareous nannofossils; the foraminifer assemblages consist predominantly of small-sized, well-sorted specimens, lacking biostratigraphic markers. Diatoms are present in the upper section of Hole 767B down to about Core 124-767B-5H (47.0 mbsf). Below this level only rare fragments were found.

The thickness and the number of the carbonate turbidites, as well as the grain size within them, increase downsection from the upper Pliocene to the lower Pliocene. An increase of benthic foraminifers relative to planktonic foraminifers, from 30% in the Pleistocene to 80% within the lower Pliocene, as well as the abundance of tunicate spines, might indicate a more important input of shallow-water material. Within the lowermost Pliocene and upper to middle Miocene, the carbonate turbidites are more distal. The turbidite sediments are very fine grained, thinner, and less numerous in this interval, finally disappearing within Core 124-767B-74X. Within the lower part of the succession (below Core 124-767B-63X, 598.5 mbsf), the carbonate turbidites are indurated and partially dolomitized. They are barren of calcareous fossils as a result of recrystalization.

A high continental input (quartz sand, plant and coal fragments, and reworked Eocene and lower middle Miocene nannofossils) can be observed from the lower part of Zone NN11 (about Core 124-767B-41X) to the middle Miocene (NN8). No fossils were found from Core 124-767B-64X to Section 124-767B-74X-2 (598.5 to about 697 mbsf).

We observed a transition from grayish green to reddish brown claystones within Core 124-767B-74X. This transition is characterized by the disappearance of the carbonate turbidites. Fish teeth, arenaceous foraminifers, and radiolarians are few to common within sieved coarse fractions of the reddish brown, deep-water claystones encountered in Cores 124-767B-74X to -78X (bottom) and in Cores 124-767C-3R to -12R. Fossils yield an early Miocene to late middle Eocene age (about 42–43 m.y.) for the red clay successions. Late middle Eocene sediments overlie the basaltic basement at the base of Core 124-767C-12R.

Nannofossils

The Quaternary was determined from Core 124-767A-1H and from Core 124-767B-1H to Sample 124-767B-17X-1, 120 cm (149.5 mbsf). Nannofossils are only present within the carbonate turbidites interbedded in a diatom-bearing volcaniclastic sequence containing several distinct ash layers. We consider that this sequence was deposited below the CCD. The nannofossils within the turbidites are generally well preserved. Traces of dissolution were observed only in a few samples. These sediments were displaced from a shallower environment located above the CCD. They contain fragments of planktonic and benthic diatoms, radiolarians, sponge spicules, fecal pellets, benthic foraminifers, and some tunicate spines. Rare reworked nannofossils from older strata have also been recognized. The planktonic foraminifers are generally of smaller size and are well sorted. Generally, these turbidites are also rich in volcanic ash.

The upper Pleistocene (Zones NN20/NN21) was recognized from the top of Hole 767B through Core 124-767B-3H (0–28.0 mbsf) by the presence of *Emiliania huxleyi* and *Gephyrocapsa oceanica*. The boundary between these two zones was determined between Cores 124-767B-2H and -3H (18.5 mbsf). Zone NN19 of the lower Pleistocene is present from the top of Core 124-767B-4H to Sample 124-767B-17X-1, 120 cm (28.0–149.5 mbsf).

The Jaramillo Event was recognized between 60 and 65 mbsf within Core 124-767B-7H. This event is normally characterized by the dominance of a very small *Gephyrocapsa* sp. (2–3 μm), whereas larger species like *Pseudoemiliania lacunosa, Gephyrocapsa oceanica, Helicosphaera carteri,* and *Cyclococcolithus leptoporus* are considerably less abundant than before and after this event (Gartner, 1977). This level is not well expressed at Hole 767B. However, it is possible to observe the dominance of *Gephyrocapsa* sp. and a remarkable decrease in larger forms. But the *Gephyrocapsa* sp. found in Core 124-767B-7H is a larger size than it should be and thus does not correspond to the tiny species mentioned by Gartner (1977).

An increase of *Discolithina japonica* can be observed within Zone NN19, which is less pronounced, however, than in other areas (Müller, 1979, 1985). The Pliocene/Pleistocene boundary was determined between Sections 124-767B-17X-1 and 124-767B-17X-2, at about 150 mbsf. This boundary is not very clear at Site 767 because of the dilution of the nannofossils by carbonate fragments, sponge spicules, and volcanic ash on the one hand and the presence of reworked nannoplankton on the other. Discoasters are only rare within the upper part.

A more detailed study is necessary to subdivide the Pliocene, which has been determined from Sections 124-767B-17X-2 to 124-767B-34X-2 (149.5–311.8 mbsf). As in the Quaternary, the presence of nannofossils is restricted to the carbonate turbidites, which were predominantly derived from a very shallow area. Turbidite numbers and thicknesses increased throughout the Pliocene, and they are more coarse grained at the base. Some lower Pliocene samples are rich in tunicate spines, shallow-water benthic foraminifers, sponge spicules, and some gastropods. There are also some plant fragments and glauconite.

The carbonate turbidites become more distal and thinner within the lowermost Pliocene and Miocene. They disappear within Core 124-767B-74X. The upper Miocene (Zones NN11–NN10) was encountered between Sections 124-767B-34X-2 and 124-767B-46X-6 (311.8–433.9 mbsf). The boundary between these two zones lies in Core 124-767B-42X at about 393.2 mbsf. Nannofossils are generally common and well preserved within the upper, more clayey part of the turbidites, whereas the discoasters sometimes show evidence of slight overgrowth within the lower parts.

A stronger influence from the continent can be observed within the lowermost part of Zone NN11 (downsection from about Core 124-767B-40X), as indicated by a remarkable increase in plant fragments and the occurrence of more terrigenous material.

Nannoplankton Zone NN9 of late middle Miocene age is present from the top of Core 124-767B-47X to Sample 124-767B-59X-CC (433.9–553.5 mbsf). Nannofossils are common, including *Discoaster bollii, Discoaster calcaris, Discoaster hamatus,* and *Discoaster neohamatus*. *Discoaster pentaradiatus* is still common within the upper part of Zone NN9. It is absent from the lower part of NN9 whereas *Catinaster coalitus* and *Catinaster calyculus* are present.

Core 124-767B-60X is barren of nannoplanktons. Cores 124-767B-62X and -63X belong to the *Catinaster coalitus* Zone (NN8). Nannofossils decrease in these cores and are absent below Core 124-767B-63X (598.5 mbsf).

The number of carbonate turbidites decreases within the middle Miocene. The sediments are characterized by a high input from the continent, with quartz sands, plant fragments, and reworked species of mainly early middle Miocene age (NN5), but there are also very rare Eocene species. Several indurated carbonate turbidites are present down to Core 124-767B-74X, but, because of compaction and pressure dissolution, the nannofossils were destroyed by recrystallization. No nannofossils were found in the underlying reddish brown, deep-water claystones from Cores 124-767B-74X to -78X or in any of the Hole 767C sediments that overlie basaltic basement.

Foraminifers

In Core 124-767A-1H and Cores 124-767B-1H through -59X (0–559.8 mbsf), foraminifers are found as displaced faunas in light colored, carbonate-rich turbidites, whereas the sediments in between are barren. The fossils are generally well preserved, but they do not permit a clear biostratigraphic zonation. As a result of size sorting, the faunas mostly consist of small specimens only, corresponding to the 63–125-μm size fraction. The most frequent species are long-ranging ones (*Globigerinita glutinata, Turborotalia humilis,* and *Globigerina* spp.), although only rare samples contain larger-sized, age-diagnostic forms.

Samples 124-767B-5H-CC, 124-767B-6H-CC, and 124-767B-7H-2, 63–64 cm, were dated as upper Pliocene–Quaternary (N22), on the basis of the presence of the zonal marker *Globorotalia truncatulinoides*. The co-occurrence of right-coiling *Globorotalia menardii* with right-coiling *Pulleniatina* spp. in Sample 124-767B-26X-4, 7–9 cm, indicates a late Pliocene age (the upper part of N19/N20 or N21). *Globorotalia margaritae,* which ranges through N18 and N19/N20, is found in Samples 124-767B-27X-4, 121–123 cm, and 124-767B-28X-2, 107–109 cm. The presence of *Globorotalia plesiotumida* in Samples 124-767B-33X, 98–100 cm, and 124-767B-32X-4, 6–8 cm, gives a late Miocene N17 age or younger.

Benthic foraminifers are abundant in the displaced faunas from Cores 124-767B-1H to -59X. Benthic frequencies, relative to the number of planktonic foraminifers, show variations that may reflect changes in the deposition depth at the source of the displaced carbonates (Fig. 24). Generally, the percentage of benthic foraminifers within the total foraminifer fauna decreases with increasing depth of deposition. This relation can be described as a logarithmic function (Wright, 1977; van Marle et al., 1987). Alternatively, the changes may be related to changes in the energy of the turbidites that influenced the size sorting.

In Cores 124-767B-4H through -8H, the benthic foraminifers are generally rare, around 20% of the foraminiferal faunas. Going downhole, the benthic frequencies increase to about 60% in Cores 124-767B-17X through -27X (150–250 mbsf), indicating a shallower deposition depth at the source, possibly the middle to outer shelf. The ratio then decreases again, to about 30% in Cores 124-767B-34X through -59X (309.8–559.8 mbsf). The lower frequencies of benthic foraminifers in the upper and lower parts of the section might correspond to a greater depositional depth at the source of the turbidites, possibly the upper bathyal.

We could not obtain foraminiferal ages for the deeper cores of Hole 767B or for cores from Hole 767C. All samples from Cores 124-767B-60X to -73X and from Cores 124-767C-1R to -2R are barren. The carbonate-rich levels in these cores are recrystallized and do not contain calcareous foraminifers. In the

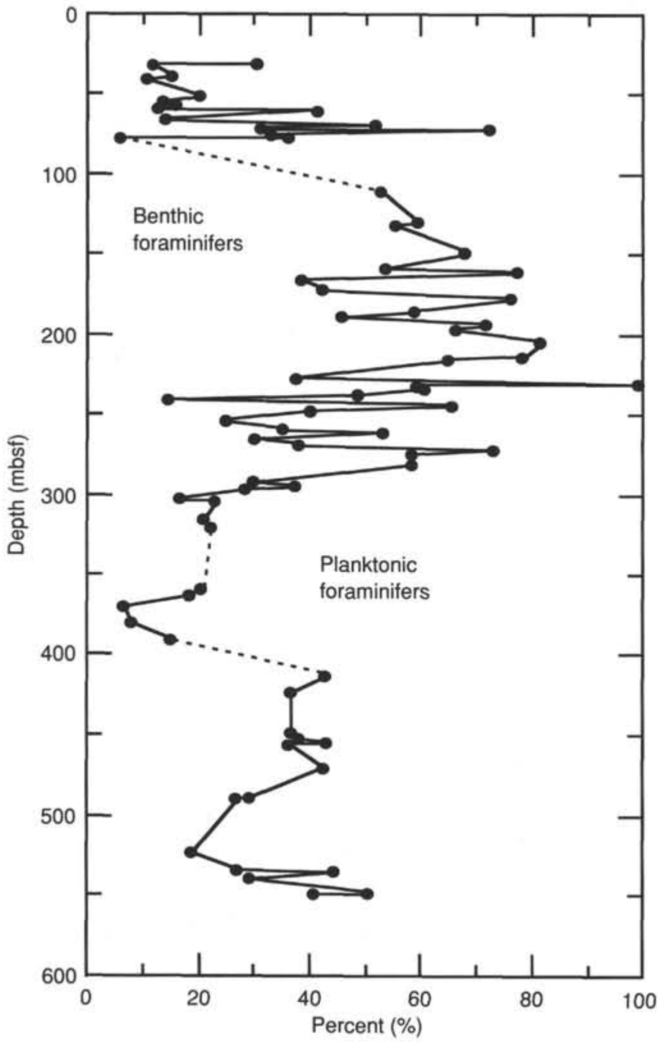

Figure 24. Percentage plot of benthic and planktonic foraminifers in the faunas from the >63-μm size fraction of calcareous turbidite samples vs. depth, Hole 767B.

red clays from Cores 124-767B-74X to -78X and from Cores 124-767C-3R to -12R, only agglutinated benthic foraminifers were found. The presence of arenaceous foraminifers, and the high concentrations of fish remains, indicate deposition below the CCD in open-ocean conditions.

Diatoms

Diatoms are present only in the upper section of Site 767. This includes all of Hole 767A and the upper part of Hole 767B. Diatoms are common and fairly well preserved in the soft, brown sediments of the upper 2 m of Cores 124-767A-1H and 124-767B-1H, but they are generally rare and poorly preserved below this level. The deepest identifiable diatom assemblage was found in Section 124-767B-5H-7 (47 mbsf), though most intervening successions are nearly barren of diatoms. Below Core 124-767B-5H, we found only rare fragments of heavily silicified benthic diatoms and the large planktonic *Ethmodiscus* sp. No diatom remains were found below Core 124-767B-9H (80 mbsf).

The disappearance of diatom tests in Site 767 sediments is primarily a function of diatom dissolution in the water column and in the sediments. Degradation and the eventual disappearance of heavily silicified sponge spicules downcore indicates biogenic silica corrosion by sediment diagenesis. Extracting a usable diatom assemblage from Site 767 sediments was further hampered by dilution of the biogenic particles by terrigenous and volcanogenic debris and by the apparent low primary productivity in the Celebes Basin.

The diatom assemblages represented in Cores 124-767B-1H to -5H are of the *Pseudoeunotia doliolis* Zone of Burckle (1972, 1977; reviewed by Barron, 1985a, 1985b) representing the late Quaternary. The assemblage consists of most taxa typical of the *P. doliolis* Zone in low-latitude sediments. These include *Azpetia nodulifer, Azpetia africana, Nitzschia marina, Thalassiosira oestrupii, Hemidiscus cuniformis,* and *Pseudoeunotia doliolis.* In addition to the planktonic diatom assemblage, benthic species were found in the sediments from Site 767. These indicate reworking and downslope transport within turbidity currents.

Radiolarians

Radiolarians are common in the upper part of the sedimentary succession at Site 767 but, like the diatoms, they are scarce in the Neogene sediments below Core 124-767B-10H (90 mbsf). No systematic study of Neogene radiolarians was performed. After more than 600 m of sediment barren of radiolarians, these fossils reappear as abundant in the coarse fraction of Paleogene pelagic red clays. Radiolarians are accompanied by ichthyoliths and rare agglutinated foraminifers in these successions. The preservation of Paleogene radiolarians is moderately poor to poor (see "Explanatory Notes" chapter, this volume).

All of the radiolarian zones discussed below are described in Sanfilippo et al. (1985). Figure 25 shows the published ranges of radiolarians identified in the Site 767 Paleogene sediments as well as those used as a guide for shipboard age determination. In some cases, poor preservation leaves certain specific identifications in doubt.

Hole 767B

The first appearance of radiolarians in Hole 767B is in Section 124-767B-76X-6 (720 mbsf), more than 25 m below the consistent occurrence of red clays. The assemblage includes abundant *Dorcadospyris ateuchus,* along with *Didymocyrtis prismatica, Theocyrtis annosa, Artophormis gracilis,* and rare *Lychnocanoma elongata,* placing it in the *Lychnocanoma elongata* Zone of Riedel and Sanfilippo (1971, emend. 1978) of the lower lower Miocene. In the core catcher of Core 124-767B-76X (723 mbsf), the assemblage lacks *L. elongata* and includes rare exam-

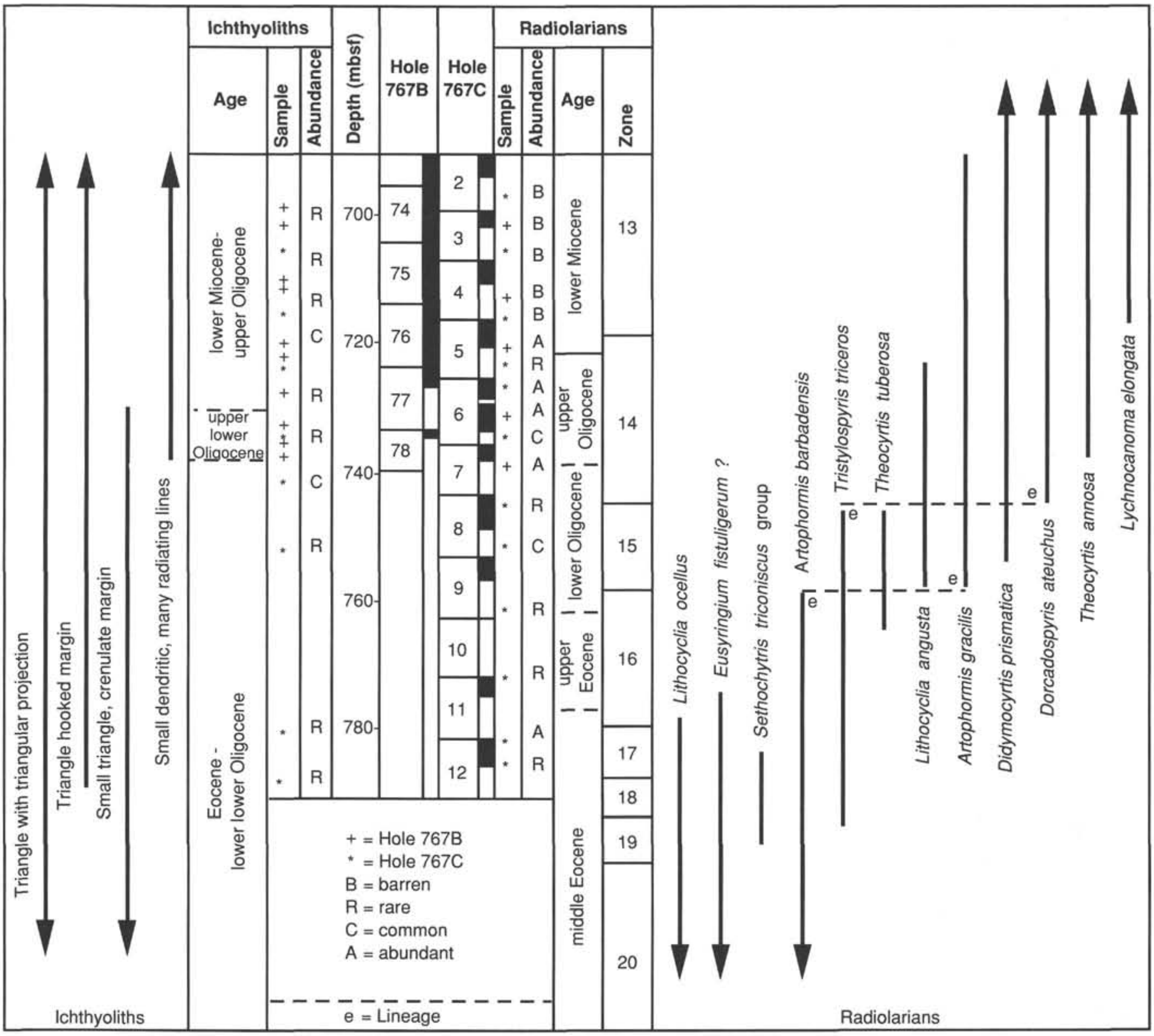

Figure 25. Published biostratigraphic ranges of selected radiolarians and ichthyoliths identified in the red clays of Site 767. Standard radiolarian zones (summarized by Sanfilippo et al., 1985) are used, calibrated to the Berggren et al. (1985a, 1985b, 1985c) time scale. Ichthyolith ranges are from Doyle and Riedel (1985). Sample positions and abundance of radiolarians and ichthyoliths re noted. Evolutionary transitions within radiolarian lineages are noted by a dashed line marked with "e". This chart is meant as a comparative model of radiolarian and ichthyolith zonations recognized in Site 767 Paleogene sediments and should not be read as a range chart. Our purpose is merely to illustrate taxa and assemblages recognized for initial age determination. More detailed biostratigraphic work will follow in the *Proceedings of the Ocean Drilling Program, Scientific Results*. Radiolarian zones, according to the notation of Berggren et al. (1985a, 1985b, 1985c), are as follows: 13 = *Lychnocanoma elongata,* 14 = *Dorcadospyris ateuchus,* 15 = *Theocyrtis tuberosa,* 16 = *Thyrsocyrtis bromia,* 17 = *Podocyrtis goetheana,* 18 = *Podocyrtis chalara,* 19 = *Podocyrtis mitra,* and 20 = *Podocyrtis ampla.*

ples of *Lithocyclia angusta,* as well as *D. ateuchus,* indicating the *Dorcadospyris ateuchus* Zone (Riedel and Sanfilippo, 1971) of the upper Oligocene.

Samples from Cores 124-767B-77X through -78X (733–739 mbsf) contain common *L. angusta. Stauralastrum* sp., which is known from the upper Oligocene successions of the Philippine Basin (DSDP Site 292; Ling, 1973), is also present in Cores 124-767B-77X and -78X. Radiolarians that appear transitional between *Dorcadospyris ateuchus* and *Tristylospyris triceros* are common as well. *Theocyrtis tuberosa* is present in Core 124-767B-78X, and *D. prismatica* is still present at the base of Core 124-767B-78X. The occurrence of these radiolarians places the bottom of Hole 767B in the upper part of the *T. tuberosa* Zone of the upper part of the lower Oligocene. Defining the upper Oligocene/lower Oligocene boundary is difficult in these sediments because of the poor preservation. Important morphologic characters that distinguish members of the *Dorcadospyris/Tristylospyris* lineage are not preserved in most specimens, and mineral overgrowths complicate the separation of *T. annosa* from *T. tuberosa.*

Hole 767C

Radiolarians are absent in the upper five cores of Hole 767C. The highest recovery of a radiolarian assemblage was in Section 124-767C-6R-5 (733 mbsf). The assemblage is similar to that of Section 124-767B-77X-CC, including *D. ateuchus, T. annosa*(?), *L. angusta, Stauralastrum* sp., *Euchitonia* sp., and *A. gracilis* in the *D. ateuchus* Zone. Preservation of radiolarians is spotty through Cores 124-767C-7R and -8R, but a lower Oligocene assemblage is present in Section 124-767C-8R-CC (753 mbsf). This assemblage includes abundant *Tristylospyris triceros* with *T. tuberosa, L. angusta, A. gracilis, Euchitonia* sp., and *D. prismatica,* placing it in the upper part of the *T. tuberosa* Zone of Riedel and Sanfilippo (1970, emend. 1971, 1978) of the early Oligocene. Preservation is poor in the recovered sections of Cores 124-767C-9R to -11R.

Core 124-767C-12R, overlying basement, contains intervals with abundant but very poorly preserved radiolarians of late middle Eocene age. This assemblage, best developed in Section 124-767C-12R-1 (782 mbsf), contains *Lithocyclia ocellus, T. triceros,* and forms resembling *Eusyringium fistuligerum, Artophormis barbadensis,* and *Sethochytris triconiscus.* Poor preservation prevents a reliable specific identification at this time, but the assemblage closely resembles the typical upper middle Eocene radiolarian assemblage of the *Podocyrtis chalara* Zone (Riedel and Sanfilippo, 1970) to the *Podocyrtis goetheana* Zone (Moore, 1971, emend. Riedel and Sanfilippo, 1978). Despite the poor preservation, this interval contains the highest abundance of radiolarians found at Site 767, suggesting a higher biogenic productivity during this interval of pelagic clay deposition. The lowest radiolarian assemblage recovered is from Sample 124-767C-12R-3, 20–23 cm (786.5 mbsf). This appears to be a similar assemblage to the one described above, but preservation is poorer. Below this level of recovered sediment, radiolarians are rare and are too poorly preserved for identification. The earliest microfossil date is about 4 m above basement, constraining the age of basalt.

Ichthyoliths

Ichthyoliths were found at Site 767 in Cores 124-767B-64X to -78X and in Cores 124-767C-3R to -12R (see Fig. 25). However, Cores 124-767B-64X to -73X only contain rare fragments that could not be identified.

The red clays at Site 767 (Cores 124-767B-74X to -78X and 124-767C-3R to -12R) contain sufficient numbers of ichthyoliths to allow for general age determinations. Although ichthyoliths are mostly rare (between 10 and 20 specimens per sample), more than half of the samples from the red clays in both holes contain one or more specimens of the Cenozoic "triangle with triangular projection."

A "small triangle crenate margin" (Eocene–lower Oligocene) was encountered in Sample 124-767B-78X-1, 90–93 cm, at a depth of approximately 733 mbsf; Sample 124-767C-6R-CC (at a depth of 735 msbf) contains a specimen of "small dendritic many radiating lines" (lower Oligocene to Holocene). The combination of these two types, at approximately the same depth in both holes, indicates a early Oligocene age for that level (Fig. 25).

In the deeper cores from Hole 767C, a "triangle hooked margin" was found in two samples from Sections 124-767C-2R-CC and 124-767C-11R-CC, respectively. This type of ichthyolith has its first occurrence at the base of the Eocene, and its presence indicates that the sediments overlying basement are of an Eocene or younger age.

PALEOMAGNETICS

Introduction

The scientific objective of Leg 124 was to investigate the origin and paleoenvironment associated with some of the marginal basins in Southeast Asia by drilling into the sediment column and the basement of the Celebes and the Sulu seas. Paleomagnetic measurements of the sediments and the basement rock play an important role in the study by providing magnetostratigraphy of the sediment column for age determination and inclination changes through time for assessment of the north-south movement of the marginal basins after their formation. Site 767, located in the northeastern part of the Celebes Sea, produced useful data that may be critical to the ultimate scientific goal.

Magnetostratigraphy

To determine the magnetic polarity sequence of the sediment column, the archive halves of all sections of APC cores (124-767A-1H and 124-767B-1H to -10H) were measured in the pass-through 2-G Enterprises cryogenic magnetometer at 10-cm intervals. All sections were measured at the natural remanent magnetization (NRM) level and at least at one demagnetization step of 10 mT. One section per core was selected for detailed demagnetization at steps of 0, 5, 10, 15, and 20 mT.

Typical paleomagnetic results of APC cores are shown in Figure 26 for Core 124-767A-1H. The declination, inclination, and magnetization intensity are plotted vs. depth below seafloor. The declination shows values close to 270° with inclina-

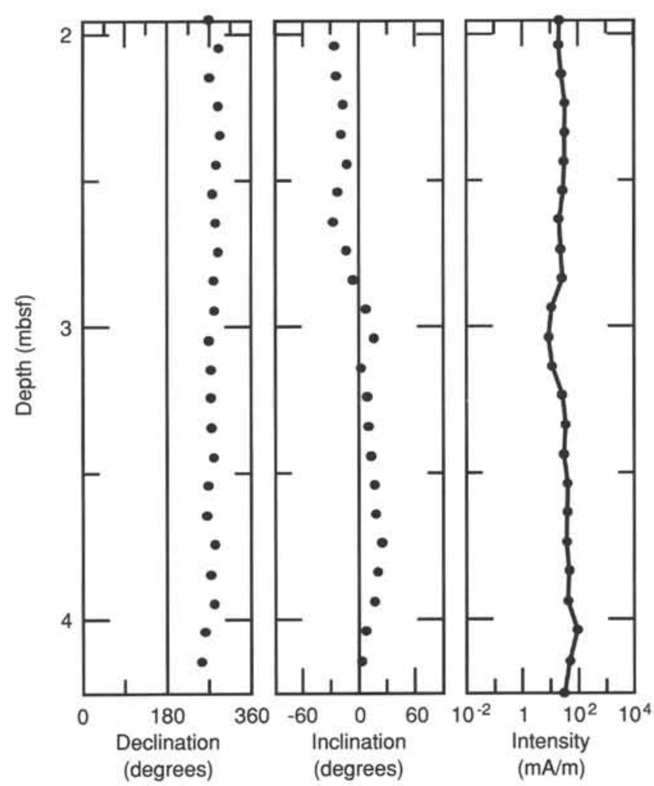

Figure 26. Magnetostratigraphic plot of declination, inclination, and intensity for Core 124-767A-1H. The declination is relative to the core-liner mark.

tions about 0°. Declinations are relative to the core-liner mark and inclinations are consistent with the site equatorial latitude.

Results from the APC cores provide excellent data for determination of polarity sequence. We were able to identify the boundary of the Brunhes/Matuyama Chrons and the beginning and end of the Jaramillo Event. The compiled results are shown in Figure 27. In the figure, all declinations are rotated to match the declinations of Core 124-767B-3H, which is corrected for core orientation by the Eastman-Whipstock Multishot core orientation tool.

The reversals identified in Figure 27 are based mainly on declination swings of 180°. Normally at middle- and high-latitude sites, a change in sign of the inclinations would also occur. This, however, is not seen very clearly in the inclination data of Site 767 as a result of the low site latitude (4.73°N), which predicts an inclination of about 2°.

The depths and ages of the three latest reversals corresponding to the Brunhes/Matuyama boundary and the beginning and end of the Jaramillo Event are listed in Table 6. The ages of these three reversals are well documented (e.g., Berggren et al.,

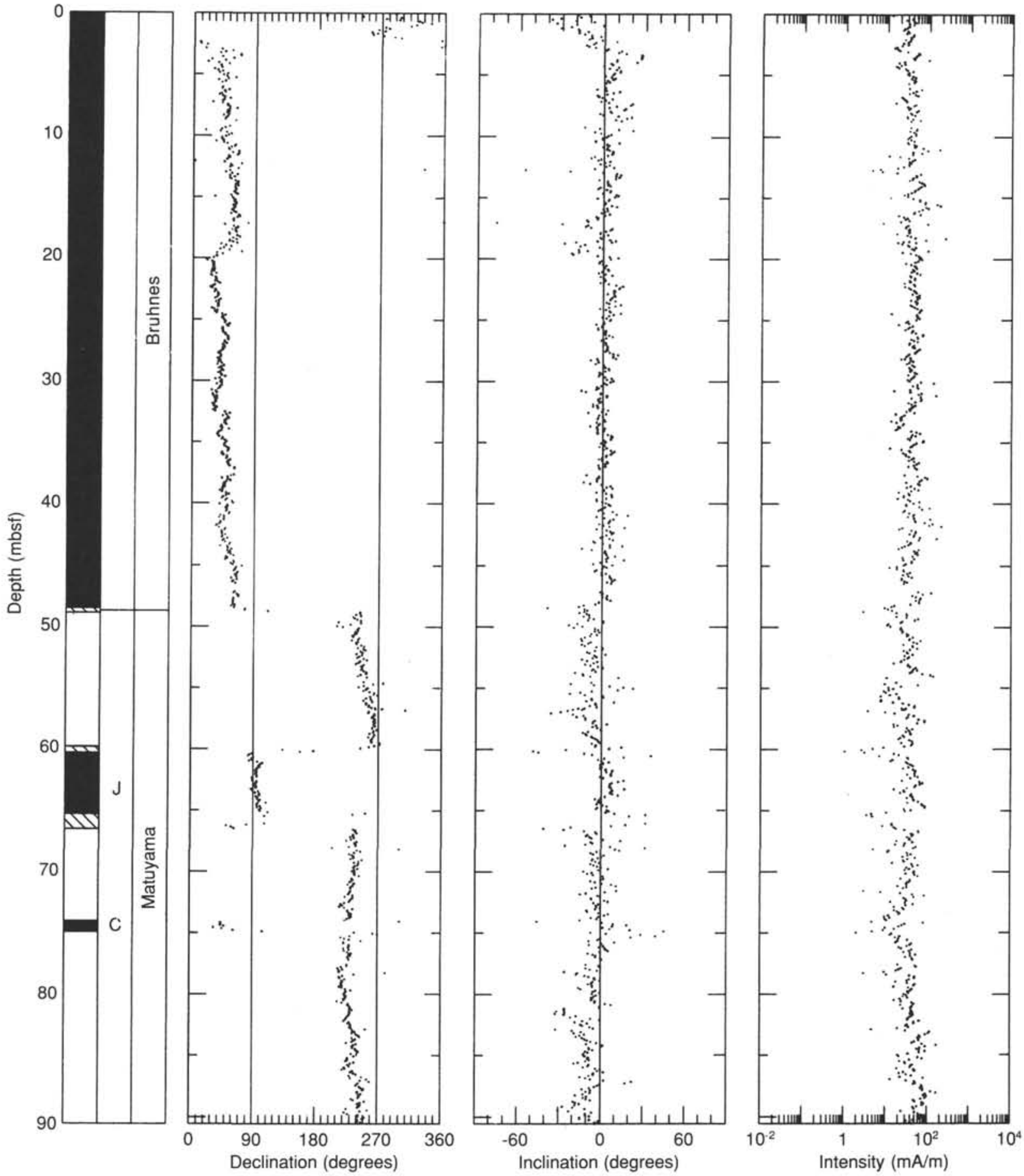

Figure 27. Magnetostratigraphic plot of paleomagnetic parameters for APC cores of Hole 767B (Cores 124-767B-1H to -10H). Declinations are corrected to match with those of Core 124-767-3H, which is corrected for core orientation. Geomagnetic reversals are identified by swings of declination for 180° and decrease in intensity. J = Jaramillo Event and C = Cobb Mountain Event.

Table 6. Depths and ages of geomagnetic reversals, Hole 767B.

Core, section, interval (cm)	Depth (mbsf)	Name	Type	Age (m.y.)
124-767B-				
6H-2, 40	48.8	Brunhes/Matuyama	R-N	0.73
7H-3, 70	60.2	End of Jaramillo	N-R	0.91
8H-1, 50	66.4	Beginning of Jaramillo	R-N	0.98
9H-2, 110	74.1	End of Cobb Mountain	N-R	1.11
9H-3, 50	74.9	Beginning of Cobb Mountain	R-N	1.12

Note: N-R = normal to reversed transition and R-N = reversed to normal transition.

1985c). A plot of these dates vs. depths gives an excellent linear relationship (Fig. 28) with an estimated sedimentation rate of 70.4 m/m.y. for the top 70 mbsf of Site 767.

A very short interval of normal polarity was observed in the Matuyama Chron (Fig. 27) between Sections 124-767B-9H-2 and 124-767B-9H-3 at about 75 mbsf (Table 6). Accompanying the swing of declinations were variations in inclination and intensity. The depth-age relation (Fig. 28) suggests an age of about 1.1 Ma. This interval may be correlated to the Cobb Mountain Event detected in lava flows in California (Mankinen et al., 1978) and DSDP cores in the North Atlantic (Clement and Kent, 1986/87).

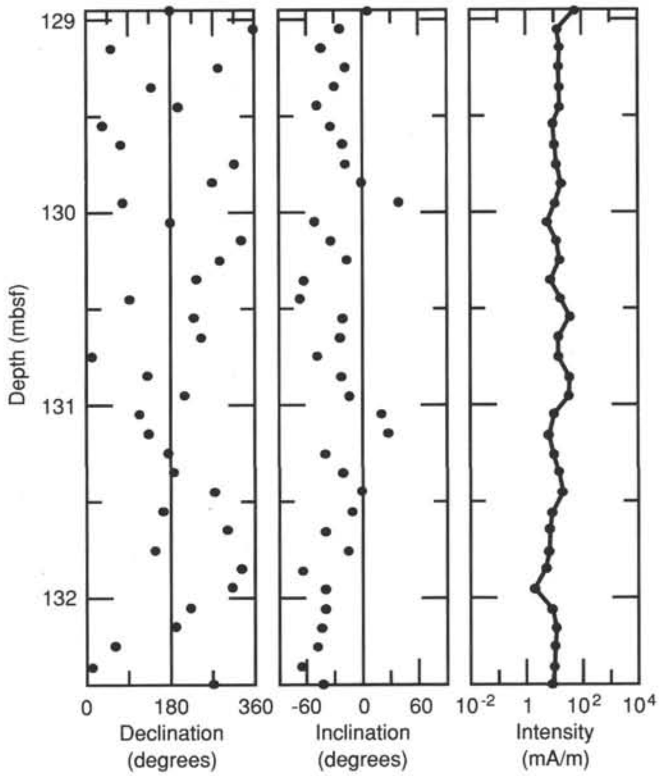

Figure 29. Magnetostratigraphic plot of paleomagnetic parameters vs. depth for Core 124-767B-15X. Note the large scatter in declination and inclination values caused by rotary disturbance.

Paleolatitudes

With the initiation of XCB coring, paleomagnetic measurements lost the azimuthal control caused by the rotary disturbance. This is well demonstrated by Core 124-767B-15X (Fig. 29). The scatter in declinations and inclinations makes determination of the polarity sequence essentially impossible.

For XCB and RCB cores, paleomagnetic measurements were continued by switching from the continuous measurement of archive halves to the measurement of discrete samples taken from the working halves. These samples were taken by pressing the sample boxes into the sediment and removed with the uphole direction noted. Samples were taken normally at a rate of one per section from areas of least disturbance. The samples were measured at NRM and selected demagnetizing steps to reveal the primary magnetization component.

During the demagnetizing experiment of the discrete samples, we found a persistent vertical component that existed within almost all samples from XCB cores. This soft secondary component could be removed normally by a field of 10 mT (Fig. 30). The soft magnetic overprint does not exist in APC and RCB cores, and we suspect that the coring shoe of the XCB may be responsible.

The inclinations (at a 20-mT demagnetization level) for selected cube samples from the XCB cores in Hole 767B and the

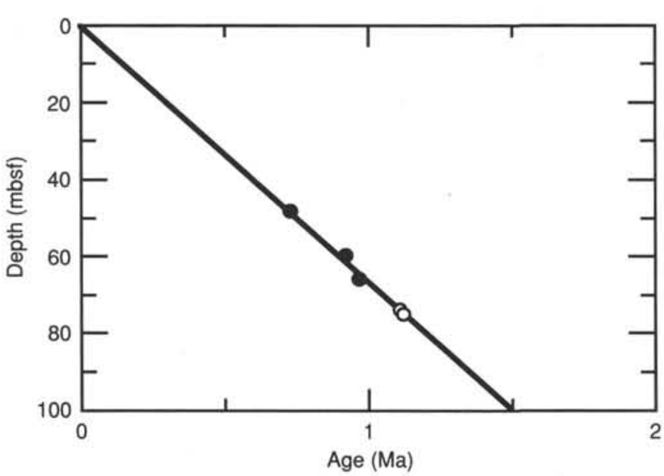

Figure 28. Plot of reversal depths vs. ages for the five reversals shown in Figure 27. The sedimentation rate is estimated at 70.4 m/m.y. Open circles represent the upper and lower boundaries of the Cobb Mountain event, closed circles represent the Brunhes/Matuyama boundary and the upper and lower boundaries of the Jaramillo event.

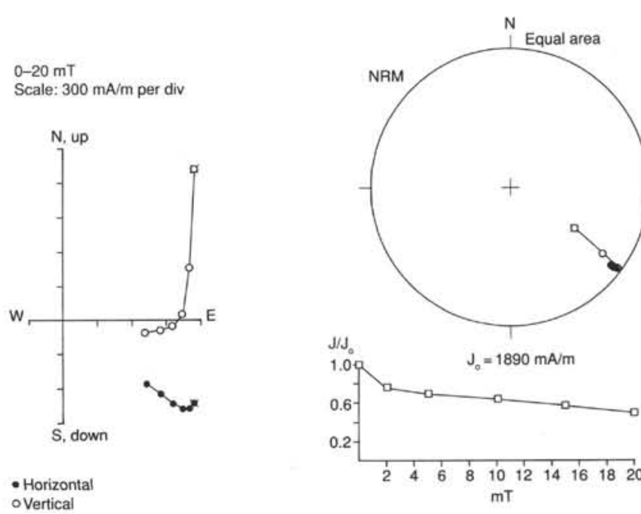

Figure 30. Zijderveld vector diagram for Sample 124-767B-22X-2, 30–32 cm. Note the large vertical component removed by alternating field demagnetization.

RCB cores in Hole 767C are converted to paleolatitudes by using the geocentric dipole formula and plotted vs. depth (Fig. 31). The selection criterion was that at least 20% of the NRM must remain after demagnetization at 20 mT. The paleolatitudes show great scatter but maintain low values consistent with equatorial site latitude. One factor contributing to the scatter of data at this time is a result of the demagnetizing capability of the 2-G Enterprises 2G600 degauss system (25 mT maximum) attached to the cryogenic magnetometer. In many cases, we could not demagnetize the samples enough to reveal the primary component. More detailed demagnetization steps (up to 100 mT) in shore-based laboratories will certainly improve the data and resolve a trend of paleolatitude change.

Susceptibility

Magnetic susceptibility is a useful parameter that, in general, reflects the amount of magnetic minerals within the sediments or the basement rocks. It is affected by many factors, however, which range from volcanic ash abundance to sedimentation rates. For Site 767, all cores were measured for volume magnetic susceptibility at 10-cm intervals. The results for Holes 767B and 767C are shown in Figure 32. Magnetic susceptibility is a dimensionless parameter.

The values discussed below are in 10^{-6} cgs. Only 1 core was recovered from Hole 767A, and 12 cores were recovered from Hole 767C with a poor recovery rate. The discussion of the whole-core susceptibility below is derived mainly from data on Hole 767B.

The volume magnetic susceptibility started with surprisingly high values in the 200–600 range with characteristic low and high frequencies. The very high susceptibility for the sediments in the Celebes Sea is likely caused by the abundance of volcanogenic sediments. An interval of low susceptibility exists from about 420 to 580 mbsf. The top boundary correlates well with the sharp increase in biotite and volcanic ashes within the sediments. The whole interval consists mainly of very fine-grained clays. The changes in magnetic susceptibility may reflect the change in sediment source and therefore paleoenvironment. The implication of the susceptibility variations should become more clear as more data are examined and integrated.

The correlation of susceptibility data between Holes 767B and 767C in the interval from 680 to 735 mbsf is shown in Figure 33. Although Hole 767C had a poor recovery rate, good correlations in the interval and shape of the data exist.

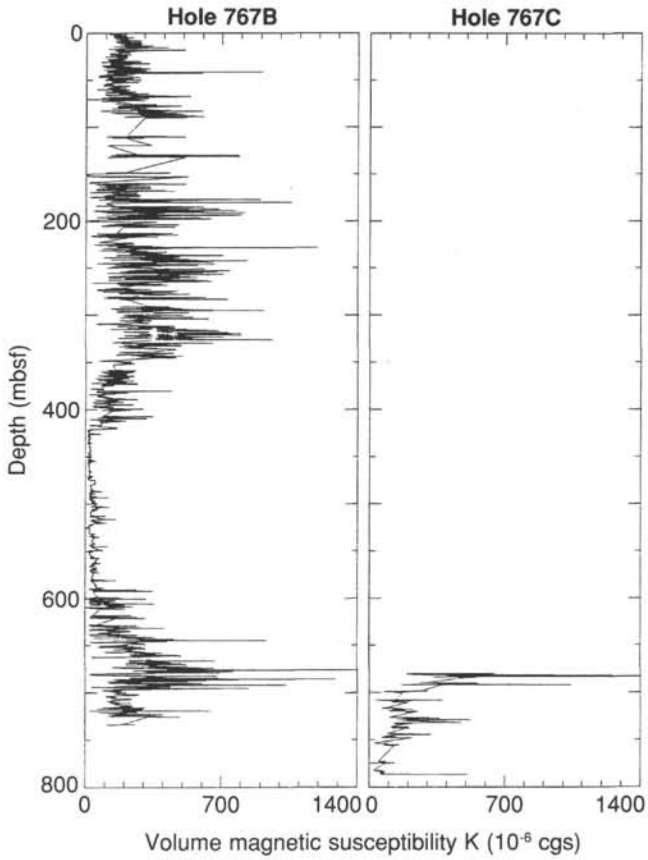

Figure 32. Magnetic susceptibility data, Holes 767B and 767C.

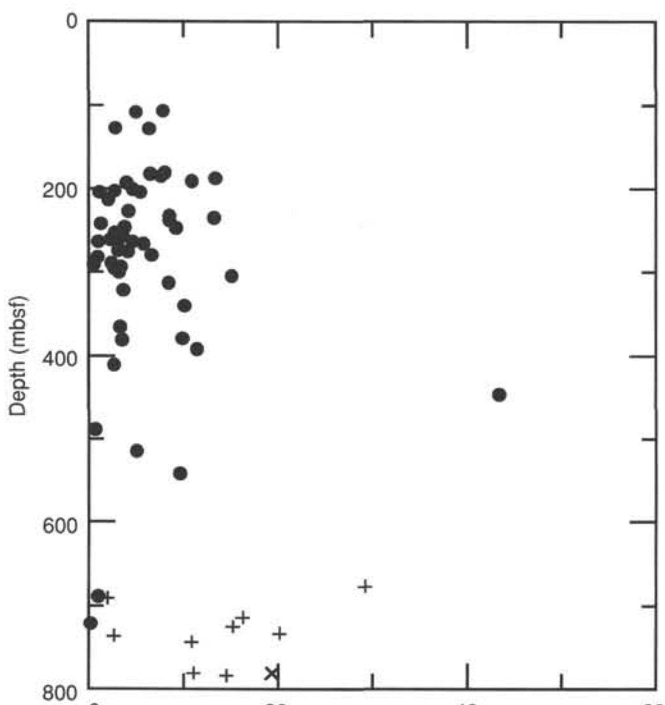

Figure 31. Paleolatitudes calculated from inclination data from Holes 767B and 767C. Solid lines are averaged inclinations for each polarity interval from APC cores. Solid circles are selected cube samples from XCB cores of Hole 767B. Crosses are selected cube samples from RCB cores of Hole 767C. The single "X" is the basement basalt sample.

Basement

Basement of the Celebes Sea at Site 767 was reached by Core 124-767-12R. Only 42 cm of altered basalt was retrieved from the core catcher. One minicore sample (1″ diameter, 0.9″ long) was taken (26–28 cm) for paleomagnetic measurement. The minicore was oriented relative to the uphole direction but not azimuthally.

The basalt sample was not too strong for the cryogenic magnetometer, and results from the cryogenic and the Molspin spinner magnetometer are comparable. The magnetization of the basalt at the NRM level is 1458.5 mA/m, which is within the normal range of altered basalt for oceanic basement (Banerjee, 1980).

Upon alternating-field (AF) demagnetization, the intensity increased slightly from 0 to 7 mT, with the vertical and horizontal components converging to a vector that shows univectoral decay toward the origin from 7 to 20 mT (Fig. 34). The demagnetization experiment data suggest that the basalt has a stable

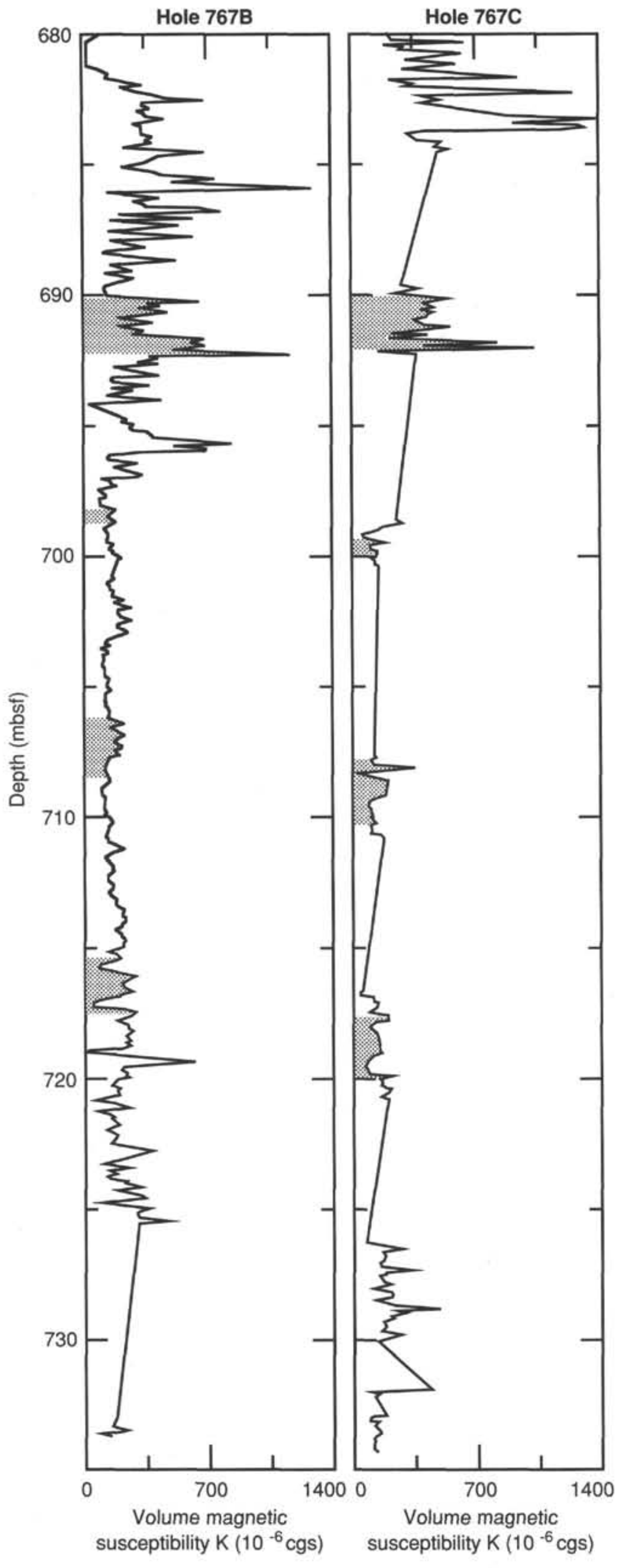

Figure 33. Magnetic susceptibility correlation of Holes 767B and 767C.

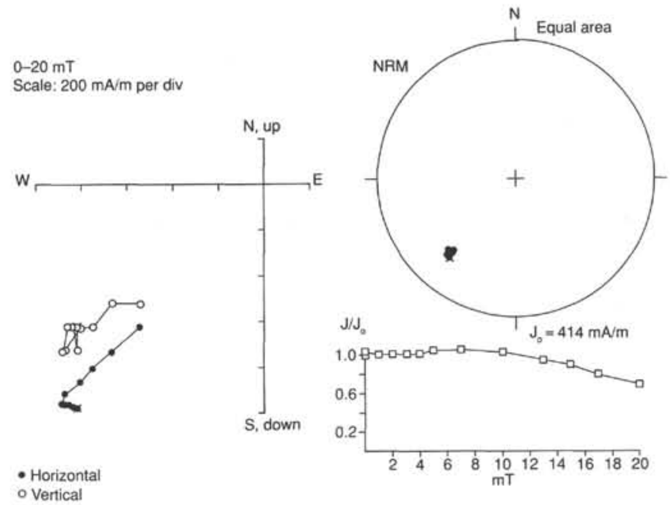

Figure 34. Zijderveld vector diagram for the basalt sample from Section 124-767B-12R-CC.

remanent magnetization that is revealed after the soft secondary magnetization is removed at 7 mT. The soft secondary magnetic overprint seems to be related to the primary component with its direction roughly anti-parallel to the primary direction (Fig. 34). This relationship is also shown by an increase followed by a decrease in the intensity and the tight clustering of remanent directions upon demagnetization (Fig. 34). It is possible that the secondary magnetization was acquired during a time of opposite polarity to that of the emplacement of the basalt.

The declination and inclination of the basalt sample at the 20-mT demagnetization level are 221° and 29°, respectively. Because of the rotary drilling disturbance, the declination would not be meaningful. The inclination of +29° indicates a paleolatitude of +16°. Because Hole 767C has a 13.5° drift and because a tilted basement block may have been cored, no interpretation of this value is attempted at this time.

The susceptibility of the basalt sample in Section 124-767C-12R-CC was also measured by the Bartington susceptibility meter. The averaged value for the basalt is about 500 (10^{-6} cgs). This value is low for oceanic basalt.

SEDIMENT ACCUMULATION RATES

We determined sediment accumulation rates at Site 767 by means of the calcareous nannoplankton zones described in Martini (1971) and the radiolarian zones defined by Riedel and Sanfilippo (1978), in correlation with the other biozones and magnetostratigraphy described in Berggren et al. (1985a, 1985b).

Foraminifers, radiolarians, and diatoms were absent or poorly preserved and were not useful in determining biozones for sedimentation rate calculations except in Hole 767C and the lower cores of Hole 767B. Preservation of calcareous nannofossils varied throughout the holes drilled at Site 767 with several zones left undifferentiated because of this problem. Preservation of calcareous nannofossils was very poor below Core 124-767B-63X (598.5 mbsf), which made the determination of calcareous nannoplankton zones impossible beneath this core. Radiolarians were poorly preserved but recognizable in Cores 124-767B-76X through -78X and in Cores 124-767C-6R, -8R, and -12R (see "Biostratigraphy" section, this chapter).

The magnetostratigraphic record in Hole 767B was determined from oriented APC cores and extends from the top of Hole 767B to Core 124-767B-10H (90.5 mbsf). One can see a continuous reversal sequence through the upper part of the Matuyama in this hole with good reversal boundaries throughout the measured interval (see "Paleomagnetics" section, this chapter). As a result of the low inclinations and rotary-disturbed cores, it was not possible on board ship to determine the magnetostratigraphy in XCB or RCB cores. The reversal stratigraphy is very short, and sedimentation rates calculated from the magnetostratigraphy (Fig. 35) agree well with sedimentation rates calculated from biostratigraphic data. Depths and ages of reversal boundaries are listed in Table 6.

Sedimentation rates determined from biostratigraphic zonations are shown in Figure 36, with age ranges, depths, and sedimentation rates of individual biozones given in Table 7.

Nannofossil Zones NN20 through NN21 (0-28 mbsf) have a combined sedimentation rate of 59.1 m/m.y. In the Pleistocene-Pliocene interval from 28 to 311.8 mbsf (NN19-NN12), the sedimentation rate averages 60.1 m/m.y. From 311.8 to 433.9 (NN11-NN10), sedimentation rates average 33.0 m/m.y. Sedimentation rates for NN9 (433.9-553.5 mbsf) average 108.7 m/m.y.

Cores 124-767B-60X through -63X contain calcareous nannoplankton from Zone NN8. From Core 124-767B-63X to -76X, poor preservation makes identification of calcareous nannofossil zones difficult. It was not possible to calculate sedimentation rates for this interval.

Cores 124-767B-76X through -78X contain identifiable radiolarians belonging to the *Lychnocanoma elongata* and *Dorcadospyris ateuchus* Zones. The *D. ateuchus* zone was identified in Cores 124-767B-77X and -78X and in Core 124-767C-6R. No identifiable radiolarians were found in Core 124-767C-7R, but in Core 124-767C-8R the radiolarian *Theocyrtis tuberosa* Zone was found. By placing the boundary between *D. ateuchus* and *T. tuberosa* in Core 124-767C-7R, we calculated an approximate sedimentation rate of 2 m/m.y.

No identifiable fossils were observed in Cores 124-767C-9R through -11R. In Core 124-767C-12R, just above basement, radiolarians of the *Podocyrtis chalara* and *Podocyrtis goetheana* Zones were identified. Sedimentation rates of 6 m/m.y. were calculated for the interval from 739.0 to 786.5 mbsf.

Red clays dominate the sedimentary column from Core 124-767B-74X to basement. For the datable red clay interval from 713.6 to 786.5, an average sedimentation rate of 4 m/m.y. was calculated. By assuming a constant sedimentation rate for the red clay, and by projecting this sedimentation rate into the overlying undated red clay, we can determine an approximate age of 18.5 ma for the top of this lithologic unit, the bottom of which is approximately 42–43 Ma (see "Biostratigraphy" section, this chapter).

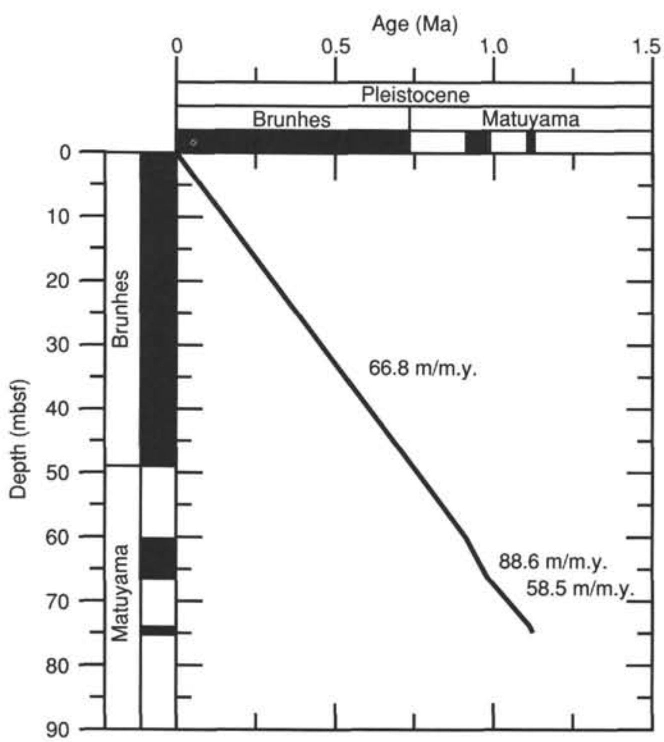

Figure 35. Sedimentation rates calculated from magnetostratigraphic data, Hole 767B.

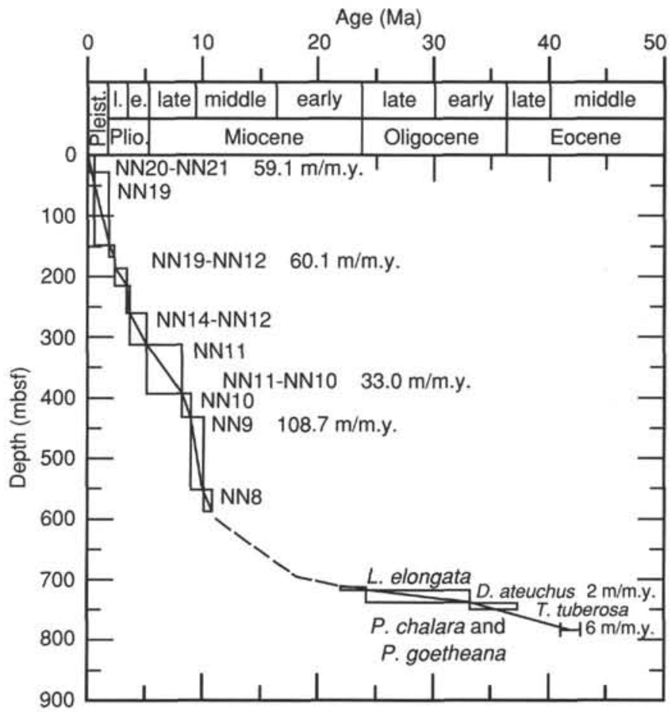

Figure 36. Sedimentation rates calculated from calcareous nannofossil and radiolarian biozones, Site 767.

Table 7. Ages, depths, and sedimentation rates for individual biozones identified at Site 767.

Biozone	Age (m.y.)	Depth (mbsf)	Sed. rate (m/m.y.)
NN21	0–0.275	0–18.5	67.3
NN20	0.275–0.474	18.5–28.0	47.7
NN19	0.474–1.89	28.0–149.5	85.8
NN18	1.89–2.35	149.5–168.0	40.2
NN17	2.35–2.45	168.0–187.0	190.0
NN16	2.45–3.4	187.0–215.4	29.9
NN15	3.4–3.7	215.4–261.4	153.3
NN14-NN12	3.7–5.2	261.4–311.8	33.6
NN11	5.2–8.2	311.8–393.2	27.1
NN10	8.2–8.9	393.2–433.9	58.1
NN9	8.9–10.0	433.9–553.5	108.7
NN8	10.0–10.8	553.5–?	
L. elongata	22.0–24.3	?–723.0	
D. ateuchus	24.3–33.2	723.0–739.0	2.0
T. tuberosa	33.2–37.3	739.0–?	\
P. goetheana	41.0–41.7	?–782.0	>6.0
P. chalara	41.7–42.8	786.5–?	/

SEDIMENT INORGANIC GEOCHEMISTRY

This section summarizes the results of shipboard analysis of calcium carbonate and dissolved constituents in the interstitial water of the sediments recovered from Site 767. Dissolved sulfate, alkalinity, ammonium, and phosphate distributions in the first 100 mbsf, are characteristic of organic matter degradation by sulfate reduction. The calcium, magnesium, and silica depth profiles are indicative of volcanic material alteration in the sediments and of basalt-seawater interactions.

Calcium Carbonate

A total of 119 sediment samples were analyzed for their carbon content with the methods described in the "Explanatory Notes" chapter (this volume). Results are shown in Table 8 and Figure 37. The carbonate content values vary widely from a low of 0.2% to a high of 88.5%. The low values observed in the volcanogenic clayey silts of Unit I are consistent with deposition below the CCD (see "Lithostratigraphy" section, this chapter). The observed sawtooth-like pattern of the carbonate distribution below 140 mbsf (Fig. 37) reflects the alternation of low-carbonate hemipelagic and volcanic components, with the graded carbonate turbidites present to various degrees in Units II and III. The reddish brown claystone recovered in Unit IV is very low in carbonate components, as evidenced by the low $CaCO_3$ levels in the samples below 700 mbsf.

Interstitial Water Chemistry

A total of 36 interstitial water (IW) samples were collected at Site 767, 32 from Hole 767B, and 4 from Hole 767C. Standard ODP squeezing techniques were used for the removal of water samples (see "Explanatory Notes" chapter, this volume). They were usually retrieved at the base of the fourth section from every core (approximately 10 m apart) in the uppermost 100 mbsf. Below this depth, IW samples were taken every third core (about 30 m apart). With the exception of a few samples in the deeper sections of the hole, whole-round core samples, 5-10 cm in length, provided sufficient IW (>10 cm^3) for analysis. Shipboard interstitial water analysis follows established ODP methods, and the results obtained are presented in Table 9. Some analyses were not performed on the deeper samples owing to insufficient amounts of IW.

Salinity and Chloride

Salinity and chloride concentrations decrease with core depth (Fig. 38), yet salinity decreases more rapidly than chloride. With the exception of two samples, salinity first decreases slowly from a value near IAPSO seawater (salinity = 36.0 g/kg) to 35.5 g/kg at 151.25 mbsf, and then drops rapidly to 32.4 g/kg at 267.35 mbsf. Below this depth salinity becomes far more variable, ranging from 33.0 to 31.5 g/kg, with an abnormally high value of 34.5 g/kg at 609.60 mbsf (Sample 124-767B-65X-1, 140-150 cm), which might represent some contamination with drilling fluid.

The variation in salinity largely reflects a net change in the sum of major dissolved ion concentrations. Above 151.25 mbsf, calcium, magnesium, chloride, and sulfate change slowly and so does salinity. Between 151.25 and 267.35 mbsf, sharp changes in calcium, magnesium, and sulfate are observed concurrent with the salinity decrease. From 267.35 to about 500 mbsf, where calcium and magnesium are essentially constant, the observed salinity decrease is the result of changes in the chloride and sulfate concentrations. Deeper in the hole, the observed salinity fluctuation results from changes in chloride, sulfate, calcium, and magnesium.

A chloride concentration consistent with the average seawater value of 559 mM was measured in all samples up to 238.55 mbsf. The chlorinity then decreases gradually to 539 mM (at 609.60 mbsf), dropping sharply to values ranging from of 500 to 520 mM in the deeper sections of the hole. A decrease in the chloride content of pore fluids has been attributed to the disso-

Table 8. Results of calcium carbonate analysis, Site 767.

Core, section, interval (cm)	Depth (mbsf)	$CaCO_3$ (%)
124-767B-		
1H-2, 60–63	2.10	1.3
1H-5, 80–83	6.80	0.6
2H-1, 85–88	9.85	2.4
2H-5, 120–123	16.20	0.5
3H-2, 40–42	20.40	0.5
3H-6, 119–122	27.19	0.4
4H-1, 122–125	29.22	0.7
4H-6, 98–101	36.48	0.3
5H-2, 32–35	39.32	3.7
5H-6, 124–127	46.24	24.2
6H-1, 79–82	47.79	0.7
6H-4, 83–86	52.33	0.6
6H-7, 54–57	56.54	0.7
7H-2, 130–133	59.30	0.8
7H-4, 123–126	62.23	1.0
7H-6, 20–23	64.20	0.5
8H-1, 135–138	67.35	0.4
8H-3, 120–123	70.20	0.4
9H-6, 85–88	79.85	0.8
10H-2, 120–123	83.70	0.4
10H-4, 80–83	86.30	0.4
10H-7, 38–41	90.38	0.5
13X-1, 102–105	110.62	0.6
15X-1, 122–125	130.12	0.6
17X-2, 85–88	150.65	83.3
17X-3, 76–79	152.06	87.1
18X-2, 58–61	160.08	1.2
18X-5, 66–69	164.66	3.6
19X-2, 41–44	169.51	4.4
19X-4, 99–102	173.09	0.4
20X-2, 32–35	179.12	3.7
20X-3, 20–23	180.50	21.8
21X-1, 115–118	184.95	68.0
21X-4, 58–61	188.88	7.3
21X-6, 82–85	192.12	1.7
22X-1, 52–55	194.02	0.2
22X-3, 56–59	197.06	39.7
22X-5, 60–61	200.10	88.5
22X-5, 90–93	200.40	86.1
23X-1, 95–98	204.25	3.0
23X-3, 16–19	206.46	1.7
23X-CC, 0–3	207.01	84.9
24X-1, 42–45	213.52	0.5
24X-1, 83–84	213.93	74.6
24X-2, 135–138	215.95	2.3
25X-1, 87–90	223.77	24.1
25X-3, 50–53	226.40	1.2
25X-3, 129–130	227.19	81.8
26X-1, 15–18	232.75	0.7
26X-2, 65–68	234.75	1.2
27X-1, 42–45	242.62	0.2
27X-3, 27–29	245.47	85.9
27X-4, 104–107	247.74	0.2
27X-6, 70–73	250.40	0.2
28X-2, 55–57	253.95	0.9
28X-4, 22–24	256.62	0.2
28X-6, 38–40	259.78	0.2
29X-1, 43–45	261.83	11.3
29X-2, 8–9	262.98	81.5
29X-3, 58–60	264.98	0.2
29X-5, 93–95	268.33	2.7
30X-1, 38–40	271.38	0.6
30X-3, 40–42	274.40	0.6
30X-4, 128–129	276.78	81.6
30X-5, 118–120	278.18	1.2
31X-1, 85–87	281.55	6.0
32X-1, 66–68	291.06	0.3
32X-6, 60–63	298.50	0.5
33X-1, 107–108	301.17	0.3
33X-6, 131–132	308.91	0.3
33X-7, 27–29	309.37	2.7
34X-2, 9–11	311.39	2.5
34X-3, 82–84	313.62	1.2
34X-6, 75–77	318.05	0.3
35X-1, 113–115	320.53	0.7

Table 8 (continued).

Core, section, interval (cm)	Depth (mbsf)	$CaCO_3$ (%)
124-767B-		
35X-4, 51–53	324.41	69.9
35X-5, 66–68	326.06	0.6
36X-2, 18–20	330.78	0.7
36X-4, 120–122	334.80	1.0
37X-5, 115–117	345.95	1.7
38X-1, 73–75	349.23	76.9
38X-2, 40–42	350.40	0.6
39X-2, 61–63	360.21	0.9
39X-4, 100–102	363.60	0.5
39X-6, 72–74	366.32	0.8
39X-6, 129–131	366.89	0.5
40X-4, 30–33	372.60	1.1
41X-2, 139–141	380.39	16.1
42X-2, 115–117	389.75	2.2
44X-2, 7–9	408.07	1.7
44X-5, 22–24	412.72	0.9
45X-3, 96–98	420.16	75.8
45X-4, 89–91	421.59	7.7
45X-5, 89–91	423.09	44.7
46X-6, 110–112	434.40	1.4
46X-7, 26–28	435.06	0.6
47X-2, 76–78	437.66	2.2
47X-4, 33–35	440.23	2.7
48X-2, 111–113	447.71	3.1
48X-4, 110–112	450.70	0.6
48X-5, 67–69	451.77	53.6
49X-2, 82–84	457.12	2.2
49X-2, 109–111	457.39	57.6
50X-3, 71–73	467.81	5.9
50X-5, 100–102	471.10	60.1
50X-5, 128–130	471.38	7.2
51X-2, 30–32	476.60	3.3
51X-4, 22–24	479.52	3.2
52X-4, 72–74	489.62	30.0
52X-6, 21–23	492.11	4.4
53X-4, 78–80	498.28	3.7
55X-4, 21–23	516.91	59.7
57X-3, 74–76	534.54	46.4
59X-5, 12–14	556.32	2.4
59X-5, 98–100	557.18	1.3
59X-CC, 0–3	557.66	72.4
60X-2, 53–55	561.83	1.7
60X-4, 23–25	564.53	1.1
60X-5, 49–51	566.29	2.8
61X-2, 61–63	571.51	2.6
61X-CC, 35–37	574.08	0.8
62X-1, 93–95	580.03	9.2
62X-5, 64–66	585.74	2.2
62X-CC, 0–3	588.52	2.3
63X-2, 116–118	591.46	1.9
63X-3, 62–64	592.42	0.7
64X-2, 35–37	600.35	1.6
64X-4, 58–60	603.58	73.5
67X-4, 130–132	633.20	0.6
67X-7, 24–26	636.64	0.7
68X-2, 136–138	639.96	0.7
68X-4, 32–34	641.92	5.9
68X-5, 102–104	644.12	0.6
69X-2, 78–80	648.58	0.6
69X-4, 29–31	651.09	0.5
69X-6, 124–126	655.04	0.3
70X-2, 75–76	658.25	0.4
70X-4, 125–127	661.75	0.2
72X-1, 89–90	676.19	0.2
72X-4, 55–57	680.35	0.4
72X-6, 109–111	683.89	0.4
73X-3, 18–20	688.08	0.3
73X-4, 109–111	690.49	0.6
73X-7, 18–20	694.08	0.5
74X-1, 105–107	695.65	3.8
74X-3, 85–87	698.45	0.3
75X-5, 20–22	710.40	0.2
76X-5, 47–49	719.97	0.2

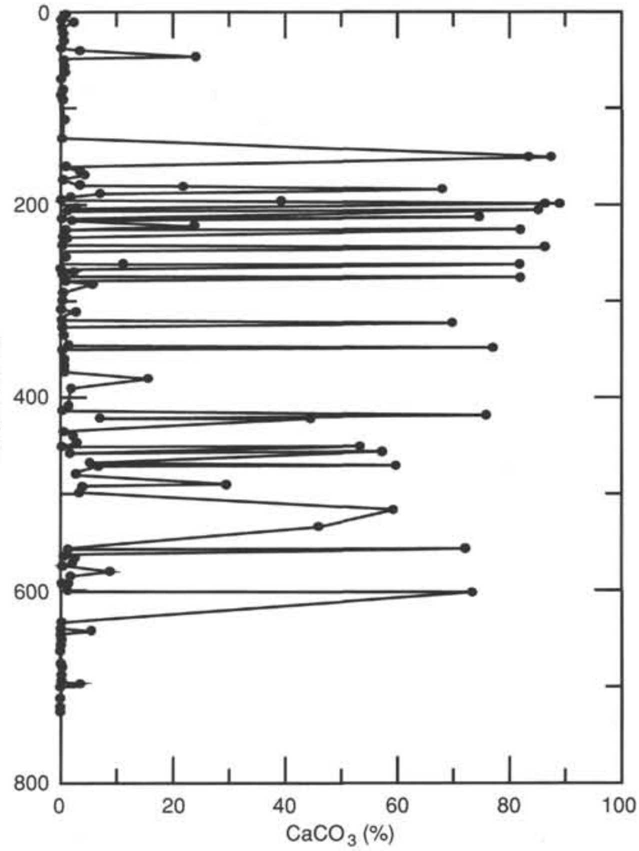

Figure 37. Downcore distribution of calcium carbonate, Hole 767B.

ciation of gas clathrates, which results in chlorinity values as low as 475 mM in the Peru Margin sediments (Suess, von Huene, et al., 1988). The concentration of methane in the sediments recovered from Site 767 is not enough to permit the formation of gas hydrates (see "Organic Geochemistry" section, this chapter), and therefore this is not a plausible cause for the low chlorinity values observed. A more likely explanation is ultra-filtration during the flow of pore fluids across clay membranes, resulting in the separation of ions from the interstitial seawater. Such a mechanism has been suggested by Hanshaw and Coplen (1973) and Marine and Fritz (1981) as an explanation for the low-chloride patterns observed in the interstitial fluids of the Barbados Ridge complex. A release of chemically bound water at depth from clays (von Huene and Lee, 1982) could also be responsible for the observed anomaly in the chlorinity profile.

pH and Alkalinity

The pH depth profile generally shows less variable and lower (more acidic) values in the upper 206.2 mbsf. Below this depth, pH increases to a maximum value of 8.50 at 296.3 mbsf and then decreases to 6.55 at 710.10 mbsf (Fig. 38). Between approximately 150 and 600 mbsf, pH changes may be related to the alteration of volcanic ash layers frequently found within the sediment column.

The alkalinity increases from 5.48 mM at 5.9 mbsf to 8.70 mM at 111.0 mbsf, whereas pH remains essentially constant (Fig. 38). The increase in alkalinity is indicative of bicarbonate production during the bacterial degradation of organic matter by sulfate reduction (see "Sulfate" section below). Below 111.05 mbsf, alkalinity drops rapidly and remains low at a mean value of approximately 2 mM for the rest of the hole. This distribution suggests a removal of bicarbonate from the interstitial

Table 9. Interstitial water analyses, Site 767.

Core, section, interval (cm)	Depth (mbsf)	Vol. (cm^3)	pH	Alk. (mM)	Sal. (g/kg)	Mg^{2+} (mM)	Ca^{2+} (mM)	Cl^- (mM)	SO_4^{2-} (mM)	PO_4^{3-} (μM)	NH_4^+ (μM)	SiO_2 (μM)	Mg^{2+}/Ca^{2+}
124-767B-1H-4, 145-150	5.95	80	7.77	5.483	35.9	49.95	10.31	557.00	28.90	22.90	136	536	4.90
124-767B-2H-4, 145-150	14.95	71	7.64	6.353	35.8	49.04	10.34	562.00	27.20	22.60	221	597	4.79
124-767B-3H-4, 145-150	24.45	72	7.72	7.431	36.0	48.33	10.50	563.00	25.70	22.10	390	654	4.65
124-767B-4H-4, 145-150	33.95	75	7.83	7.621	34.5	48.46	10.68	561.00	25.00	13.60	392	685	4.58
124-767B-5H-4, 145-150	43.45	72	7.71	7.993	36.5	48.10	10.65	559.00	24.40	9.25	413	689	4.56
124-767B-6H-4, 145-150	52.95	17	7.79	8.269	35.5	47.37	10.67	563.00	23.70	6.05	590	637	4.48
124-767B-7H-4, 140-150	62.40	70	7.76	8.008	35.8	46.72	10.62	562.00	23.90	4.40	653	674	4.44
124-767B-8H-3, 140-150	70.40	80	7.84	8.597	35.6	46.69	11.06	559.00	23.50	4.30	766	644	4.26
124-767B-9H-3, 145-150	77.45	45	7.89	8.728	35.8	46.24	11.18	560.00	23.10	4.80	773	642	4.18
124-767B-10H-4, 145-150	86.95	70	7.68	8.678	35.5	45.13	11.36	562.00	22.50	4.90	820	670	4.01
124-767B-13X-1, 145-150	111.05	51	7.59	8.702	35.2	43.86	11.98	559.00	22.80	4.80	870	742	3.77
124-767B-17X-2, 145-150	151.25	41	7.42	7.122	35.5	42.29	12.06	560.00	19.20	2.10	1086	809	3.61
124-767B-20X-1, 145-150	178.75	53	7.65	6.349	35.0	40.52	12.27	556.00	16.80	1.80	971	910	3.40
124-767B-23X-2, 145-150	206.25	56	7.63	3.718	34.5	32.64	18.68	559.00	14.80	1.10	838	721	1.80
124-767B-26X-4, 145-150	238.55	35	7.97	1.944	33.3	25.56	25.83	558.00	10.20	0.90	651	390	1.02
124-767B-29X-4, 145-150	267.35	25	8.31	1.002	32.4	19.73	29.97	553.00	7.50	1.10	692	187	0.68
124-767B-32X-4, 140-150	296.30	13	8.50	0.711	32.5	12.12	31.26	549.00	4.30	1.50	699	178	0.40
124-767B-35X-4, 140-150	325.30	41	8.41	1.423	32.4	9.59	32.89	547.00	3.00	1.10	797	167	0.30
124-767B-38X-2, 140-150	351.40	19	8.22	1.539	33.0	9.84	33.20	546.00	2.80	1.50	715	159	0.31
124-767B-41X-4, 140-150	383.40	16	8.28	1.700	32.5	10.96	32.69	544.00	3.80	2.10	713	152	0.35
124-767B-44X-3, 140-150	410.90	15	8.34	2.426	31.7	14.32	31.90	528.00	5.00	0.80	678	109	0.46
124-767B-47X-2, 140-150	438.30	10	8.07	2.717	31.5	13.31	31.89	544.00	3.30	0	523	177	0.43
124-767B-50X-4, 140-150	470.00	13	8.04	2.405	31.5	13.00	31.89	537.00	2.10	0	543	146	0.42
124-767B-53X-4, 140-150	498.90	12	7.85	3.359	32.2	15.44	30.34	540.00	4.30	0	429	214	0.52
124-767B-56X-3, 140-150	525.50	20	8.02	1.580	32.5	13.19	31.11	545.00	7.50	0	471	127	0.43
124-767B-59X-3, 140-150	554.60	10	8.07	1.580	31.5	11.60	34.54	536.00	2.70	0	473	105	0.34
124-767B-62X-4, 140-150	585.00	9			32.1	12.22	38.44	545.00	4.50	0	498	300	0.32
124-767B-65X-1, 140-150	609.60	17	7.98	1.962	34.5	10.94	44.17	539.00	7.70	0	422	107	0.25
124-767B-68X-4, 140-150	643.00	1								0			
124-767B-71X-4, 140-150	671.50	3				8.27	51.16	547.00	4.60	0	402	189	0.16
124-767C-1R-2, 140-150	682.90	30	7.74	0.858	32.5	8.94	52.07		3.80				0.17
124-767B-74X-4, 140-150	700.50	2				8.94	57.85	500.00	6.80	0	302	331	0.08
124-767C-4R-1, 140-150	708.90	5	6.33		32.4	11.75	60.09		10.60				0.20
124-767B-75X-4, 140-150	710.10	10	6.55	1.449	32.5	4.58	61.72	520.00	5.70	0	302	331	0.10
124-767C-8R-2, 140-150	746.20	1							5.80				
124-767C-11R-1, 140-150	773.80	7	6.70		33.8	13.85	66.40		16.80				0.21

water, presumably by carbonate reduction and bacterial methanogenesis, which is evidenced by a significant increase in the methane concentration at about 300 mbsf (see "Organic Geochemistry" section, this chapter).

Sulfate

The sulfate concentration drops exponentially from 28.90 mM at 5.95 mbsf to 22.5 mM at 86.95 mbsf. Below this depth it decreases almost linearly with depth to a value of 4.30 mM at 296.3 mbsf (Fig. 38). The observed distribution results from bacterially mediated sulfate reduction. This process is evident from the observed linear relationship between sulfate and alkalinity in the first 100 mbsf (Fig. 39), and it leads to the formation of pyrite nodules (Fig. 40) recovered in the sediments (see "Lithostratigraphy" section, this chapter). At a depth of approximately 300 mbsf, sulfate reduction is complete, and further decomposition of organic matter proceeds by carbonate reduction/methanogenesis (see "Organic Geochemistry" section, this chapter).

Phosphate and Ammonium

Phosphate and ammonium are metabolic products of the decomposition of organic matter. Their downhole distributions are shown in Figure 38. Ammonium steadily increases from 136 μM at 5.95 mbsf to a maximum of 1086 μM at 151.25 mbsf. The gradual decreases to 302 μM in the deeper sections of the hole are probably the result of ion exchange reactions on clay mineral surfaces. The fact that the ammonium maximum corresponds to the pH minimum (Fig. 38) would support an ion exchange process whereby the hydrogen ions are being displaced by ammonium (Rosenfeld, 1979; von Breymann and Suess, 1988).

The release of phosphate by organic matter degradation results in an accumulation of this ion in the pore waters in excess of the seawater values (approximately 2 μM). Because it is preferentially released during organic matter degradation, the phosphate maximum occurs at a shallower depth than the ammonium maximum (Gieskes, 1983). The dissolved phosphate concentrations in this site decrease sharply from 22.90 μM at 5.95 mbsf to 4.40 μM at 62.40 mbsf. Below this depth it remains low (1–4 μM) for the rest of the hole. The sharp decrease in phosphate probably results from diagenetic uptake of dissolved phosphate into sedimentary mineral phases.

Silica

Silica concentrations increase gradually from 536 μM at 5.95 mbsf to a maximum value of 910 μM at 178.75 mbsf. The concentration of silica then drops rapidly to 187 μM at 267.35 mbsf, below which it remains essentially constant with sporadic variations for the remainder of the hole (Fig. 38). The correspondence between high pH values and the sharp decrease in dissolved silica, together with the observed poor preservation of biogenic siliceous tests below 56 mbsf (see "Biostratigraphy" section, this chapter), suggests a diagenetic reconstitution of biogenic opal-A into opal-CT.

Kastner and Gieskes (1976) have suggested such a silification process in the sediments of DSDP Site 323 in the Bellingshausen Abyssal Plain. They have shown that in these sediments the silification reactions are associated with the alteration of detrital silicates of volcanic origin, where Mg uptake replaces Ca to form smectites (Gieskes, 1975). This process leads to dissolved Mg and Ca distributions similar to those observed at Site 767 between 300 and 500 mbsf (see "Calcium and Magnesium" section below). Furthermore, Gieskes et al. (1982) have reported a

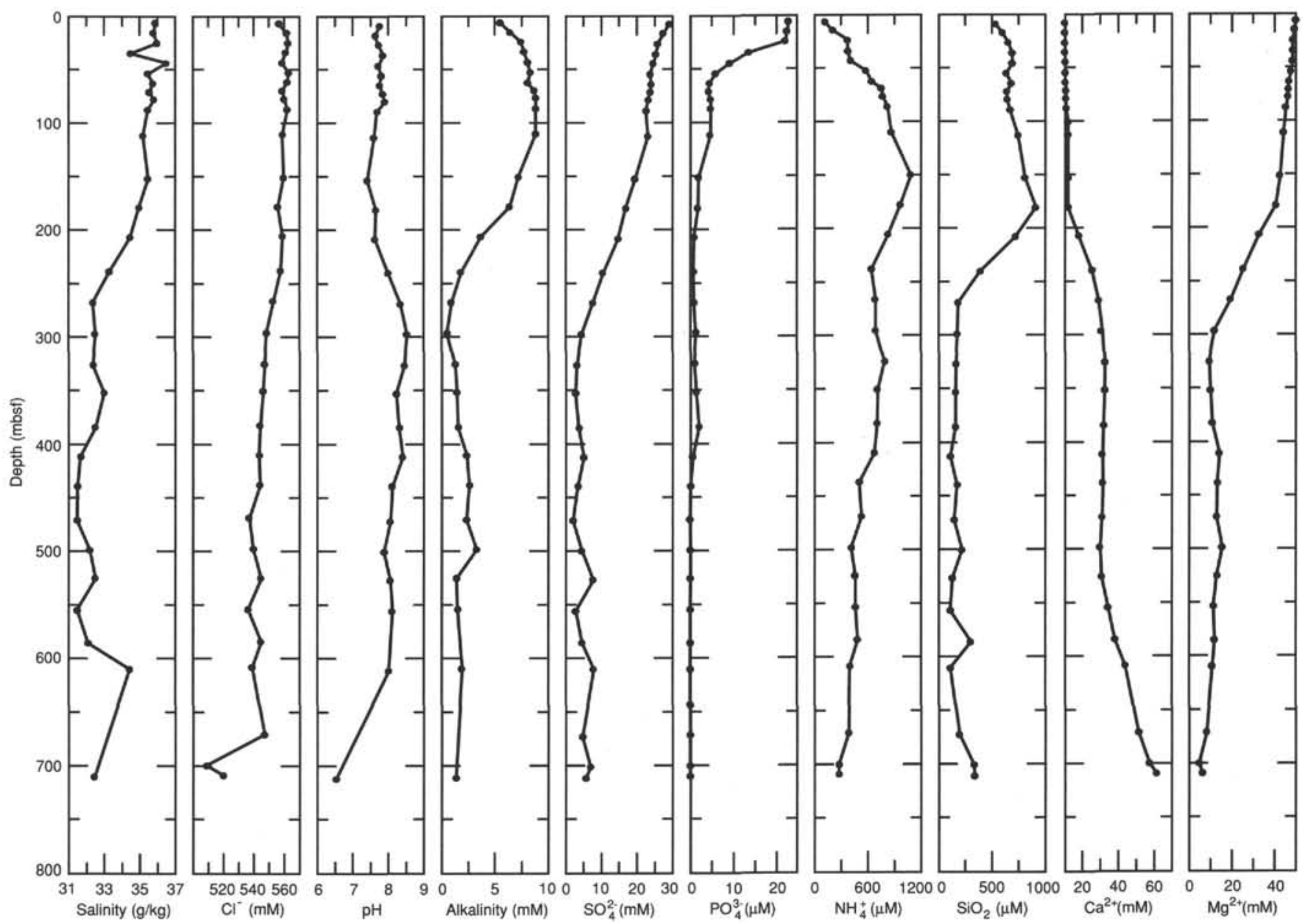

Figure 38. Summary of interstitial water analyses, Hole 767B, as a function of depth.

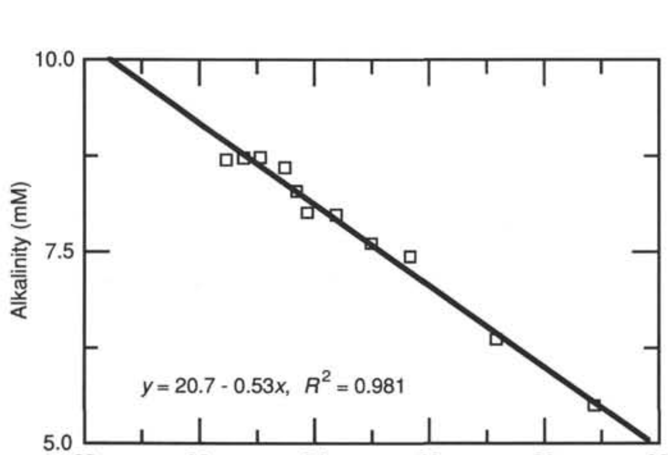

Figure 39. Relationship between alkalinity and dissolved sulfate in the upper 100 mbsf of Hole 767B.

Figure 40. Pyrite nodules found in Sample 124-767B-47X-CC, 18–21 cm.

set of pore-water profiles for Si, Ca, Mg, and K in the Gulf of California, consistent with the silicification reaction and the alteration of volcanic material proposed by Kastner and Gieskes (1976) for Site 323. The nature of the sediments recovered at Site 767 further supports this hypothesis; the sediments are very rich in volcanogenic material, and they record a marked increase in the degree of alteration of the volcaniclastics below 270 mbsf (see "Lithostratigraphy" section, this volume).

Calcium and Magnesium

The dissolved calcium and magnesium distribution for Site 767 are shown in Figure 38. The calcium profile is almost a mirror image of the magnesium distribution.

The observed linear concentration-depth gradients of dissolved calcium and magnesium in the upper 200 m of the hole suggest that their distribution is controlled by diffusion processes alone, and that the calcium source and the magnesium sink must lie in the sediments below 200 mbsf. In contrast, calcium and magnesium profiles show distinct upward curvatures, indicating a release of calcium and an uptake of magnesium between 200 and 500 mbsf, a zone characterized by an increase in the degree of alteration of the volcaniclastic material (see "Lithostratigraphy" section, this chapter).

The increase in dissolved calcium could also result from the dissolution of calcium carbonate (Gieskes, 1983; Manheim, 1976; Manheim and Sayles, 1974; Sayles and Manheim, 1975). However, this would imply a substantial increase in dissolved bicarbonate, although we observe in fact a decrease in alkalinity. Therefore, we conclude that the diagenetic alteration of volcanic material between 200 and 500 mbsf is responsible for the calcium and magnesium concentration gradients observed in the upper portion of the hole.

From 500 mbsf to the sediment/basement interface, calcium increases and magnesium decreases with depth. This distribution reflects basalt-seawater alteration reactions, also recorded at many other DSDP/ODP sites (Gieskes et al., 1975; Gieskes and Lawrence, 1981; McDuff and Gieskes, 1981; Kastner and Gieskes, 1976).

ORGANIC GEOCHEMISTRY

Beside monitoring hydrocarbons, which is performed for safety considerations, the shipboard organic geochemistry studies had two main purposes during Leg 124. The first refers to one of the objectives of the leg itself, that is, the reconstruction of the sedimentary history of the Celebes and Sulu sea basins by assessing the amount and type of organic matter along the sedimentary column. The second purpose is to compare the amount, type, and preservation of organic matter and the composition of gases that could be generated by biogenic or thermogenic processes. Shore-based studies will investigate kerogen petrology and geochemistry, isotope composition of gases, and interstitial waters. The following summarizes the preliminary shipboard results of Site 767 (Celebes Sea).

Samples

Details concerning analytical methods and equipment are given in the "Explanatory Notes" chapter (this volume). We collected 87 samples from Site 767 (approximately one per core) for subsequent headspace and Rock-Eval analysis. We also took 10 g of wet sediment just after cutting the core into 1.5-m sections. In addition, 35 selected samples were collected for shipboard Rock-Eval pyrolysis and shorebased organic-petrologic studies.

Results

Rock-Eval Pyrolysis

The amount of organic matter in the sediment was assessed by the total organic carbon (TOC) content measured with Rock-Eval. The data are given in Table 10 and Figure 41.

Generally, the TOC values are low (<1%). However, some differences can be observed within the sedimentary column. In the upper part (0–120 mbsf), the values show variations of large relative amplitude (0.08%–0.79%), but the general trend is a decrease of TOC concentration with increasing depth. From 120 to 400 mbsf, no characteristic trend can be noticed, the values remaining low (<0.5%) except in two samples at 190 and 364 mbsf. The highest values are observed between 400 and 580 mbsf (up to 5%) with a general background of about 0.75%. The lowest part of the sedimentary column (below 500 mbsf) is characterized by very low relative concentrations of organic carbon.

Except for some samples, the low TOC values generally observed do not permit a reliable interpretation of the pyrolysis results because of the relative effect of absorption phenomena by the mineral matrix. It is also probable that the oxygen indexes are affected by a release of CO_2 from an inorganic origin. These effects are particularly significant at low TOC values.

The organic matter contained in the three organic-rich samples belongs to a type III kerogen (Durand and Monin, 1980), characterized by low hydrogen indexes (<300 mg HC/g TOC) as well as oxygen indexes ranging from 45 to 91 mg CO_2/g TOC. This is in agreement with the macroscopic core descriptions and the microscopic observations from smear slides (see "Biostratigraphy" section, this chapter). The T_{max} for these samples indicate a low thermal evolution level (T_{max} between 429°C and 434°C) that corresponds to the lignite or immature stage.

Hydrocarbon Gases

Light hydrocarbons observed at Site 767 consist of methane and ethane. Concentrations are low (<11 ppm) up to 335 mbsf (Fig. 41 and Table 11). Below this depth, methane concentrations increase steadily from about 29 ppm to a maximum concentration of 8792 ppm at 477 mbsf. Below 477 mbsf a concentration decrease with increasing depth is noticed, although the values are highly scattered. A similar trend is observed for ethane with the exception that the onset of higher ethane concentrations begins at 450 mbsf. A deviation from this overall trend concerning concentration and molecular composition is recognized for the gas sample from Section 124-767B-20X-CC, at 181.26 mbsf (Table 12). This gas sample contains C_1–C_6 alkanes as well as ethylene and propylene.

Discussion

Amount, Type, and Maturity of Organic Matter

The higher amounts of terrestrial organic matter observed between 400 and 580 mbsf correspond to strong turbiditic events that occurred during the middle to late Miocene (see "Lithostratigraphy" section, this chapter). Such events were previously reported as a possible mechanism to generate organic-rich layers (Dean and Gardner, 1982). The fact that this material is still immature supports the hypothesis of a direct origin from higher-plant biomass, or from peat or coal at an early stage of diagenesis, rather than from a reworking of more mature coals.

On the other hand, the presence of a background of marine autochthonous organic matter along the whole sedimentary column is assumed. Indeed, for many samples, no organic ligneous fragments are observed in smear slides although TOC values are

Table 10. Rock-Eval data, Site 767.

Core, section, interval (cm)	Depth (mbsf)	S_1 (mg/g)	S_2 (mg/g)	S_3 (mg/g)	TOC (%)	C (%)	HI	OI	T_{max} (°C)	PI	S_2/S_3
124-767A-1H-1, 23–28	0.23	0.58	4.69	1.67	0.59	0.43	794	283	452	0.11	2.80
124-767A-1H-2, 145–150	2.95	0.43	2.91	1.71	0.57	0.27	570	335	518	0.13	1.70
124-767A-1H-CC, 11–16	4.05	0.36	2.24	2.36	0.45	0.41	497	524	466	0.14	0.94
124-767B-1H-5, 0–3	6.00	0.38	2.83	1.61	0.58	0.26	487	277	464	0.12	1.75
124-767B-2H-1, 43–48	9.43	0.46	3.58	2.97	0.73	0.33	490	406	547	0.11	1.20
124-767B-2H-5, 0–3	15.00	0.25	1.86	1.25	0.34	0.17	547	367	518	0.12	1.48
124-767B-3H-1, 12–17	18.62	0.27	2.73	2.85	0.39	0.25	700	730	544	0.09	0.95
124-767B-3H-5, 0–3	24.50	0.27	1.71	3.28	0.47	0.16	363	697	584	0.14	0.52
124-767B-4H-1, 10–15	28.10	0.51	2.07	2.97	0.79	0.21	269	375	583	0.20	0.69
124-767B-4H-5, 0–3	34.00	0.25	1.20	0.54	0.15	0.12	800	360	473	0.17	2.22
124-767B-5H-1, 10–15	37.60	0.39	1.93	2.81	0.38	0.19	507	739	586	0.17	0.68
124-767B-5H-5, 0–3	43.50	0.24	1.69	0.95	0.34	0.16	497	279	518	0.12	1.77
124-767B-6H-1, 20–25	47.20	0.30	2.05	0.65	0.22	0.19	931	295	518	0.13	3.15
124-767B-6H-5, 0–3	53.00	0.30	2.52	0.80	0.32	0.23	787	250	502	0.11	3.15
124-767B-7H-5, 0–3	62.50	0.27	0.94	6.35	0.69	0.10	136	920	387	0.22	0.14
124-767B-8H-4, 0–3	70.50	0.32	2.27	2.62	0.68	0.21	333	385	556	0.12	0.86
124-767B-9H-6, 0–3	79.00	0.07	0.19	6.09	0.11	0.02	172	5536	349	0.27	0.03
124-767B-10H-5, 0–3	87.00	0.18	2.10	0.62	0.31	0.19	677	200	505	0.08	3.38
124-767B-10H-5, 95–97	87.95	0.18	2.16	0.33	0.25	0.19	864	132	544	0.08	6.54
124-767B-13X-2, 0–3	111.10	0.12	0.89	4.30	0.08	0.09	1112	5375	535	0.12	0.20
124-767B-15X-2, 0–3	130.40	0.34	3.81	0.76	0.34	0.34	1120	223	517	0.08	5.01
124-767B-17X-3, 0–3	151.30	0.12	0.13	1.19	0.10	0.02	130	1190	437	0.50	0.10
124-767B-18X-5, 0–3	164.00	0.17	0.74	3.85	0.28	0.07	264	1375	475	0.19	0.19
124-767B-19X-1, 15–20	167.75	0.17	2.43	0.40	0.30	0.21	810	133	531	0.07	6.07
124-767B-19X-5, 0–3	173.60	0.02	0.13	2.47	0.08	0.01	162	3087	307	0.14	0.05
124-767B-20X-2, 0–3	178.80	0.28	3.13	0.54	0.32	0.28	978	168	515	0.08	5.79
124-767B-21X-5, 0–3	189.80	0.21	3.69	1.11	0.93	0.32	396	119	573	0.05	3.32
124-767-22X-1, 18–23	193.68	0.10	3.35	0.25	0.28	0.28	1196	89	528	0.03	13.40
124-767B-22X-5, 0–3	199.50	0	0.04	1.10	0.05	0.00	80	2200	436	0	0.03
115-767B-23X-3, 0–3	206.30	0.16	1.66	1.59	0.17	0.15	976	935	587	0.09	1.04
115-767B-24X-3, 0–3	216.10	0	0	2.23	0.10	0	0	2230	363	0	0
115-767B-25X-4, 76–78	228.16	0.06	0.58	0.41	0.05	0.05	1160	820	570	0.09	1.41
115-767B-25X-5, 0–3	228.90	0.09	1.59	0.60	0.23	0.14	548	206	523	0.05	2.65
115-767B-26X-5, 0–3	238.60	0.09	1.14	0.36	0.13	0.10	876	276	563	0.07	3.16
115-767B-27X-5, 0–3	248.20	0.15	1.95	0.50	0.35	0.17	557	142	496	0.07	3.90
115-767B-28X-5, 0–3	257.90	0.07	2.55	0.78	0.36	0.21	708	216	532	0.03	3.26
115-767B-29X-5, 0–3	267.40	0.10	1.35	0.72	0.22	0.12	613	327	519	0.07	1.87
115-767B-30X-1, 27–29	271.27	0.03	2.60	0.26	0.21	0.21	1238	123	470	0.01	10.00
115-767B-30X-5, 0–3	277.00	0.06	0.81	1.51	0.26	0.07	311	580	593	0.07	0.53
115-767B-31X-2, 0–3	282.20	0.18	0.37	2.57	0.21	0.04	176	1223	437	0.33	0.14
115-767B-32X-5, 0–3	296.40	0.14	0.41	2.86	0.15	0.04	273	1906	308	0.26	0.14
115-767B-33X-5, 0–3	306.10	0.14	2.39	0.88	0.38	0.21	628	231	473	0.06	2.71
115-767B-34X-5, 0–3	315.80	0.03	0.04	2.13	0.10	0	40	2130	301	0.50	0.01
115-767B-35X-1, 69–71	320.09	0.34	1.03	0.43	0.11	0.11	936	390	423	0.25	2.39
115-767B-35X-5, 0–3	325.40	0.02	0.81	0.02	0.10	0.06	810	20	542	0.02	40.50
115-767B-36X-5, 0–3	335.10	0.09	1.38	1.47	0.21	0.12	657	700	467	0.06	0.93
115-767B-37X-5, 0–3	344.80	0.08	1.51	0.84	0.15	0.13	1006	560	464	0.05	1.79
115-767B-38X-3, 0–3	351.50	0.03	1.57	0.73	0.15	0.13	1046	486	507	0.02	2.15
115-767B-39X-4, 89–92	363.49	0.10	1.97	1.08	0.17	0.17	1158	635	457	0.05	1.82
115-767B-39X-5, 0–3	364.10	0.18	2.04	1.78	0.61	0.18	334	291	462	0.08	1.14
115-767B-40X-3, 134–136	372.14	0.11	0.80	4.90	0.07	0.07	1142	7000	520	0.12	0.16
115-767B-40X-4, 0–3	372.30	0.06	0.80	1.17	0.21	0.07	380	557	461	0.07	0.68
115-767B-41X-CC, 0–3	386.86	0.05	1.54	1.23	0.21	0.13	733	585	462	0.03	1.25
115-767B-42X-5, 0–3	393.10	0.08	2.11	0.79	0.25	0.18	844	316	465	0.04	2.67
115-767B-42X-7, 33–35	396.43	0	2.77	2.49	0.42	0.23	659	592	464	0	1.11
115-767B-43X-3, 0–3	399.80	0.12	2.92	1.29	0.27	0.25	1081	477	457	0.04	2.26
115-767B-44X-4, 0–3	411.00	0.12	2.11	1.60	0.44	0.18	479	363	466	0.05	1.31
115-767B-45X-5, 0–5	422.20	0	2.34	1.69	0.36	0.19	650	469	528	0	1.38
115-767B-45X-CC, 0–3	425.60	0	0.55	1.47	0.59	0.04	93	249	429	0	0.37
115-767B-45X-CC, 28–31	425.88	0.04	1.45	1.09	0.12	0.12	1208	908	492	0.03	1.33
115-767B-46X-5, 0–3	431.80	0.10	3.03	1.52	1.02	0.26	297	149	441	0.03	1.99
115-767B-47X-3, 0–3	438.40	0.11	1.24	4.22	0.76	0.11	163	555	504	0.08	0.24
115-767B-48X-5, 0–3	451.10	0.03	0.29	5.06	0.33	0.02	87	1533	366	0.09	0.05
115-767B-49X-2, 0–3	456.30	0.03	1.62	4.78	0.81	0.13	200	590	562	0.02	0.33
115-767B-50X-3, 24–28	467.34	0.16	1.09	4.58	0.10	0.10	1090	4580	474	0.13	0.23
115-767B-50X-5, 0–3	470.10	0	1.24	1.95	0.42	0.10	295	464	467	0	0.63
115-767B-51X-3, 0–3	477.80	0	0.98	3.35	0.67	0.08	146	500	538	0	0.29
115-767B-52X-5, 0–3	490.40	0.06	0.45	3.12	0.41	0.04	109	760	420	0.12	0.14
115-767B-53X-5, 0–3	499.00	0.06	1.08	3.96	0.75	0.09	144	528	580	0.05	0.27
115-767B-54X-3, 0–3	505.50	0.02	2.40	1.39	2.61	0.20	91	53	434	0.01	1.72
115-767B-54X-3, 80–82	506.30	0.19	7.74	3.01	0.65	0.66	1190	462	428	0.02	2.57
115-767B-54X-3, 133–134	506.83	2.03	36.79	17.18	64.38	3.23	57	26	387	0.05	2.14
115-767B-55X-4, 0–3	516.70	0.02	2.76	1.14	0.52	0.23	530	219	455	0.01	2.42
115-767B-56X-4, 0–3	525.60	0.10	0.93	5.41	0.85	0.08	1	636	531	0.10	0.17
115-767B-57X-4, 0–3	535.30	0.20	2.31	4.52	0.86	0.20	268	525	566	0.08	0.51
115-767B-58X-5, 0–3	546.50	0.01	0.38	3.30	0.49	0.03	72	673	393	0.03	0.11
115-767B-59X-4, 0–3	554.70	0.10	0.82	3.38	0.79	0.07	103	427	422	0.11	0.24
115-767B-60X-2, 30–33	561.60	0	0.73	2.11	0.64	0.06	114	329	569	0	0.34
115-767B-60X-2, 100–103	562.30	0.05	3.01	2.36	2.75	0.25	109	85	435	0.02	1.27

Table 10 (continued).

Core, section, interval (cm)	Depth (mbsf)	S_1 (mg/g)	S_2 (mg/g)	S_3 (mg/g)	TOC (%)	C (%)	HI	OI	T_{max} (°C)	PI	S_2/S_3
115-767B-60X-3, 13–16	562.93	0	3.16	2.29	4.99	0.26	63	45	430	0	1.37
115-767B-60X-3, 70–73	563.50	0.01	1.53	0.84	0.25	0.12	612	336	483	0.01	1.82
115-767B-60X-3, 90–93	563.70	0.18	2.51	2.43	2.93	0.22	85	82	429	0.07	1.03
115-767B-60X-5, 0–3	565.80	0.03	1.15	3.10	0.69	0.09	166	449	577	0.03	0.37
115-767B-60X-5, 19–23	565.99	0.06	1.37	2.91	0.75	0.11	182	388	517	0.04	0.47
115-767B-61X-2, 30–34	571.20	0.09	1.11	3.08	0.73	0.10	152	421	507	0.07	0.36
115-767B-61X-3, 0–3	572.40	0.06	1.51	3.05	0.68	0.13	222	448	514	0.04	0.49
115-767B-61X-3, 112–116	573.52	0.06	0.92	0.58	0.39	0.08	235	148	474	0.06	1.58
115-767B-62X-5, 0–3	585.10	0.07	1.11	2.60	0.09	0.09	1233	2888	496	0.06	0.42
115-767B-63X-3, 0–3	591.80	0	1.36	1.05	0.12	0.11	1133	875	467	0	1.29
115-767B-64X-5, 0–3	604.50	0	0.78	0.76	0.13	0.06	600	538	471	0	1.11
115-767B-65X-2, 140–150	611.10	0.01	2.60	0.92	0.21	0.21	1238	438	475	0	2.82
115-767B-66X-3, 0–3	620.80	0.02	0.32	8.18	0.02	0.02	1600	409	365	0.06	0.03
115-767B-67X-5, 0–3	633.40	0.05	2.06	0.77	0.17	0.17	1211	452	478	0.02	2.67
115-767B-68X-6, 0–3	644.60	0.01	1.47	0.56	0.12	0.12	1225	466	513	0.01	2.62
115-767B-69X-5, 0–3	652.30	0.04	1.18	0.41	0.10	0.10	1180	410	514	0.03	2.87
115-767B-70X-4, 0–3	660.50	0.22	1.31	0.44	0.12	0.12	1091	366	504	0.14	2.97
115-767B-70X-5, 79–81	662.79	0.04	0.77	0.75	0.46	0.06	167	163	473	0.05	1.02
115-767B-71X-5, 0–3	671.60	0.13	1.11	0.48	0.10	0.10	1110	480	503	0.10	2.31
115-767B-72X-4, 90–93	680.70	0	0.39	1.10	0.08	0.03	487	1375	470	0	0.35
115-767B-72X-5, 0–3	681.30	0.09	0.62	0.67	0.05	0.05	1240	1340	523	0.13	0.92
115-767C-1R-3, 0–3	683.00	0	0	0.53	0.08	0	0	662	376	0	0
115-767B-73X-5, 0–3	690.90	0.04	0.70	0.22	0.06	0.06	1166	366	520	0.05	3.18
115-767C-2R-2, 0–3	691.00	0.35	1.04	0.65	0.13	0.11	800	500	458	0.25	1.60
115-767C-3R-1, 0–3	698.50	0.02	0.78	0.09	0.07	0.06	1114	128	426	0.02	8.66
115-767B-74X-5, 0–3	700.60	0	3.58	0.25	0.29	0.25	1234	86	479	0	14.32
115-767B-75X-1, 127–129	705.47	0.05	1.12	0	0.14	0.09	800	0	460	0.04	0
115-767C-4R-2, 0–3	709.00	0	1.05	0.05	0.09	0.08	1166	55	462	0	21.00
115-767B-75X-5, 0–3	710.20	0.02	2.04	0.28	0.17	0.17	1200	164	465	0.01	7.28
115-767B-76X-5, 0–3	719.50	0.01	2.19	0	0.18	0.18	1216	0	493	0	0
115-767C-5R-3, 128–130	720.78	0.07	2.56	0.01	0.21	0.21	1214	4	471	0.03	
115-767B-77X-2, 0–3	724.70	0	2.72	0	0.22	0.22	1236	0	483	0	0
115-767C-6R-2, 0–3	727.70	0	1.48	0	0.12	0.12	1233	0	488	0	0
115-767B-78X-1, 91–93	733.81	0	0.97	0.15	0.07	0.08	1385	214	504	0	6.46
115-767C-7R-2, 0–3	737.30	0	1.26	0	0.10	0.10	1260	0	460	0	0
115-767C-8R-3, 0–3	746.30	0	3.68	0	0.30	0.30	1276	0	459	0	0
115-767C-9R-2, 0–3	754.03	0.08	2.65	0	0.22	0.22	1204	0	473	0.03	0
115-767C-11R-2, 0–3	773.90	0.09	2.68	0.53	0.22	0.23	1208	240	435	0.03	5.05
115-767C-12R-1, 142–145	783.52	0	0.16	0.38	0.01	0.01	1600	3800	430	0	0.42

Note: HI = hydrogen index, OI = oxygen index, and PI = production index.

not negligible. In addition, many hydrogen indexes are high. This cannot be explained only by a possible under-evaluation of the organic carbon content. These two last assumptions have to be confirmed by further petrologic studies on isolated kerogen.

Hydrocarbon Gases

Background gas concentrations were observed between 0 and 360 mbsf. The genetic characterization of these gases was not possible. However, the molecular composition of the light hydrocarbons detected below 335 mbsf in Hole 767B suggests a bacterial origin, since no higher hydrocarbons than ethane were detected and methane concentrations exceeded ethane concentrations by 2–3 orders of magnitude (Bernard, 1979; Claypool and Kvenvolden, 1983). This interpretation is supported by the fact that the onset of increasing methane coincides with the minimum in the dissolved sulfate concentration (see "Sediment Inorganic Geochemistry" section, this chapter).

High sulfate concentrations seem to prohibit methanogenesis, whereas low sulfate contents enable bacterial methane production (Bernard, 1979; Claypool and Kvenvolden, 1983). Methane and ethane concentrations show parallel trends below 420 mbsf. This suggests that ethane is also generated by bacterial activity in Hole 767B. A possible pathway of bacterial ethanogenesis was reported recently (Whiticar, pers. comm.). The amounts of organic carbon do not seem to influence the concentration of bacterial hydrocarbons in Hole 767B insofar as no correlation between methane concentration and the amount of organic matter is observed (Fig. 42).

The gas sample from Section 124-767B-20X-CC (181.26 mbsf) contains greater portions of higher alkanes and unsaturated hydrocarbons (Table 12). Higher alkanes are normally associated with natural thermocatalytic gases from organic-rich source rocks. These gases do not contain unsaturated components (Hunt, 1979). However, higher concentrations of ethylene and propylene were detected in borehole gases (Faber et al., 1988) where extensive drilling and insufficient cooling of the drill pipe caused cracking of organic matter and the generation of unsaturated hydrocarbons and higher alkanes. On the basis of the molecular composition of the gas sample from Section 124-767B-20X-CC, it is most likely that these hydrocarbons were produced by similar processes.

Conclusions

Organic carbon contents were usually low in sediments from Site 767 (<0.5%), except for depths ranging from 400 to 580 mbsf, where higher values (up to 4.9%) related to turbiditic events were observed. The turbiditic organic matter is derived from terrestrial plants.

Background concentrations of gaseous hydrocarbons were observed between 0 and 335 mbsf. Higher concentrations of gases of bacterial origin occur below 335 mbsf. The concentration of bacterial gases seems to be independent of the amount of organic matter.

The light hydrocarbons of the gas sample from Section 124-767B-20X-CC were most likely generated during drilling by thermal cracking of organic substances.

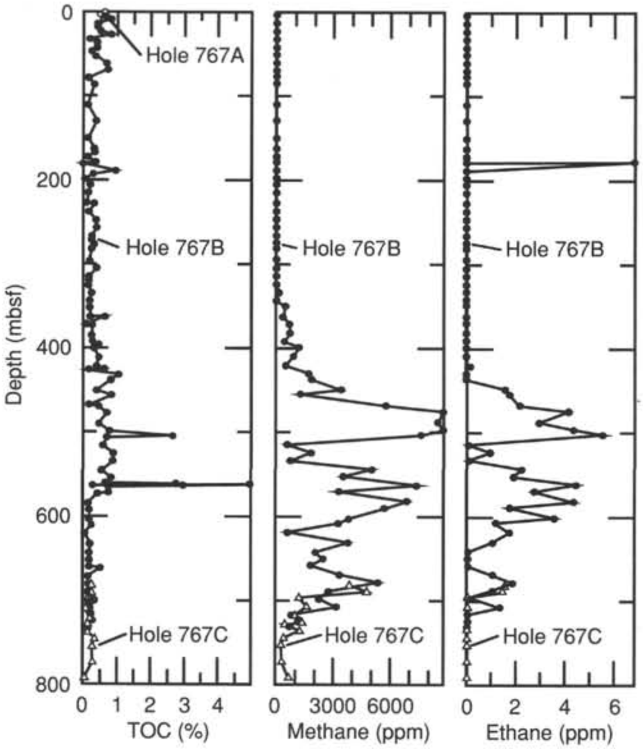

Figure 41. Distribution of total organic carbon (TOC), methane, and ethane concentrations in headspace gas samples vs. depth, Site 767.

PHYSICAL PROPERTIES

Introduction

Physical properties measurements made at Site 767 include the standard ODP suite of analyses:

1. Index properties were determined with a pycnometer and balance; they include wet-bulk density, grain density, porosity, water content, and void ratio.
2. The GRAPE wet-bulk density and compressional wave velocity were measured on whole cores with a continuous logger and on discrete samples with a Hamilton Frame Velocimeter.
3. Thermal conductivity was measured on undisturbed cores from the upper sections of the holes.
4. Vane shear strength was measured on selected undisturbed intervals of the core samples.

Details of the methods used for physical properties measurement are described in the "Explanatory Notes" chapter of this volume.

Three holes were cored at Site 767. Specific details concerning the coring procedures and depths can be found in the "Operations" section (this chapter). The lithologic units referred to in this section are those described in the "Lithostratigraphy" section (this chapter). Velocities and index properties were measured on a majority of the cores. The GRAPE wet-bulk density measurements were performed to a depth of 600 mbsf in Hole 767B only. Thermal conductivity measurements were made on competent material in Holes 767A, 767B, and 767C. Vane shear measurements from Hole 767B were not obtained below 258 mbsf. The values of the various physical properties measured are listed in Tables 13–16, and the variations of these properties with depth are plotted in Figures 43–47.

Table 11. Total organic carbon content and composition of headspace gas samples from sediments of Site 767.

Core, section, interval (cm)	Depth (mbsf)	TOC (%)	CH_4 (ppm)	C_2H_6 (ppm)	C_1/C_2
124-767A-					
1H-1, 23–28	0.23	0.59			
1H-2, 145–150	2.95	0.51			
1H-CC, 11–16	3.90	0.45			
124-767B-					
1H-5, 0–3	6.00	0.58	8.5	0	
2H-1, 43–48	9.43	0.73			
2H-5, 0–3	15.00	0.34	3.7	0	
3H-1, 12–17	18.62	0.39			
3H-5, 0–3	24.50	0.47	4.3	0	
4H-1, 10–15	28.10	0.79			
4H-5, 0–3	34.00	0.15	1.8	0	
5H-1, 10–15	37.60	0.38			
5H-5, 0–3	43.50	0.34	2.1	0	
6H-1, 20–25	47.20	0.22			
6H-5, 0–3	53.00	0.32	4.0	0	
7H-5, 0–3	62.50	0.69	6.8	0	
8H-4, 0–3	70.50	0.68	7.5	0	
9H-6, 0–3	79.00	0.11	10.0	0	
10H-5, 0–3	87.00	0.31	0	0	
10H-5, 95–97	87.95	0.25			
13X-2, 0–3	111.10	0.08	3.3	0	
15X-2, 0–3	130.40	0.34	2.7	0	
17X-3, 0–3	151.30	0.10	0	0	
18X-5, 0–3	164.00	0.28	2.8	0	
19X-1, 15–20	167.75	0.30			
19X-5, 0–5	173.60	0.08	3.1	0	
20X-2, 0–3	178.80	0.32	2.6	0	
20X-CC	181.26	0	11.4	6.8	1.7
21X-1, 0–3	183.82				
21X-5, 0–3	189.80	0.93	0	0	
22X-1, 18–23	193.68	0.28			
22X-5, 0–3	199.50	0.05	2.6	0	
23X-3, 0–3	206.30	0.17	0	0	
24X-3, 0–3	216.10	0.10	0	0	
25X-4, 76–78	228.16	0.05			
25X-5, 0–3	228.90	0.29	0	0	
26X-5, 0–3	238.60	0.13	2.8	0	
27X-5, 0–3	248.20	0.35	3.2	0	
28X-5, 0–3	257.90	0.36	3.5	0	
29X-5, 0–3	267.40	0.22	3.3	0	
30X-1, 27–29	271.27	0.21			
30X-5, 0–3	277.00	0.26	3.1	0	
31X-2, 0–3	282.20	0.21	3.6	0	
32X-5, 0–3	296.40	0.15	8.6	0	
33X-5, 0–5	306.10	0.38	3.1	0	
34X-5, 0–3	315.80	0.10	4.0	0	
35X-1, 69–71	320.09	0.11			
35X-5, 0–3	325.40	0.10	3.7	0	
36X-5, 0–3	335.10	0.21	29.2	0	
37X-5, 0–3	344.80	0.15	11.3	0	
38X-3, 0–3	351.50	0.15	422.0	0	
39X-4, 89–92	363.49	0.17			
39X-5, 0–3	364.10	0.61	289.3	0	
40X-3, 134–136	372.14	0.07			
40X-4, 0–3	372.30	0.21	608.4	0	
41X-5, 0–3	383.50		644.0	0	
41X-CC, 0–3	386.86	0.21			
42X-5, 0–3	393.10	0.25	353.0	0	
42X-7, 33–35	396.43	0.42			
43X-3, 0–3	399.80	0.27	1153.0	0	
44X-4, 0–3	411.00	0.44	862.2	0	
45X-5, 0–5	422.20	0.36	422.2	0	
45X-CC, 0–3	425.60	0.59			
45X-CC, 28–31	425.88	0.12			
46X-5, 0–3	431.80	1.02	1597.0	0	
47X-3, 0–3	438.40	0.76	1764.0	0	
48X-5, 0–3	451.10	0.33	3359.0	1.5	2239.3
49X-2, 0–3	456.30	0.81	1179.0	1.7	693.5
50X-3, 24–28	467.34	0.10			
50X-5, 0–3	470.10	0.42	5744.0	2.1	2735.2
51X-3, 0–3	477.80	0.67	8792.0	4.1	2144.4

Table 11 (continued).

Core, section, interval (cm)	Depth (mbsf)	TOC (%)	CH_4 (ppm)	C_2H_6 (ppm)	C_1/C_2
124-767B-					
52X-5, 0-3	490.40	0.41	8520	2.9	2937.9
53X-5, 0-3	499.00	0.75	8756.0	4.3	2036.3
54X-3, 0-3	505.50	2.61	7553.0	5.5	1373.3
54X-3, 80-82	506.30	0.65			
55X-4, 0-3	516.70	0.52	537.0	0	
56X-4, 0-3	525.60	0.85	1751.0	0.9	1945.6
57X-4, 0-3	535.30	0.86	692.9	0	
58X-5, 0-3	546.50	0.49	5006.0	2.2	2275.5
59X-4, 0-3	554.70	0.79	3465.0	1.9	1823.7
60X-2, 30-33	561.60	0.64			
60X-2, 100-103	562.32	2.75			
60X-3, 13-16	562.93	4.99			
60X-3, 70-73	563.50	0.25			
60X-3, 90-93	563.70	2.93			
60X-5, 0-3	565.80	0.69	7302.1	4.4	1659.6
60X-5, 19-23	565.99	0.75			
61X-2, 30-34	571.20	0.73			
61X-3, 0-3	572.40	0.68	3288.0	2.7	1217.8
61X-3, 112-116	573.52	0.39			
62X-5, 0-3	585.10	0.09	6825.0	4.3	1587.2
63X-3, 0-3	591.80	0.12	5689.0	1.7	3406.6
64X-5, 0-3	604.50	0.13	3742.0	3.5	1063.1
65X-2, 0-3	609.70		3248.0	1.1	2952.7
65X-2, 140-150	611.10	0.21			
66X-3, 0-3	620.80	0.02	526.0	1.7	309.4
67X-5, 0-3	633.40	0.17	3760	1.0	3836.7
68X-6, 0-3	644.60	0.12	2028.0	0	
69X-5, 0-3	652.30	0.10	2449.0	0	
70X-4, 0-3	660.50	0.12	1720.8	0	
70X-5, 79-81	662.79	0.46			
71X-5, 0-3	671.60	0.10	3252.0	1.0	3252.0
72X-4, 90-93	680.70	0.08			
72X-5, 0-3	681.30	0.05	5294.0	1.8	
73X-5, 0-3	690.90	0.06	2723.0	1.0	
74X-5, 0-3	700.60	0.29	2207.0	0	
75X-1, 127-129	705.47	0.14			
75X-5, 0-3	710.20	0.17	3103.3	1.3	
76X-5, 0-3	719.50	0.18	776.7	0	
77X-2, 0-3	724.70	0.22	1130.3	0	
78X-1, 91-93	733.81	0.07	673.0	0	
78X-CC, 10-13	738.60	0.08			
124-767C-					
1R-3, 0-3	683.00	0.08	3812.0	1.5	2508.0
2R-2, 0-3	691.00	0.13	4692.3	1.4	3352.0
3R-1, 0-3	698.50	0.07	1166.6	0	
4R-2, 0-3	709.00	0.09	1559.9	0	
5R-3, 128-130	719.50	0.21	957.2	0	
6R-2, 0-3	727.70	0.12	1236.6	0	
6R-3, 0-3	729.20	0.10	378.2	0	
7R-2, 0-3	737.30	0.10	1203.8	0	
8R-3, 0-3	746.30	0.30	328.6	0	
9R-2, 0-3	754.50	0.22	195.8	0	
11R-2, 0-3	773.90	0.22	192.0	0	
12R-1, 142-145	793.10	0.01	591.8	0	

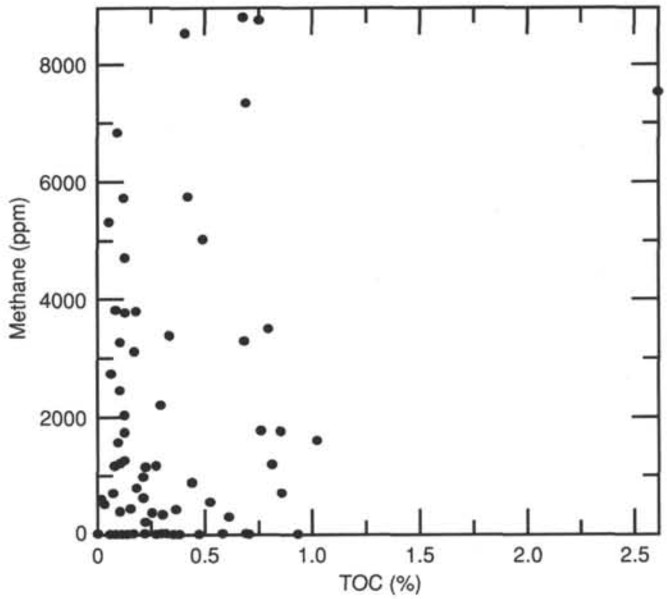

Figure 42. Methane concentrations in headspace gas samples vs. total organic carbon (TOC) content in sediments at Site 767.

Results

Index Properties

Wet-bulk density, grain (or matrix) density, porosity, water content (dry basis), and void ratio values determined for the samples from Holes 767A, 767B, and 767C are listed in Table 13 and plotted relative to depth in Figure 43.

The plot of bulk density obtained from index properties (Fig. 43) shows a consistent trend of increasing values with depth. Surface and near-surface sediment samples have bulk densities tightly clustered around 1.36 g/cm^3. Sample bulk densities increase smoothly downhole to values of roughly 2.15 g/cm^3 near the base of the hole.

There are five points with rather high bulk densities located between 324 and 604 mbsf. These points correspond to samples of carbonate-rich sediment associated with turbidity deposits. Another high bulk density value was measured for the basement basalt sample at 787 mbsf. About six samples gave low bulk density values; these samples were taken from core that was highly biscuited, with the biscuits showing shear distortion and fractures. These low values, therefore, may be a result of excessive sample disturbance during drilling. With the exception of these anomalous values, the bulk densities plotted on Figure 43 show a very consistent overall trend of increasing density with depth. Local variations from this trend may be indicative of lithological changes. The second column of Figure 43 combines the bulk density data from the index properties analyses with data obtained from the GRAPE and is discussed in the "GRAPE" section (this chapter).

Figure 43 also presents grain density as a function of depth. Grain density is a parameter that generally falls within a narrow range of values for most sedimentary materials. The six points on Figure 43 that lie above 2.85 g/cm^3 and the six points that lie below 2.35 g/cm^3 are probably erroneous. The grain density values provide a convenient check on the validity of all index property values since most grain density measurements fall within a

Table 12. Hydrocarbon gas composition of the headspace sample (Section 124-767C-20X-CC), Site 767.

Core, section, interval (cm)	Depth (mbsf)	CH_4 (ppm)	C_2H_4 (ppm)	C_2H_6 (ppm)	C_3H_6 (ppm)	C_3H_8 (ppm)	i-C_4H_{10} (ppm)	n-C_4H_{10} (ppm)
124-767C-20X-CC	181.26	11.4	13.4	6.5	10.3	3.2	26.3	2.6

Table 13. Index property data, Site 767.

Core, section, interval (cm)	Depth (mbsf)	Wet-bulk density (g/cm^3)	Grain density (g/cm^3)	Porosity (%)	Water content (%)	Void ratio
124-767A-						
1H-1, 40–43	0.40	1.39	2.57	81	150	4.28
2H-2, 40–43	1.90	1.35	2.60	84	177	5.41
124-167B-						
1H-2, 60–63	2.10	1.36		83	165	4.83
1H-5, 80–83	6.80	1.35		85	178	5.45
2H-1, 85–88	9.85	1.35		81	162	4.34
2H-5, 120–123	16.20	1.38				
3H-2, 40–42	20.40	1.34		84	179	5.25
3H-6, 119–122	27.19	1.36		85	176	5.60
4H-1, 122–125	29.22	1.37	2.57	82	155	4.41
4H-6, 98–101	36.48	1.36	2.55	83	165	4.83
5H-2, 32–35	39.32	1.34	2.62	85	185	5.60
5H-6, 124–127	46.24	1.34	2.62	85	183	5.44
6H-1, 79–82	47.79	1.37	2.49	81	154	4.21
6H-4, 83–86	52.33	1.40	2.33	80	141	4.04
6H-7, 54–57	56.54	1.39	2.40	84	162	5.12
7H-2, 130–133	59.30	1.36	2.21	75	131	3.07
7H-4, 123–126	62.23	1.38	2.38	77	133	3.31
7H-6, 20–23	64.20	1.41	2.12	70	102	2.30
8H-1, 135–138	67.35	1.47	2.66	79	122	3.72
8H-3, 120–123	70.20	1.42	2.65	81	141	4.31
9H-6, 85–88	79.85	1.42	2.54	79	133	3.82
10H-2, 120–123	83.70	1.42	2.63	80	138	4.11
10H-4, 80–83	86.30	1.44	2.59	80	131	3.93
10H-7, 38–41	90.38	1.50	2.69	77	110	3.27
13X-1, 102–105	110.62	1.45	2.50	78	123	3.49
15X-2, 122–125	131.62	1.38	2.58	80	145	3.92
17X-2, 85–88	150.65	1.78	2.69	58	50	1.37
17X-3, 76–79	152.06	1.83	2.75	54	44	1.19
18X-2, 58–61	160.08	1.45	2.37	76	115	3.10
18X-5, 66–69	164.66	1.39	2.19	73	116	2.69
19X-2, 41–44	169.51	1.46	2.56	77	118	3.39
19X-4, 99–102	173.09	1.39		61	81	1.54
20X-2, 32–35	179.12	1.66	2.64	65	68	1.88
20X-3, 20–23	180.50	1.48	2.45	78	118	3.53
21X-1, 115–118	184.95	1.77	2.71	62	57	1.65
21X-4, 58–61	188.88	1.45	2.51	78	122	3.47
21X-6, 82–85	192.12	1.44	2.62	77	121	3.33
22X-1, 52–55	194.02	1.64	2.67	67	72	2.05
22X-3, 56–59	197.06	1.54	2.75	76	102	3.12
22X-5, 90–93	200.40	1.83	2.68	57	47	1.33
23X-1, 95–98	204.25	1.62	2.71	70	80	2.37
23X-3, 16–19	206.46	1.52	2.61	74	100	2.89
24X-1, 42–45	213.52	1.51	2.63	74	101	2.85
24X-2, 135–138	215.95	1.55	2.66	74	95	2.80
25X-1, 87–90	223.77	1.55	2.63	72	91	2.56
25X-3, 50–53	226.40	1.62	2.66	69	78	2.26
25X-5, 30–33	229.20	1.56	2.67	74	93	2.77
26X-1, 15–18	232.75	1.55	2.60	72	91	2.62
26X-2, 65–68	234.75	1.53	2.36	73	96	2.75
27X-1, 42–45	242.62	1.54	2.65	74	95	2.77
27X-4, 104–107	247.74	1.65	2.62	69	76	2.27
28X-2, 55–57	253.95	1.59	2.69	71	84	2.44
28X-4, 22–24	256.62	1.61	2.54	69	79	2.26
28X-6, 38–40	259.78	1.61	2.67	70	80	2.34
29X-1, 43–45	261.83	1.61	2.63	70	79	2.28
29X-3, 58–60	264.98	1.54	2.56	64	75	1.79
29X-5, 93–96	268.33	1.60	2.58	67	74	1.99
30X-1, 38–40	271.38	1.60	2.48	68	77	2.12
30X-3, 40–42	274.40	1.63	2.73	70	78	2.28
30X-5, 118–120	278.18	1.68	2.52	62	60	1.60
31X-1, 85–86	281.55	1.53	2.49	65	78	1.89
32X-1, 66–68	291.06	1.66	2.66	66	68	1.90
33X-1, 107–108	301.17	1.61	2.63	69	78	2.19
33X-6, 131–132	308.91	1.62	2.47	65	70	1.86
33X-7, 27–29	309.37	1.63	2.57	66	72	1.97
34X-2, 9–11	311.39	1.65	2.58	67	70	1.98
34X-3, 82–84	313.62	1.58	2.42	67	76	1.98
34X-6, 75–77	318.05	1.55	2.33	67	78	1.99
35X-1, 113–115	320.53	1.60	2.36	63	67	1.70
35X-4, 51–53	324.41	2.19	2.63	35	20	0.54
35X-5, 66–68	326.06	1.66	2.61	65	66	1.82
36X-2, 18–20	330.78	1.60	2.46	65	71	1.84
36X-4, 120–122	334.80	1.58	2.35	68	78	2.07
37X-5, 115–117	345.95	1.55	2.44	68	80	2.08
38X-1, 73–75	349.23	2.48	2.81	24	11	0.32

Table 13 (continued).

Core, section, interval (cm)	Depth (mbsf)	Wet-bulk density (g/cm^3)	Grain density (g/cm^3)	Porosity (%)	Water content (%)	Void ratio
124-167B-						
38X-2, 40–42	350.40	1.68	2.54	68	70	2.10
39X-2, 61–63	360.21	1.65	2.56	66	69	1.92
39X-4, 100–102	363.60	1.64	2.69	71	80	2.50
39X-6, 72–74	366.32	1.67	2.71	75	85	2.99
39X-6, 129–131	366.89	1.71	2.50	71	74	2.48
40X-4, 30–33	372.60	1.62	2.44	70	79	2.28
41X-2, 139–141	380.39	1.84	2.90	61	52	1.58
42X-2, 115–117	389.75	1.62	2.74	73	85	2.67
44X-2, 7–9	408.07	1.73	2.79	69	69	2.22
44X-5, 22–24	412.72	1.64	2.76	72	81	2.53
45X-3, 96–98	420.16	2.59	2.74	17	7	0.20
45X-4, 89–91	421.59	2.01	3.07	59	43	1.44
45X-5, 89–91	423.09	1.86	2.74	65	56	1.87
46X-6, 110–112	434.40	1.26	2.65	33	37	0.50
46X-7, 26–28	435.06	1.71	2.87	67	67	1.99
47X-2, 76–78	437.66	1.41	2.75	36	35	0.56
47X-4, 33–35	440.23	2.02	2.76	46	30	0.85
48X-2, 111–113	447.71	1.99	2.71	49	34	0.97
48X-4, 110–112	450.70	1.75	2.73	63	58	1.69
48X-5, 67–69	451.77	1.94	2.57	56	42	1.25
49X-2, 82–84	457.12	1.70	2.66	64	62	1.74
49X-2, 109–111	457.39	2.08	2.86	47	30	0.90
50X-3, 71–73	467.81	1.82	2.77	59	49	1.41
50X-5, 100–102	471.10	1.92	2.68	52	39	1.09
50X-5, 128–130	471.38	1.98	2.75	48	33	0.92
51X-2, 30–32	476.60	2.02	2.71	46	30	0.84
51X-4, 22–24	479.52	2.07	2.69	43	27	0.75
52X-4, 72–74	489.62	1.83	2.71	57	47	1.32
52X-6, 21–23	492.11	2.02	2.75	46	30	0.85
53X-4, 78–80	498.28	2.07	2.71	44	28	0.80
57X-3, 74–76	534.54	1.91	2.64	54	41	1.17
58X-4, 102–104	546.02	1.89	2.76	57	45	1.34
58X-6, 18–20	548.18	1.83	2.66	57	47	1.34
59X-5, 12–14	556.32	2.19	2.79	44	26	0.78
59X-5, 98–100	557.18	2.04	2.73	47	31	0.87
59X-CC, 19–21	557.85	2.55	2.64	10	4	0.11
60X-2, 53–55	561.83	1.25	2.63	22	22	0.28
60X-4, 23–25	564.53	2.08	2.64	42	26	0.73
60X-5, 49–51	566.29	1.24	2.59	25	26	0.33
61X-2, 61–63	571.51	2.11	2.74	41	25	0.68
61X-CC, 35–37	574.08	1.88	2.59	55	43	1.23
62X-1, 93–95	580.03	1.96	2.71	49	35	0.97
62X-5, 8–10	585.18	2.15	2.73	42	25	0.73
62X-CC, 24–26	588.76	1.50	2.62	27	23	0.37
63X-2, 116–118	591.46	2.14	2.72	39	23	0.64
63X-3, 62–64	592.42	1.93	2.74	56	42	1.28
64X-2, 35–37	600.35	1.76	2.59	62	57	1.64
64X-4, 58–60	603.58	2.87	2.69	10	4	0.12
66X-CC, 24–26	622.11	2.24	2.77	39	22	0.65
67X-4, 130–132	633.20	2.18	2.86	47	28	0.88
67X-7, 24–26	636.64	2.12	2.81	65	46	1.86
68X-2, 136–138	639.96	2.12	2.76	42	25	0.71
68X-4, 32–34	641.92	2.10	2.84	49	31	0.95
68X-5, 102–104	644.12	2.11	2.75	43	27	0.76
69X-2, 78–80	648.58	2.08	2.82	50	33	0.99
69X-4, 29–31	651.09	2.07	2.75	48	31	0.91
69X-6, 124–126	655.04	2.14	2.82	46	28	0.85
70X-2, 75–77	658.25	2.10	2.75	44	27	0.77
70X-4, 125–127	661.75	2.05	2.68	50	34	1.01
72X-1, 89–90	676.19	1.96	2.72	51	36	1.02
72X-4, 55–57	680.35	2.02	2.72	49	33	0.96
72X-6, 109–111	683.89	1.97	2.72	52	37	1.09
73X-3, 18–20	688.08	2.02	2.76	49	33	0.97
73X-4, 109–111	690.49	2.00	2.62	51	35	1.03
73X-7, 18–20	694.08	2.05	2.71	47	31	0.90
74X-1, 105–107	695.65	1.99	2.72	64	49	1.74
74X-3, 85–87	698.45	2.17	2.67	45	27	0.81
75X-5, 20–22	710.40	2.14	2.70	42	25	0.73
76X-5, 47–49	719.97	1.95	2.47	54	40	1.18
77X-1, 96–98	724.16	2.07	2.68	48	31	0.92
124-767C-						
1R-1, 24–26	680.24	1.97	2.73	52	37	1.08
1R-2, 85–87	682.35	1.94	2.69	51	37	1.05
2R-2, 87–89	691.87	2.06	2.77	49	32	0.95
2R-2, 105–107	692.05	1.93	2.73	54	41	1.19
3R-2, 18–20	700.18	2.10	2.75	46	29	0.85

Table 13 (continued).

Core, section, interval (cm)	Depth (mbsf)	Wet-bulk density (g/cm^3)	Grain density (g/cm^3)	Porosity (%)	Water content (%)	Void ratio
124-767C-						
4R-1, 27–29	707.77	2.12	2.70	43	26	0.77
5R-2, 2–4	718.02	2.21	2.69	46	27	0.86
5R-3, 50–52	720.00	2.17	2.85	47	28	0.88
6R-1, 37–39	726.57	2.03	2.74	52	35	1.07
6R-2, 30–32	728.00	2.20	2.76	46	27	0.86
7R-1, 60–62	736.40	2.21	2.84	46	27	0.87
7R-2, 37–39	737.67	2.16	2.73	45	27	0.82
8R-1, 47–49	743.77	2.20	2.79	46	27	0.85
8R-2, 58–60	745.38	2.19	2.71	41	24	0.70
9R-1, 43–45	753.43	2.29	2.80	40	22	0.68
11R-1, 103–106	773.43	2.24	2.71	39	22	0.64
12R-1, 50–52	782.60	2.05	2.56	42	27	0.72
12R-1, 142–144	783.52	2.10	2.60	43	27	0.76
12R-2, 91–93	784.51	2.08	2.59	43	27	0.75
12R-3, 64–66	785.74	2.14	2.69	43	26	0.76
12R-CC, 26–28	786.86	2.78	2.77	3	1	0.03
	Averages	1.78	2.65			

typical range (generally from 2.35 to 2.85 g/cm^3). If grain density determinations fall outside this range, then the other index data for that sample are likely to be incorrect.

Variability in grain density decreases below 500 mbsf. This decrease is probably caused in part by an improvement of the balance operation made prior to the measurements taken on the samples from Hole 767C. From 0 to 400 mbsf, grain densities display the greatest fluctuations, with only a slight trend toward increasing density with depth. From 400 to 786 mbsf, grain densities do not vary consistently with depth and range between 2.56 and 2.86 g/cm^3.

Variations in porosity, water content, and void ratio plotted vs. depth are shown in the last three columns of Figure 43. These plots show an expected decrease of these properties with increasing depth.

Figure 43 shows that porosities are more variable at some depths than at others. This may be a reflection of the more variable lithology at these depth intervals. Porosity drops from around 83% at the seafloor to about 40% at 785 mbsf. The points with the highest wet-bulk densities in Figure 43 have correspondingly low porosities.

Decreases in water content are nonlinear, with the greatest rate of change occurring near the seafloor. Water contents near the seafloor range between 150% and 185%, whereas in the interval between 728 and 785 mbsf water content ranges from 22% to 27%. This decrease in porosity and water content is related to the compaction (or consolidation) of the deeper sediments caused by gravitational loading when sediments were deposited above. At about 410 mbsf an abrupt decrease in water content is seen. This depth interval corresponds closely to the lithologic boundary between Units II and III. The carbonate-rich turbidite deposits, which have high bulk densities and low porosities, also have low water contents.

The last column in Figure 43 shows that the void ratio (the ratio of voids to solids) exhibits the same trend as the water content.

GRAPE

Wet-bulk densities determined with the gamma-ray attenuation porosity evaluation technique (GRAPE), along with corresponding values determined from index properties, are plotted in Figure 43. Grape bulk densities were obtained for APC and XCB cores from Hole 767B; no GRAPE measurements were taken on RCB cores from Hole 767C. GRAPE measurements were conducted to a depth of 600 mbsf in Hole 767B. Below roughly 400 mbsf, the core diameter became sporadically smaller than the inside diameter of the liner tube, which resulted in greater apparent fluctuations in the bulk density values and introduced erroneous results. GRAPE measurements ended at 600 mbsf when the core became consistently smaller than the liner and biscuiting became severe. GRAPE measurements were taken at 10-cm intervals but were averaged over 0.5 m for presentation in Figure 43.

Figure 43 shows that the discrete bulk density and the GRAPE bulk density show a great deal of variability with depth. However, the two methods are in close agreement to a depth of roughly 400 mbsf. Below this depth the index bulk density tends to be higher than the GRAPE bulk density. The primary reason for the discrepancy is the error associated with the reduction of the core diameter and the associated presence of a lower density slurry around the fairly undisturbed core. Both effects serve to decrease the measured GRAPE bulk densities.

Bulk density shows an abrupt increase at about 410 mbsf. This change is probably related to the lithologic boundary between Units II and III. The bulk densities show other less dominant trends that may reflect characteristics of the sediments. For example, the depth interval from about 145 to 230 mbsf contains a significant number of higher bulk density values. These correspond to the presence of discrete higher density, graded carbonate sand/sandstone horizons. The bulk density plot also shows a relative density low between ~300 and 400 mbsf that is mirrored by increased porosity and void ratio in the same interval.

Velocity

The compressional wave velocity data were measured with the Hamilton Frame Velocimeter on samples from Hole 767B. However, because of a procedural error discovered after the measurements for Hole 767B were taken, we discarded this data. The procedural error was corrected, and good Hamilton Frame velocity determinations were obtained on samples from Hole 767C. The continuous compressional wave logger was not operating correctly, and all data obtained from this apparatus were rejected. Figure 44 presents the data from the Hamilton Frame and shows a trend of constant velocities, with averages of 1.87 km/s in the greenish gray claystone and 1.96 km/s in the reddish brown claystone (Units IIIC and IV). An abrupt increase in velocity at 791 mbsf is associated with the change from reddish brown claystone to the moderately altered basaltic crust of the Celebes Sea. The measured velocity from a single sample of basalt was 4.91 km/s.

The lack of reliable velocity data from Hole 767B prevented the determination of potential depth-dependent velocity changes or correlations with other physical properties in the interval from 0 to 680 mbsf.

Some variability in the data from Hole 767C is caused, in part, by the sampling procedure used. Samples were taken to be as representative as possible of the sediment section as a whole. However, sample selection depended upon the relative frequency, thickness, and homogeneity of a particular sequence.

Another source of velocity variability was the presence of time-dependent velocity changes following core sampling (generally velocity increased with time) for some of the sediment samples. Shortly after the core was split, velocity samples were taken and cut on the twin parallel saw to obtain the planar parallel faces necessary for the Hamilton Frame. These samples were rinsed in seawater immediately after being cut while using freshwater. We then mounted the samples into the Hamilton Frame, using seawater to ensure acoustic coupling. Traveltimes were immediately measured and monitored for a short period of time (2–4 min). Certain samples displayed a time-dependent increase in velocity, with the rate of increase slowing over the

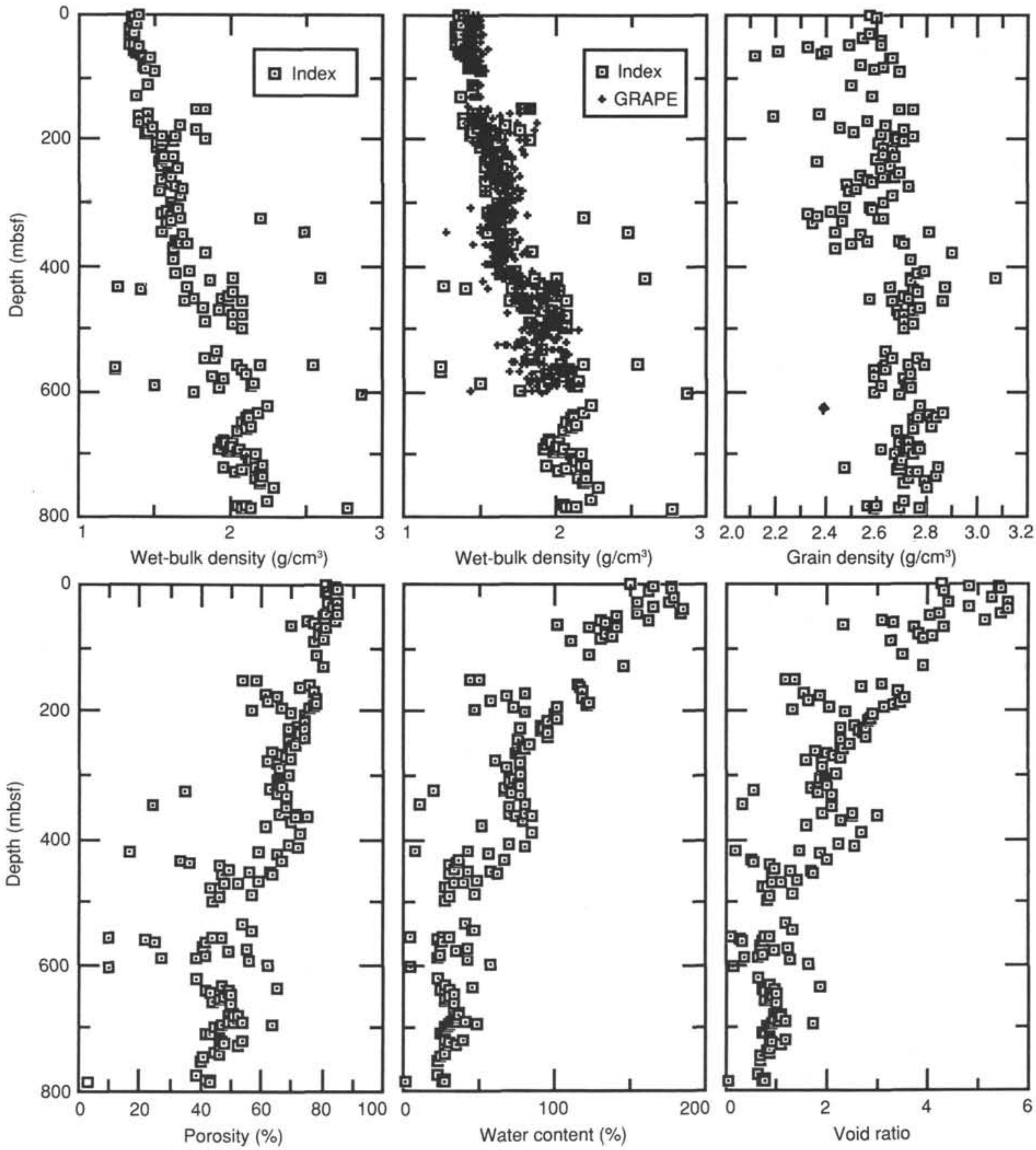

Figure 43. Downhole changes in index properties (wet-bulk density, GRAPE bulk density, grain density, porosity, water content, and void ratios), Site 767.

short period of time in which the samples were monitored. The values of compressional velocity listed in Table 14 and plotted in Figure 44 are the velocities obtained at the end of the monitoring period.

As a means of comparing the physical properties with the seismic reflection data, an acoustic impedance plot (Fig. 45) was created by multiplying the sediment bulk density by the corresponding velocity and plotting the result as a function of depth. Since the bulk density was fairly constant for all sediment samples from Hole 767C, the acoustic impedance plot essentially shows the same trend as the velocity plot.

Thermal Conductivity

Thermal conductivities of cores from Holes 767A, 767B, and 767C are shown in Table 15 and Figure 46. All values were obtained with needle probes inserted through core liners into full core sections. An attempt was made to insert the probes at locations along each core section that appeared to be the least disturbed. However, an annulus of disturbed sediment and drill fluid was often present along the inside of the liner, which prevented reliable visual identification of the more intact segments in the core. The core sections were allowed to reach thermal

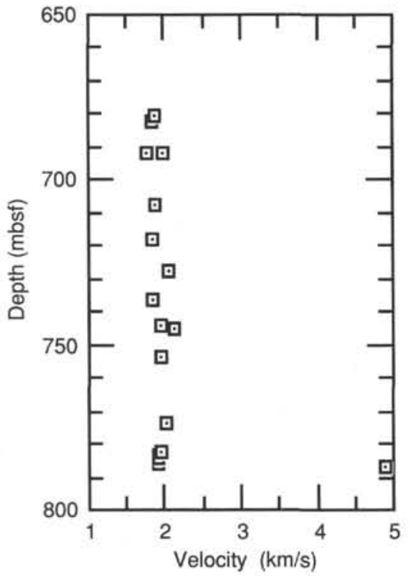

Figure 44. Hamilton Frame compressional velocity vs. depth, Hole 767C.

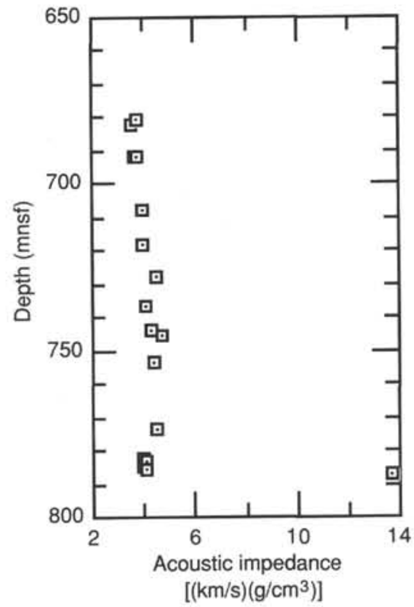

Figure 45. Acoustic impedance vs. depth, Hole 767C.

Table 14. Compressional wave velocity data, Site 767.

Core, section, interval (cm)	Depth (mbsf)	Velocity (km/s)
124-767C-		
1R-1, 26–28	680.26	1.89
1R-2, 87–89	682.37	1.85
2R-2, 84–86	691.84	1.78
2R-2, 107–109	692.07	1.98
4R-1, 27–29	707.77	1.88
5R-2, 2–4	718.02	1.83
6R-2, 30–32	728.00	2.06
7R-1, 60–62	736.40	1.83
8R-1, 47–49	743.77	1.95
8R-2, 58–60	745.38	2.13
9R-1, 43–45	753.43	1.94
11R-1, 103–106	773.43	2.03
12R-1, 52–54	782.62	1.93
12R-1, 144–146	783.54	1.93
12R-2, 89–91	784.49	1.93
12R-3, 66–68	785.76	1.91
12R-CC, 26–28	786.86	4.91

equilibrium with the laboratory temperature (about 24 °C), which usually took between 2 and 3 hr. The readings were then obtained over a 10–12-min period.

Thermal conductivity at Site 767 showed a consistent increase with increasing depth, with values ranging from about 0.85 W/m · K at the seafloor to about 1.5 W/m · K at 600 mbsf. The amount of scatter also increased with depth. Increasing variability in thermal conductivity was probably related to core disturbance and core biscuiting, both of which tend to increase with depth. A heavily biscuited core contains individual segments of fairly intact sediment separated and often surrounded by a slurry of sediment and drilling fluid. The placement of the thermal conductivity probes in these types of cores will often result in the probe being inserted into slurry rather than into intact sediment segments. This causes the thermal conductivity measurement to fluctuate between values for the slurry and values for the intact sediments. The scatter was largest for sediments obtained between 430 to 610 mbsf. There appears to be about a 0.2 W/m · K downward shift in thermal conductivities at 610 mbsf, with the values measured on cores obtained between 610 and 785 mbsf fluctuating around 1.35 W/m · K.

Vane Shear Strength

Values for undrained shear strength were obtained by means of a four-bladed, motorized vane shear apparatus on samples taken from APC and XCB cores from Hole 767B. The APC and XCB cores displayed evidence of sample disturbance, and thus the measured shear strengths may vary significantly from those *in situ*. The resulting peak and remolded shear strengths are given in Table 16 and are plotted as a function of depth in Figure 47. The vane was set to rotate at about 20°/min, which generally resulted in 10°–14° of rotation before peak shear strength was achieved. The vane was permitted to continue rotation for at least 120°, allowing the shear strength to drop to a fairly constant value for determining the remolded shear strength.

Undrained peak shear strength increased rapidly with increasing depth below seafloor until a depth of approximately 50 mbsf was reached. At this depth the failure mechanism around the vane became dominated by cracks that propagated away from the ends of the vane; the equations for shear strength determination determined from a cylindrical failure surface around the vane were no longer valid. At depths greater than 258 mbsf, the samples tended to crack during vane insertion and testing was ended. The remolded shear strength displayed a similar increase with depth over the interval from 0 to 50 mbsf with sensitivity fluctuations ranging from 2 to 3. At depths greater than 50 mbsf, the remolded shear strength showed wide variations, which was also reflected in the sensitivity fluctuations (with ranges from 2 to 5).

Shear strengths determined over the depth interval from 50 to 258 mbsf are not intended to provide reliable strength parameters; rather, they were taken to indicate the variability in shear strength caused by the cracking failure mode in stiffer sediments.

Conclusions

The sediment index properties, compressional wave velocities, thermal conductivities, and vane shear strengths provide a good characterization of the sediments at Site 767. In general, all physical properties displayed expected depth-dependent variations. Bulk density values increase with depth, almost certainly a result of compaction caused by gravitational loading. This observation is corroborated by the porosity, water content, and

Table 15. Thermal conductivity data, Site 767.

Core, seciton, interval (cm)	Depth (mbsf)	Thermal conductivity (W/m · K)
124-767A-		
1H-1, 50–51	0.50	0.857
1H-2, 50–51	2.00	0.897
1H-3, 50–51	3.50	0.823
124-767B-		
1H-1, 50–51	0.50	0.960
1H-2, 50–51	2.00	0.847
1H-3, 50–51	3.50	0.878
1H-4, 50–51	5.00	0.886
2H-1, 50–51	9.50	0.876
2H-3, 50–51	12.50	0.903
2H-5, 50–51	15.50	0.869
2H-6, 50–51	17.00	0.869
3H-1, 50–51	19.00	0.904
3H-2, 50–51	20.50	0.914
3H-3, 50–51	22.00	0.900
3H-4, 50–51	23.50	0.938
4H-1, 50–51	28.50	0.858
4H-2, 50–51	30.00	0.855
4H-3, 50–51	31.50	0.900
4H-4, 50–51	33.00	0.957
5H-2, 50–51	39.50	0.890
5H-3, 50–51	41.00	0.898
5H-4, 50–51	42.50	0.875
5H-5, 50–51	44.00	0.901
6H-2, 50–51	49.00	0.866
6H-3, 50–51	50.50	0.886
6H-5, 50–51	53.50	0.925
6H-6, 50–51	55.00	0.957
7H-1, 50–51	57.00	0.871
7H-2, 50–51	58.50	0.864
7H-4, 50–51	61.50	0.880
7H-6, 50–51	64.50	0.934
8H-1, 50–51	66.50	0.885
8H-2, 50–51	68.00	0.973
9H-1, 50–51	72.00	0.879
9H-3, 50–51	75.00	0.884
9H-5, 50–51	78.00	0.948
9H-7, 30–31	80.80	0.886
10H-2, 50–51	83.00	0.927
10H-4, 50–51	86.00	0.923
10H-6, 50–51	89.00	1.005
10H-7, 50–51	90.50	0.980
13X-1, 50–51	110.10	0.942
13X-2, 50–51	111.60	0.944
15X-1, 50–51	129.40	0.910
15X-2, 50–51	130.90	0.989
17X-1, 50–51	148.80	0.938
17X-2, 50–51	150.30	1.205
17X-3, 50–51	151.80	1.294
17X-4, 40–41	153.20	0.915
18X-2, 75–76	160.25	0.957
18X-4, 75–76	163.25	1.008
18X-6, 75–76	166.25	1.121
18X-7, 20–21	167.20	0.958
19X-2, 75–76	169.85	1.236
19X-4, 75–76	172.85	0.945
19X-6, 75–76	175.85	0.976
21X-1, 50–51	184.30	0.955
21X-3, 50–51	187.30	0.945
21X-4, 50–51	188.80	0.983
21X-6, 50–51	191.80	0.966
22X-1, 50–51	194.00	1.033
22X-3, 50–51	197.00	0.920
22X-4, 80–81	198.80	0.985
22X-5, 50–51	200.00	1.306
24X-1, 88–89	213.98	1.298
24X-2, 65–66	215.25	1.046
24X-3, 100–101	217.10	1.075
24X-4, 50–51	218.10	1.044
25X-1, 50–51	223.40	1.086
25X-3, 100–101	226.90	1.118
25X-4, 50–51	227.90	1.034
25X-6, 50–51	230.90	1.155

Table 15 (continued).

Core, seciton, interval (cm)	Depth (mbsf)	Thermal conductivity (W/m · K)
124-767B-		
26X-1, 50–51	233.10	1.029
26X-3, 50–51	236.10	1.085
26X-4, 45–46	237.55	1.073
26X-6, 50–51	240.60	1.017
27X-1, 75–76	242.95	1.021
27X-2, 75–76	244.45	1.029
27X-4, 75–76	247.45	1.067
27X-6, 20–21	249.90	1.063
28X-1, 75–76	252.65	0.905
28X-3, 75–76	255.65	0.993
28X-5, 75–76	258.65	1.078
28X-7, 20–21	261.10	1.055
29X-1, 60–61	262.00	0.955
29X-2, 60–61	263.50	0.978
29X-4, 60–61	266.50	1.095
29X-6, 40–41	269.30	1.083
30X-1, 75–76	271.75	1.092
30X-3, 75–76	274.75	1.051
30X-4, 75–76	276.25	1.081
30X-6, 40–41	278.90	1.020
31X-1, 75–76	281.45	0.909
31X-2, 75–76	282.95	0.999
31X-3, 16–17	283.86	1.185
32X-1, 75–76	291.15	1.074
32X-3, 75–76	294.15	1.072
32X-5, 75–76	297.15	1.263
32X-6, 75–76	298.65	1.133
33X-1, 75–76	300.85	1.053
33X-3, 75–76	303.85	1.063
33X-5, 75–76	306.85	1.188
33X-7, 20–21	309.30	1.015
34X-1, 75–76	310.55	0.752
34X-2, 75–76	312.05	0.989
34X-4, 75–76	315.15	1.048
34X-6, 75–76	318.05	0.902
35X-1, 75–76	320.15	1.005
35X-2, 75–76	321.65	1.138
35X-3, 75–76	323.15	1.031
35X-5, 75–76	326.15	1.006
36X-1, 75–76	329.85	0.968
36X-3, 75–76	332.85	1.062
36X-4, 75–76	334.35	1.074
36X-5, 50–51	335.60	1.024
37X-1, 75–76	339.55	0.701
37X-2, 75–76	341.05	0.926
37X-4, 75–76	344.05	1.074
37X-5, 75–76	345.55	1.037
38X-1, 75–76	349.25	1.420
38X-2, 55–56	350.55	1.092
38X-3, 60–61	352.10	1.066
39X-1, 81–82	358.91	1.109
39X-3, 93–94	362.03	1.154
39X-5, 107–108	365.17	1.118
39X-6, 81–82	366.41	1.062
40X-1, 75–76	368.55	1.153
40X-2, 75–76	370.05	0.989
40X-4, 94–95	373.24	1.094
40X-5, 75–76	374.55	1.136
41X-1, 50–51	378.00	1.293
41X-3, 50–51	381.00	1.050
41X-4, 50–51	382.50	1.080
41X-6, 50–51	385.50	1.073
42X-1, 50–51	387.60	1.102
42X-3, 50–51	390.60	1.161
42X-4, 50–51	392.10	1.102
42X-6, 67–68	395.27	1.004
44X-1, 50–51	407.00	1.078
44X-2, 50–51	408.50	1.108
44X-3, 50–51	410.00	1.251
44X-5, 80–81	413.30	1.138
45X-1, 50–51	416.70	1.137
45X-3, 75–76	419.95	1.137
45X-4, 50–51	421.20	1.131
45X-5, 36–37	422.56	1.033
46X-1, 75–76	426.55	1.141
46X-3, 75–76	429.55	1.552
46X-5, 75–76	432.55	1.228

Table 15 (continued).

Core, seciton, interval (cm)	Depth (mbsf)	Thermal conductivity (W/m · K)
124-767B-		
46X-7, 25-26	435.05	1.139
47X-1, 75-76	436.15	1.180
47X-2, 50-51	437.40	1.191
47X-3, 75-76	439.15	1.429
47X-4, 20-21	440.10	1.556
50X-1, 68-69	464.78	1.372
50X-3, 52-53	467.62	1.189
50X-5, 114-115	471.24	1.200
50X-6, 34-35	471.94	1.360
55X-1, 40-41	512.60	1.488
55X-3, 75-76	515.95	1.486
55X-4, 75-76	517.45	1.236
55X-6, 35-36	520.05	
56X-1, 75-76	521.85	1.286
56X-3, 75-76	524.85	1.054
56X-4, 75-76	526.35	1.275
56X-5, 40-41	527.50	1.229
57X-1, 75-76	531.55	1.202
57X-2, 75-76	533.05	1.525
57X-3, 75-76	534.55	1.347
57X-4, 45-46	535.75	1.626
58X-1, 75-76	541.25	1.535
58X-3, 75-76	544.25	1.700
58X-5, 75-76	547.25	1.267
58X-7, 20-21	549.70	1.608
59X-1, 75-76	550.95	1.443
59X-2, 75-76	552.45	1.190
59X-4, 75-76	555.45	1.222
59X-5, 75-76	556.95	1.449
62X-3, 69-70	582.79	1.535
62X-4, 85-86	584.45	1.514
62X-5, 54-55	585.64	1.562
62X-6, 89-90	587.49	1.591
64X-1, 75-76	599.25	1.681
64X-3, 75-76	602.25	1.396
64X-5, 75-76	605.25	1.325
64X-6, 55-56	606.55	1.720
66X-1, 75-76	618.55	1.368
66X-2, 84-85	620.14	1.130
69X-1, 75-76	647.05	1.310
69X-3, 75-76	650.05	1.342
69X-5, 75-76	653.05	1.297
69X-6, 75-76	654.55	1.286
71X-1, 63-64	666.23	1.288
71X-3, 75-76	669.35	1.347
71X-5, 97-98	672.57	1.334
71X-6, 56-57	673.66	1.322
74X-2, 52-53	696.62	1.344
74X-4, 73-74	699.83	1.535
74X-6, 103-104	703.13	1.519
74X-CC, 18-19	704.17	1.227
76X-1, 70-71	714.20	1.352
76X-3, 62-63	717.12	1.341
77X-2, 50-51	725.20	1.487
124-767C-		
1R-2, 82-83	682.32	1.399
1R-3, 50-51	683.50	1.229
5R-1, 54-55	717.04	1.270
5R-2, 93-94	718.93	1.563
5R-3, 103-104	720.53	1.530
6R-3, 45-46	729.65	1.330
8R-1, 118-119	744.48	1.349
8R-2, 52-53	745.32	1.172
8R-3, 21-22	746.51	1.478
12R-1, 23-24	782.33	1.137
12R-2, 76-77	784.36	1.217
12R-3, 15-16	785.26	1.406

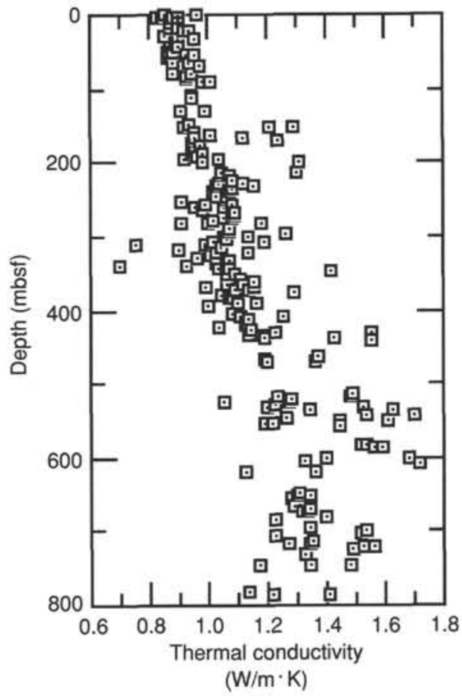

Figure 46. Thermal conductivity vs. depth, Site 767.

Table 16. Shear strength data, Site 767.

Core, section, interval (cm)	Depth (mbsf)	Shear strength Peak	Shear strength Remolded	Sensitivity
124-767B-				
2H-1, 60-61	9.60	9.4	4.2	2.24
2H-1, 118-119	10.18	13.1	5.0	2.62
2H-6, 57-58	17.07	14.5	6.4	2.27
3H-2, 36-37	20.36	20.2	8.5	2.38
3H-2, 45-46	20.45	21.9	11.2	1.96
3H-6, 114-115	27.14	18.6	7.7	2.42
3H-6, 127-128	27.27	19.9	7.7	2.58
4H-1, 77-78	28.77	24.3	9.9	2.45
4H-1, 89-90	28.89	25.2	11.0	2.29
4H-6, 18-19	35.68	32.9	15.3	2.15
4H-6, 107-108	36.57	41.6	12.0	3.47
5H-2, 40-41	39.40	37.2	13.1	2.84
5H-2, 50-51	39.50	35.1	13.1	2.68
5H-6, 41-42	45.41	46.0	7.7	5.97
5H-6, 60-61	45.60	50.4	11.0	4.58
10H-2, 114-115	83.64	50.4	19.7	2.56
10H-2, 135-136	83.85	50.4	14.2	3.55
10H-7, 49-50	90.49	70.1	16.4	4.27
15X-2, 91-92	131.31	38.3	15.3	2.50
15X-2, 132-133	131.72	52.6	23.0	2.29
18X-2, 41-42	159.91	51.5	17.5	2.94
18X-2, 81-82	160.31	37.2	8.8	4.23
18X-5, 112-113	165.12	66.8	30.7	2.18
19X-2, 52-53	169.62	55.9	18.6	3.01
19X-2, 120-121	170.30	50.4	13.1	3.85
20X-1, 84-85	178.14	50.4	15.3	3.29
23X-2, 40-41	205.20	46.0	19.7	2.34
23X-3, 44-45	206.74	24.1	13.1	1.84
24X-1, 32-33	213.42	18.6	6.6	2.82
28X-5, 40-41	258.30	49.3	9.9	4.98

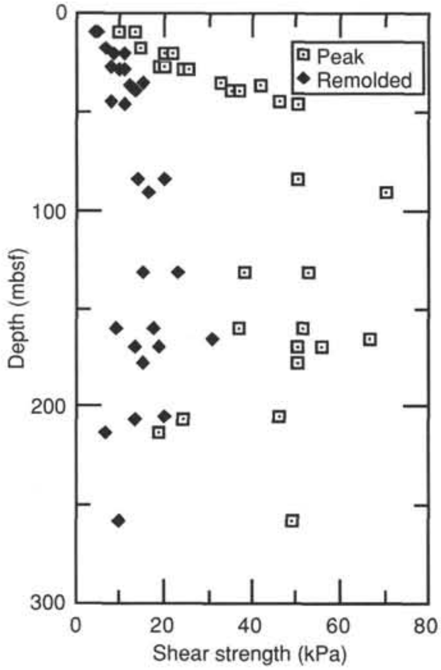

Figure 47. Peak and remolded shear strength vs. depth, Hole 767B.

void ratio values, all of which decrease with depth. Grain densities remain nearly constant over the cored depth. From the limited velocity data obtained, an increase in velocity with depth was also observed. Peak shear strength displayed a strong increase with depth over the interval from 0 to 50 mbsf.

A boundary between different physical properties was noted at a depth of about 410 mbsf, corresponding to the boundary between Units II and III. An extremely abrupt change in physical properties occurs at the contact with the basalt oceanic crust.

BASEMENT LITHOLOGY

A total of 42 cm of basaltic rock, composed of four pieces and some small fragments, were recovered in the core catcher of Core 124-767C-12R at 791.28 mbsf. Red clays overlie the basalt, but no contact relationships were recovered. The igneous rocks represent the acoustic "basement" of Site 767.

The principal characteristics and depth of recovery of the igneous rocks, which occur between 786.68 and 786.90 mbsf in the core catcher of Core 124-767C-12R, are shown in the core barrel sheets, which appear at the end of the book. The four larger pieces and smaller fragments make up a total thickness of 30 cm or approximately 79% of the core catcher. The similarities in mineralogy and textures, the distribution of the vesicles, the increase in degree of crystallinity and grain size, and the decrease in the amount of alteration between Samples 124-767C-12R-CC (Piece 1) and 124-767C-12R-CC (Piece 4), as described in this chapter, suggest that they are all derived from a single lava flow. The quench texture, which is well displayed in these samples, has also been recorded in Mid-Atlantic Ridge basalts (Augustithis, 1979, figs. 614–616). The mottled color distribution shown by Sample 124-767C-12R-CC (Pieces 1–3) reflects the variations in the rock texture and is accentuated by weathering.

Four thin sections, one from each piece of the igneous rock recovered from Site 767, were examined under the microscope. The results of the mineral identifications and petrographic descriptions are summarized in Table 17.

The pieces are all angular, are up to 10 cm in maximum dimension, and occur below the red pelagic clay (Unit IV; see "Lithostratigraphy" section, this chapter), which has a maximum age of late middle Eocene. They are light yellow-brown and orange-brown to gray in color.

There are no phenocrysts present in the samples, and the grain size and degree of crystallinity varies within and between the different pieces. In Sample 124-767C-12R-CC (Piece 1), approximately 5% of the rock is made up of radiate and parallel aggregates of thinly tabular olivine (<1.0 mm), which has been pseudomorphed by a strongly oxidized replacement mineral, together with intergrowths of skeletal plagioclase laths (<0.5 mm) and skeletal microliths of clinopyroxene (<0.1 mm). The remainder of the rock is made up of dense unresolvable aggregates, probably of plagioclase and mafic minerals, together with irregular areas of smectite and iddingsite replacing the rock mesostasis and former olivine crystals.

Similar textures and minerals occur in Sample 124-767C-12R-CC (Pieces 2 and 3), but the proportion of resolvable minerals increases systematically to a maximum of 30%, together with the grain size. Sample 124-767C-12R-CC (Piece 4) is more than 90% crystalline, composed mainly of aggregates of skeletal plagioclase laths (labradorite) up to 2 mm long intergrown with skeletal and prismatic olivines (<2 mm) and skeletal clinopyroxenes <0.5 mm long, forming a generally fasciculate texture. These plagioclase and pyroxene aggregates commonly radiate from euhedral olivine crystals that have been completely pseudomorphed by a pale green clay mineral (smectite or serpentine); the skeletal olivines are replaced by a red-brown amorphous mineral.

Very fine-grained (<0.03 mm) iron oxide is distributed uniformly through all the pieces of basalt. The fasciculate textures shown by these rocks result from rapid quenching of a superheated basaltic melt (Augustithis, 1979, pp. 65–67; Walker et al., 1979, fig. 5). Vesicles are distributed uniformly in each sample and vary from a minimum of 2–3% in Pieces 1 and 2, to a maximum of 10% in Piece 3, and Piece 4 contains approximately 5%. They are filled with green clay (smectite), carbonate, iron ore, and zeolites, which occur in layers in some of the

Table 17. Petrographic data for igneous rocks, Site 767.

			Groundmass							
Core, section, interval (cm)	Piece	Texture	[a]Ol (%)	[a]Pl (%)	[a]Cpx (%)	Interg. (%)	Amg. (%)	Total (%)	Alt. (%)	Occurrence
124-767C-										
12R-CC, 3–11	1	Variolitic	5	10	5	77	3	100	22	Unknown
12R-CC, 18–20	2	Arborescent/ variolitic	3	25	10	60	2	100	12	Unknown
12R-CC, 26–28	3A	Arborescent	10	10	5	65	10	100	20	Unknown
12R-CC, 36–33	4	Intersertal	5	55	30	5	5	100	10	Unknown

Note: Ol = olivine, Pl = plagioclase, Cpx = clinopyroxene, Interg. = unresolvable crystals in the groundmass, Amg. = amygdules, and Alt. = secondary minerals.
[a] Resolvable crystals in the groundmass.

vesicles. Thin (<0.5 mm) irregular, discontinuous veins of green clay, carbonate, and chalcedony occur, together with patches of green clay replacing the rock mesostasis.

The small pieces of basalt recovered in the core catcher at the bottom of Hole 767C are slightly to moderately altered. The secondary minerals that are present as veins, in vesicles, and replacing the mesostasis and primary minerals include green clay (smectite), calcite, zeolites, iddingsite, and hematite. Pieces 1-4 of Sample 124-767C-12R-CC (Pieces 1-4) are progressively less altered.

Vesicle and Cavity Fillings

All of the igneous rocks contain sparse (<10%), small (<2 mm), generally spherical vesicles that are filled with a variety of secondary minerals. The largest vesicles are irregular in form and may be only partly filled. The vesicles may be filled with brown or green clays or carbonate. Some contain layers of these minerals, commonly with clay outer layers and carbonate in the core. The irregular unfilled vesicles contain layers of brown clays and have fibrous zeolites lining the cavity. Iddingsite and a pale green clay replace primary olivine crystals. Much of the rock is stained by limonite. The vesicles, veins, and other occurrences of alteration minerals are all too small to allow them to be separated and identified by X-ray diffraction (XRD). The general nature of the alteration is typical of that occurring at low temperatures between basalts and seawater.

BASEMENT GEOCHEMISTRY

Two samples (124-767C-12R-CC, Pieces 3 and 4) recovered from the bottom of Hole 767C were analyzed, in duplicate, for major and trace elements by X-ray fluorescence (XRF) on board ship (see "Explanatory Notes" chapter, this volume, for analytical details and Table 18 for the results of the analyses). Sample 124-767C-12R-CC (Piece 3) is a slightly altered olivine basalt containing prominent quenched plates of olivine. Sample 124-767C-12R-CC (Piece 4) is the least-altered basalt sample recovered from Hole 767C; it is a fine-grained olivine basalt in which olivine occurs as quenched plates and prismatic crystals at the center of radiating aggregates of plagioclase intergrown with skeletal pyroxene.

The duplicate analyses of each piece are very similar, but there are differences between the samples. In the slightly altered sample, the SiO_2 and CaO contents are lower and the Fe_2O_3 and the total alkalis are higher than they are in the freshest sample (Table 18). The two samples are believed to come from one rapidly quenched unit in which little fractionation could have taken place, and the differences are interpreted as resulting from post-crystallization alteration.

Sample 124-767C-12R-CC (Piece 3) contains approximately 2% normative olivine, and Sample 124-767C-12R-CC (Piece 4) contains approximately 2% normative quartz. They are both tholeiitic basalts, according to the criteria of Macdonald and Katsura (1964). The major element and trace compositions of these rocks (Table 18) are generally similar to the average composition of oceanic tholeiitic basalt (Engel et al., 1965, p. 721, table 2) and to fresh basalts from the Carlsberg Ridge (Cann, 1969, p. 4, table 2).

The incompatible trace element content of Sample 124-767C-12R-CC (Piece 3; normalized ocean-floor tholeiite) has been included with the other samples from the Celebes basement recovered in Site 770 (see "Site 770" chapter, Fig. 17, this volume). The distribution shows a pattern similar to that of N-MORB, but unlike low-K (arc) tholeiites or back-arc tholeiites, both of which have higher concentrations of the lighter incompatible elements (Holm, 1985).

Table 18. Major element composition, normative mineralogy, and trace element contents of the igneous rocks, Site 767, compared with selected ocean-floor basalts.

Core, section, interval (cm)	12R-CC 26-28	12R-CC 36-39	OFB	CR
Major elements:				
SiO_2	48.03	49.08	49.34	49.13
TiO_2	1.59	1.59	1.49	1.61
Al_2O_3	16.87	16.87	17.04	16.31
ΣFe_2O_3	11.98	9.90	9.57	10.53
MnO	0.29	0.31	0.17	0.20
MgO	4.99	5.35	7.19	7.82
CaO	12.07	12.84	11.72	10.84
Na_2O	2.51	2.28	2.73	2.92
K_2O	0.29	0.16	0.16	0.21
P_2O_5	0.12	0.28	0.16	0.07
Total	[a]98.74	98.66		
LOI	1.55	2.31		
Q	0	1.89		
Or	1.78	0.98		
Ab	23.35	21.15		
An	35.14	36.24		
Di	20.40	21.08		
My	12.30	13.73		
Ol	2.07	0.00		
Mt	2.17	1.78		
Il	2.30	2.28		
Ap	0.40	0.90		
$\frac{An}{Ab + An}$ %	60.08	63.15		
Trace elements:				
Rb	5	3		
Ba	12	13		
K	2374	1272		
Nb	2	2		
Ce	8	8		
Sr	124	123		
P	524	742		
Zr	91	92		
Ti	10012	10431		
Y	33	36		
V	386	344		
Ni	172	171		
Cr	344	353		
Zn	107	201		
Cu	71	28		

Note: Major element composition is given in oxide wt%, normative mineralogy in wt%, and trace element contents in ppm element. OFB = average oceanic tholeiitic basalts (Engel et al., 1965), CR = basalts from the Carlsberg Ridge (Cann, 1969).

[a] Totals systematically below 100% have been obtained for onboard analyses and are interpreted as result of hydration of the sample between ignition and weight.

Concluding Remarks

The variations in grain size and degree of crystallinity, the presence of quenched textures, and the distribution of vesicles and alteration suggest that the four pieces of basalt are all derived from a single lava flow. The major and trace element chemistry of the two samples analyzed suggests that the rocks may be ocean-floor tholeiitic basalts.

DOWNHOLE MEASUREMENTS

In this section we discuss first the shipboard processing of logs and evaluations of log quality and then the geological interpretation of the downhole logs from the standpoint of lithologic units, types of source region, and heat flow. Other sections summarize logging operations at Site 767 (see "Operations" section, this chapter) and the types of tools run (see "Explanatory Notes" chapter, this volume).

Log Quality and Processing

All logging tools worked properly, and log quality was generally quite good. Two exceptions were the caliper and aluminum logs, both discussed subsequently. The quality of upcoming logs was consistently higher than that of downgoing logs because of slower logging speeds; only upcoming logs are discussed subsequently. Logs from several tools were reprocessed: sonic, natural gamma, and gamma spectroscopy. In addition, logs were merged and depth shifted.

Sonic logging at Site 767 used a long-spaced sonic tool. This tool yields traveltimes over source-receiver distances of 2.4, 3.0, and 3.7 m, from which two formation traveltimes (short and long spaced) are calculated in real time. These raw sonic logs exhibit very close agreement throughout almost the entire logged interval (Fig. 48), and the logs are thought to be generally reliable. However, several spikes are evident on both logs as a result of cycle skipping. Consequently, the original source-receiver traveltimes were reprocessed with an algorithm designed to reject cycle skips (Shipboard Scientific Party, 1987), yielding a more reliable sonic log (Fig. 48). This algorithm was expanded to include calculation of a caliper log (see "Explanatory Notes" chapter, this volume). Although the resulting caliper log (Fig. 48) is sensitive to assumed fluid velocity, it is probably superior to the hole diameter measured by the caliper tool (Fig. 48). However, neither type of caliper log is considered to be very accurate at this site.

The natural gamma tool provides useful data in the open hole and through the drill pipe. However, pipe attenuation causes a major reduction in the number of gamma rays received by the tool. The different attenuation effects of the bottom-hole assembly, drill pipe, and drill collars are readily visible on the raw logs (Fig. 49). To correct for this attenuation, a simple gain model was constructed on the basis of the known changes of pipe thickness and a scaling factor derived from the difference in natural gamma signals immediately above and below the base of the bottom-hole assembly. Figure 49 illustrates this correction for the total gamma-ray (TGR) response. Figure 50 shows pipe-corrected logs from the natural gamma tool run as part of the seismic stratigraphic combination.

The empirically estimated maximum gains used were 4.5 for SGR, 3 for CGR (total gamma ray minus uranium contribution), 7 for potassium, 1.6 for thorium, and 2 for uranium. These gains are generally similar but not identical to those previously determined in ODP holes (Shipboard Scientific Party, 1988a, 1988b). It should be emphasized that there is no theoretical basis for the use of different gains for different elements in the same hole, or for the same element in different holes. Thus, these through-pipe corrections must be considered only approximate. Nevertheless, with adequate signal strengths, such corrections have been found to yield good replicability for duplicate logging runs obtained with pipe at different locations (Prell, Niitsuma, et al., 1988b).

An alternative processing sequence was used for the natural gamma logs shown following the barrel sheets at the back of the book. Reprocessing on an Elite 1000 work station slightly changed computed values for total gamma ray, K, Th, and U. The final plots are a merge of the best portions of NGT logs from the seismic stratigraphic and geochemical runs: 4916–4995 m below rig floor (mbrf) is from the geochemical run, with the pipe correction determined from a simple offset; 4995–5025 mbrf is from the seismic stratigraphic run, with approximate depth shifting to a geochemical run standard; and 5025–5562 mbrf is from the geochemical run.

Gamma spectrometry logs obtained in ODP exhibit some inversion interference of the very strong chlorine count rate with the other, weaker elemental count rates (see figures after the barrel sheets at the back of the book). This interference is manifest as a strong but spurious inverse correlation between chlorine and calcium, and weaker correlations with other elements. The interference affects ratios such as the iron indicator ratio and the lithology indicator ratio (see figures after the barrel sheets at the back of the book) that would otherwise be independent of chlorine counts.

The interference is unavoidable in ODP holes because the minimum pipe diameter is too small to permit use of the boron sleeve used to suppress chlorine counts in industry logging. Most of this interference effect was removed from the calcium, iron, and sulfur count-rate logs by adding the product of chlorine counts and slope of the regression of each element on chlorine.

For the regression, we used a short interval (509–631 mbsf) rather than the entire logged interval to avoid the possibility that real long-term trends would dominate the regression determination of interference effects. No such correlation was applied to silicon or hydrogen because their correlations with chlorine are weak. The final step in gamma-spectroscopy reprocessing was to isolate elements exclusively in the formation (Ca, Si, Fe, S) from those primarily in the borehole and pores (Cl and H) by expressing Ca, Si, Fe, and S counts as a percentage of the total counts Ca + Si + Fe + S.

Depth shifting of two types was employed. First, both seismic stratigraphic runs and the geochemical run were separately depth shifted by constant amounts, so that the readily identifiable "mudline" increases in gamma-ray signal corresponded to the seafloor depth. For the seismic stratigraphic combination, this depth shift was confirmed by checking the depths at which all logs responded to the base of pipe. This depth shift is a correction for cable stretch to a standard based on pipe depths. It should be noted that pipe depths are also subject to error, but the goal of the correction is consistency of core and log depths.

Following this first depth correction, the two seismic stratigraphic runs were merged as follows. For 0–81.5 mbsf, we used pipe-corrected logs from run #2; through-pipe logs obtained during run #1 had a lower signal-to-noise ratio because of higher logging speed. For 81.5–112.9 mbsf, we used open-hole logs from run #1 in preference to through-pipe logs of run #2. For 112.9–272.9 mbsf, both runs obtained open-hole logs and the two were averaged. For 272.9–670.1 mbsf, only run #2 obtained logs from all tools.

A second phase of depth shifting, to deal with depth counter errors within a logging run, is not normally necessary but was required for Hole 767B. Particularly below about 400 mbsf, repeated tool sticking was encountered, caused mainly by changes in the hole diameter in this deviated hole and also perhaps by sticky clays. When the upward motion of the tool string is slowed or sometimes even temporarily stopped, the winch continues to reel in cable until cable tension increases enough to pull the tool suddenly free. As the depth counter is adjacent to the winch rather than to the tool, depth errors arise. A completely stopped tool can be detected by short intervals of constant log response on several logs, with depth offsets between these intervals corresponding to the distance between the logging tools on the tool string.

At Hole 767B, the tools rarely stopped completely; an example is the short interval of artificially constant velocity at 546–549 mbsf on Figure 48. Nevertheless, more subtle sticking problems are pervasive, as evidenced by three factors: (1) gradual increases in cable tension followed by sharp drops; (2) variable

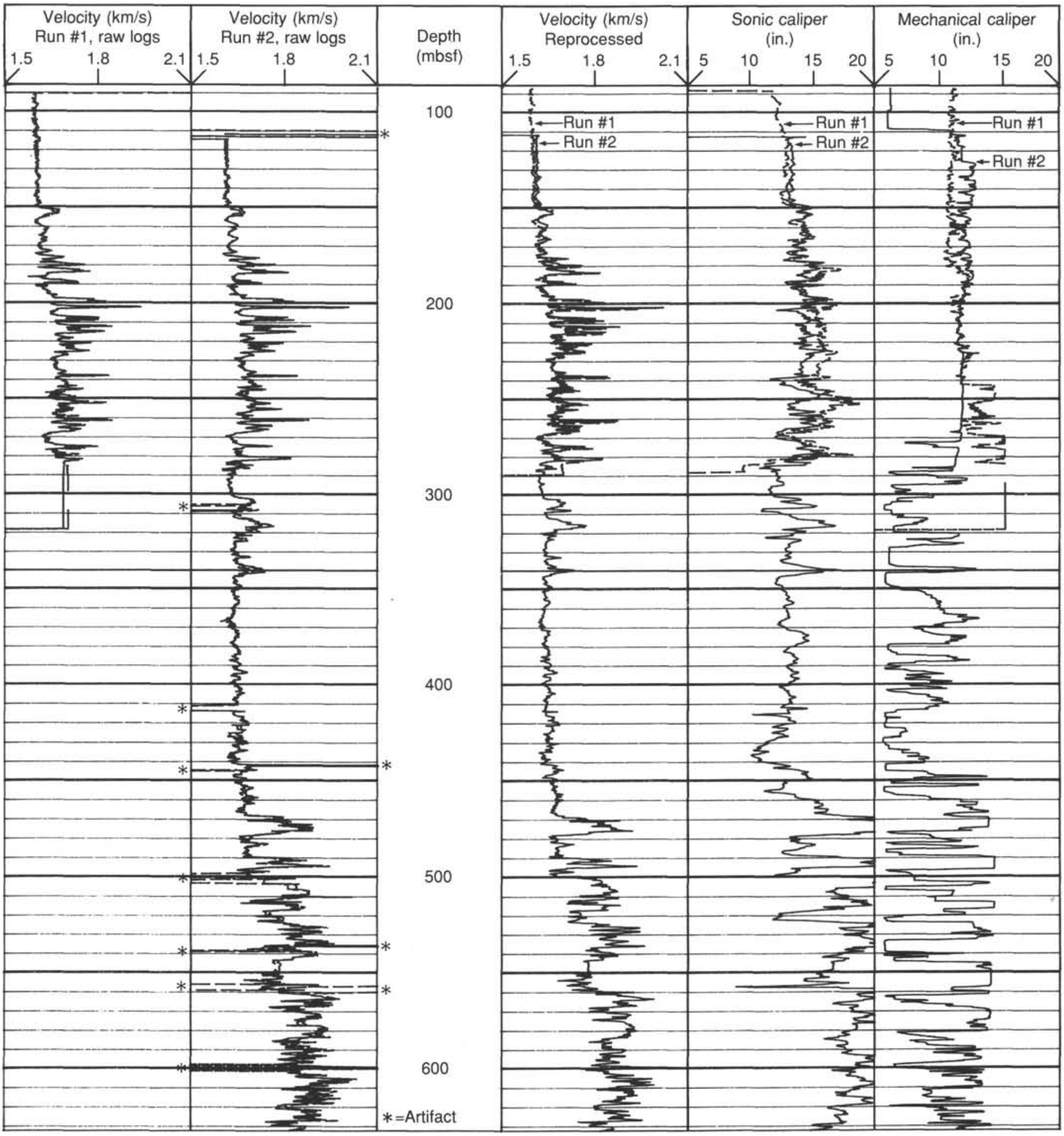

Figure 48. Comparison of raw sonic logs (left two tracks) with reprocessed sonic logs (center track), and of caliper logs calculated from sonic reprocessing (right track) with those measured by a mechanical caliper tool (far right track). Note that sonic reprocessing has successfully removed cycle skips (asterisks) and determined a caliper with better replicability than the mechanical caliper. Raw logs at left show both short-spaced (solid lines) and long-spaced (dashed lines) logs, converted from μs/ft to km/s.

depth shifts between correlatable parts of natural gamma logs run on both seismic stratigraphic and geochemical combinations; and (3) aluminum log excursions to very low values overlying spikes to very large values. The aluminum log is the only log that records erroneous values caused by tool sticking. This tool uses a neutron source and adjacent gamma-ray detector to measure induced gamma emissions, and the delay between irradiation and measurement must be accurately known. Most of the aluminum log below about 300 mbsf is consequently unreliable.

We used the natural gamma logs recorded on both tool strings to variably depth shift the seismic stratigraphic logs to a geo-

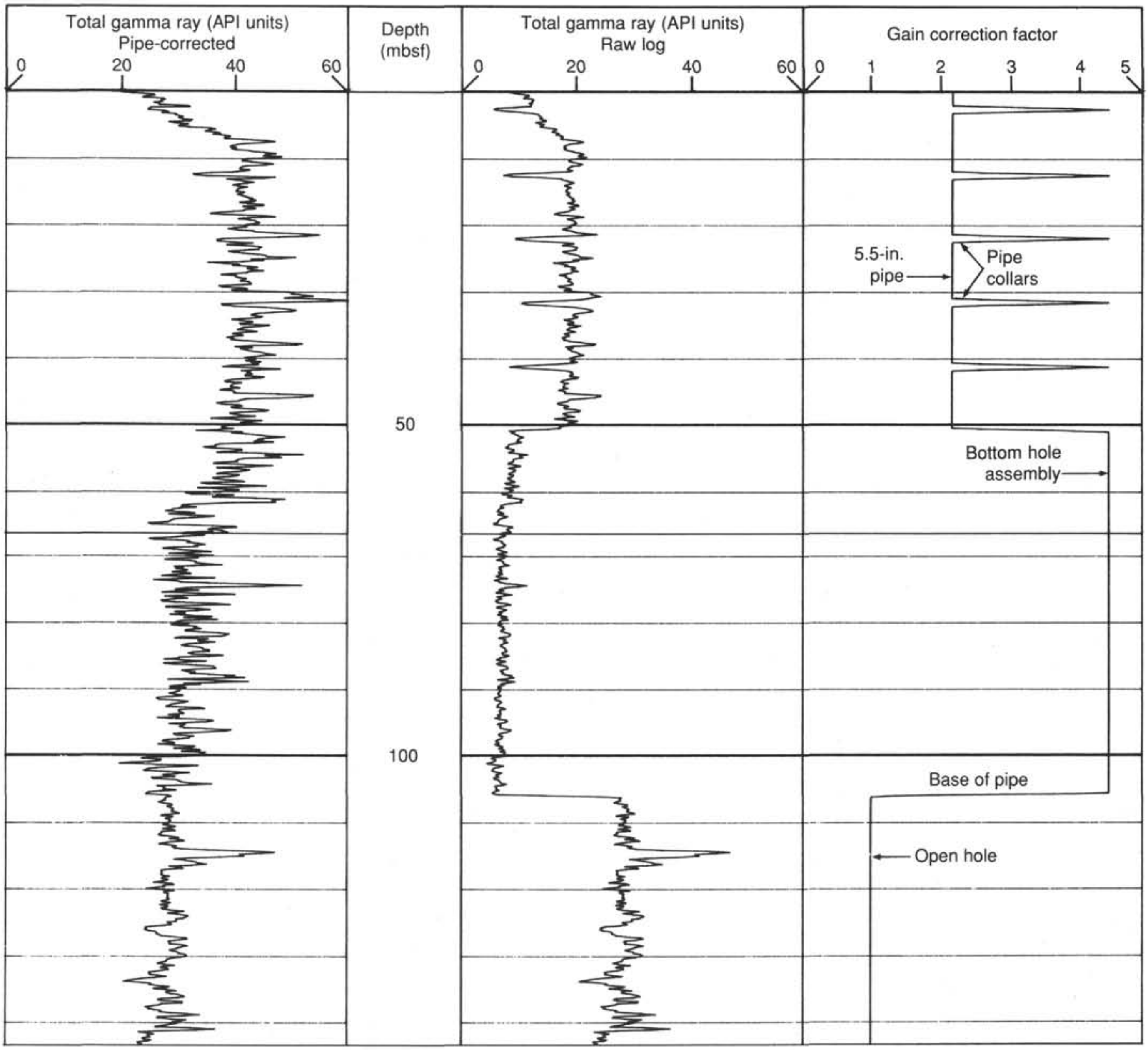

Figure 49. Example of the use of a gain correction factor to remove the attenuation effects on the natural gamma-ray log of variations in pipe thickness.

chemical run standard. This correction does not imply that the geochemical run is free of tool sticking; tool sticking was present but less dramatic on the geochemical run. Such a correction is necessary for a reliable comparison of logs between the two runs. The first step was identification of 30 initial ties, the most reliably identifiable corresponding points on the two gamma-ray logs. Next, these ties were used as the starting point for a nonlinear mapping algorithm, which iteratively determines the local stretches and compressions of one signal (gamma ray from the seismic stratigraphic run) with respect to a reference signal (gamma ray from the geochemical run) for maximum coherence between the two (Martinson et al., 1982). The resulting optimum depth corrections (Fig. 51), ranging from a 3.6-m upward shift to a 3.5-m downward shift, were applied to all merged logs from the seismic stratigraphic combination.

The neutron log obtained by the geochemical tool string uses a much stronger source than conventional neutron tools as part of aluminum measurement. Neutron porosities have not been calibrated for this stronger source, but they appear to be too high by about a factor of 3 or 4. Thus, the neutron log shown in Figures 52 and 53 should be used only for relative porosity variations. In addition, the neutron log obtained through pipe for the interval from 0 to 79 mbsf exhibits spikes every 9.4 m because of pipe collars, and the neutron log obtained through the bottom-hole assembly (79–109 mbsf) exhibits a large pipe-suppression effect (Fig. 54).

The neutron log for these three intervals (0–79, 79–109, and 109–665 mbsf) was rescaled with different gains for each depth interval in order to match core measurements (Fig. 54). A pseudodensity log (Fig. 54) was calculated from this rescaled neu-

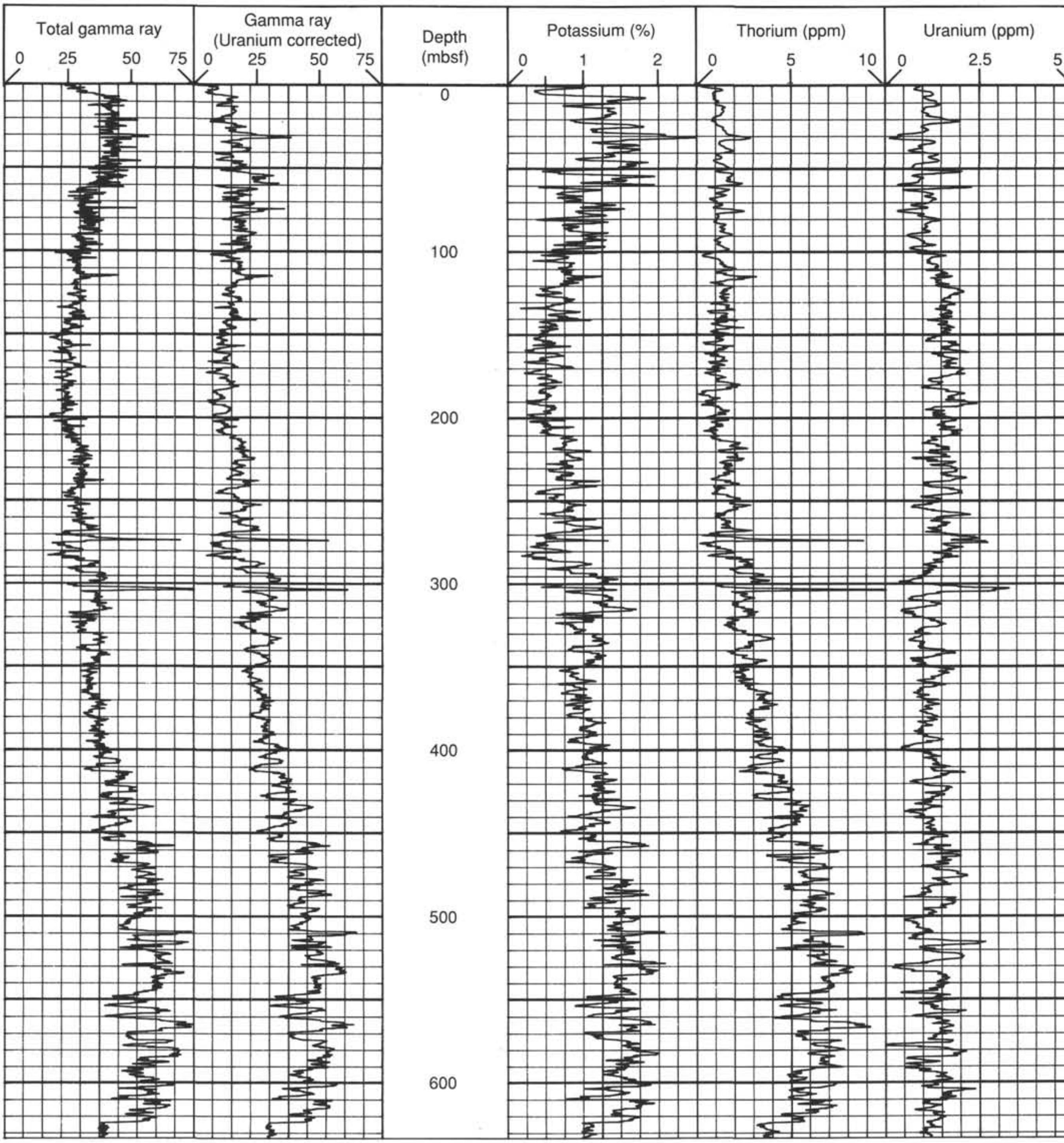

Figure 50. Natural gamma-ray logs from the seismic stratigraphic tool string, after correction for pipe attenuation effects but before depth shifting to a geochemical-string standard.

tron log using laboratory measurements of grain density (see "Physical Properties" section, this chapter). Average grain densities used were 2.57 g/cm^3 for 0–110 mbsf, 2.61 g/cm^3 for 110–300 mbsf, 2.56 g/cm^3 for 300–406 mbsf, 2.72 g/cm^3 for 406–484 mbsf, 2.69 g/cm^3 for 484–574 mbsf, and 2.72 g/cm^3 for 574–665 mbsf. No corrections were made for a bound-water contribution to the neutron log, stand-off effects on the neutron log, or effect of rebound (expansion) of core on laboratory porosity measurements.

The three logs are useful, but they should be used with caution. The resistivity log exhibits a suspicious blocky character in its bottom half, as well as a lower correlation with sonic velocity than is normally observed. The reason for this behavior is not known, and downhole calibration tests were satisfactory. The

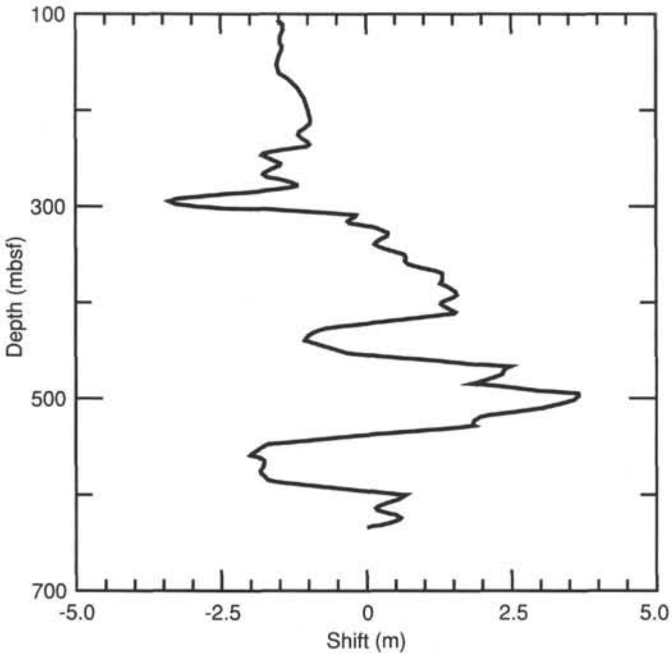

Figure 51. Depth shifts calculated to adjust logs from the seismic stratigraphic tool string to a geochemical-string standard. Negative shifts are upward.

gamma spectroscopy elements Ca, Si, Fe, and S are expressed as percentages of the total counts from these four elements, not as true percentages by weight or volume. Because variations in Si and Ca are much higher than those of Fe and S, an inverse correlation between normalized Si and Ca is nearly always present, and ambiguity exists about which of these two elements is changing most at any depth.

Lithologic Units

Unit I (0–56.8 mbsf) consists of heterogeneous volcanogenic clayey silt, with very thin ash layers and rare interbeds of calcareous clayey silt (see "Lithostratigraphy" section, this chapter). This unit was logged through pipe by the geochemical logging tools; of these, only logs from the natural gamma and neutron tools have been pipe-corrected. The unit appears to be characterized by quite high and variable potassium content (Fig. 50), in comparison to underlying Unit II. Given the K and total gamma ray (TGR) response alone, the base of Unit I would be placed at about 60 mbsf. Although through-pipe logs should be interpreted with caution because of the low signal-to-noise ratio, we tentatively attribute the high K contents primarily to potassium-rich clays and ash.

A substantial illite (K = 3.5–8.3%) component is suggested by the K contents of 1%–2%, significantly higher than the 0%–0.6% K contents of other clay minerals (Serra, 1986). The consistently low Th/K ratio of about 1×10^{-4} is also much more consistent with illite than with other clay minerals. The XRD measurements indicate that illite comprises about 15%–20% of the clay-mineral fraction of Unit I (see "Lithostratigraphy" section, this chapter). Thus, a substantial portion of the potassium must be in the silt-size ashes.

Subunit IIA (56.8–109.6 mbsf) is primarily volcanogenic clayey silt, with rare interbeds of volcanic ash and a downhole increase in occurrence of rare interbeds of carbonate silt (see "Lithostratigraphy" section, this chapter). Log responses suggest that this subunit is transitional in K and Th between Unit I and Subunit IIB. Short-period (1–2 m) and long-period (about 20 m) variations are evident in the potassium log (Fig. 50).

Subunit IIB (109.6–300.1 mbsf) is similar to Subunit IIA, except that volcanic ash layers are absent and carbonate interbeds are more abundant (see "Lithostratigraphy" section, this chapter). On the basis of the log responses, the top of this subunit is a gradual transition to Subunit IIA rather than a sharp change. The base of this subunit is a <2-m-thick clay interbed at 303 mbsf (Fig. 50). This clay bed differs in clay mineralogy from most of Unit II. It is characterized by very high Th and U and only moderate K, suggestive of chlorite and/or montmorillonite.

The carbonate layers of Subunit IIB are much higher in velocity and lower in porosity than the more clay-rich dominant lithology (see "Physical Properties" section, this chapter). Their maximum abundance occurs in the interval from 148 to 213 mbsf (see "Lithostratigraphy" section, this chapter). The logs clearly show the distinctive physical properties and abundance variations of the carbonate layers. Logs sensitive to porosity variations (velocity, resistivity, and neutron porosity) exhibit over 24 spikes to high velocity, high resistivity, and low porosity in the interval from 152 to 285 mbsf (Fig. 52), in contrast to bracketing intervals. These spikes are associated with relative highs in calcium, as a result of higher calcium carbonate, and lows in potassium and aluminum, as a result of lower clay and ash (Fig. 53). Above 175 mbsf, the velocity log is least sensitive to these variations, because the sensitivity of velocity to porosity change is much lower at higher porosities (Raymer et al., 1980).

Two short intervals of Subunit IIB depart significantly in their log responses from the general pattern of carbonate or clay dominance. The interval from 183 to 196 mbsf exhibits typical log responses for the carbonate-rich interbed, but the remainder of this interval is very low in aluminum and high in neutron porosity, for unknown reasons. The bottom 19 m of Subunit IIB (282–301 mbsf) is unusually low in velocity yet also low in neutron porosity (Fig. 52). Potassium, thorium, silica, and possibly iron exhibit gradual downhole increases through this lower interval, to the higher average values of Subunit IIC (Figs. 50 and 55). In contrast, uranium and calcium smoothly decrease to a lower Subunit IIC average.

These changes may represent a transition from the dominantly clayey silts of Subunit IIB to the silty clays that define the top of Subunit IIC. Clay minerals cause lower velocity and higher neutron porosity than silts; apparently, the clay minerals are also geochemically distinct from the ashes that compose the silts, in spite of the fact that the clay minerals are partly the product of *in-situ* alteration of ashes. A similar but more subtle downhole compositional change to greater ash content may be present at 212 mbsf (Figs. 50, 52, and 55).

Subunit IIC (300.1–406.5 mbsf) is predominantly silty claystone. The volcanic silt component is less common than in Subunit IIB, but discrete tuff beds are more common. Carbonate turbidites decrease in abundance downward through the unit (see "Lithostratigraphy" section, this chapter). Carbonate beds may be present at 301–306, 309, 314–320, and 340–342 mbsf, given the velocity and resistivity highs (Fig. 52); however, the calcium response to these changes is inconsistent (Fig. 55).

Several sharp changes in log responses occur at 350 mbsf, in the middle of Subunit IIIC. Resistivity increases, and neutron porosity, potassium, and possibly thorium decrease. Either calcium decreases or silicon increases; it is not possible to distinguish which because calcium and silicon counts are expressed as a percentage of total (Ca + Si + Fe + S) counts. This sharp change may reflect a significant drop in clay mineral percentage.

Subunit IIIA (406.5–484.4 mbsf) is dominantly thick-bedded claystone and silty claystone, with rare carbonate interbeds. The claystones are dominantly hemipelagic in the upper part of the subunit and turbidites with graded transitions to silty claystone

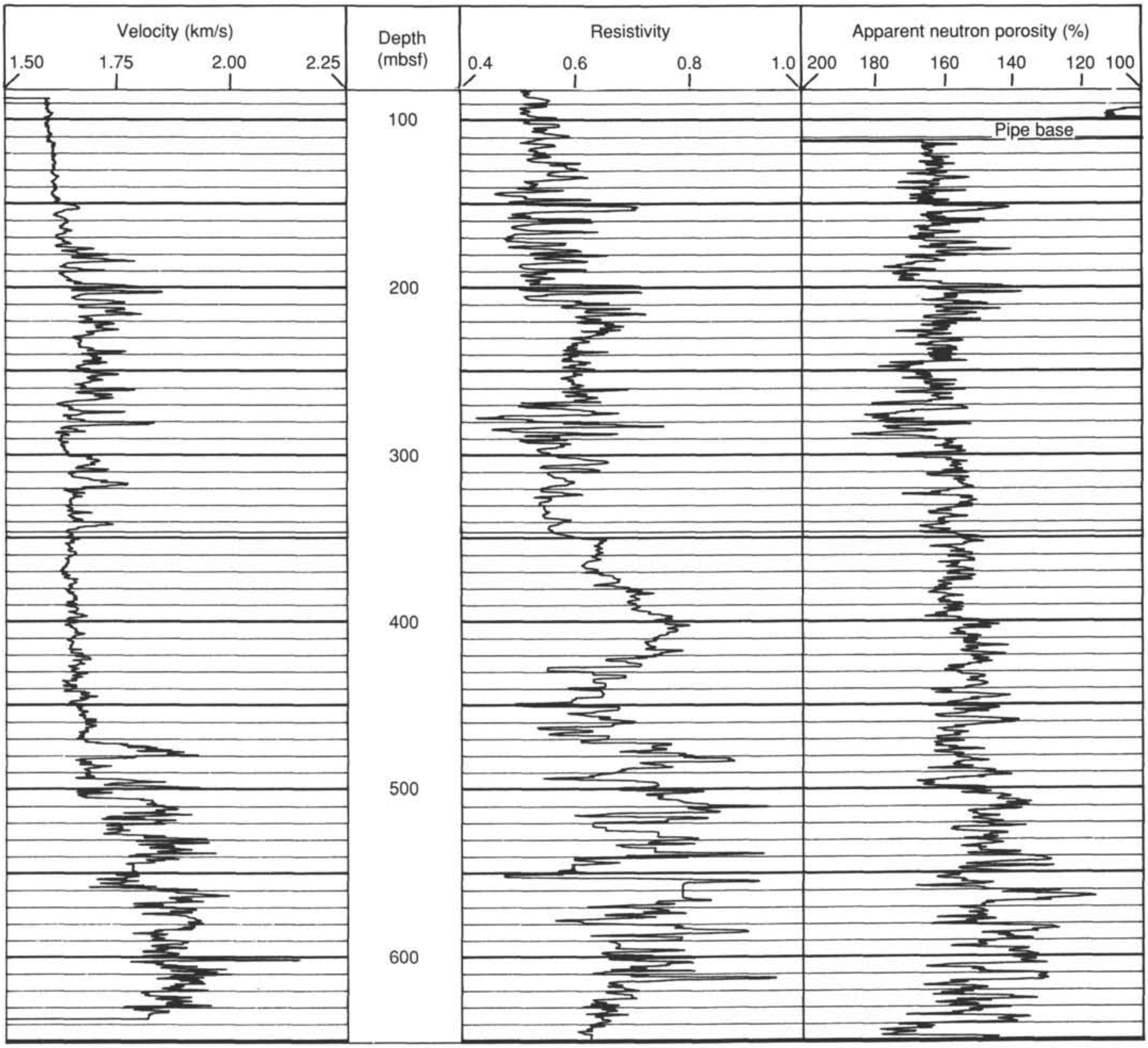

Figure 52. Logs of velocity, resistivity, and apparent neutron porosity. See text for a discussion of the high, uncalibrated nature of neutron porosity measurements.

in the lower part (see "Lithostratigraphy" section, this chapter). On the basis of the log responses and the velocity log in particular (Fig. 52), the base of this subunit would be placed at 472 mbsf, the top of the first occurrence of the high-velocity sands with continental provenance that characterize Subunit IIIB.

Subunit IIIA is significantly lower in porosity than overlying units, as indicated by the neutron log and core measurements (Fig. 54). From the standpoint of potassium and thorium abundances, Subunit IIIA continues the trend established in Subunit IIC of gradual downhole enrichment (Fig. 50), implying a transition toward more potassium-rich clay minerals. This observation is broadly consistent with XRD measurements, which indicate a significant rise in illite in this interval. However, a detailed comparison of illite abundance measurements with the log is limited by the high variability of both at scales of less than 20 m.

Subunit IIIB (484.4–573.7 mbsf) contains beds of quartz sandstone and siltstone, in addition to graded silty claystone/claystone beds similar to lower Subunit IIA. Smectite is greatly reduced in comparison to Units I and II, and both illite and chlorite are significantly higher (see "Lithostratigraphy" section, this chapter). Log responses in this unit are complex. Although silica is unusually high for much of the unit (500–566 mbsf), the first probable siltstone on the basis of log responses is at 470–477 mbsf, or lowest Subunit IIIA. Including this bed as Subunit IIIB, velocities are higher in the subunit than in any overlying unit, giving rise to a suite of high-amplitude seismic reflectors (see "Seismic Stratigraphy" section, this chapter).

Not all of the high-velocity interbeds, varying from <1 m to about 10 m in thickness, can be understood from log responses alone, but all are probably low in clay minerals in comparison

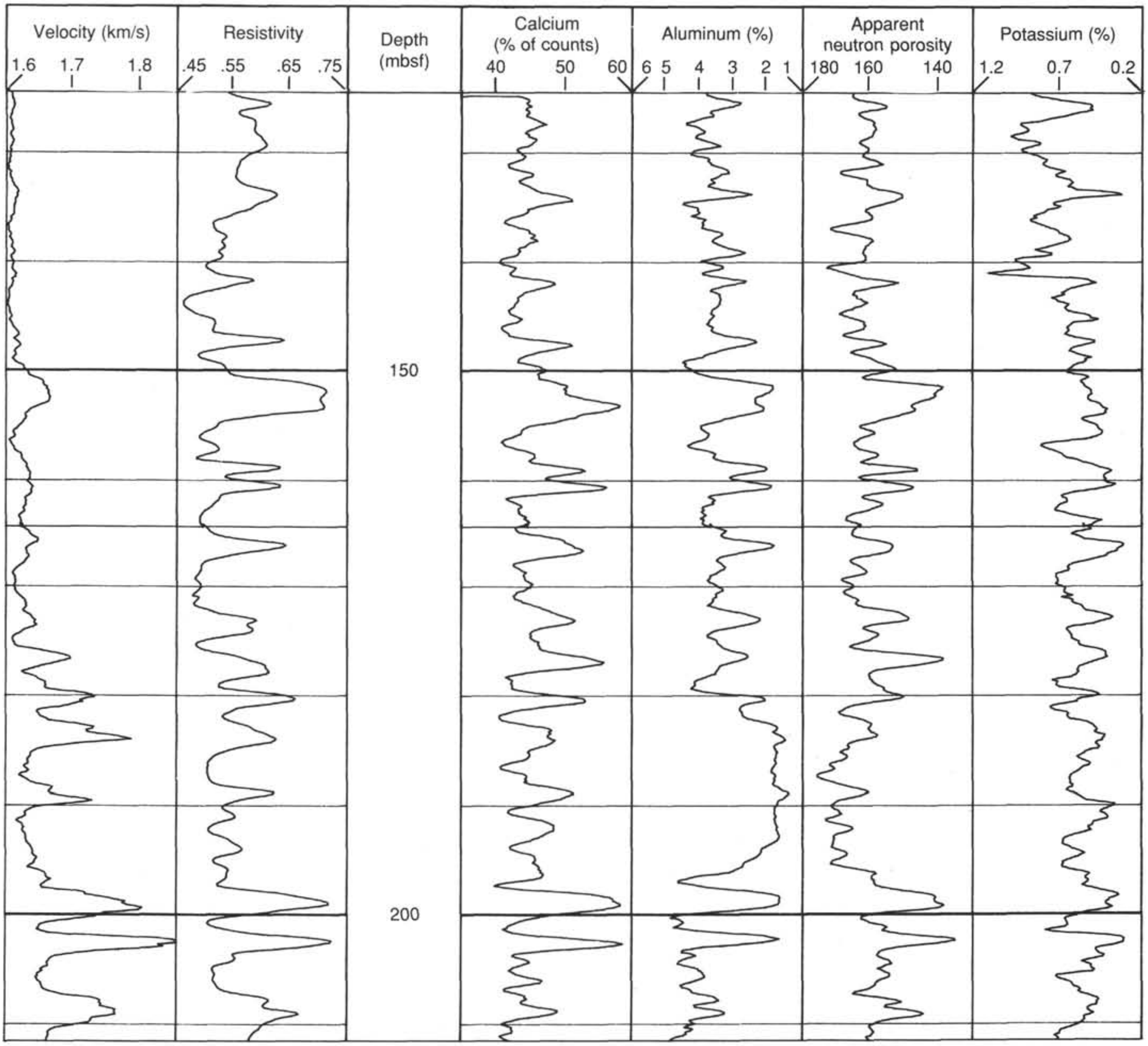

Figure 53. Comparison among porosity-sensitive logs (velocity, resistivity, and apparent neutron porosity) and geochemical logs (calcium, aluminum, and potassium) for an interval of alternating calcite and clay-rich beds. Note that the three tracks on the right have values increasing to the left, in contrast to the three tracks on the left, so that a lithologic change causes all tracks to move in the same direction.

with silt and sand-size grains. A low-velocity limit trend is evident on the velocity log, increasing from 1.65 km/s at the top of Subunit IIIB to 1.80 km/s in central Subunit IIIC, approximating the compaction response of pure clay. The high-velocity interbed at 470–477 mbsf has nondiagnostic log responses except for its high resistivity (low porosity); it may be a muddy silt.

Two very thin (< 1 m) beds at 491 and 494 mbsf (Fig. 52) are near the vertical resolution of the tools and of the depth shifting. Apparently, the upper bed is enriched in Si and the lower bed is enriched in Ca. Several fast beds are clearly enriched in Si (Fig. 55), presumably quartz, generally with low porosities suggestive of silt or sand and with a low content of clay minerals and therefore of potassium, thorium, and uranium: 502–509, 514–516, 538–542, and 570–572 mbsf. However, an intervening fast, very low-porosity bed at 559–567 mbsf is high not only in silica but also in potassium and especially in thorium; it may be a less mature silt, with biotite or potassium feldspar.

Subunit IIIC (573.7–698.9 mbsf) is dominantly claystone and silty claystone like Subunit IIB, but with less abundant sandstone and siltstone (see "Lithostratigraphy" section, this chapter). Most beds appear to be about 3 m thick, based particularly on the neutron log. Porosity lows correspond with high values of potassium and thorium, suggesting that the silts are rich in illite or biotite, whereas the claystones are rich in a nonradioactive clay such as montmorillonite.

Source Regions

Although some logged elements (e.g., U, S) are mobilized in the sediment column, others (e.g., Si, Fe, K, Th, and sometimes Ca) retain a record of the geochemistry of source regions. In

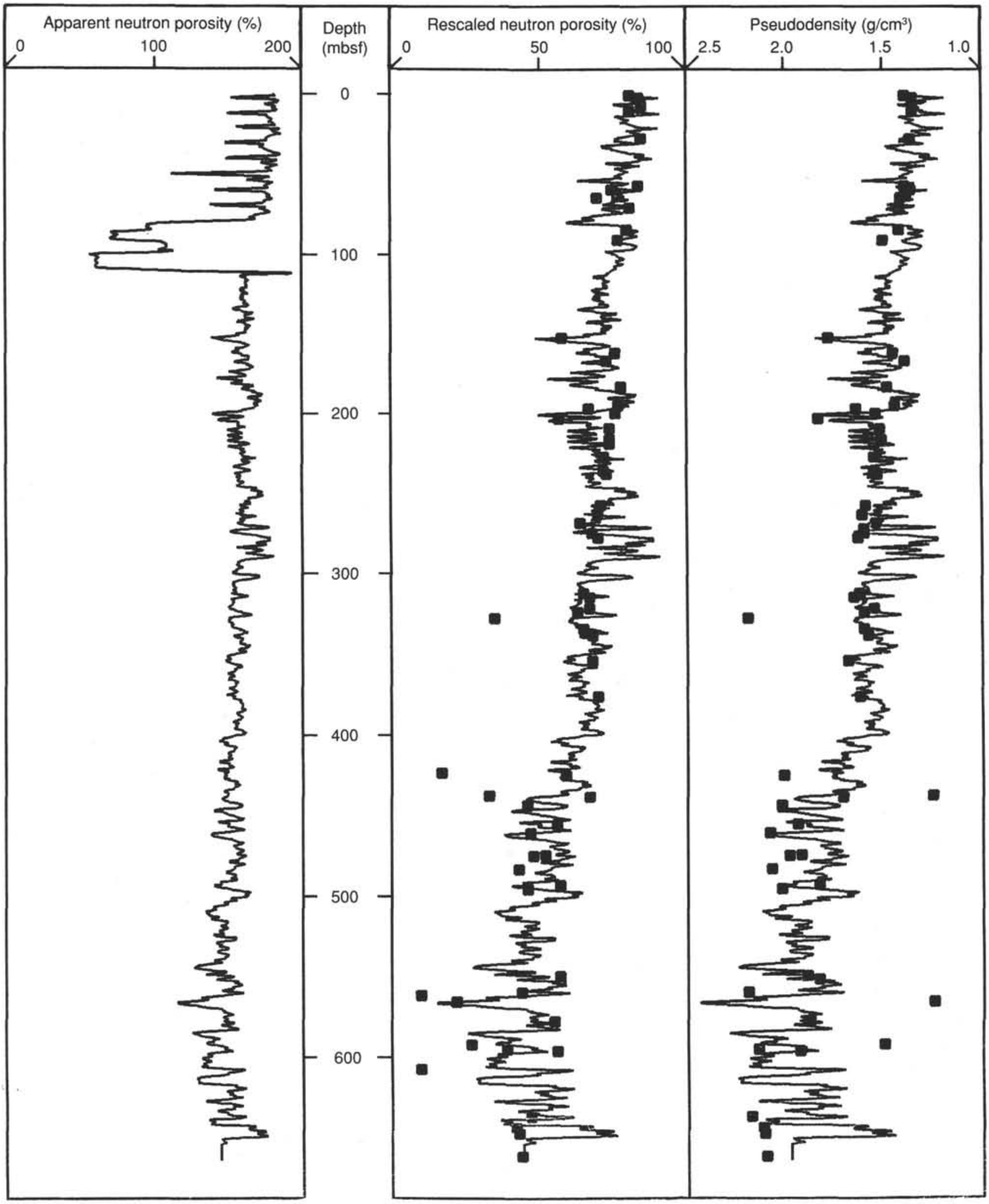

Figure 54. The plot on the left displays the raw log of apparent neutron porosity; the one in the center gives the rescaled neutron porosity log, to approximately match core porosity measurements (squares); and the plot on the right shows the pseudodensity log, which was calculated from the rescaled neutron porosity log and the core measurements of grain density, compared with the core density measurements (squares).

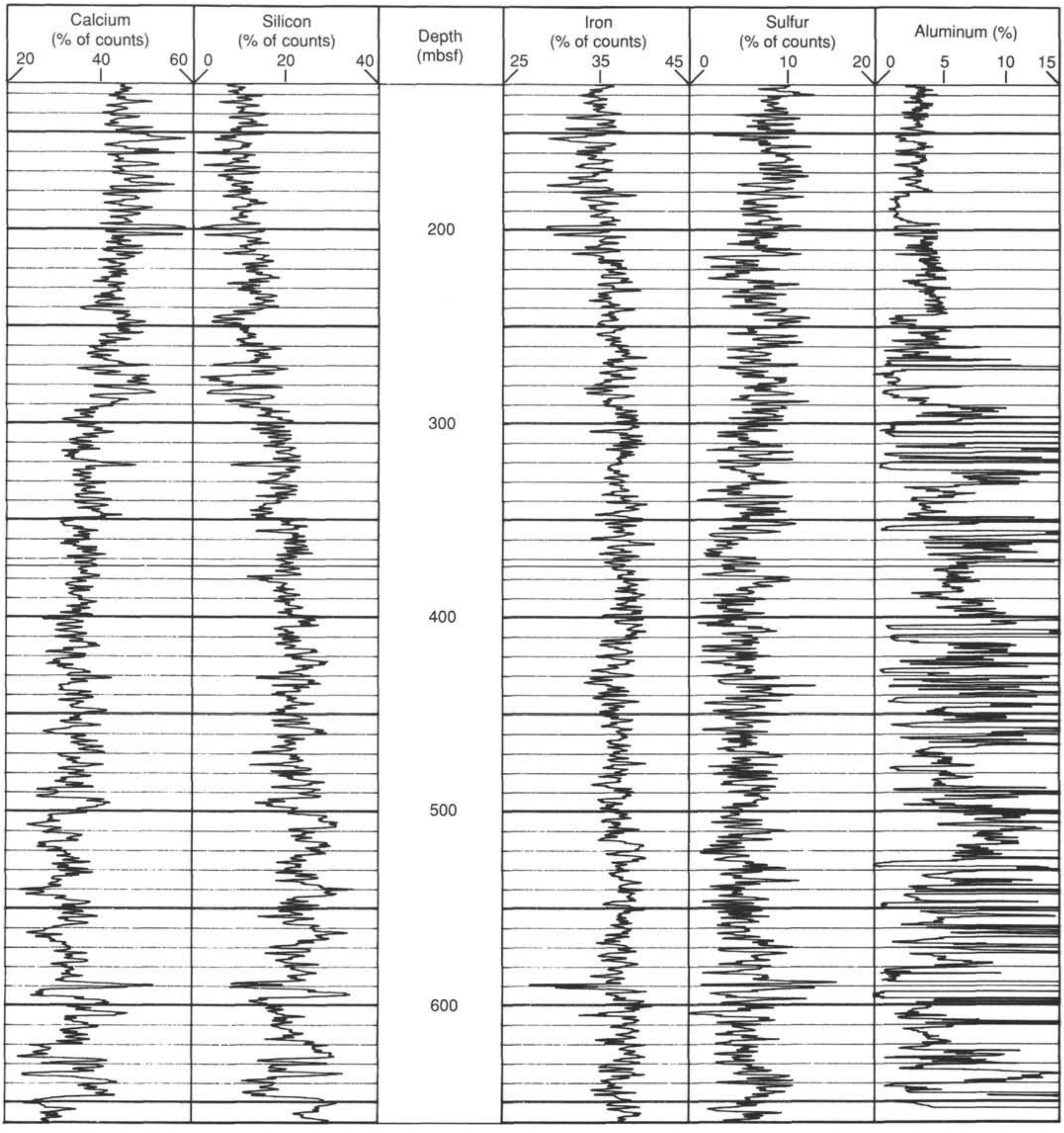

Figure 55. Geochemical logs from Hole 767B. Calcium, silicon, iron, and sulfur are expressed as percentage of the total counts for these four elements by the gamma spectroscopy tool. Aluminum is expressed as apparent volume percent, before calibration. Note that much of the aluminum log below 300 mbsf is considered to be unreliable because of inaccurate logging-speed corrections, as discussed in the text.

particular, acidic rocks such as granite are high in Si, K, and Th and low in Fe and Ca in comparison with andesites or even more basic rocks such as basalt. Thus, these elemental abundances in the logs can be used as a proxy indicator of acidic vs. basic sources, or of continentality of sources.

Here we use three source-region indicators: K, Th (Fig. 50), and Si (Fig. 55). Although our Si abundances are expressed as percentage of total counts Si + Fe + Ca + S rather than weight percentage, the usefulness of this log should not be strongly hampered. Serra (1986) shows that the ratio Si/(Fe + Ca) is much higher for acidic rocks than for basic rocks, and our Si ratio should be strongly correlated with this ratio, because the S component is very minor in comparison to Si, Fe, and Ca. Abundant biogenic calcite would adversely affect Si-index usefulness, but calcite is extremely low except for some thin beds in the interval from 150 to 270 mbsf (Fig. 53, and "Inorganic Geochemistry" section, this chapter).

Figures 50 and 55 exhibit a strong correlation among Si, K, and Th for long-term trends and short-term variability. These curves provide a qualitative picture of the changing composition of source rocks for Hole 767B through time. In the top 50 m, K implies an acidic source but Th does not; clay mineralogy indicates a small illite component (see "Lithostratigraphy" section, this chapter). Silica, potassium, and thorium decrease downhole to a minimum between 140 and 260 mbsf, an interval with a very low continentality index given the high smectite content and the absence of chlorite and illite.

From this least acidic level, K, Si, and Th rise throughout most of the interval from 210 to 460 mbsf, implying a waning of arc sources and increasingly acidic continental component downhole. This gradual change is indicated only in a subtle way by clay mineralogy data (see "Lithostratigraphy" section, this chapter). Indeed, the broad pattern shows substantial and important short-term variability. For example, the interval from 270 to 285 mbsf exhibits levels as low as those for 140–260 mbsf. From 460 mbsf to the deepest log data at 660 mbsf, the Si, K, and Th logs indicate rapid variations between highly acidic and somewhat basic sources, with a dominance of the more acidic sources. This interval corresponds to the interval of quite variable but generally high continentality given the clay mineralogy and the occurrence of quartz sands (see "Lithostratigraphy" section, this chapter). We concluded that the geochemical logs contain a continuous record of fluctuations in source regions for the interval from 0 to 660 mbsf at Hole 767B, but that a more quantitative analysis is needed.

Heat Flow

As discussed previously (see "Operations" section, this chapter), no successful heat flow measurements were obtained from the Uyeda probe at Site 767. Continuous temperature logs were obtained on the first and second deployments of the seismic stratigraphic logging tool string. Both runs exhibited thermal lags of 5–10 min, as a possible result of the inhibition of fluid flow past the thermistors by the end piece used to open and close the lockable flapper valve. This thermal lag does not significantly affect the temperatures discussed below, because in each case the tool remained at a depth long enough for thermal equilibration with the surrounding waters.

Bottom-water temperatures were measured as 3.85°C ± 0.1° on both runs. The minimum temperature measured was 3.55°C ± 0.1°, near the center of the water column. It is possible that the apparently slightly warmer bottom waters are an artifact of pipe conduction of formation heat, but pipe conduction for over 1 km seems unlikely. On deployment #1, the maximum temperature reached was 20.8°C at 298 mbsf. No circulation was used during this run, but substantial circulation occurred 7 hr earlier, associated with hole conditioning. On deployment #2, the deepest logged interval prior to extensive circulation and pipe movement was 283 mbsf, with a measured temperature of 21.8°C. The highest temperature encountered was 27.5°C at 538 mbsf, shortly after lowering the pipe past that depth.

Using averages of measured thermal conductivities (see "Physical Properties" section, this chapter), apparent heat flow can be calculated for the intervals 0–298, 0–283, and 283–538 mbsf. These estimates are minimum heat flows, because of insufficient time after circulation for complete equilibration of borehole temperatures with undisturbed formation temperatures. Thus, the heat flow estimate of 56 mW/m^2 for 0–298 mbsf obtained 7 hr after circulation is somewhat lower than the estimate of 62 mW/m^2 for almost the same depth interval obtained 19 hr after circulation. Equilibrium temperatures, if measured, would probably be 10%–30% higher than the 62 mW/m^2 estimate. The calculated heat flow for the lower interval is only 26 mW/m^2, clearly showing substantial cooling of borehole fluids caused by lowering the cold drill pipe into the lower portion of the hole immediately before the temperature tool was lowered to 538 mbsf.

SEISMIC STRATIGRAPHY

Multichannel seismic reflection profiles SO49-1 and SO49-2 (Fig. 56) were acquired aboard the *Sonne* in April 1987 and processed by the Bundesanstalt für Geowissenschaften und Rohstoffe (BGR) in February 1988 (see "Site Survey of the Celebes and Sulu Basins" chapter, this volume). In addition, pre-site single-channel seismic reflection data were shot aboard the *JOIDES Resolution* prior to drilling on 9 November 1988 (see "Underway Geophysics" chapter, this volume). *Sonne* navigation was obtained with transit satellites, Loran C, and doppler sonar. The *JOIDES Resolution* used the global positioning system (GPS) for the entire survey.

We interpreted the above data in our preparations for drilling Site 767. The structure of the lower plate is characterized by tilted fault blocks bounded by normal faults that are only weakly reactivated by the flexure of the plate. We noted a possible structural trend of N60E for the normal faults, given the correlations between line SO49-2 and a north-trending, single- channel seismic line recorded on board *JOIDES Resolution* as we left Site 767 (see "Underway Geophysics" chapter, this volume). These divergent seismic profiles (Fig. 57) show a reasonable correlation of southeast-facing blocks, spaced 10–20 km apart.

Correlation is more difficult to ascertain in the extreme northeast parts of respective profiles, but there a crustal block 10 km wide, bounded on both flanks by normal faults, can be identified in both profiles. The northeast-trending fault blocks may represent the fabric of the crust in this region (the orientations of sheeted dikes in the crust). This structural trend in the oceanic crust agrees with that of the magnetic anomalies mapped by Lee and McCabe (1986) in this part of the basin and by Weissel (1980) in the southwest part of the Celebes Sea. The trend is also close to that of the northeast-trending fault blocks along the southeast flank of the Sulu Archipelago (Hamilton, 1979).

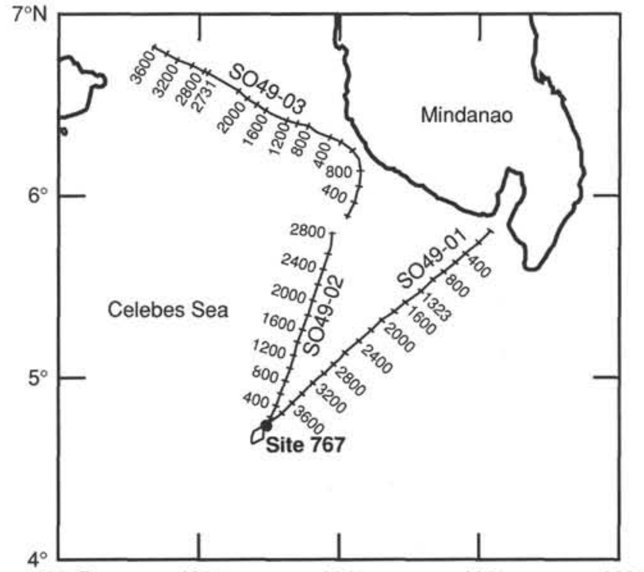

Figure 56. Location of geophysical lines in the Celebes and Sulu seas (from K. Hinz, BGR unpubl. rept. 103.463, 1988).

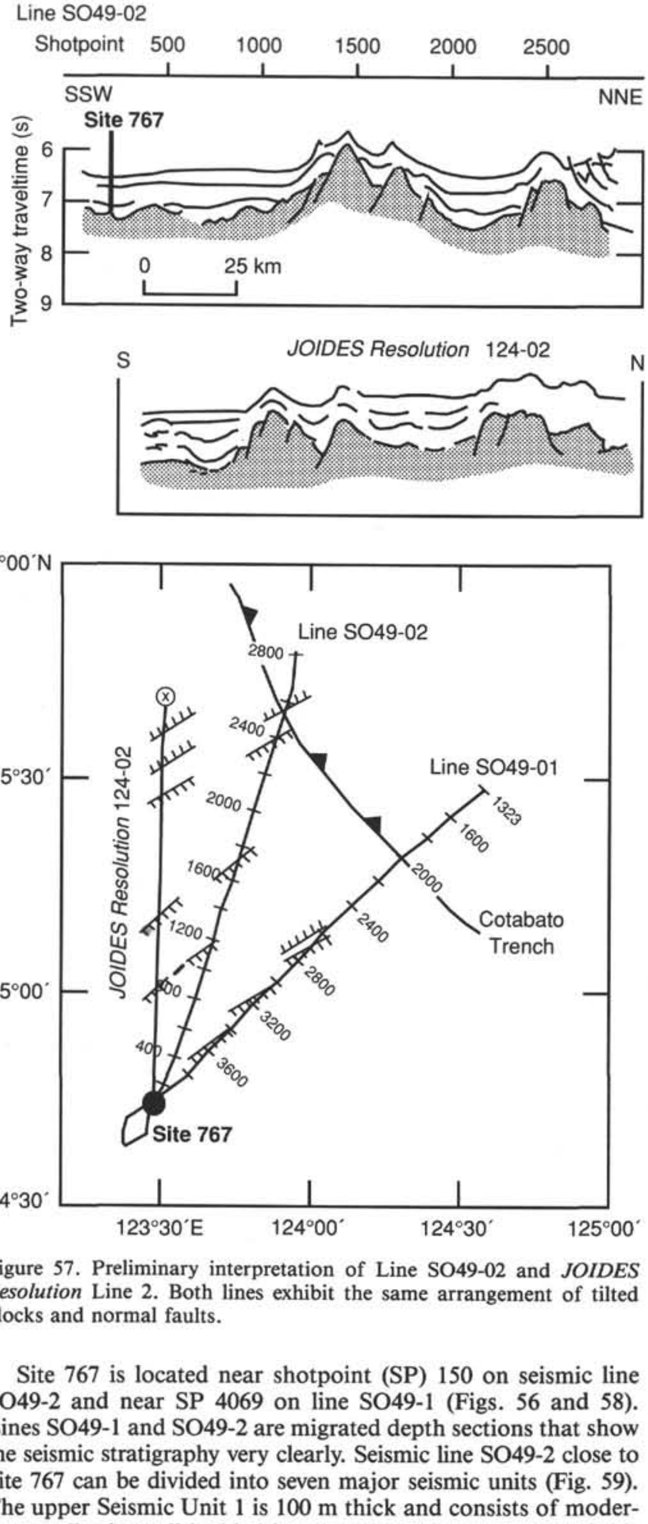

Figure 57. Preliminary interpretation of Line SO49-02 and *JOIDES Resolution* Line 2. Both lines exhibit the same arrangement of tilted blocks and normal faults.

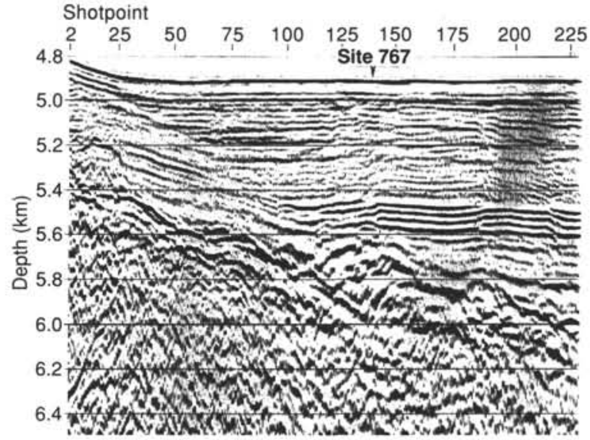

Figure 58. Migrated and depth-corrected multichannel seismic reflection profile SO49-2 crossing Site 767.

Site 767 is located near shotpoint (SP) 150 on seismic line SO49-2 and near SP 4069 on line SO49-1 (Figs. 56 and 58). Lines SO49-1 and SO49-2 are migrated depth sections that show the seismic stratigraphy very clearly. Seismic line SO49-2 close to Site 767 can be divided into seven major seismic units (Fig. 59). The upper Seismic Unit 1 is 100 m thick and consists of moderate-amplitude, well-bedded layers. The uppermost 50 m of this unit is nonreflecting. The seafloor, as seen on 3.5-kHz records, is cut by numerous very small channels, suggestive of the distal portion of a submarine fan system. Cored material, consisting of silty clay with local thin sand layers, thin ash, and carbonate turbidites, supports this interpretation.

Seismic Unit 2 is about 100 m thick and shows signs of local current bedding, with bedding terminations against both the upper and lower boundaries. Seismic Unit 3 is about 120 m thick, but it may be composed of two sequences. The first, Sequence 3A, shows numerous terminations on its upper boundary and a few on its lower. Sequence 3B has a weak tendency to develop clinoform bedding. The base of Sequence 3B has been dated as the Miocene/Pliocene boundary.

Seismic Unit 4 is about 220 m thick and is composed of two sequences, 4A and 4B. Sequence 4A is 40–60 m thick and is defined by clinoform reflectors, truncated at both the upper and lower boundaries of the sequence. Sequence 4B is 140–180 m thick and has local development of clinoform bedding.

Seismic Unit 5 has variable thickness. At Site 767 it is about 200 m thick, but it attains thicknesses of 350 m in the deepest part of the basin. The top of the unit is marked by a prominent set of high-amplitude reflectors. In this location, the high-amplitude reflectors form a set of four parallel, high-amplitude peaks. Beneath the prominent high-amplitude peaks is a variable thickness of low-amplitude reflectors that rest disconformably on the unit below. Seismic Unit 5 appears to be more restricted to structural basins since it pinches out at the margins of the basin.

Beneath Seismic Unit 5 is a layer that drapes the basement, attaining thicknesses of up to 200 m, and pinches out where the basement shoals. It has a very low-frequency signature on line SO49-2, but appears to be continuous with Seismic Unit 6 on line SO49-1. At Site 767, Seismic Unit 6 is about 100 m thick. We interpret Seismic Unit 7 to be a pelagic unit deposited on basaltic basement.

The basement reflector itself is of low frequency and high relative amplitude, and it is very irregular, indicative of oceanic crust. To the northeast of Site 767, we find tilted fault blocks to be a common basement structure. In the Site 767 region, numerous faults cut the basement and extend up through Sequence 4A. Some faults extend up into Seismic Unit 2, and none appear to cut Seismic Unit 1. Two faults appear to have a reverse sense of vertical separation. Thus, the regional pattern of faulting is complex and difficult to discern without additional seismic coverage.

Seismic Unit 1 corresponds to sediments of late Pleistocene age. We recognized the Brunhes/Matuyama boundary at 50 mbsf (see "Paleomagnetics" section, this chapter). This unit appears as reflectorless, perhaps indicative of the uniformity of the ash. Seismic Unit 2 corresponds to sediments of early Pleistocene age, although age determinations in this section were difficult (see "Biostratigraphy" section, this chapter). However, the first Pliocene sediments were recovered in the vicinity of 150 mbsf, just at the top of Seismic Unit 3. Upper Miocene was first noted at 311 mbsf, very close to the top of Sequence 4A. A

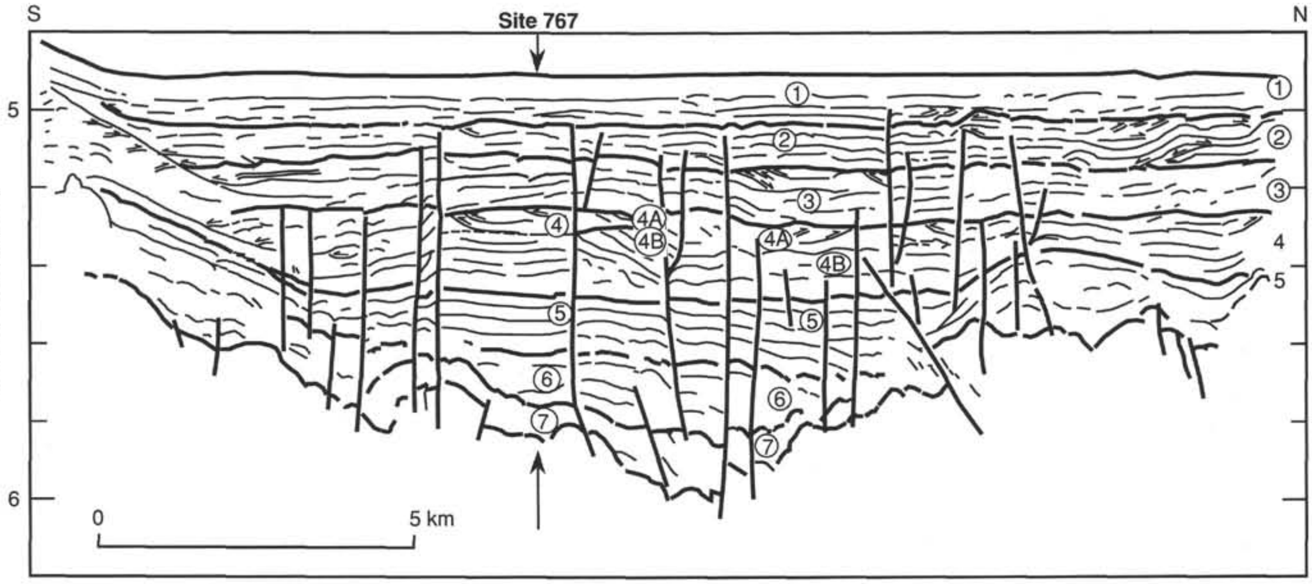

Figure 59. Line-drawing interpretation of seismic profile in Figure 57 illustrating the interpreted seismic stratigraphy in the region of Site 767.

broad peak in the seismic record within Sequence 4B was associated with an abundance of sand in Cores 124-767B-52X to -54X. One can say in general that the high-amplitude reflectors indicate the presence of sand in the section.

The upper part of Seismic Unit 5, consisting of four to five high-amplitude reflectors, coincides with increased terrigenous turbidite influx (see "Lithostratigraphy" section, this chapter), though no clear stratigraphic event was noted to account for the high-amplitude nature of the reflectors. We interpret the difference in amplitude with depth in Seismic Unit 5 to reflect subtle differences in abundances of sand and silt turbidites. These abundances do decrease in the core from the interval at 640–700 mbsf.

Seismic Unit 6 is marked by a seismic reflector that is followed by an unreflective zone for about 100 m to the basement reflector. This zone corresponds closely with a major change in lithology, from olive gray, ash-rich clays and silts, to red-brown clay, rich in manganese micronodules, associated with a significant decrease in sedimentation rate. Basement was reached at 786.9 mbsf, placing us at or near the crest of a small basement ridge in profile SO49-2.

Seismic impedance modeling with the velocity logs and 25-, 30-, and 35-Hz Ricker wavelets show a fair correspondence of amplitude distribution vs. depth for the synthetic and the seismic record (Fig. 60). The synthetic log was generated under the assumption that no significant impedance contrasts were associated with changes in density, so only the velocity log (shown in Fig. 60) was used to determine an impedance log. The impedance log was convolved with 25-Hz and 35-Hz Ricker wavelets to create synthetic seismograms. The result with the 25-Hz wavelet is shown in Figure 60. The synthetic seismogram shows a good correspondence with the migrated time record in the upper 450 mbsf. The reflectorless upper 50 m of Seismic Unit 1, the moderate amplitude reflectors between 50 and 300 mbsf, and the lower-amplitude zone down to 450 mbsf are also predicted on the synthetic. The high-amplitude set of reflectors at the top of Seismic Unit 5 occurs at 550 mbsf in the seismic record, but at about 470 mbsf in the synthetic. The base of the high-amplitude reflectors on the seismic record coincides with that of the synthetic record.

The high-amplitude reflectors at the top of Seismic Unit 5 seemed to suggest a major geological event, but drilling showed that this was not the case. The synthetic seismogram reasonably explains most of the observed character of the seismic record, but it predicts initiation of the high-amplitude unit higher in the section. This discrepancy is not understood at present and will require the addition of the density log as well. A major source of uncertainty is the seismic wavelet, which is likely to be a greater problem than the lack of a density log.

SUMMARY AND CONCLUSIONS

Site 767 records deposition within a deep basin below the CCD, as shown by the low carbonate content and paucity of calcareous biogenic particles in the pelagic/hemipelagic background sediment. Within that depositional framework are major changes in depositional processes and provenance of sediment. The major changes we have recognized are (1) an upward transition from pelagic clay deposition in Unit IV to deposition of volcanogenic hemipelagic mud in Units III to I; (2) an upward coarsening of hemipelagic muds from claystone in Unit III to clayey silt in Units II and I; (3) a major influx of quartz-bearing muddy to sandy turbidites with continental provenance in Unit III; (4) a variable influx of fine-grained carbonate turbidites in Units III and II; and (5) significant changes in frequency and composition of volcanic ash throughout the section.

The base of Site 767 is olivine basalt, with some vesicularity and quench texture, indicating that it is likely a flow. Overlying the apparent oceanic basement at Site 767 is a sequence of nearly 100 m of reddish brown claystones (Unit IV) that accumulated from middle Eocene to early Miocene time. On the seismic lines (see "Seismic Stratigraphy" section, this chapter), this sequence appears as if it is mantling the faulted basement. These deposits have the characteristics of deep-ocean pelagic clay: the fauna is sparse, consisting mainly of fish teeth, poorly preserved radiolarians, and agglutinated foraminifers; manganese oxide occurs as discrete micronodules; and rates of sedimentation were low (< 10 m/m.y.). Thin turbidites of volcanogenic silt in the upper part of Unit IV provide the first noticeable indication of volcanogenic sediment influx into the basin.

Unit III (lower to upper Miocene) records a significant increase in the rate of sedimentation in the basin as the result of a major episode of terrigenous turbidite deposition, accompanied by a change from pelagic clay to volcanogenic hemipelagic clay

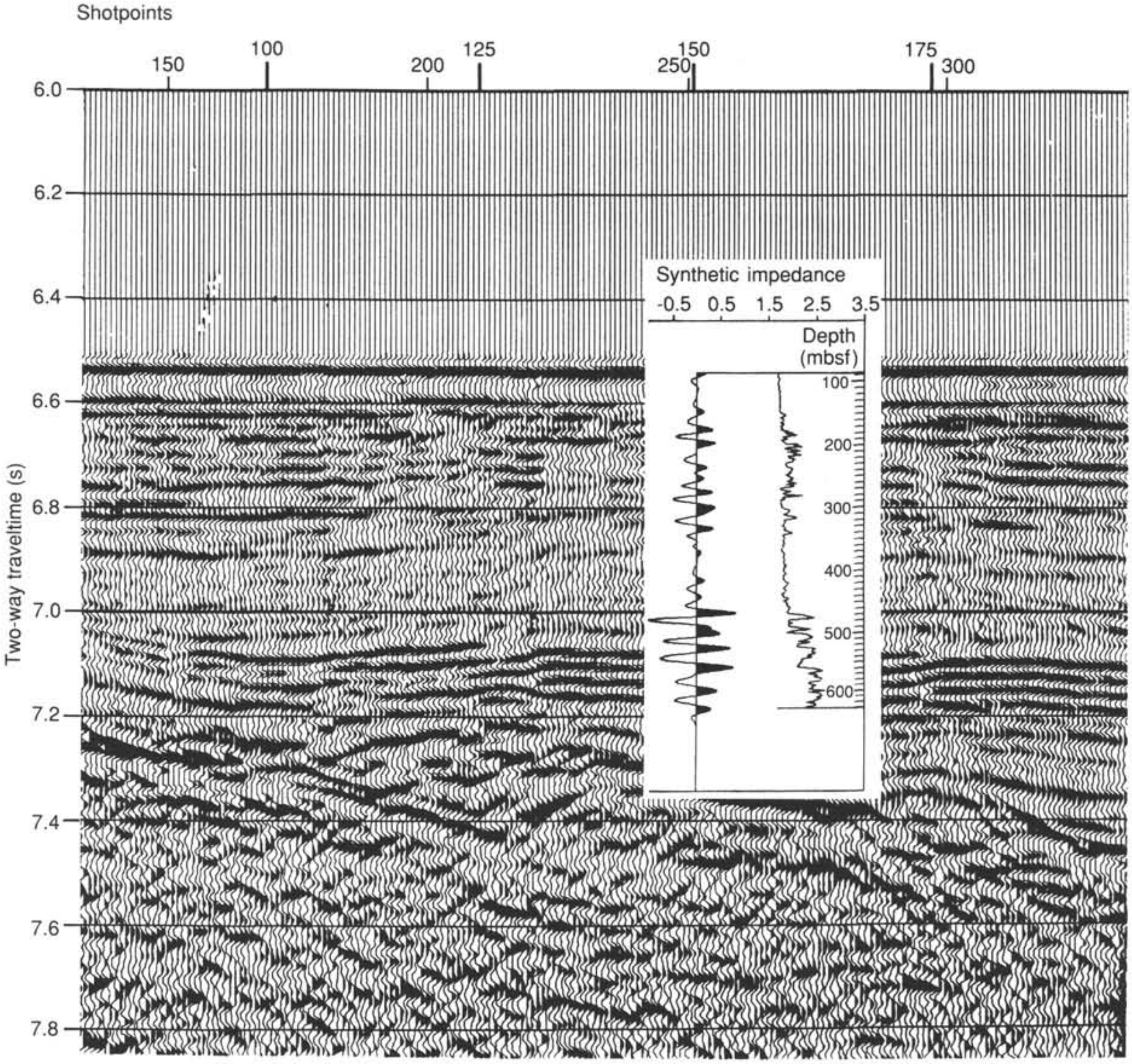

Figure 60. Migrated time section of multichannel seismic reflection profile of Line SO49-2, with synthetic seismogram inserted at the site. The insert shows the synthetic seismogram in the left wiggle trace and the velocity log in the right wiggle trace.

as the background sediment. The well-rounded quartz, abundant plant fragments, and coal clasts in the turbidites clearly demonstrate a continental provenance. The turbidite package appears to represent a single symmetrical depositional megacycle, with turbidite progradation followed by a waning of terrigenous turbidite deposition. The turbidites coarsen upward from silty claystone and claystone in Subunit IIIC to fine sand and rare conglomerate in Subunit IIIB, then fining upward again through Subunit IIIA.

The variation in grain size is accompanied by a change in relative proportion of turbidite to hemipelagic sediment: turbidites make up over 75% of the section in Subunit IIIB and decrease upward and downward in Subunits IIIA and IIIC, respectively. The large volume of thick, fine-grained turbidite beds and the abundance of plant debris suggest that the most likely source for this sediment was a major delta complex within a low-lying coastal plain. A prime candidate for such a delta is the North Mahakam Delta of Borneo, which provides the western Celebes Sea with sediments from the Crocker Belt, deposited along the rifted margin of the South China Sea.

During deposition of the early to late Miocene terrigenous turbidite cycle, the background hemipelagic sediment was predominantly clay. Within the overlying Unit II, the hemipelagic sediment gradually coarsens upward to clayey silt, with the silt-size component consisting largely of volcanic ash. This increase in grain size records a major increase in influx of airborne ash to the basin in late Miocene time, which is also reflected in the appearance of common ash layers in Unit II. This important volcanic influence on hemipelagic sedimentation has continued up to the present.

The waning of terrigenous turbidite deposition in the upper part of Unit III (middle to upper Miocene) was accompanied by the appearance of carbonate turbidite layers, which persist throughout the overlying Unit II (upper Miocene to Pleistocene). The composition and structures of these turbidites and the absence of carbonate in the enclosing hemipelagic sediment clearly indicate redeposition of shallower-water sediment into a deep basin below the CCD. Both shelf and deeper-water sources are indicated by the nature of the biogenic constituents in the turbidites, with a decrease in shelf-derived carbonate from early Pliocene to Pleistocene time (see "Biostratigraphy" section, this chapter). Redeposited carbonate beds are rare in Unit I.

Site 767 records several major events in the history of the Celebes Sea. The basement is basalt and overlain by middle Eocene red clays. The age is consistent with the magnetic anomaly interpretation by Weissel (1980), but not with the hypothesis of Lee and McCabe (1986). The basal red clays show low rates of sedimentation and the presence of manganese micronodules, fish teeth, and radiolarians, indicative of open-ocean environments. This part of the section corresponds well with that observed at DSDP Site 291 (Ingle, Karig, et al., 1975) in the southern Philippine Sea just to the east of the Philippine Islands (see "Geological Setting of the Celebes and Sulu Seas" chapter, this volume).

The boundary between Units II and III at 406 mbsf is present in a number of indicators. Methane, ethane, and total organic carbon are very low above this level and increase sharply below. The continentality index of clays, defined here as the log of the sum of the abundances of chlorite, smectite, and illite, divided by the abundance of smectite, increases dramatically at 406 mbsf and then decreases to red clay levels in the lower part of Subunit IIIC. Biotite disappears below 406 mbsf, and volume susceptibility drops dramatically. The high susceptibility and biotite content above 406 mbsf indicates the abundance of volcanic ash, whereas the high quartz and plant debris below that level are clear indications of continentality. The maximum in continental indicators and abundances of continentally derived turbidites in Subunit IIIB indicate the greatest continental influence in the middle Miocene.

Logs of silica, potassium, and thorium show a rise throughout depths from 210–460 mbsf, implying a waning of arc sources and increasing acidic continental component of the core downhole. From 460 to 660 mbsf the silica, potassium, and thorium logs show rapid variations between highly acidic and somewhat basic sources, with a dominance of the more acidic sources.

A significant lithologic change occurs between Subunits IIB and IIC (base of Pliocene) at 300 mbsf, above which the background sediment is a silt and below, a clay. Bulk and GRAPE density show a decrease just below 300 mbsf, and a corresponding increase in porosity and void ratio. Potassium, thorium, and silica show step increases and a calcium decrease below this level (see "Downhole Measurements" section, this chapter). This change suggests greater proximity to the volcanic source region in the Pliocene. Calcareous turbidites are most abundant in Subunit IIB, in Pliocene to early Pleistocene time.

Paleomagnetic studies of the oriented APC cores showed a very clear magnetic stratigraphy in the upper 100 m of the site. Changes in declination document the Brunhes/Matuyama boundary, both boundaries of the Jaramillo Event within the Matuyama, and an unidentified, short event below the Jaramillo, which may indicate a regional excursion.

The Celebes Sea originated in the middle Eocene in a setting like that of the southern Philippine Sea. From the early Miocene onward, the sea has been the site of high rates of volcanogenic turbidite deposition; but from the early to late middle Miocene, continental sources played a major role in providing sediments to the basin. By late Miocene time, the continental sources were cut off, perhaps caused by the initiation of the Cotabato and North Sulawesi trenches, which now act to trap sediment along the margins of the basin. In the late Pleistocene, abundant volcanic ash, much of it air-fall in origin, dominated the sedimentation of the Celebes Sea.

REFERENCES

Augustithis, S. S., 1979. *Atlas of the Textural Patterns of Basic and Ultrabasic Rocks and Their Genetic Significance:* New York (Walter de Gruyter).

Banerjee, S. K., 1980. Magnetism of the oceanic crust: evidence from ophiolite complexes. *J. Geophys. Res.,* 85:3556–3566.

Barron, J. A., 1985a. Late Eocene to Holocene diatom biostratigraphy of the equatorial Pacific Ocean, Deep Sea Drilling Project Leg 85. *In* Mayer, L., Theyer, F., et al., *Init Repts. DSDP,* 85: Washington (U.S. Govt. Printing Office), 413–456.

________, 1985b. Miocene to Holocene planktic diatoms. *In* Bolli, H. M., Saunders, J. B., and Perch-Nielsen, K. (Eds.), *Plankton Stratigraphy:* Cambridge (Cambridge Univ. Press), 763–810.

Berggren, W. A., Kent, D. V., and Flynn, J. J., 1985a. Jurassic to Paleogene: Part 2. Paleogene geochronology and chronostratigraphy. *In* Snelling, N. J. (Ed.), *The Chronology of the Geological Record.* Geol. Soc. Mem. (London), 10:141–195.

Berggren, W. A., Kent, D. V., Flynn, J. J., and Van Couvering, J. A., 1985b. Cenozoic geochronology. *Geol. Soc. Am. Bull.,* 96:1407–1418.

Berggren, W. A., Kent, D. V., and Van Couvering, J. A., 1985c. The Neogene: Part 2, Neogene geochronology and chronostratigraphy. *In* Snelling, N. J. (Ed.), *The Chronology of the Geological Record.* Geol. Soc. Mem. (London), 10:211–260.

Bernard, B. B., 1979. Light hydrocarbons in marine sediments [Ph. D. dissert.]. Texas A&M Univ., College Station.

Broecker, W. S., Andree, M., Klas, M., Bonani, G., Wolfli, W., and Oeschger, H., 1988. New evidence from the South China Sea for an abrupt termination of the last glacial period. *Nature,* 333:156–158.

Burckle, L. H., 1972. Late Cenozoic diatom zones from the eastern equatorial Pacific. *Nova Hedwigia,* 39:217–246.

________, 1977. Pliocene and Pleistocene diatom datum levels for the equatorial Pacific. *Quat. Res.,* 7:330–340.

Cann, J. R., 1969. Spilites from the Carlsberg Ridge, Indian Ocean. *J. Petrol.,* 10:1–19.

Claypool, G. E., and Kvenvolden, K. A., 1983. Methane and other hydrocarbon gases in marine sediment. *Annu. Rev. Earth Planet. Sci.,* 11:299–327.

Clement, B. M., and Kent, D. V., 1986/87. Short polarity intervals within the Matuyama: transitional field records from hydraulic piston corded sediments from the North Atlantic. *Earth Planet. Sci. Lett.,* 81:253–264.

Dean, W. E., and Gardner, J. W., 1982. Origin and geochemistry of redox cycles of Jurassic to Eocene age, Cape Verde Basin (DSDP Site 367), continental margin of northwest Africa. *In* Schlanger, S. O., and Cita, M. B. (Eds.), *Nature and Origin of Cretaceous Carbon-Rich Facies*: London (Academic Press), 55–78.

Doyle, P. S., and Riedel, W. R., 1985. Cenozoic and Late Cretaceous ichthyoliths. *In* Bolli, H. M., Saunders, J. B., and Perch-Nielsen, K. (Eds.), *Plankton Stratigraphy:* Cambridge (Cambridge Univ. Press), 965–994.

Durand, B., and Monin, J. C., 1980. Elemental analysis of kerogens (C, H, O, N, S, Fe). *In* Durand, B. (Ed.), *Kerogen:* Paris (Ed. Technip), 113–142.

Engel, A.E.J., Engel, C. G., and Havens, R. G., 1965. Chemical characteristics of oceanic basalts and the upper mantle. *Geol. Soc. Am. Bull.,* 76:719–734.

Ewart, A., 1979. A review of the mineralogy and chemistry of Tertiary-Recent dacitic, latitic, rhyolitic and related salic volcanic rocks. *In* Barker, F. (Ed.), *Trondhjemites, Dacites, and Related Rocks:* Amsterdam (Elsevier), 13–121.

Faber, E., Dumke, I., and Gerling, P., 1988. Gaseous hydrocarbons of unknown origin found while drilling. *In* Novelli, L., and Mattavelli, G. (Eds.), *Advances in Organic Geochemistry, 1987* (Vol. 13): London (Pergamon Press), 875–879.

Gartner, S., Jr., 1977. Calcareous nannofossil biostratigraphy and revised zonation of the Pleistocene. *Mar. Micropaleontol.,* 2:1–25.

Gieskes, J. M., 1975. Chemistry of interstitial waters of marine sediments. *Annu. Rev. Earth Planet. Sci.,* 3:433–453.

________, 1983. The chemistry of interstitial waters of deep-sea sediments: interpretation of deep-sea drilling data. *In* Riley, J. P., and Chester, R. (Eds.), *Chemical Oceanography* (Vol. 8): London (Academic Press), 222–269.

Gieskes, J. M., Elderfield, H., Lawrence, J. R., Johnson, J., Meyers, B., and Campbell, A., 1982. Geochemistry of interstitial waters and sediments, Leg 64, Gulf of California. *In* Curray, J. R., Moore, D. G., et al., *Init. Repts. DSDP,* 64: Washington (U.S. Govt. Printing Office), 675–694.

Gieskes, J. M., Kastner, M., and Warner, T. B., 1975. Evidence for extensive diagenesis, Madagascar Basin, Deep Sea Drilling Site 245. *Geochim. Cosmochim. Acta,* 39:1385–1393.

Gieskes, J. M., and Lawrence, J. R., 1981. Alteration of volcanic matter in deep sea sediments: evidence from the chemical composition of interstitial waters from deep sea drilling cores. *Geochim. Cosmochim. Acta,* 45:1687–1703.

Griffin, J. J., Windom, H., and Goldberg, E. D., 1968. The distribution of clay minerals in the world ocean. *Deep-Sea Res.,* 15:433–459.

Hamilton, W., 1979. Tectonics of the Indonesian region. *Geol. Surv. Prof. Pap. (U.S.),* No. 1078.

Hanshaw, B. B., and Coplen, T. B., 1973. Ultrafiltration by a compacted clay membrane. II. Sodium ion exclusion at various ionic strengths. *Geochim. Cosmochim. Acta,* 37:2311.

Hatherton, T., and Dickinson, W. R., 1968. The relationship between andesitic volcanism and seismicity in Indonesia, the Lesser Antilles, and other island arcs. *J. Geophys. Res.,* 74:5301–5310.

Holm, P. E. 1985. The geochemical fingerprints of different tectonomagmatic environments using hygromagmatophile element abundances of tholeiitic basalts and basaltic andesites. *Chem. Geol.,* 51: 303–323.

Hunt, J., 1979. *Petroleum Geochemistry and Geology:* San Francisco (Freeman).

Ingle, J., Karig., D. E., et al., 1975. *Init. Repts. DSDP,* 31: Washington (U.S. Govt. Printing Office).

Jacobs, J. A., 1984. *Reversals of the Earth's Magnetic Field:* Bristol U.K. (Adam Hilger).

Kastens, K. A., Mascle, J., et al., 1987. *Proc. ODP, Init. Repts.,* 107: College Station, TX (Ocean Drilling Program).

Kastner, M., and Gieskes, J. M., 1976. Interstitial water profiles and sites of diagenetic reactions, Leg 35, DSDP, Bellingshausen Abyssal Plain. *Earth Planet. Sci. Lett.,* 33:11–20.

Lee, C. S., and McCabe, R., 1986. The Banda-Celebes-Sulu basins: a trapped piece of Cretaceous Eocene oceanic crust? *Nature,* 322: 51–54.

Ling, H. Y., 1973. Radiolaria: Leg 31 of the Deep Sea Drilling Project. *In* Karig, D. E., Ingle, J. C., Jr., et al. *Init. Repts. DSDP,* 31: Washington (U.S. Govt. Printing Office), 703–762.

Macdonald, G. A., and Katsura, T., 1964. Chemical composition of Hawaiian lavas. *J. Petrol.,* 5:82–133.

McDuff, R. E., and Gieskes, J. M., 1981. Major cation gradients in DSDP interstitial waters: the role of diffusive exchange between seawater and upper oceanic crust. *Geochim. Cosmochim. Acta,* 45: 1705–1713.

Mammerickx, J., Fisher, R. L., Emmel, F. J., and Smith, S. M., 1976. Bathymetry of the east and southeast Asian seas. *Geol. Soc. Am.,* MC-17.

Manheim, F. T., 1976. Interstitial waters of marine sediments. *In* Riley, J. P., and Chester, R. (Eds.), *Chemical Oceanography* (Vol. 6): London (Academic Press), 115–186.

Manheim, F. T., and Sayles, F. L., 1974. Composition and origin of interstitial waters of marine sediments, based on deep sea drill cores. *In* Goldberg, E. D. (Ed.), *The Sea* (Vol. 5): *Marine Chemistry*: New York (Wiley-Interscience), 527–568.

Mankinen, E. A., Donnelly, J. M., and Gromme, C. S., 1978. Geomagnetic polarity event recorded at 1.1 m.y. B.P. on Cobb Mountain, Clear Lake volcanic field, California. *Geology,* 6:653–656.

Marine, I. W., and Fritz, S. J., 1981. Osmotic model to explain anomalous hydraulic heads. *Water Pressure Res.,* 17:73.

Martini, E., 1971. Standard Tertiary and Quaternary calcareous nannoplankton zonation. *In* Farinacci, A. (Ed.), *Proceedings of the Second International Conference on Planktonic Microfossils, Roma:* Rome (Ed. Tecnoscienza), 739–785.

Martinson, D. G., Mienke, W., and Stoffa, P., 1982. An inverse approach to signal correlation. *J. Geophys. Res.,* 87:4807–4808.

Mitchell, A.H.G., Hernandez, F., and Dela Cruz, A. P., 1986. Cenozoic evolution of the Philippine Archipelago. *J. Southeast Asian Earth Sci.,* 1:3–22.

Moore, C., Mascle, A., Taylor, E., Andreieff, P., Alvarez, F., Barnes, R., Beck, C., Behrmann, J., Blanc, C., Brown, K., Clark, M., Dolan, J., Fisher, A., Gieskes, J., Hounslow, M., McLellan, P., Moran, K., Ogawa, Y., Sakai, T., Schoonmaker, J., Vrolijk, P., Wilkens, R., and Williams, C., 1988. Tectonics and hydrogeology of the northern Barbados Ridge: results from Ocean Drilling Program Leg 110. *Geol. Soc. Am. Bull.,* 100:1578–1593.

Moore, G. F., and Silver, E. A., 1983. Collision processes in the northern Molucca Sea. *In* Hayes, D. E. (Ed.), *The Tectonic and Geologic Evolution of Southeast Asian Seas and Islands* (Pt. 2). Am. Geophys. Union Monogr., 27:360–372.

Moore, T. C., 1971. Radiolaria. *In* Tracey, J. I., Sutton, G. H., et al., *Init. Repts. DSDP,* 8: Washington (U.S. Govt. Printing Office), 727–775.

Mottl, M. J., and Holland, H. D., 1978. Chemical exchange during hydrothermal alteration of basalt by seawater–I. Experimental results for major and minor components of seawater. *Geochim. Cosmochim. Acta,* 42:1103–1115.

Müller, C., 1979. Calcareous nannoplankton from the North Atlantic (Leg 48). *In* Montadert, L., Roberts, D. G., et al., *Init. Repts. DSDP,* 48: Washington (U.S. Govt. Printing Office), 589–639.

________, 1985. Late Miocene to Recent biostratigraphic and paleoenvironmental results from the Mediterranean based on calcareous nannoplankton. *In* Stanley, D. J., and Wezel, F. C. (Eds.), *Geological Evolution of the Mediterranean Basin:* Berlin-Heidelberg-New York (Springer-Verlag), 471–485.

Murauchi, S., Ludwig, W. J., Den, N., Notta, H., Asanuma, T., Yoshii, T., Kubotera, A., and Hagiwara, K., 1973. Structure of the Sulu Sea and the Celebes Sea. *J. Geophys. Res.,* 78:3437–3447.

Rangin, C., 1989. The Sulu Sea: a back-arc basin setting within a Neogene collision zone. *Tectonophysics,* 161:119–141.

Raymer, L. L., Hunt, E. R., and Gardner, J. S., 1980. An improved sonic transit time-to-porosity transform. *SPWLA 21st Ann. Log. Symp. Trans.,* Paper P.

Riedel, W. R., and Sanfilippo, A., 1970. Radiolaria, Leg 4, Deep Sea Drilling Project. *In* Bader, R. G., Gerard, R. D., et al., *Init. Repts. DSDP,* 4: Washington (U.S. Govt. Printing Office), 503–575.

________, 1971. Cenozoic radiolaria from the western tropical Pacific. *In* Winterer, E. L., Riedel, W. R., et al., *Init. Repts. DSDP,* 7: Washington (U.S. Govt. Printing Office), 1529–1672.

________, 1978. Stratigraphy and evolution of tropical Cenozoic radiolarians. *Micropaleontology,* 23:81–96.

Rosenfeld, J. K., 1979. Ammonium adsorption in nearshore anoxic sediments. *Limnol. Oceanogr.,* 24:356–364.

Sanfilippo, A., Westberg-Smith, M. J., and Riedel, W. R., 1985. Cenozoic Radiolaria. *In* Bolli, H. M., Saunders, J. B., and Perch-Nielsen, K. (Eds.), *Plankton Stratigraphy:* Cambridge (Cambridge Univ. Press), 631–712.

Sayles, F. L., and Manheim, F. T., 1975. Interstitial solutions and diagenesis in deeply buried marine sediments: results from the Deep Sea Drilling Project. *Geochim. Cosmochim. Acta,* 39:103–127.

Sclater, J. G., Parsons, B., and Jaupart, C., 1981. Oceans and continents: similarities and differences in the mechanisms of heat loss. *J. Geophys. Res.,* 86:11,535–11,552.

Serra, O., 1986. *Fundamentals of Well-Log Interpretation* (Vol. 2): *The Interpretation of Logging Data:* Amsterdam (Elsevier).

Shipboard Scientific Party, 1987. Site 645. *In* Srivastava, S., Arthur, M. A., et al., *Proc. ODP, Init. Repts.,* 105: College Station, TX (Ocean Drilling Program), 61–418.

________, 1988a. Site 722. *In* Prell, W., Niitsuma, N., et al., *Proc. ODP, Init. Repts.,* 117: College Station, TX (Ocean Drilling Program), 255–317.

________, 1988b. Site 723. *In* Prell, W., Niitsuma, N., et al., *Proc. ODP, Init. Repts.,* 117: College Station, TX (Ocean Drilling Program), 319–384.

Silver, E. A., McCaffrey, R., and Smith, R. B., 1983. Collision, rotation, and the initiation of subduction in the evolution of Sulawesi, Indonesia. *J. Geophys. Res.,* 88:9407–9418.

Silver, E. A., and Moore, J. C., 1978. The Molucca Sea collision zone, Indonesia. *J. Geophys. Res.,* 83:1681–1691.

Stainforth, R. M., Lamb, J. L, Luterbacher, H. P., Beard, J. H., and Jeffords, R. M., 1975. Cenozoic planktonic foraminiferal zonation and characteristics of index forms. *Univ. Kansas Paleontol. Contrib.,* No. 62.

Suess, E., von Huene, R., et al., 1988. *Proc. ODP, Init. Repts.,* 112: College Station, TX (Ocean Drilling Program).

van Marle, L. J., van Hinte, J. E., and Nederbragt, A. J., 1987. Plankton percentage of the foraminiferal fauna in seafloor samples from the Australian–Irian Jaya continental margin, Eastern Indonesia. *Mar. Geol.,* 77:151–156.

von Breymann, M. T., and Suess, E., 1988. Magnesium in the marine sedimentary environment: Mg-NH_4 ion exchange. *Chem. Geol.,* 70: 359–371.

von Huene, R., and Lee, H., 1982. The possible significance of pore fluid pressures in subduction zones: studies in continental margin geology. *AAPG Mem.,* 37:781–789.

Walker, D., Shibata, T., and DeLong, S., 1979. Abyssal tholeiites from the Oceanographer Fracture Zone. *Contrib. Mineral. Petrol.,* 70: 111–125.

Watts, A., 1975. Gravity field of the Northwest Pacific Ocean Basin and its margin: Philippine Sea. *Geol. Soc. Am. Map Chart Ser.,* MC-12.

Weissel, J. K., 1980. Evidence for Eocene oceanic crust in the Celebes Basin. *In* Hayes, D. E. (Ed.), *The Tectonic and Geologic Evolution of Southeast Asian Seas and Islands.* Am. Geophys. Union Monogr., 23:37–47.

Wright, R. G., 1977. Planktonic-benthonic ratio in foraminifera as paleobathymetric tool: quantitative evaluation. *Annu. Am. Assoc. Petr. Geol. Soc. Econ. Paleontol. Mineral. Conf.,* Washington, D.C., No. 65 (Abstract).

Ms 124A-110

NOTE: All core description forms ("barrel sheets") and core photographs have been printed on coated paper and bound as Section 3, near the back of the book, beginning on page 423.

Summary Log for Site 767

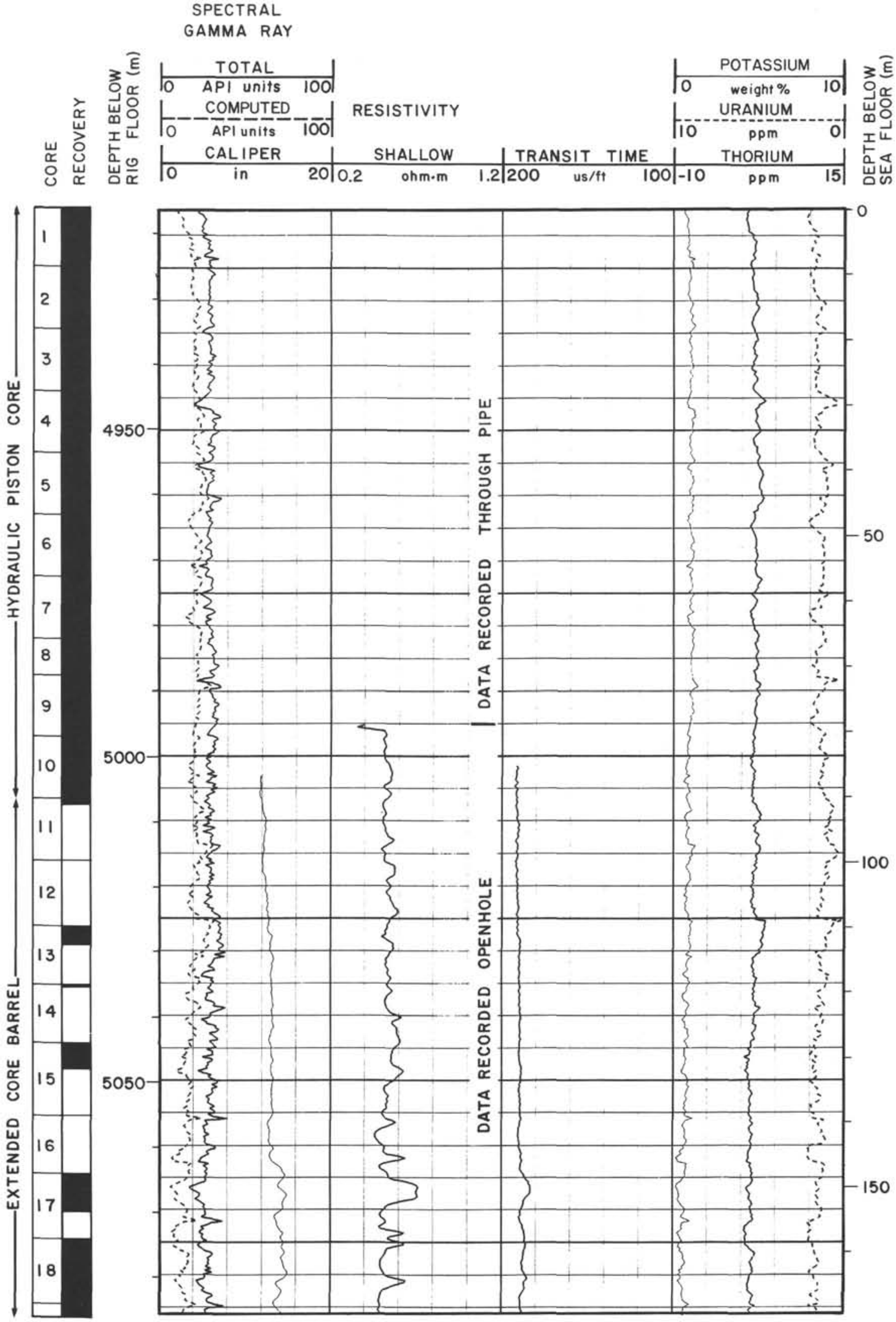

Summary Log for Site 767 (continued)

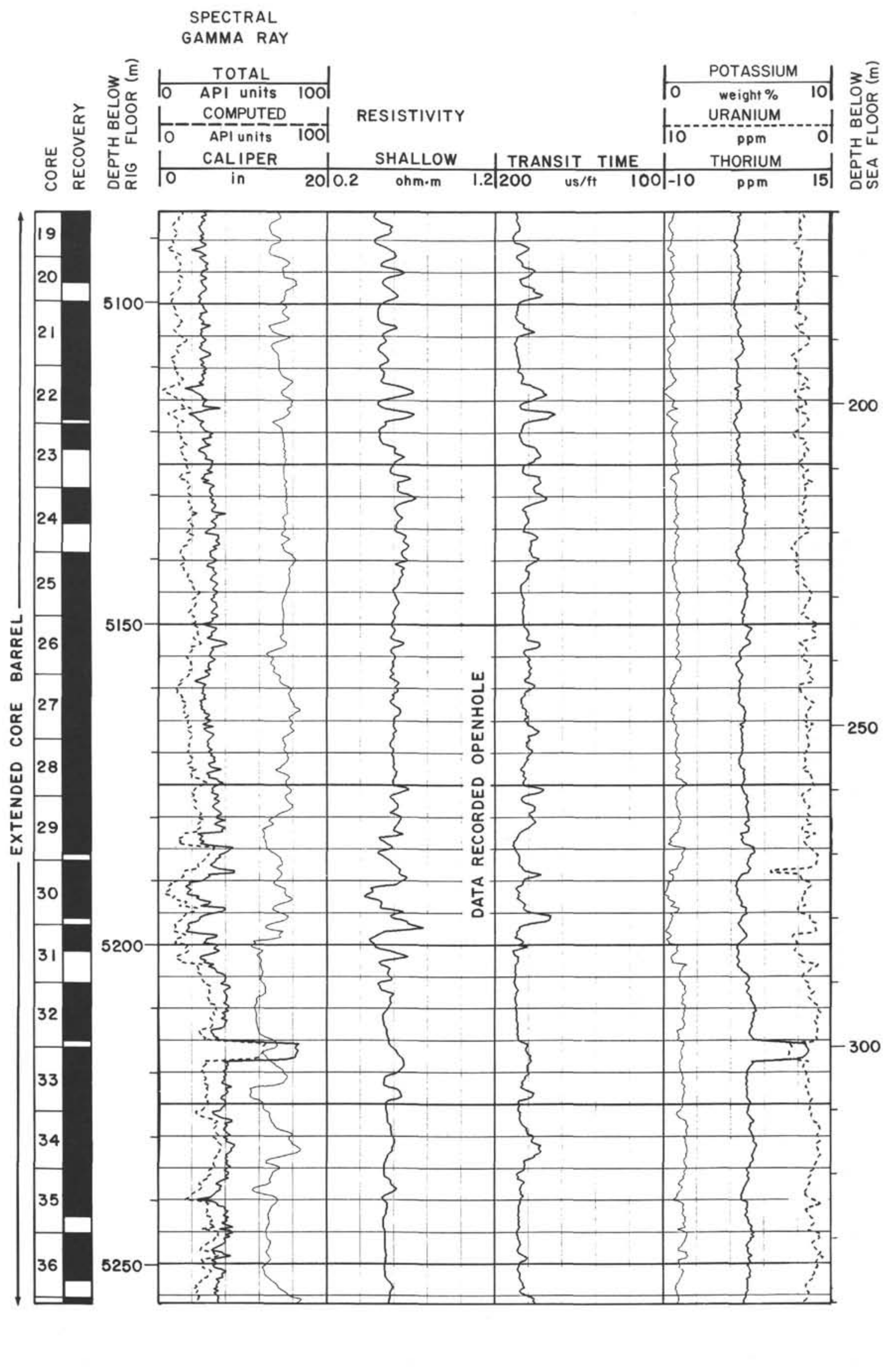

Summary Log for Site 767 (continued)

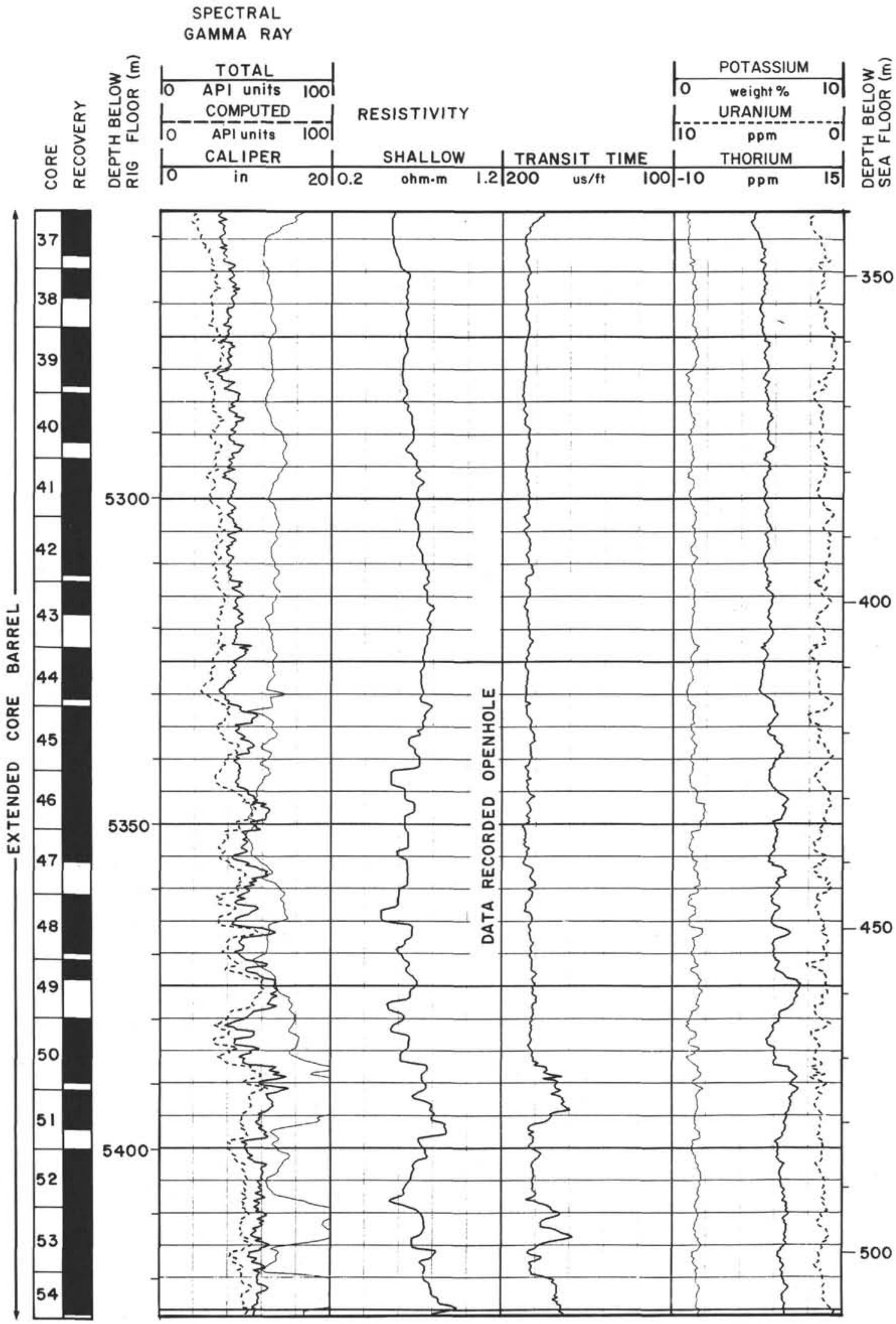

Summary Log for Site 767 (continued)

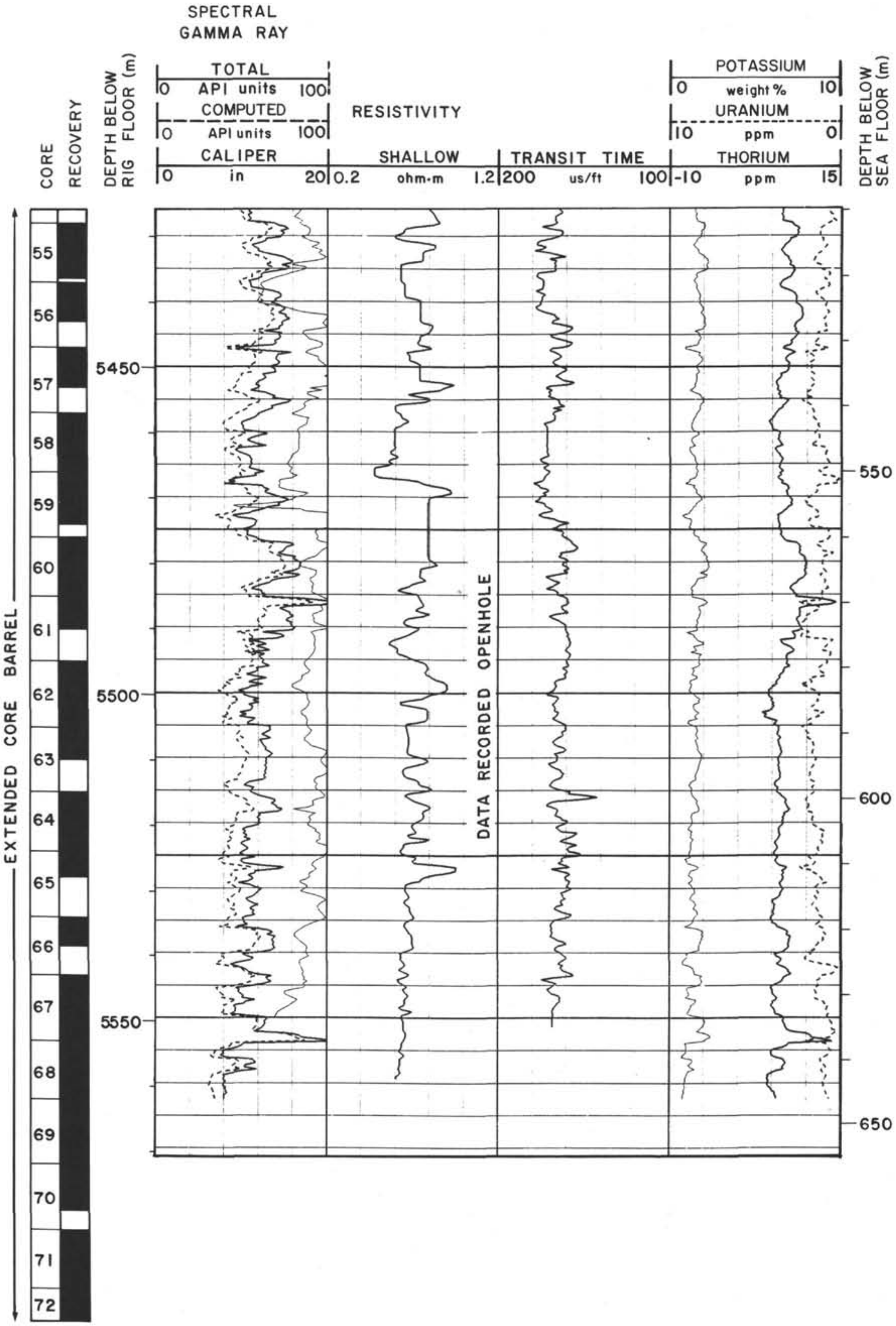

Summary Log for Site 767 (continued)

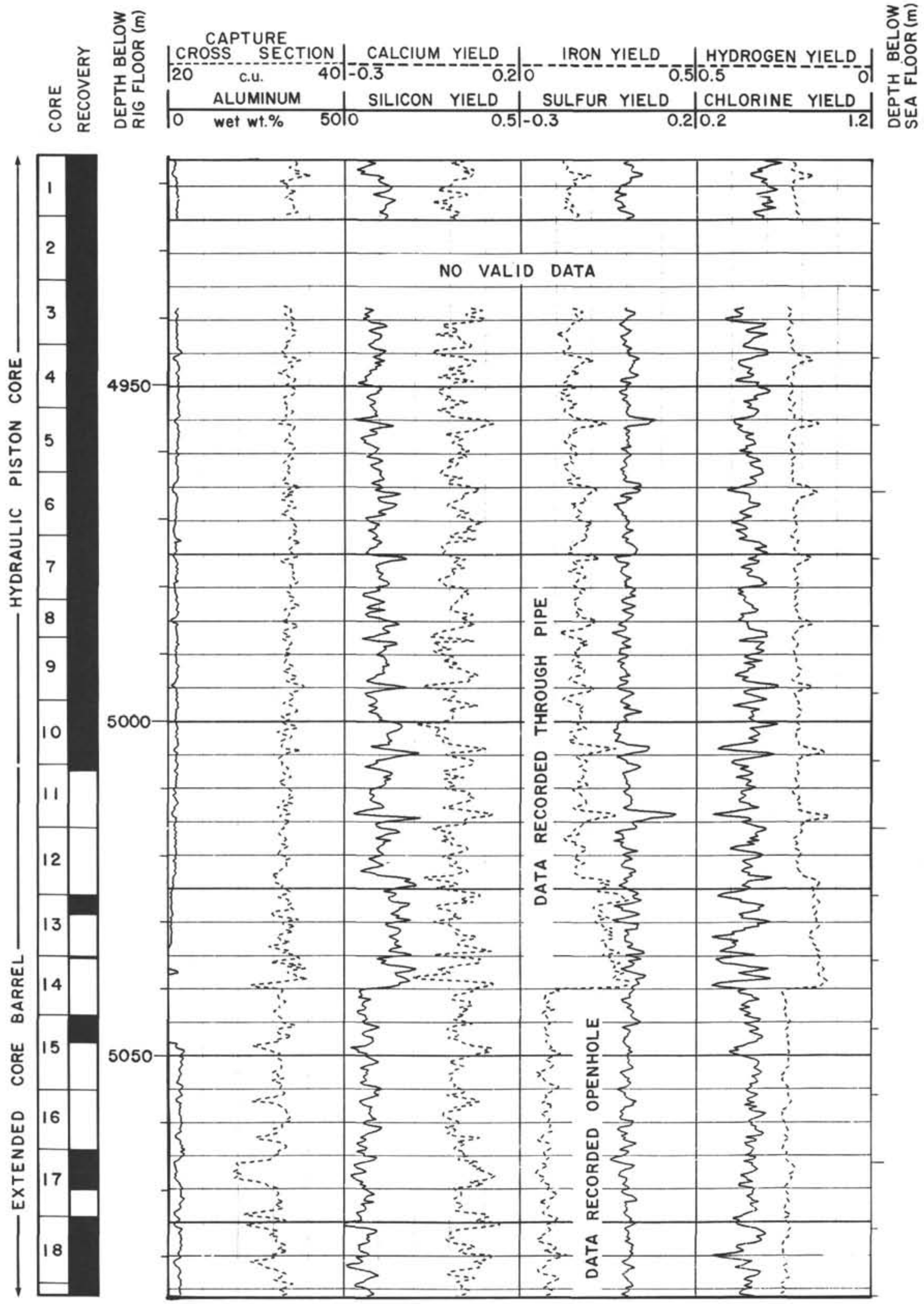

Summary Log for Site 767 (continued)

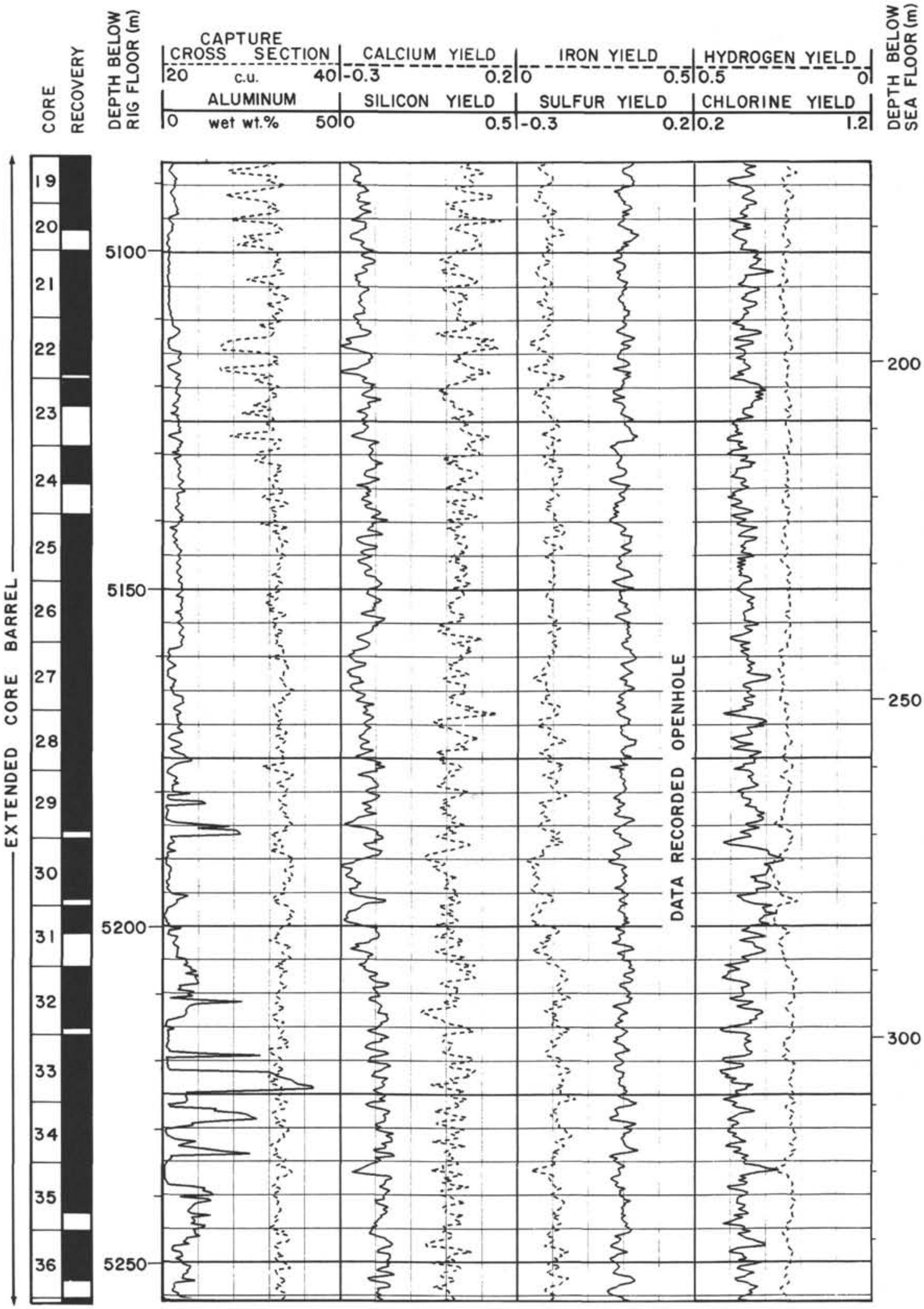

Summary Log for Site 767 (continued)

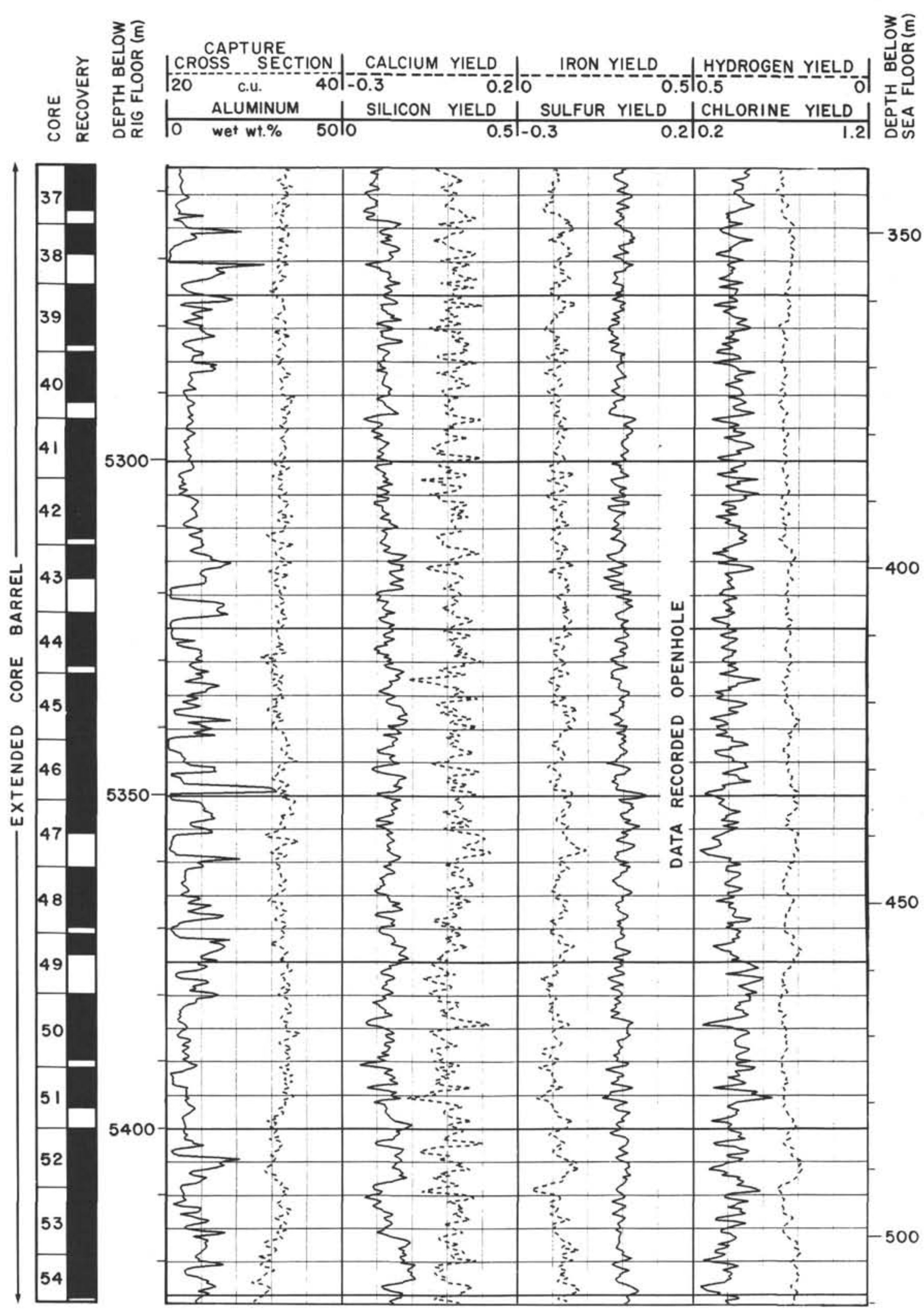

Summary Log for Site 767 (continued)